

EXPERIMENTALLY VERIFIED NUMERICAL SIMULATION OF  
SINGLE CRYSTAL GROWTH PROCESS WITH A LOW MELT HEIGHT  
AND AN AXIAL VIBRATION

by

Aidin Sheikhi

B.S., Mechanical Engineering, Khaje Nasireddin Toosi University of Technology, 2008

M.S., Mechanical Engineering, Bogazici University, 2012

Submitted to the Institute for Graduate Studies in  
Science and Engineering in partial fulfilment of  
the requirements for the degree of  
Doctor of Philosophy

Graduate Program in Mechanical Engineering

Boğaziçi University

2018

EXPERIMENTALLY VERIFIED NUMERICAL SIMULATION OF  
SINGLE CRYSTAL GROWTH PROCESS WITH A LOW MELT HEIGHT  
AND AN AXIAL VIBRATION

APPROVED BY:

Assoc. Prof. Ercan Balıkçı .....

(Thesis Supervisor)

Assoc. Prof. Hakan Ertürk .....

Assist. Prof. Nazlı Dönmezer .....

Assist. Prof. Melis Şerefoglu .....

Assoc. Prof. Necip Ünlü .....

DATE OF APPROVAL: 22.06.2018

## ACKNOWLEDGEMENTS

I would like to thank my parents Mohammad Sheikhi and Amansoltan Sheikhi for their continuous support, encouragement, and sympathy in my whole life, especially during my education at Bogazici University.

Undoubtedly, I am grateful to my advisor, Dr. Ercan Balıkçı, for giving me the opportunity to take part in TUBITAK 212M030 project, a part of which has formed this Ph.D. dissertation. I should express my appreciation to him for his passion, wise guidance, patience, and constant support and encouragement during my graduate studies. Also, I want to express my sincere thanks to Dr. Ali Eçder and Dr. Jeremy K. Mason for their help in the beginning of this work and Dr. Nuri Ersoy for his compassion and support. Additionally, I would like to thank members of my committee, Dr. Hakan Ertürk, Dr. Melis Şerefoğlu (Koç University), Dr. Nazlı Dönmezer, and Dr. Necip Ünlü (Istanbul Technical University) for their valuable advice and suggestions.

I would like to thank all my colleagues and friends, especially Mr. Pouya Yousefi Louyeh for his valuable contributions as my partner in this project. I also want to acknowledge my friend, Dr. Mehdi Montakhab, for his favorable suggestions in my research.

The work in this study is funded by The Scientific and Technological Research Council of Turkey (TUBITAK), under the grant number 212M030. I am thankful for their support.

## ABSTRACT

### **EXPERIMENTALLY VERIFIED NUMERICAL SIMULATION OF SINGLE CRYSTAL GROWTH PROCESS WITH A LOW MELT HEIGHT AND AN AXIAL VIBRATION**

This Ph.D. dissertation investigates experimental and numerical crystal growth of antimony-doped germanium (Ge-Sb) single crystals. The investigation is a part of the TUBITAK project 212M030. The single crystal growth of Ge-Sb from the melt is investigated by the Vertical Bridgman (VB), Axial Heat Processing (AHP), and Axial Vibrational Control (AVC) techniques. The effects of method dependent growth parameters on the quality of the grown single crystals have been analyzed. To this end, two different pulling rates (10 mm/h and 20 mm/h), different initial melt heights (5 mm, 10 mm, 14 mm, and 58 mm), and three different sets of vibrational parameters (2 mm amplitude and 0.25 Hz frequency, 0.25 mm amplitude and 1 Hz frequency, and 0.25 mm amplitude and 25 Hz frequency) are applied in the growth of seven different crystals. It is observed that the highest single crystal length with the most homogeneous solute redistribution and the least dislocation density are achieved in an AHP crystal which is grown with the lowest pulling rate (10 mm/h). However, it is determined that an appropriate control of the vibration parameters in the AVC technique makes it possible to achieve almost the same crystal quality with doubled growth rate, so the production yield is decreased.

Moreover, global and local numerical simulations are performed in order to investigate the effects of the growth parameters on the convective flow patterns. Also, results of the numerical simulations contribute to make better and more reliable interpretations of the experimental observations. The simulation results provide useful information for the experimentalists to investigate the effects of growth parameters on the temperature and solute distribution, flow pattern, and the interface shape. According to the numerical results, it is possible to clarify how the insertion of the baffle, adjusting the melt height, and optimizing the vibrational parameters of the baffle contribute the thermal and the solutal homogenization in the melt, interface stability, and consequently improved crystal quality.

## ÖZET

### **DÜŞÜK SIVI YÜKSEKLİĞİYLE VE EKSENEL TİTREŞİMLE BÜYÜTÜLMÜŞ TEK KRİSTALLERİN DENEYSEL OLARAK ONAYLANMIŞ NÜMERİK SİMÜLASYONU**

Bu Ph.D. tezi antimony (Sb) ile katkılı germanyum (Ge) tek kristallerinin deneysel ve sayısal simülasyon ile kristal büyümesini incelemektedir. Bu araştırma 212M030 numaralı TÜBİTAK projesinin bir parçasıdır. Ge-Sb'nin sıvıdan tek kristal büyümesi, Vertical Bridgman (VB), Axial Heat Processing (AHP) ve Axial Vibrational Control (AVC) yöntemleri ile incelenmiştir. Metot bağımlı büyüme parametrelerinin büyütülen tek kristallerin kalitesi üzerindeki etkileri analiz edilmiştir. Bu amaçla, iki farklı çekme hızı (10 mm/saat ve 20 mm/saat), farklı başlangıç sıvı yükseklikleri (5 mm, 10 mm, 14 mm ve 58 mm) ve üç farklı titreşim parametre seti (2 mm genlik ve 0.25 Hz frekans, 0.25 mm genlik ve 1 Hz frekans, 0.25 mm genlik ve 25 Hz frekans) ile yedi farklı kristal büyütülmüştür. Katışkı atomlarının en homojen yeniden dağılımı, en küçük dislokasyon yoğunluğu, ve en yüksek tek kristal uzunluğu en düşük çekme hızıyla (10 mm/saat) büyütülen bir AHP kristalinde elde edildiği gözlenmiştir. Ancak, AVC tekniğindeki titreşim parametrelerinin optimum kontrolü, iki kat çekme hızıyla neredeyse aynı kristal kalitesini elde etmeyi ve üretim verimliliğinin artmasını mümkün kılmıştır.

Diğer taraftan, büyüme parametrelerinin konvektif akış üzerindeki etkilerini araştırmak için global ve yerel sayısal simülasyonlar yapılmıştır. Ayrıca, sayısal simülasyonların sonuçları, deneysel gözlemlerin daha iyi ve güvenilir yorumlanmasına katkıda bulunmuştur. İlaveten, simülasyon sonuçları, büyüme parametrelerinin sıcaklık ve katışkı dağılımı, akış şekli ve arayüzey şekli üzerindeki etkilerini araştırmak için deneysel çalışma yapan araştırmacılara yararlı bilgiler sağlamaktadır. Simülasyon sonuçları, sıvıdaki akışın hızının ve hem sıvı hem de kristal içindeki sıcaklık alanın değerlerini sağlar. Bu bilgilere göre, sıvı yüksekliğinin ayarlanması ve sıvıdaki titreşim parametrelerinin optimize edilmesi, özellikleri iyileştirilmiş kristallerin büyütülmesine katkı sağlar.

## TABLE OF CONTENTS

ACKNOWLEDGEMENTS .....	iii
ABSTRACT.....	iv
LIST OF FIGURES .....	ix
LIST OF TABLES .....	xx
LIST OF SYMBOLS .....	xxi
LIST OF ACRONYMS/ABBREVIATIONS .....	xxv
1. INTRODUCTION .....	1
2. SCIENTIFIC BACKGROUND .....	4
2.1. Solidification.....	4
2.1.1. Thermodynamics .....	4
2.1.2. Kinetics .....	6
2.2. Crystal Growth from the Melt.....	12
2.2.1. Available Methods .....	12
2.3. Solute redistribution.....	18
2.3.1. Equilibrium Solidification (Infinite diffusion in liquid and solid) .....	18
2.3.2. Complete mixing in liquid and no diffusion in solid .....	19
2.3.3. Diffusional mixing in liquid and no diffusion in solid .....	20
2.3.4. Partial mixing in liquid and no diffusion in solid .....	21
2.3.5. Floating Zone method .....	22
2.4. Dislocations.....	24
2.4.1. Formation.....	24
2.4.2. Visualization .....	24
2.5. Morphological Stability .....	26

2.5.1. Constitutional Supercooling .....	26
2.5.2. Mullins and Sekerka Criterion .....	27
2.5.3. Favier and Rouzaud Approach .....	29
2.5.4. Kinetic Stability .....	30
2.6. Solidification Modeling Methods .....	32
3. MOTIVATION AND OBJECTIVES .....	33
4. MATERIALS AND METHODS .....	35
4.1. Experimental Apparatus and Procedures .....	35
4.1.1. Crystal Growth Unit.....	35
4.1.2. Experimental Procedures .....	39
4.1.3. Characterization .....	41
4.2. ANSYS Fluent Solidification/Melting Model .....	44
4.2.1. Global Geometry.....	47
4.2.2. Local Geometry .....	52
5. RESULTS .....	53
5.1. Experimental Results .....	53
5.1.1. VB20-58.....	54
5.1.2. AHP10-10 .....	57
5.1.3. AHP20-14 .....	60
5.1.4. AHP20-5 .....	62
5.1.5. AVC20-15-0.25-25 .....	65
5.1.6. AVC20-20-0.25-1 .....	67
5.1.7. AVC20-10-2-0.25 .....	69
5.1.8. Dislocations .....	73
5.2. Numerical Simulations.....	77
5.2.1. Global Geometry.....	77
5.2.2. Local Geometry .....	82

5.3. Species Transport.....	95
5.3.1. Setup and Initialization .....	95
5.3.2. Solute redistribution results .....	96
6. DISCUSSION .....	110
6.1. Melt height .....	110
6.2. Radial temperature gradient .....	115
6.3. Convective flow .....	115
6.4. Solute redistribution.....	118
6.5. Vibrational parameters .....	124
6.6. Dislocations.....	127
6.7. Interface shape and Morphological Instability.....	134
7. CONCLUSIONS.....	140
8. FUTURE WORK.....	143
REFERENCES .....	144
APPENDIX A: FLUENT GRAPHICAL USER INTERFACE (GUI) FIGURES .....	161
APPENDIX B: DISLOCATION FIGURES .....	170



## LIST OF FIGURES

Figure 2.1. Variation of the Gibbs free energy for pure metals [31]. .....	5
Figure 2.2. Phase diagram of Ge-Sb [32]. .....	6
Figure 2.3. Variation of the free energy of the system with respect to the radius of the embryo [31]. .....	7
Figure 2.4. Interfacial energy relationships between the Mould (M), the Liquid (L), and the solid (S) [31]. .....	9
Figure 2.5. Comparison of growth kinetics [30]. .....	11
Figure 2.6. Schematic of Czochralski method [41]. .....	13
Figure 2.7. Schematic of the Floating Zone method [53]. .....	14
Figure 2.8. Vertical Bridgman configuration. ....	15
Figure 2.9. Schematic of AHP / AVC configuration. 1) Crucible, 2) Four-zone furnace, 3) Pedestal, 4) Water cooled molybdenum rod, 5) Baffle. T1 to T3 are baffle thermocouples, T4 to T7 are pedestal thermocouples, and T8 to T13 are crucible thermocouples. ....	17
Figure 2.10. Equilibrium solute redistribution [30]. .....	19
Figure 2.11. Scheil solute redistribution profile [30]. .....	20
Figure 2.12. Diffusional mixing solute redistribution profile [30]. .....	21

Figure 2.13. Solute redistribution in FZ method. Solid crystal(S), Liquid zone (L), and solid charge of the FZ method are also shown [30]. .....	22
Figure 2.14. Comparison of analytical solute redistribution models [30]. .....	23
Figure 2.15. Visualization of dislocations with different etchants. ....	25
Figure 2.16. Striations at the onset of instability and the growth rate components. ....	30
Figure 2.17. KS stability for different vicinal angles. ....	31
Figure 4.1. The crystal growth unit used in BUSCG LAB. ....	36
Figure 4.2. Internal parts of the growth chamber [15]. ....	38
Figure 4.3. A crystal cut into two halves for revealing the characterization of the grown crystal. ....	42
Figure 4.4. Four-point-probe schematic grid points. ....	43
Figure 4.5. 16 zones where Dislocation densities are determined. ....	44
Figure 4.6. Global geometry. ....	48
Figure 4.7. Mesh of the global geometry. ....	49
Figure 4.8. Local Geometry and the created mesh. ....	51
Figure 5.1. Striations (a) and isoconcentrations (b) of VB20-58. ....	55
Figure 5.2. Radial solute redistribution of VB20-58. ....	56

Figure 5.3. Axial solute redistribution of VB20-58. The red dashed line shows where the single crystallinity is ended.....	56
Figure 5.4. Striations (a) and isoconcentrations (b) of AHP10-10. ....	58
Figure 5.5. Solidification parameters during the growth for AHP10-10. ....	58
Figure 5.6. Radial solute redistribution of AHP10-10.....	59
Figure 5.7. Axial solute redistribution of AHP10-10. The red dashed line shows where the single crystallinity is ended.....	59
Figure 5.8. Striations (a) and isoconcentrations (b) of AHP20-14. ....	60
Figure 5.9. Solidification parameters during the growth for AHP20-14. ....	61
Figure 5.10. Radial solute redistribution of AHP20-14.....	61
Figure 5.11. Axial solute redistribution of AHP20-14. The red dashed line shows where the single crystallinity is ended. ....	62
Figure 5.12. Striations (a) and isoconcentrations (b) of AHP20-5. ....	63
Figure 5.13. Solidification parameters during the growth for AHP20-5. ....	63
Figure 5.14 Radial solute redistribution of AHP20-5.....	64
Figure 5.15. Axial solute redistribution of AHP20-5. The red dashed line shows where the single crystallinity is ended. ....	64
Figure 5.16. Striations (a) and isoconcentrations (b) of AVC20-15-0.25-25.....	66
Figure 5.17. Solidification parameters during the growth for AVC20-15-0.25-25.....	66

Figure 5.18. Radial solute redistribution of AVC20-15-0.25-25.....	67
Figure 5.19. Axial solute redistribution of AVC20-15-0.25-25. The red dashed line shows where the single crystallinity is ended.....	68
Figure 5.20. Striations (a) and isoconcentrations (b) of AVC20-20-0.25-1.....	69
Figure 5.21. Solidification parameters during the growth for AVC20-20-0.25-1.....	70
Figure 5.22. Radial solute redistribution of AVC20-20-0.25-1.....	70
Figure 5.23. Axial solute redistribution of AVC20-20-0.25-1. The red dashed line shows where the single crystallinity is ended.....	71
Figure 5.24. Striations (a) and isoconcentrations (b) of AVC20-10-2-0.25.....	71
Figure 5.25. Solidification parameters during the growth for AVC20-10-2-0.25.....	72
Figure 5.26. Radial solute redistribution of AVC20-10-2-0.25.....	73
Figure 5.27. Axial solute redistribution of AVC20-10-2-0.25. The red dashed line shows where the single crystallinity is ended.....	74
Figure 5.28. Radial distribution of dislocation densities of VB20-58 in 5 mm, 15 mm, 25 mm, and 35 mm axial heights.....	75
Figure 5.29. Radial distribution of dislocation densities of AHP10-10 in 7 mm, 17 mm, 27 mm, and 37 mm axial heights.....	75
Figure 5.30. Radial distribution of dislocation densities of AHP20-5 in 7 mm, 17 mm, 27 mm, and 37 mm axial heights.....	76

Figure 5.31. Radial distribution of dislocation densities of AHP20-14 in 5 mm, 15 mm, 25 mm, and 35 mm axial heights.....	76
Figure 5.32. Radial distribution of dislocation densities of AVC20-10-2-0.25 in 6.5 mm, 16.5 mm, 26.5 mm, and 36.5 mm axial heights. ....	77
Figure 5.33. Radial distribution of dislocation densities of AVC20-15-0.25-25 in 5.5 mm, 15.5 mm, 25.5 mm, and 35.5 mm axial heights. ....	77
Figure 5.34. Temperature distribution (left) and velocity contours and the interface shape (right) for the global geometry of VB20-58.....	78
Figure 5.35. Temperature distribution (left) and velocity contours and the interface shape (right) for the global geometry of AHP10-10. ....	79
Figure 5.36. Temperature distribution (left) and velocity contours and the interface shape (right) for the global geometry of AHP20-5. ....	79
Figure 5.37. Temperature distribution (left) and velocity contours and the interface shape (right) for the global geometry of AHP20-14. ....	80
Figure 5.38. Temperature profile on the outer side of the crucible in global geometry of VB20-58. ....	80
Figure 5.39. Temperature profile on the outer side of the crucible in global geometry of AHP10-10 (AHP20-10).....	81
Figure 5.40. Temperature profile on the outer side of the crucible in global geometry of AHP20-5.....	81
Figure 5.41. Temperature profile on the outer side of the crucible in global geometry of AHP20-14.....	82

Figure 5.42. Velocity magnitude along the horizontal line 5mm above the seed base of the Steady state solution of AHP20-10. ....	83
Figure 5.43. The temperature distribution, velocity magnitude, and the interface shape for initial (a) and 2400 s(b) for local geometry of VB20-58. ....	84
Figure 5.44. Radial temperature along the horizontal line 2mm above the interface in local geometry of VB20-58. ....	85
Figure 5.45. Velocity magnitude along the horizontal line 2mm above the interface in local geometry of VB20-58. ....	86
Figure 5.46. The temperature distribution, velocity magnitude, and the interface shape for initial (a) and 2400 s(b) for local geometry of AHP10-10.....	86
Figure 5.47. Radial temperature along the horizontal line 2mm above the interface in local geometry of AHP10-10.....	87
Figure 5.48. Velocity magnitude along the horizontal line 2mm above the interface in local geometry of AHP10-10.....	87
Figure 5.49. The temperature distribution, velocity magnitude, and the interface shape for initial (a) and 2400 s(b) for local geometry of AHP20-10.....	88
Figure 5.50. Radial temperature along the horizontal line 2mm above the interface in local geometry of AHP20-10.....	89
Figure 5.51. Velocity magnitude along the horizontal line 2mm above the interface in local geometry of AHP20-10.....	89
Figure 5.52. The temperature distribution, velocity magnitude, and the interface shape for initial (a) and 2400 s(b) for local geometry of AHP20-14.....	90

Figure 5.53. Radial temperature along the horizontal line 2mm above the interface in local geometry of AHP20-14.....	91
Figure 5.54. Velocity magnitude along the horizontal line 2mm above the interface in local geometry of AHP20-14.....	92
Figure 5.55. The temperature distribution, velocity magnitude, and the interface shape for initial (a) and 2400 s(b) for local geometry of AVC20-10-2-0.25. ....	92
Figure 5.56. Radial temperature along the horizontal line 2mm above the interface in local geometry of AVC20-10-2-0.25.....	93
Figure 5.57. Velocity magnitude along the horizontal line 2mm above the interface in local geometry of AVC20-10-2-0.25.....	93
Figure 5.58. Numerical results for interface shape in VB20-58, AHP10-10, AHP20-10,AHP20-14, and AVC20-10-2-0.25 (from left to right) in 0, 120, 240, 360, 600, 1200, 1800, and 2400 seconds.....	94
Figure 5.59. The solute distribution, velocity magnitude, and the interface shape for 600s (a) and 2400 s(b) for VB20-58.....	97
Figure 5.60. Simulated Radial solute distribution of VB20-58. ....	98
Figure 5.61. VB20-58 Axial Solute Distribution along 0mm Axis (center).....	98
Figure 5.62. VB20-58 Axial Solute Distribution along 4mm Axis. ....	99
Figure 5.63. VB20-58 Axial Solute Distribution along 8mm Axis. ....	99
Figure 5.64. VB20-58 Axial Solute Distribution along 12mm Axis.....	100
Figure 5.65. VB20-58 Axial Solute Distribution along 16mm Axis. ....	100

Figure 5.66. VB20-58 Axial Solute Distribution along 20mm Axis (wall). .....	101
Figure 5.67. The solute distribution, velocity magnitude, and the interface shape for 600s (a) and 5400 s (b) for AHP10-10. ....	101
Figure 5.68. Radial solute distribution of AHP10-10. ....	102
Figure 5.69. AHP10-10 Axial solute distribution at the center. ....	103
Figure 5.70. AHP10-10 Axial solute distribution at 4 mm from the center. ....	103
Figure 5.71. AHP10-10 Axial solute distribution at 8 mm from the center. ....	104
Figure 5.72. AHP10-10 Axial solute distribution at 12 mm from the center. ....	104
Figure 5.73. AHP10-10 Axial solute distribution at 16 mm from the center. ....	105
Figure 5.74. AHP10-10 Axial Solute Distribution along 20mm (wall).....	105
Figure 5.75. The solute distribution, velocity magnitude, and the interface shape for 600s(a) and 2400 s(b) for AHP20-10. ....	106
Figure 5.76. Radial solute distribution of AHP20-10. ....	106
Figure 5.77. AHP20-10 Axial Solute Distribution along 0mm axis (center). ....	107
Figure 5.78. AHP20-10 Axial Solute Distribution along 4mm Axis.....	107
Figure 5.79. AHP20-10 Axial Solute Distribution along 8mm Axis.....	108
Figure 5.80. AHP20-10 Axial Solute Distribution along 12mm Axis.....	108
Figure 5.81. AHP20-10 Axial Solute Distribution along 16mm Axis.....	109



Figure 5.82. AHP20-10 Axial Solute Distribution along 20mm Axis (Wall). .....	109
Figure 6.1. The single crystal length in the grown crystals. ....	110
Figure 6.2. Variation of the effective melt height during the solidification process, experimental data. ....	112
Figure 6.3. Comparison of the melt height at different axial heights of the crystals. ....	112
Figure 6.4. Rate of change of the melt height. ....	113
Figure 6.5. Local geometry simulation results for the melt height variation in AHP10-10, AHP20-10, AHP20-14, and AVC20-10-2-0.25. ....	113
Figure 6.6. Rate of change of the melt height up to first 10 mm axial position according to the simulation results in Figure 6.5. ....	114
Figure 6.7. Simulation results for deviation between the pulling rate and the interface growth rate at the center radial position in the local geometry of VB20-58, AHP10-10, AHP20-10, AHP20-14, and AVC20-10-2-0.25. ....	114
Figure 6.8. Simulation results for radial temperature gradients in the local geometry of VB20-58, AHP10-10, AHP20-10, AHP20-14, and AVC20-10-2-0.25. ....	116
Figure 6.9. Archimedes number in different times. ....	117
Figure 6.10. Velocity magnitude at 2400s for VB20-58, AHP10-10, AHP20-10, AHP20-14, and AVC20-10-2-0.25. ....	119
Figure 6.11. Axial solute redistribution at the center and at the side in VB20-58, AHP10-10, and AHP20-10. ....	121

Figure 6.12. Average solute concentration (obtained from four-point probe test of the experimentally grown crystals) along the axial direction.....	122
Figure 6.13. Numerical results for average solute concentration along the axial direction in VB20-58 and AHP20-10.....	122
Figure 6.14. Averaged radial solute segregation along the crystals. The values in the parentheses are the single crystal lengths. ....	123
Figure 6.15. Comparison of solute segregation in the grown crystals.....	123
Figure 6.16. Numerical results for strain rate in VB20-58, AHP10-10, AHP20-10, AHP20-14, and AVC20-10-2-0.25 (from left to right) at 2400 s.....	126
Figure 6.17. Convective cells inside the melt during the vibrational motion of the baffle in AVC20-10-2-0.25 .....	127
Figure 6.18. Temperature variations of the grown crystals at T10 thermocouple position during the solidification.....	129
Figure 6.19. Axial temperature gradient in crystals during growth, calculated using data measured by T10 thermocouple as shown in Figure 6.18. ....	129
Figure 6.20. Average dislocation densities of the grown crystals up to the point where the single crystallinity is lost. ....	130
Figure 6.21. Dislocation density at the center and periphery of the crystals at 15 mm axial height from the seed base. ....	133
Figure 6.22. Numerical results of the axial solute redistribution inside the melt at the center and at the sides in VB20-58, AHP10-10, and AHP20-10. ....	137
Figure A.1. Solver selection. ....	161

Figure A.2. Solidification and Melting model parameters. ....	162
Figure A.3. Selecting Boussinesq option for density of germanium. ....	163
Figure A.4. Operating conditions. ....	164
Figure A.5. Solution methods. ....	165
Figure A.6. Time step settings. ....	166
Figure A.7. Species model. ....	167
Figure A.8. Mixture setting.....	168
Figure A.9. Initialization and patching the solute and temperature fields. ....	169
Figure B.1. Dislocations at different radial and axial positions in VB20-58.....	170
Figure B.2. Dislocations at different radial and axial positions in AHP10-10. ....	171
Figure B.3. Dislocations at different radial and axial positions in AHP20-5. ....	172
Figure B.4. Dislocations at different radial and axial positions in AHP20-14. ....	173
Figure B.5. Dislocations at different radial and axial positions in AVC20-10-2-0.25. ....	174
Figure B.6. Dislocations at different radial and axial positions in AVC20-15-0.25-25. ....	175

## LIST OF TABLES

Table 2.1. Different etchants and their compositions. ....	25
Table 4.1. Material properties. ....	50
Table 5.1 Grown crystals and their growth parameters. ....	54
Table 5.2. Material properties of Germanium, Antimony, and the mixture [29]. ....	96
Table 6.1. Dislocation density in radial planes at given axial positions starting from the seed base. ....	131
Table 6.2. CS and MS stability criteria. ....	138
Table 6.3. FR and KS stability criteria. ....	139

## LIST OF SYMBOLS

$A$	Vibration amplitude
$A_{mush}$	Mushy constant
$A_{SL}$	Solid/liquid interfacial area
$Ar$	Archimedes number
$c_s$	Specific heat of solid
$c_l$	Specific heat of liquid
$C_L$	Solute concentration in the liquid
$C_S$	Solute concentration in the solid
$C_0$	Initial solute concentration in liquid
$dn/dt$	Rate of formation of new embryos
$D_{th}$	Thermal diffusivity of liquid
$D'_{th}$	Thermal diffusivity of solid
$D_L$	Solute diffusivity in the liquid
$D_S$	Solute diffusivity in the solid
$\varepsilon$	Infinitesimal amplitude
$E$	Internal energy
$\eta$	Atomic vibration frequency
$f$	Vibration frequency
$f_{LS}$	Frequency with which atoms jump across the interface
$f_L$	Frequency with which atoms jump in the liquid
$f_l$	Mass fraction in the liquid

$f_s$	Mass fraction in the solid
$f(\theta)$	Shape factor
$g$	Gravitational acceleration/force
$G$	Gibbs free energy
$G_L$	Temperature gradient in the liquid
$G_S$	Temperature gradient in the solid
$G_f$	Thermal gradient of the furnace
$\Delta G$	Free energy change
$\Delta G_A$	Free energy of activation for the transfer of atoms from liquid to solid
$\Delta G_{cr}$	Required free energy to form a nucleus with critical size
$\Delta G_{cr}^{het}$	Required free energy to form a heterogeneous nucleus of critical radius
$\Delta G_V$	Free energy change per unit volume
$h$	Melt height
$h'$	Sensible heat
$h_{ref}$	Reference enthalpy
$H$	Enthalpy
$\Delta H$	Latent heat
$\Delta H_f$	Latent heat of fusion per unit volume
$I_{het}$	Heterogeneous nucleation rate
$I$	Homogeneous nucleation rate
$I_r$	Current

$K_L$	Thermal conductivity of liquid
$K_S$	Thermal conductivity of solid
$k$	Partition coefficient / solute segregation coefficient
$K_{eff}$	Effective partition coefficient
$K_B$	Boltzmann's constant
$\bar{K}$	Average thermal conductivity
$L$	Enthalpy of the liquid
$m_L$	Liquidus slope
$n_L$	Number of atoms
$P$	Pressure
$R_s$	Resistivity
$r_{cr}$	Critical radius
$s$	Distance between the probe needles
$S$	Entropy
$\Delta S_f$	Entropy of fusion per unit volume
$t$	Time
$T$	Temperature
$T'$	Temperature in solid
$T_L$	Liquidus temperature
$T_L$	Solidus temperature
$T_m$	Melting temperature
$T_{ref}$	Reference temperature
$\Delta T$	Under cooling

$V$	Growth rate
$V_r$	Voltage
$\beta_T$	Thermal expansion coefficient
$\beta_S$	Solutal expansion coefficient
$\delta$	Boundary layer
$\lambda$	Wavelength
$\gamma_{SL}$	Solid/liquid interfacial free energy
$\rho$	Density
$\rho_L$	Density in the liquid
$\rho_S$	Density in the solid
$\omega$	Wave number



## LIST OF ACRONYMS/ABBREVIATIONS

AHP	Axial Heat Processing
AVC	Axial Vibrational Control
CMOS	Complementary Metal-Oxide Semiconductor
CS	Constitutional Supercooling
Cz	Czochralski
FZ	Favier and Rouzaud
FZ	Floating Zone
IC	Integrated circuits
KS	Kinetic Stability
MODFET	Modulation-Doping Field Effect Transistor
MS	Mullins-Sekerka
PID	Proportional Integral Derivative
SCR	Silicon-Controlled Rectifier
SIMPLE	Semi-Implicit Method for Pressure Linked Equation
VB	Vertical Bridgman

## 1. INTRODUCTION

Semiconductors are used widely in many modern electronic devices such as the transistors, lasers, solar cells [1-3], and integrated circuits (IC). Among other semiconductors, prominent material properties such as a higher hole and electron mobility than Silicon (Si) make Germanium (Ge) favorable for many applications. Moreover, electronic and optical properties and compatibility with modern Complementary Metal-Oxide Semiconductors (CMOS) technology have awakened an interest in Ge-based structures in recent years [4-7]. The electrical properties of semiconductors can be altered in a controllable way by doping them. Ge-based structures such as optoelectronic devices, terahertz emitters, and modulation-doping field effect transistors (MODFETs) should include selectively doped n-type and p-type regions [8, 9].

The demand for a large-scale integration requires uniform electrical properties (uniform dopant distribution) in a melt grown crystal which is then wafered and cut for electronic devices. Moreover, defects like dislocations which affect electrical and optoelectronic properties of the semiconductors [10, 11] should be avoided. In addition, in order to reduce the costs, the crystal growth should be performed in a fast rate. However, a fast growth rate causes morphological instability, which is a change in the shape of the solid/liquid (s/l) interface from a planar one to a cellular or dendritic one. This leads to uneven distribution of the solute and breaks down the homogeneity of the grown crystal. It, in fact, introduces defects such as grain boundaries. Thus, parameters should be carefully controlled in a directional solidification set up to keep the s/l interface as flat as possible in order to reduce the amount of such defects. Nevertheless, it is difficult to control all the parameters during an experiment. Therefore, it is required to look for a suitable technique which enables the close control of the growth parameters and the melt flow during the crystal growth. There are conventional techniques in the literature for growing single crystal of Ge-Sb such as Czochralski (Cz) method, Floating Zone (FZ), and Vertical Bridgman (VB). However, in all of these methods, heat source is applied radially which leads to radial temperature gradient in the melt. The natural convection arising from this

radial temperature gradient results in inhomogeneous solute redistribution and eventually leads to instability of the interface.

New, innovative methods, called Axial Heat Processing (AHP) and Axial Vibrational Control (AVC), have been developed to overcome problems encountered when growing single crystals with the abovementioned conventional methods. The AHP method has been used to grow  $\text{Bi}_4\text{Ge}_3\text{O}_{12}$  and  $\text{Li}_2\text{B}_4\text{O}_7$  [12, 13], Ge-Si [14-16], and Ge-Sb [17-21] and AVC method is used to grow PbTe, CdTe, and  $\text{NaNO}_3$  [22-28]. Details of these methods are provided in Section 2.1.1.

In this present study, melt growth of Sb-doped Ge crystals is investigated by the conventional Vertical Bridgman (VB) and novel methods of Axial Heat Processing (AHP) and Axial Vibrational Control (AVC). In the VB method, melt is contained in a crucible and withdrawn downward in a temperature gradient. This allows solidification to start at the bottom and move upward in the crucible. The AHP and AVC methods modify the VB method. In the AHP method, a baffle is immersed in the crucible to adjust the melt height to a desired value. Although the forced flow through the gap between the baffle and the crucible suppresses the natural convection and improves homogeneity of the solute redistribution, radial temperature gradient remains as a problem especially at high pulling rates. In the AVC method, the baffle vibrates axially at a desired melt height. Stirring the melt with an appropriate amplitude and frequency of the vibrating baffle provides effective mixing in the melt for homogeneous solute redistribution even at high pulling rates. Thus, it is possible to increase the production yield by applying the AVC method. The VB and AHP methods have been used before for growing Ge-Si [14-16] and Ge-Sb [17-21, 29]. Nevertheless, the AVC technique is applied for growing Ge-Sb for the first time in the world in this current study. The homogeneity of the solute, stability of the interface, and the dislocation density in the grown single crystals have been investigated with regards to the growth parameters such as the pulling velocity, the effective melt height, and the amplitude and frequency of the vibrating baffle.

The fluid flow in the melt is very effective in the evolution of the s/l interface during the growth. Unfortunately, it is not practical to detect the fluid flow during growth of an opaque crystal, like germanium. Hence, numerical simulation of the growth process can help understand the fluid flow during the growth. In this study, ANSYS Fluent software is used. The numerical simulations enable testing many growth parameters in a time and cost effective way. Then, the growth can be realized with optimized parameter from the simulations. The velocity magnitude of the flow near the interface is determined via the simulations. In this way, it is possible to conclude whether the natural convection is suppressed or not according to the Archimedes number which is the ratio of the Grashof number to the square of the Reynolds number.

In addition, the dislocation density, which is another quality assessment parameter of the grown crystals, has not been investigated yet. In this study, the effect of growth parameters on the morphology of the emergent dislocations and the density of the dislocations in the grown crystals is investigated.

## 2. SCIENTIFIC BACKGROUND

### 2.1. Solidification

The crystal growth process takes place by solidification of the melt on the pre-existing crystal. Solidification is a process in which a phase transformation occurs from a liquid to a solid phase. However, this phase transformation does not happen spontaneously. There are certain conditions that should be supplied for such a transformation. In studying single crystal growth it is important to understand these conditions and the rate at which this phase transformation occurs. The driving force for the phase transformation is determined via thermodynamics, and the rate of this phase transformation is determined by kinetics. The following subsections, which are taken from two main references [30, 31], provide more detailed information about the mechanism of the solidification.

#### 2.1.1. Thermodynamics

In crystal growth, the phase transformation occurs at the S/L interface where the system is assumed at an equilibrium state, and its Gibbs free energy is at minimum. Gibbs has defined this energy as a function of the system properties such as the internal energy ( $E$ ), the pressure ( $P$ ), the volume ( $v$ ), the temperature ( $T$ ), and the entropy ( $S$ ) as the following:

$$G = E + Pv - TS \quad (2.1)$$

Therefore, solidification takes place if the Gibbs free energy of the initial state (liquid) is higher than that of the final state (solid). The variation of the Gibbs free energy (for both the solid and the liquid states) with temperature at a constant pressure for pure metals is shown in Figure 2.1.

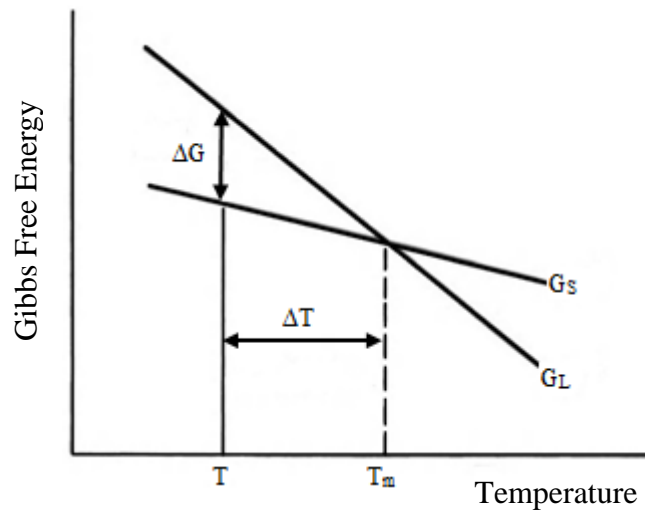


Figure 2.1. Variation of the Gibbs free energy for pure metals [31].

The intersection of the solid and liquid energy lines is called the equilibrium melting temperature. As shown in the figure, at temperatures above the melting temperature, the stable phase is the liquid, and below the melting temperature, the solid phase is stable. Hence, the driving force for the solidification is a finite undercooling,  $\Delta T$  ( $\Delta T = T_m - T$ ), of the system below its melting temperature,  $T_m$ . However, in alloys, like Ge-Sb considered in this study, in addition to pressure and temperature variables, the Gibbs free energy also depends on the composition of the system. In order to find the range in which the system of a binary alloy is in equilibrium state for all of the temperature and composition combinations at the atmospheric pressure, the phase diagram of the system is used. The phase diagram for Ge-Sb is shown in Figure 2.2 [32]. Also, note that in the calculation of  $\Delta T$ , the  $T_m$  depends on the composition of the system.

### 2.1.2. Kinetics

Although the required driving force for the occurrence of the solidification is the undercooling, it cannot itself determine when and at which rate the solidification will happen. Kinetics provides information about the possibility of the solidification and its rate. The equations in this subsection are mostly taken from [30].

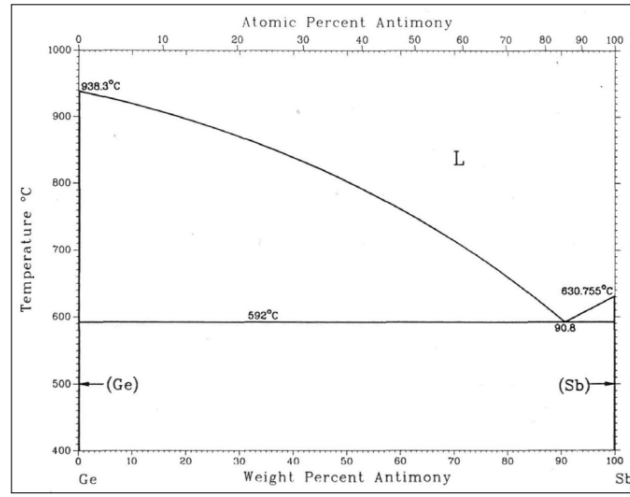


Figure 2.2. Phase diagram of Ge-Sb [32].

The solidification starts with a nucleation where aggregates of solid atoms (embryos) are created in the liquid phase. The associated interface energy increases the free energy of the system, so in order to avoid the melt back of the created embryo, the amount of undercooling of the system should be sufficient. If the embryo survives and grows to a critical size and becomes stable, it forms a nucleus. Since the nucleus and the liquid phase have the same composition this phenomenon is called homogeneous nucleation. Once the embryo of radius  $r$  is formed in the liquid, the free energy of the system is decreased due to formation of the solid phase and increased as a result of formation of the S/L interface, so the change in free energy of the system is calculated as:

$$\Delta G = -v_s \Delta G_v + A_{SL} \gamma_{SL} = -\frac{4}{3} \pi r^3 \Delta G_v + 4 \pi r^2 \gamma_{SL} \quad (2.2)$$

Where  $v_s$  is the volume of the formed solid,  $A_{SL}$  is the formed S/L interface area,  $\gamma_{SL}$  is the surface energy of the interface, and  $\Delta G_v$  is the free energy per unit volume of the formed solid which is defined as

$$\Delta G_v = \Delta S_f \Delta T \text{ and } \Delta S_f = \frac{\Delta H_f}{T_m}$$

Where  $\Delta S_f$  is the entropy of fusion per unit volume and  $\Delta H_f$  is the latent heat of fusion per unit volume. This free energy change with respect to the radius of the embryo is shown in Figure 2.3 [31].

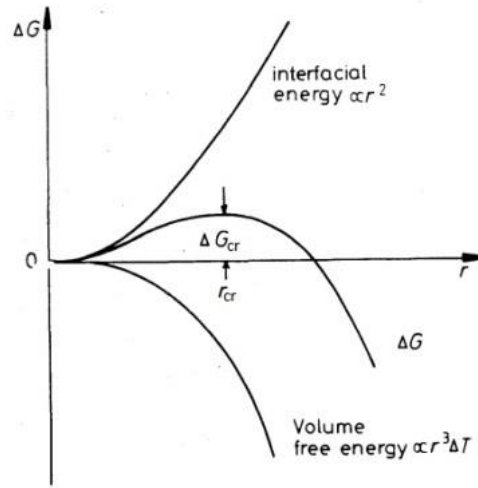


Figure 2.3. Variation of the free energy of the system with respect to the radius of the embryo [31].

The first derivative of Equation 2.2 gives the critical radius of the embryo as:

$$r_{cr} = \frac{2\gamma_{SL}}{\Delta G_v} = \frac{2\gamma_{SL}T_m}{\Delta H_f \Delta T} \quad (2.3)$$

By substituting Equation 2.3 into Equation 2.2, the critical free energy required for the homogeneous nucleation can be derived as:

$$\Delta G_{cr} = \frac{16\pi\gamma_{SL}^3 T_m^2}{3\Delta H_f^2 \Delta T^2} \quad (2.4)$$

The number of homogeneous embryos,  $n_i^{cr}$ , forming in the liquid in a given temperature  $T$  which has  $n_L$  atoms per unit volume can be obtained as



$$n_i^{cr} = n_L \exp\left(\frac{-\Delta G_{cr}}{K_B T}\right)$$

Where  $K_B$  is the Boltzman's constant. For the occurrence of the solidification, this number should be greater than unity. Therefore, a critical change in free energy of the system ( $\Delta G_{cr}$ ) and consequently a critical undercooling ( $\Delta T_{cr}$ ) is required for the beginning of the solidification. Also, Equation 2.3 indicates that if the undercooling is not sufficient and is very low, the critical radius tends to be infinite which means that the solidification will not take place. For Ge this amount of undercooling is 218 K [29].

If the rate of formation of new embryos in liquid ( $dn/dt$ ) can be defined as  $dn/dt = \eta \exp(-\Delta G_A/K_B T)$ , the velocity of homogeneous nucleation ( $I$ ) can be achieved as  $I = n_i^{cr} \cdot \frac{dn}{dt} = n_L \eta \exp\left(\frac{-\Delta G_{cr}}{K_B T}\right) \exp\left(-\frac{\Delta G_A}{K_B T}\right)$ . Where,  $\eta$  is the atomic vibration frequency and  $\Delta G_A$  is the activation energy required for transferring atoms from liquid to solid.

Since, as mentioned earlier, high amount of undercooling is required for the homogeneous nucleation, it is not expected to occur in practical solidification methods. In fact, nucleation occurs on preferential sites such as container walls or impurities in liquid which accelerate and ease the nucleation. Formation of the nucleus on these heterogeneous sites is called heterogeneous nucleation. The free energy required for heterogeneous nucleation is:

$$\Delta G_{cr}^{het} = \Delta G_{cr} \cdot f(\theta) \quad (2.5)$$

Where  $f(\theta) = \frac{1}{4}(2 + \cos\theta)(1 - \cos\theta)^2$  is the shape factor and  $\theta$  is the wetting angle as indicated in Figure 2.4 [31].

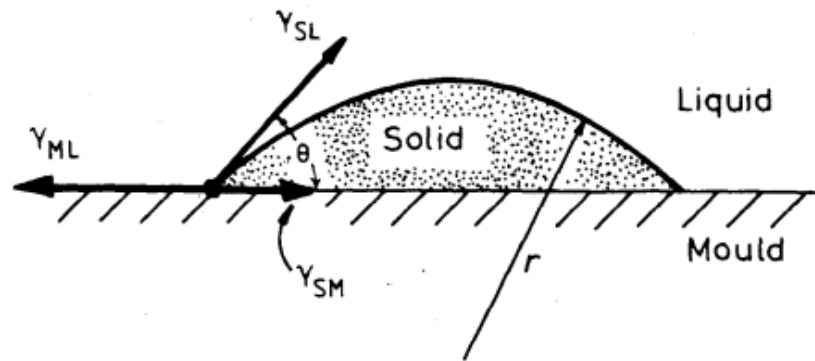


Figure 2.4. Interfacial energy relationships between the Mould (M), the Liquid (L), and the solid (S) [31].

Since  $f(\theta)$  is always less than or equal to one, the undercooling required for heterogeneous nucleation is several orders smaller than that required for homogeneous nucleation. The wetting angle between graphite and liquid germanium is quite high ( $166^\circ$  [33]) which leads to the  $f(\theta)$  close to one, so the heterogeneous undercooling becomes close to that for the homogeneous nucleation and the heterogeneous nucleation is also not expected.

The number of created embryos in liquid and the velocity of the heterogeneous nucleation can be achieved similar to that for homogeneous nucleation. However, instead of the number of atoms per unit volume of liquid ( $n_L$ ), the number of atoms of nucleation sites per unit volume ( $n_a$ ) should be used in the relevant equations. Therefore, the velocity of the heterogeneous nucleation is  $I_{het} = n_a \eta \exp\left(\frac{-\Delta G_{cr}^{het}}{K_B T}\right) \exp\left(-\frac{\Delta G_A}{K_B T}\right)$ .

As mentioned earlier, the first step of the solidification is formation of the nuclei for establishing an s/l interface for the growth whether by homogeneous or heterogeneous nucleation. However, in crystal growth, the required s/l interface for the growth is formed by imposing a temperature gradient on a solid seed to melt it partially. The mechanism of the growth depends on the nature of the interface. It can be either diffuse (atomically rough) or sharp (atomically smooth). In diffuse interface there are no preferential sites for

attachment of the atoms, so the incoming atoms randomly incorporate to the surface and the interface advances into the liquid by continuous growth which leads to non-faceted interface. On the other hand, in sharp interfaces atoms preferentially attach to steps or kinks on layers of the interface which leads to lateral growth and forming faceted interface. Then, the spreading of these lateral steps provides normal growth of the interface. The velocity of the continuous growth is defined by Turnbull [34] as

$$V = \mu_0(\Delta T) \quad \text{with } \mu_0 = \frac{\beta D_L \Delta H_f}{a k_B T_m^2} \quad \text{and } \beta = \left(\frac{a}{\zeta}\right)^2 \frac{6 f_{LS}}{f_L} \quad (2.6)$$

Where  $a$  is the advent of the interface due to addition of an atom,  $D_L$  is the diffusivity in the liquid,  $\zeta$  is a jump distance for an atom in liquid,  $f_{LS}$  and  $f_L$  are the frequency with which atoms jump across the S/L interface and jump in the bulk liquid respectively.

Since the latent heat of fusion of Ge is high, the s/l interface is faceted [35] and the growth mechanism is the lateral growth. The preferential steps or kinks for the atomic attachments are provided either by intersection of screw dislocations with the interface or 2D nucleation of solid islands on a faceted interface. The fact that intersection of screw dislocations with the interface can provide preferential sites for the lateral growth was first recognized by Frank [36]. Later, Hilling and Turnbull [37] established an equation relating dislocation effects on normal growth rate which is then corrected by Cahn *et al.* [38] to be

$$V = \mu_1(\Delta T)^2 \quad \text{with } \mu_1 = \frac{1 + 2g^{1/2}}{g} \frac{\beta D_L \Delta H_f^2}{4\pi\gamma_{sl} k_B T_m^3 v_m} \quad (2.7)$$

Where,  $v_m$  is the molar volume, and  $g$  is the diffuseness parameter which is equal to 1 for perfectly faceted interfaces and too small for the diffuse interfaces.

For 2D nucleation, just like homogeneous and heterogeneous nucleation, there are critical size and critical free energy associated with the 2D nucleus forming on the faceted interface which are defined as

$$r_{cr} = \frac{\gamma_{sl}}{\Delta G_v} = \frac{\gamma_{sl} T_m}{\Delta H_f \Delta T} \quad \text{and} \quad \Delta G_{cr} = \frac{\pi a \gamma_{sl}^2 T_m}{\Delta H_f \Delta T} \quad (2.8)$$

Also, the growth rate can be defined as an exponential equation given by Turnbull [37]:

$$\begin{aligned} V &= \mu_4 \exp\left(\frac{\mu_3}{3\Delta T}\right) \quad \text{with} \quad \mu_3 = \mu_0 \frac{\pi g B^2 a T_m^2}{\beta D_L} \quad \text{and} \quad \mu_4 \\ &= \mu_0 \left(\frac{\Delta H_f}{k_B T_m^2}\right)^{1/6} (\Delta T)^{7/6} (2 + g^{-1/2}) \end{aligned} \quad (2.9)$$

Where  $B = v_m \gamma / (a \Delta H_f)$  is the empirical relationship between  $\gamma_{sl}$  and  $\Delta H_f$  defined by Turnbull. Figure 2.5 compares three different growth kinetics, continuous growth, screw dislocations, and 2D nucleation, which are discussed above. It is shown that for the same amount of undercooling, continuous growth is the fastest and the growth rate changes linearly with the undercooling which is also perceptible from Equation 2.6. Also, it is indicated that considerably a higher undercooling is required for 2D nucleation growth. However, after achieving the required undercooling, the growth rate is increased instantaneously with the amount of undercooling in the exponential manner (Equation 2.9).

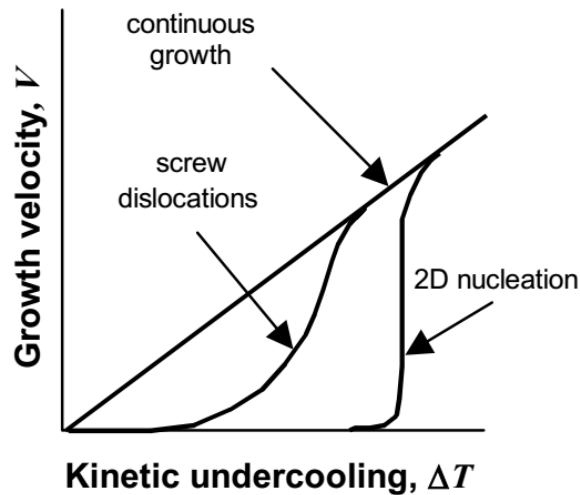


Figure 2.5. Comparison of growth kinetics [30].

## 2.2. Crystal Growth from the Melt

### 2.2.1. Available Methods

In order to achieve a single crystal, solidification should occur from a single crystal seed. To this end, a portion of the single crystal seed is melted to create a solid/liquid (s/l) interface and a directional solidification normal to this interface occurs to grow the single crystal. There are several methods for growing single crystal from the melt such as Czochralski (Cz), Floating Melting Zone (FZ), VB, and AHP. There are many other methods such as Verneuil, Kyropoulos, Stepanov (EFG), and Skull melting process. However, only the important ones are outlined below. In all these methods, the aim is keeping the solid/liquid interface as flat as possible, homogenizing material properties, and minimizing defects during the growth.

2.2.1.1. Czochralski method. The Czochralski (Cz) method, which is the earliest crystal growth technique, is invented in 1917 by Czochralski [39]. In this method, the seed is attached to a pull rod and a portion of the seed is dipped into a crucible containing the melt in order to create the s/l interface. This interface is maintained by a temperature gradient imposed by the radial heaters surrounding the crucible. Then, the seed is pulled out of the melt to begin the growth. Rotation of the pull rod during the solidification can help mixing the melt near the s/l interface. The schematic of this method is shown in Figure 2.6. The advantage of this method is that the crystal is not in contact with the crucible, so it is possible to avoid stress induced defects in the grown crystals. However, the radial temperature gradient inside the melt leads to non-planar interface during the growth and thermal stress induced defects in the crystal. Teal and Little were the first who grew the single crystal of germanium with the Czochralski method [40].

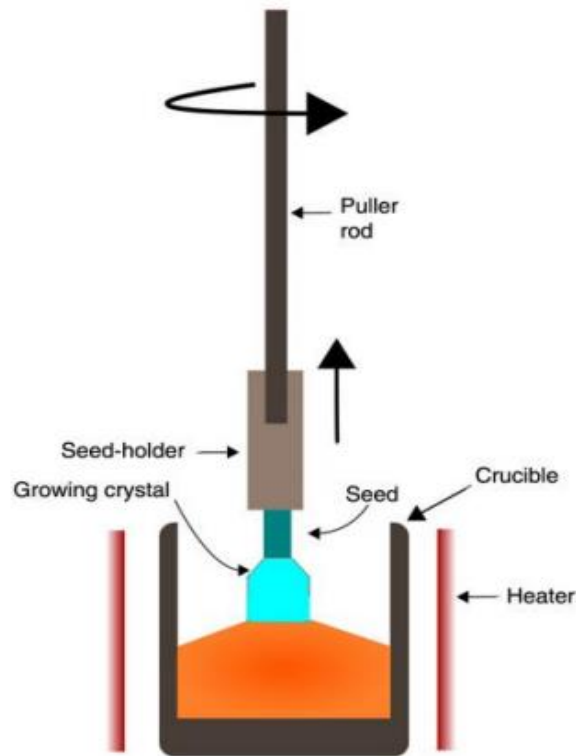


Figure 2.6. Schematic of Czochralski method [41].

2.2.1.2. Floating Zone (FZ) Method. This method is first designed by Henry Theuerer [42] in 1955 at Bells laboratories for purification of Si [43, 44]. In this method, radial heaters are positioned around a polycrystalline ingot contacting the single crystal seed to create a melting zone above the seed (Figure 2.7). The solidification and single crystal formation occurs by upward motion of the heaters. Like the Cz method, the crystal is not in contact with the crucible and additionally, the melt is not touching the crucible. Therefore, both defects induced by thermal stress and contaminations can be avoided. However, the created molten zone is unstable, so it is hard to control the interface shape during the growth. While this method is favorable for purifying the silicon and alloys having high segregation coefficient [45-51], it is not suitable for germanium growth. The reason is that germanium is twice denser than liquid silicon while both have almost the same surface tension, which brings the destabilization of the melt zone during the growth. Moreover, lower melting point of germanium and the lower radiative heat loss comparing to silicon, reduce the stability in the FZ method. Therefore, it is only possible to grow small crystals of germanium with this method. However, recent modifications in the design of the FZ

method and changing the growth conditions make it possible for growing larger germanium crystals [52].

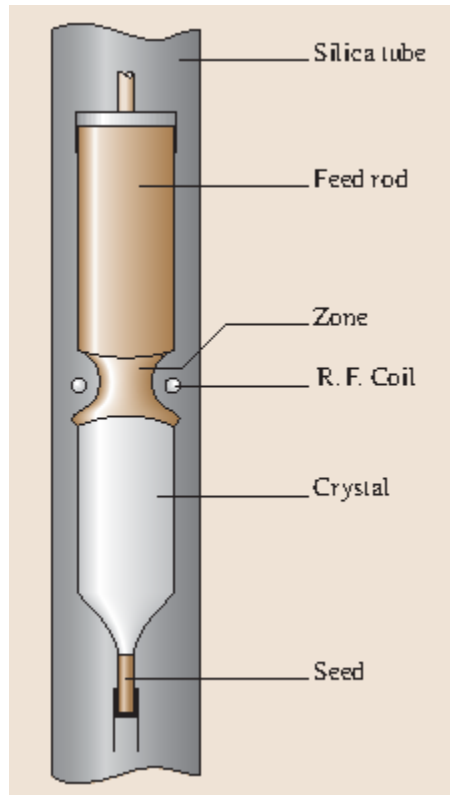


Figure 2.7. Schematic of the Floating Zone method [53].

2.2.1.3. Vertical Bridgman (VB) Method. This method is less intricate comparing to the previously mentioned methods. In this method, which is first invented in 1928 by Percy Williams Bridgman [54], the seed and a bulk charge material are placed on a movable pedestal inside a crucible and radial heaters around the crucible are set appropriately to create an axial temperature gradient along the crucible to establish the s/l interface (Figure 2.8). Then, the crucible and the pedestal are slowly moved downward to begin the growth on the seed. The simplicity of this method makes it desirable for growing single crystal compound semiconductors [55-58]. Also, by applying crucibles with different shapes casting of superalloys with complicated geometries such as turbine blade [59, 60] is possible with the Bridgman method. However, since the crystal and the melt are in contact with the crucible, both contamination and stress induced defects are inevitable. Moreover,

radial temperature gradient is still a problem in achieving planar flat interface during the growth.

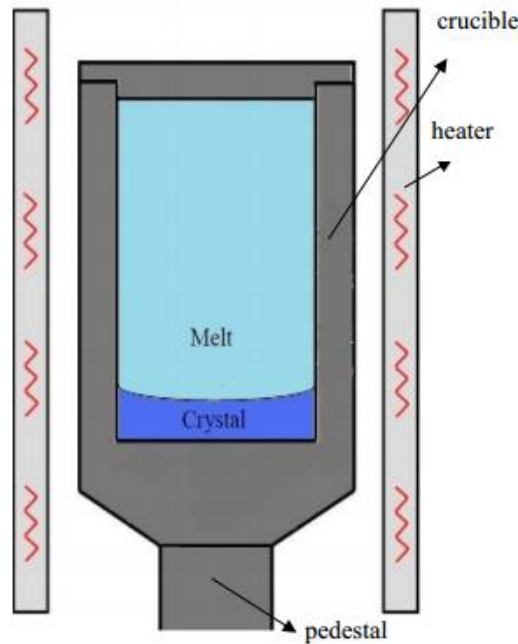


Figure 2.8. Vertical Bridgman configuration.

2.2.1.4. Axial Heat Processing (AHP) Method. In all previously mentioned methods, radial temperature gradient is the main reason of the breaking of the planar interface during the growth and consequently not achieving a single crystal. In AHP method, which is a modification of the VB method, either a baffle containing a heater or a baffle made of a high thermal conductivity material is immersed in the melt to reduce the radial temperature gradient ahead of the s/l interface. The baffle can be adjusted to any axial position that reduces the melt height. Moreover, incorporating thermocouples into the baffle provides direct measurement of the thermal profile near the s/l interface. Figure 2.9 shows the schematic of this method. The AHP method has been used to grow  $\text{Bi}_4\text{Ge}_3\text{O}_{12}$  and  $\text{Li}_2\text{B}_4\text{O}_7$  [12, 13], Ge-Sb [17-21], and Ge-Si [14-16] crystals successfully. The AHP method is also used for single crystal growth of metallic materials (super alloys) successfully [61]. In [14-16] the morphological stability and dopant redistribution during the growth of Ge-Si single crystal with the VB and AHP methods are investigated. The pulling rates were 0.75 mm/h and 2 mm/h and the initial Si concentrations were 5 at% and 12 at %. It is observed that reducing the pulling rate results in increased single crystal length and reduced solute



segregation. Also, it is shown that while reducing the melt height in the AHP method has no effect on increasing the single crystal length, the homogenization of solute redistribution is improved in the AHP method and the solute segregation is decreased by decreasing the melt height above the interface. In [19, 20], single crystal growth of Ge-Sb via the AHP method is investigated using an embedded heater in the baffle. It is reported that the heater reduces the radial temperature gradient, promotes faceted growth at the center, and retard the morphological instabilities. In this work, the growth was done in two stages. First, the crystal was grown with 5 mm/h and after 7.5 hours of the growth, the pulling rate was abruptly increased to 16mm/h. The initial Sb concentration was  $2 \times 10^{20}$  atoms/cc and the initial melt height was 6 mm. In [18, 21] the stability of the interface during the single crystal growth of Ge-Sb in the AHP method is investigated. Different growth rates in the range of 3 mm/h to 20 mm/h with initial Sb concentration varying from  $5 \times 10^{19}$  to  $1.5 \times 10^{20}$  are adopted to investigate the effects of the growth parameters on solute redistribution and morphological stability of the grown crystals. Also, the effect of the misorientation is investigated applying bicrystal seed in [21]. Moreover, seeds with different geometries, conical and round, are used in order to investigate the detached growth of Ge-Sb with the AHP method in [17].

2.2.1.5. Axial Vibrational Control (AVC) Method. The fluid flow close to the s/l interface, which arises from the radial temperature gradient, can lead to uneven solute redistribution in the vicinity of the interface in the growing crystal. Due to dependency of melting temperature to the solute concentration, the interface planarity and consequently the interface stability may be lost. Stirring the melt by an axial vibration of the immersed baffle can suppresses these uneven convective flows [62] providing more homogeneous solute redistribution and promote stable planar interface during the growth. Figure 2.9 shows the schematic of this method. This method is called Axial Vibrational Control (AVC) and has been used in the growth of PbTe, CdTe, and NaNO<sub>3</sub> [22-28] crystals in the Cz and VB configurations.

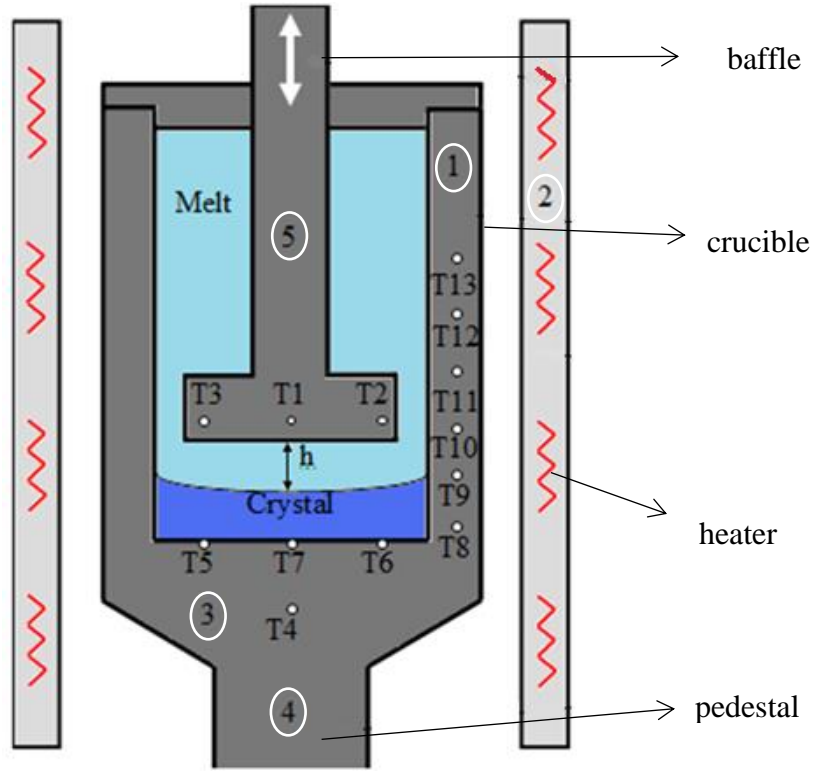


Figure 2.9. Schematic of AHP / AVC configuration. 1) Crucible, 2) Four-zone furnace, 3) Pedestal, 4) Water cooled molybdenum rod, 5) Baffle. T1 to T3 are baffle thermocouples, T4 to T7 are pedestal thermocouples, and T8 to T13 are crucible thermocouples.

This is for the first time that the AVC is applied in the VB configuration for growing Ge-Sb single crystal. In [21] different growth rates are investigated. It has been observed that the single crystal length is decreased with increasing the pulling rate. The maximum pulling rate was 20 mm/h and in this rate the single crystal length decreased about 42% in comparison with the crystal that was grown with 10 mm/h. In this study, while the pulling rate and the initial Sb concentration are fixed to 20 mm/h and  $1 \times 10^{20}$  atoms/cc respectively, different combinations of amplitude and frequency of the vibrating baffle are applied in order to investigate the effect of the forced convective flow due to the vibration of the baffle. Moreover, in the previous works [14-21], the effect of decreasing melt height on suppressing the natural convection was only evaluated by the Grashof number and the intensity of the flow was not mentioned.

### 2.3. Solute redistribution

In a binary alloy in which the segregation coefficient is less than unity, as in Ge-Sb ( $k = 0.003$  [32]), the solute is being rejected to the liquid phase during the solidification. This solute build up in front of the interface creates a solute boundary layer of thickness  $\delta$  ahead of the interface in which the distribution of the solute is by diffusion. This diffusion boundary layer affects the growth and the morphology of the interface. There are several theories for describing the distribution of the solute during the solidification which are explained in the followings.

#### 2.3.1. Equilibrium Solidification (Infinite diffusion in liquid and solid)

Assuming that the interface is at the equilibrium state, the diffusion rate in both solid and liquid is the same and the amount of solute in solid ( $C_s$ ) can be achieved by multiplying amount of solute in liquid ( $C_l$ ) by equilibrium segregation coefficient,  $k$ , as  $C_s = kC_l$ . If the diffusion rate is infinite in both solid and liquid ( $D_s = D_L = \infty$ ), the solute is distributed homogeneously in solid and liquid sides of the interface. Therefore, by proceeding the solidification, the variation of solute concentration in solid and liquid ( $C_s$  and  $C_l$ ) will be along the solidus and liquidus lines in the phase diagram. Assuming the initial solute concentration in the liquid is  $C_0$ , due to the local equilibrium, the first solid formation will attain the concentration of  $C_s = kC_0$  and due to infinite diffusion in solid the whole solid will attain this amount of solute. Since the solid has less solute than the liquid, the solute is rejected to the liquid during the solidification and the concentration in the liquid ( $C_l$ ) is increased and becomes higher than  $C_0$  through the whole liquid because of the infinite diffusion rate in the liquid. Consequently, the solute concentration in the newly formed solid will increase from  $kC_0$ . This process continues until the entire liquid turns into solid with  $C_0$  solute amount (see Figure 2.10).

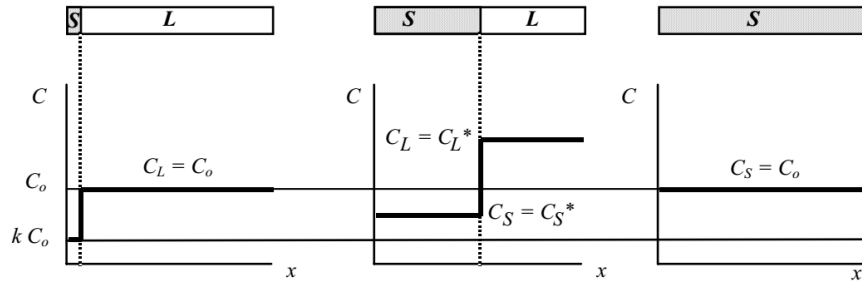


Figure 2.10. Equilibrium solute redistribution [30].

Applying solute conservation leads to:

$$C_s f_s + C_l f_l = C_0 \text{ where } f_s + f_l = 1 \quad (2.10)$$

Where  $C_0$  is the initial solute concentration in the liquid and  $f_s$  and  $f_l$  are the mass fraction of solid and liquid respectively. This equation is known as equilibrium Lever rule. Therefore, the amount of solute in the solid can be achieved as [30]:

$$C_s = \frac{kC_0}{1 - (1 - k)f_s} \quad (2.11)$$

### 2.3.2. Complete mixing in liquid and no diffusion in solid

In this assumption, it is assumed that the liquid is mixed properly so the diffusion rate in the liquid is so rapid and there is no diffusion in the solid. Also, due to complete mixing in the liquid there is no solute boundary layer ahead of the interface. The solute is rejected to the liquid during the solidification, so the solidifying liquid has greater solute content than the initial state. Since there is no diffusion in the solid, a concentration gradient is formed in the solidified region and the solute is increasing from its initial value ( $kC_0$ ). Mass balance dictates that the amount of rejected solute when an infinitesimal solid ( $df_s$ ) is formed should be equal to the increase in the amount of solute in the liquid (see Figure 2.11). Using this mass balance, Gulliver [63] and Scheil [64] derived an equation for the solute content in the solid as a function of solid fraction ( $f_s$ ). This is known as non-equilibrium Lever rule or Gulliver-Scheil equation.

$$\begin{aligned}
 (C_L - C_S)df_s &= (1 - f_s)dC_L \text{ or } \int_0^{f_s} \frac{df_s}{1 - f_s} = \frac{1}{1 - k} \int_{kC_0}^{C_S} \frac{dC_S}{C_S} \text{ or } C_S \\
 &= kC_0(1 - f_s)^{(k-1)}
 \end{aligned}
 \tag{2.12}$$

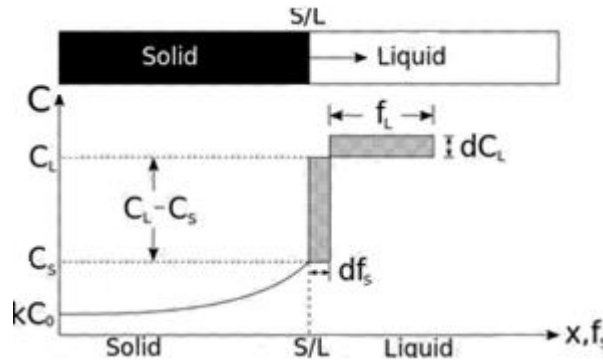


Figure 2.11. Scheil solute redistribution profile [30].

### 2.3.3. Diffusional mixing in liquid and no diffusion in solid

If the liquid is not stirred, the distribution of the rejected solute into the liquid will be done solely by diffusion, as there is no convection and mixing in the liquid. This case is proposed by Smith, Tiller, and Rutter [65]. Since the diffusion rate is not infinite (in contrast to that in the Scheil assumption), the rejected solute is accumulated in front of the interface and diffuses away into the liquid. Therefore, a concentration gradient is formed by this solute pile up ahead of the interface. The amount of solute in the solid is increased until it reaches the initial  $C_0$  (initial transient). When the solute content in the solid reaches  $C_0$ , the rejected solute from the interface becomes equal to the solute diffuses away from the interface into the liquid and the solute content remains  $C_0$  (steady state). When the remaining liquid length becomes less than the solute boundary layer, the rejected solute atoms will not have enough space to diffuse away the interface and the solute content in the solid increases above the  $C_0$  (final transient). Figure 2.12 shows these three zones in the diffusional mixing solute redistribution. Solving the Fick's second law for diffusion for the initial transient, the distribution of the solute in the solid can be achieved as [66]

$$C_s(x) = C_0[1 - (1 - k)\exp(-kVx/D_L)] \quad (2.13)$$

Where  $V$  is the solidification rate,  $D_L$  is the diffusion in liquid, and  $x$  is the distance solidified. Note that according to Equation 2.13, increasing the solidification rate (the pulling rate) leads to increase in the solute content in the solid at the interface.

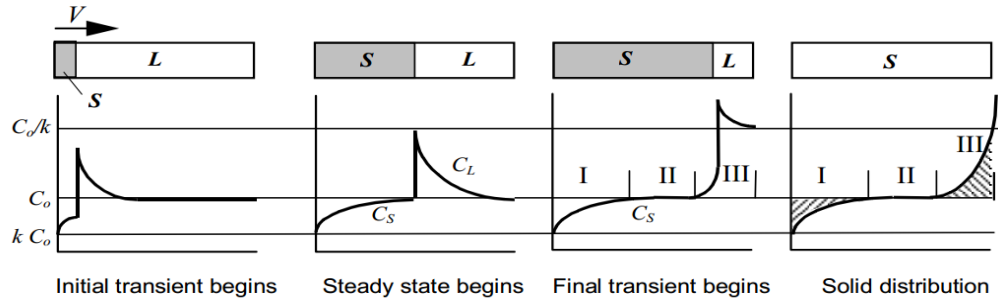


Figure 2.12. Diffusional mixing solute redistribution profile [30].

#### 2.3.4. Partial mixing in liquid and no diffusion in solid

Both the complete mixing (Scheil) and pure diffusional mixing in liquid are rarely achieved in a real solidification case. The actual solute distribution mechanism is between these two limiting cases. Therefore, the length of solute boundary layer ( $\delta$ ) is decreased due to convection effects rather than that in the pure diffusion case. Using boundary layer theory, Burton, Prim, and Slichter [67] defined an effective distribution coefficient to treat the mixing in the solute boundary layer.

$$k_{eff} = \frac{k}{k + (1 - k)\exp(-V\delta/D_L)} \quad (2.14)$$

Note that if  $\delta$  goes to zero (case of complete mixing), the effective partition coefficient becomes equal to the equilibrium partition coefficient, and if  $\delta$  goes to infinity, the partition coefficient goes to unity, which means no convective mixing occurs (case of diffusional mixing). By substituting  $k_{eff}$  into Equation 2.12, the solute distribution in the solid for partial mixing can be achieved as

$$C_s = k_{eff} C_0 (1 - f_s)^{(k_{eff}-1)} \quad (2.15)$$

### 2.3.5. Floating Zone method

Unlike the VB, the melt in front of the S/L interface is finite in the Floating Zone (FZ) method. If the molten zone has the length of  $h$ , applying the flux balance at the interface (Figure 2.13) gives

$$(C_0 - C_s)dz = h dC_L \quad (2.16)$$

Integration from  $kC_0$  to  $C_s$  and from 0 to  $z$  results in

$$C_s = C_0 [1 - (1 - k) \exp(-kz/h)] \quad (2.17)$$

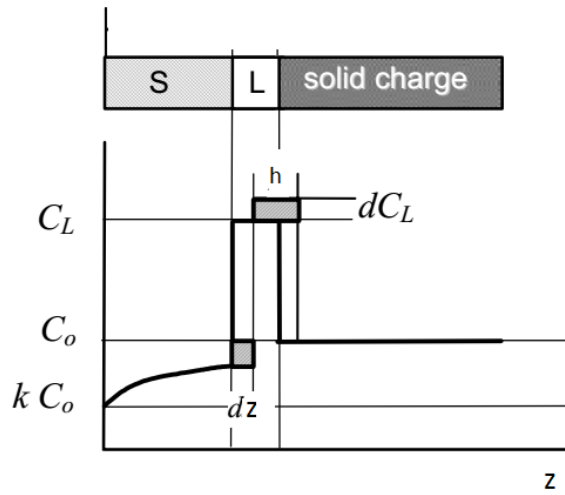


Figure 2.13. Solute redistribution in FZ method. Solid crystal(S), Liquid zone (L), and solid charge of the FZ method are also shown [30].

This equation was first developed by Pfann [68] for the Floating Zone method in the case of complete mixing where  $z$  is the distance from the interface and  $h$  is liquid zone length. It is also assumed that the solute concentration is the same in both the liquid zone

and solid charge (in the case of AHP/AVC, below and above the baffle) and it is equal to  $C_0$ . If it is not the case, Equation 2.17 can be written as

$$C_s = C_{02} - (C_{02} - kC_{01})\exp(-kz/h) \quad (2.18)$$

Where  $C_{02}$  is the initial concentration above the baffle and  $C_{01}$  is the initial concentration in the liquid zone below the baffle.

Also, Tiller [66] derived an equation for the diffusional mixing assumption in the transient regime as

$$C_s = C_0[1 - (1 - k)\exp(-\chi z)] \quad (2.19)$$

Where,  $\chi = \frac{kV/D_L}{[1 - \exp(-Vh/D_L)]}$ .

Just like in the FZ method, in AHP and AVC methods there is a finite liquid zone in front of the interface which is separated from the bulk liquid by the insertion of the baffle. Therefore, the solute redistribution equations developed for the FZ method are used for the AHP and AVC methods in this study. Note that in AVC liquid below and above baffle mixes, which is not the case in AHP.

All of the solute redistribution models discussed above is summarized in Figure 2.14.

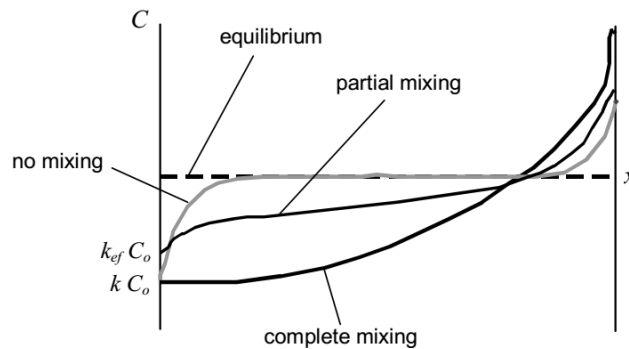


Figure 2.14. Comparison of analytical solute redistribution models [30].



## 2.4. Dislocations

### 2.4.1. Formation

As mentioned earlier in section 2.1.2, existence of screw dislocations and their intersection with the interface provide preferential site for the lateral growth and consequently affect the stability of the interface. The main source of dislocation generation is thermal stresses [69-74] arising from radial temperature gradient which leads to deflected interfaces during the growth. Dislocations can be emerged during the growth (grown-in dislocations). The dislocations forming in the seed can proceed through the crystal by propagation of the interface during the growth. Also, dislocations can be emerged after the growth (post-growth dislocations) by initiating thermal stress in the crystal due to cooling from the temperature close to the melting temperature to the room temperature [75]. Moreover, thermal gradients that create convective patterns near the s/l interface perturb the growth rate and cause solute segregation, which can be another source of dislocations [76-79].

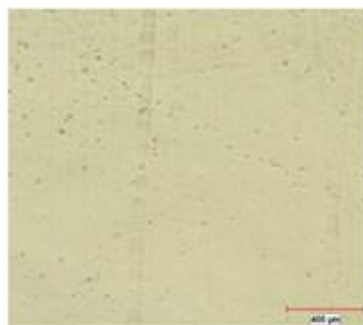
### 2.4.2. Visualization

In order to be able to investigate the effect of growth parameters on dislocation density, dislocations should be visualized. There are many methods for observation of the dislocations such as surface methods, decoration methods, X-ray diffraction method, and field ion microscopy and atom probe tomography [80]. However, the easiest and the most practical method is the surface method in which the atoms are removed from the surface of the crystal either by chemical or electrolytic etching [81]. Since the atom removal rate is higher in the dislocation emergence points, a pit is formed in these regions which indicate the existence of the dislocations. The reason that the rate of removal of the atoms is higher around the dislocations is the lattice distortion and the concentration of the impurity atoms at the dislocations that change the local chemical composition. The shape of the pits depends on the orientation of the surface [81]. It is square for [100] planes and triangular

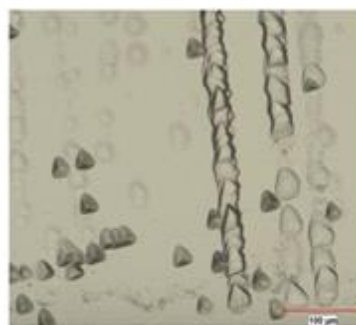
for [111] orientation. There are many etchants proposed for dislocation visualization [82-89]. However, it is important to use the appropriate etchant to get the useful results. Three different etchants with different compositions (Table 2.1) [90] are used. Figure 2.15 shows the etched surface of the sample with different etchants. The triangular shapes represent dislocations. As shown in Figure 2.15, the etchant No.2 is more proper to measure dislocation density for germanium.

Table 2.1. Different etchants and their compositions.

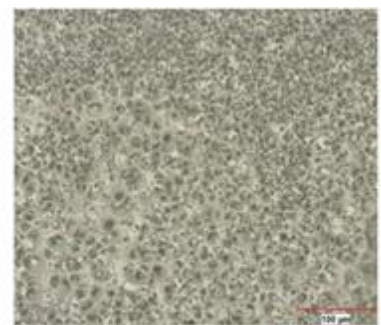
Etchant No.	Composition	Temperature (°C)	Duration of etching
1	3 parts HF and 5 parts HNO <sub>3</sub>	70	20 sec
2	8 g K <sub>3</sub> Fe(CN) <sub>6</sub> and 12 g KOH per 100 cm <sup>3</sup> H <sub>2</sub> O	100	3-4 min
3	10 cm <sup>3</sup> HF, 15 cm <sup>3</sup> HNO <sub>3</sub> , 5 cm <sup>3</sup> CH <sub>3</sub> COOH, 20 cm <sup>3</sup> H <sub>2</sub> O, 8 mg I and 2 mg KI	20	12 min



Etchant No.1



Etchant No.2



Etchant No.3

Figure 2.15. Visualization of dislocations with different etchants.

## 2.5. Morphological Stability

As mentioned earlier, the growth mechanism for germanium is the lateral growth in which the solidification proceeds layer by layer on an initial planar interface. However, temperature field and the composition of the solute in the melt at the vicinity of the interface may cause perturbations at the interface. If these perturbations are not damped out and amplified in time, the stability of the planar interface breaks down and it takes different morphological patterns such as cellular, dendritic, and equiaxed. It is important to maintain the planarity of the interface in the single crystal growth. Therefore, it is crucial to find out when and under which conditions these perturbations appear, how they are amplified in time, and how the stability of the planar interface breaks down. There are many theories to predict the instability of the interface which are covered in the following subsections. When a planar s/l interface changes its shape into cellular or wavy patterns it breaks down the homogeneity of the solute distribution and the single crystalline structure of the crystal.

### 2.5.1. Constitutional Supercooling

In alloy solidification, the liquidus temperature depends on the solute concentration. If the variation in the concentration of the solute increases the liquidus temperature in a way that the temperature gradient imposed by the furnace in the liquid ( $G_L$ ) becomes less than the liquidus temperature gradient ahead of the interface ( $G_L < \frac{dT_L}{dx}|_{x=0}$ ), a supercooled region is formed in front of the s/l interface. Hence, the portion of the interface has a driving force to grow into this region which eventually leads to formation of cellular patterns in the planar interface. This phenomenon is called constitutional supercooling (CS). Increasing the constitutional undercooling, leads to increase in the space between the cells which makes it possible for solid growth in the direction perpendicular to the growth direction and formation of dendrites. Even further increase in constitutional undercooling leads to nucleation of equiaxed grains in the undercooled liquid away from the interface.

This constitutional supercooling was quantified first by Rutter and Chalmers [91], and then together with Tiller and Jackson [66] a criterion for the stability was established as

$$\frac{G_L}{V} > \frac{m_L C_0 (1 - k)}{k D_L} \quad (2.20)$$

Where  $m_L$  is the slope of the liquidus line in the phase diagram. The liquidus temperature in a binary alloy is achieved as  $T_L = T_m + m_L C_L$ . Therefore,  $\frac{dT_L}{dx}|_{x=0} = m_L \frac{dC_L}{dx}|_{x=0}$ . Assuming that the redistribution of the solute in the liquid is solely by diffusion,  $\frac{dC_L}{dx}|_{x=0} = -\frac{VC_0(1-k)}{kD_L}$ . Substituting this equation into the criterion  $G_L < \frac{dT_L}{dx}|_{x=0}$  gives the Equation 2.20 as the constitutional supercooling criterion. According to Equation 2.20, a high temperature gradient of the furnace and a low solidification rate are required for maintaining the stability.

### 2.5.2. Mullins and Sekerka Criterion

A completely different criterion is based on the perturbation theory, which is first developed by Mullins and Sekerka [92]. They analyzed whether if a planar interface ( $z = 0$ ) is perturbed by an infinitesimal amplitude  $\varepsilon$  ( $z = \varepsilon \sin(\omega x)$ ), this sinusoidal perturbation at the interface will grow or decay. To this end, the rate of change of the amplitude of perturbation ( $\dot{\varepsilon} = d\varepsilon/dt$ ) should be determined. This requires determination of the velocity of the interface in terms of the local thermal and diffusional fields. The local governing equations for the thermal and the diffusional fields are

$$\nabla^2 C + (V/D_L)(\partial C/\partial z) = 0 \quad (2.21)$$

$$\nabla^2 T + (V/D_{th})(\partial T/\partial z) = 0 \quad (2.22)$$

$$\nabla^2 T' + (V/D'_{th})(\partial T'/\partial z) = 0 \quad (2.23)$$

Where  $D_L$  is the diffusion coefficient of the solute in the liquid,  $D_{th} = K_L/c_L$  is the thermal diffusivity of the liquid,  $D'_{th} = K_S/c_S$  is thermal diffusivity of the solid,  $K_S$  and  $K_L$

are the thermal conductivity of solid and liquid,  $c_s$  and  $c_L$  are the specific heat of liquid per unit volume and the specific heat of solid per unit volume, and  $T'$  is the temperature in the solid. The boundary conditions that should be satisfied at the interface are

$$T = m_L C + T_N \text{ where } T_N = T_m - T_m \Gamma_{SL} \varepsilon \sin(\omega x) \quad (2.24)$$

$$V = \frac{1}{\Delta H_f} \left[ K_S \left( \frac{\partial T'}{\partial z} \right) - K_L \left( \frac{\partial T}{\partial z} \right) \right] = \frac{D_L}{C(k-1)} \left( \frac{\partial C}{\partial z} \right) \quad (2.25)$$

Where  $\Gamma_{SL} = \gamma_{SL}/\Delta H_f$  is the capillarity constant,  $\gamma_{SL}$  is the specific s/l interface free energy, and  $\Delta H_f$  is the latent heat of fusion of the solvent. The solutions for Equation 2.21 to 2.23 are

$$C(x, z) - C_0 = \left( \frac{G_c D_L}{V} \right) \left( 1 - e^{-\left( \frac{Vz}{D_L} \right)} \right) + \varepsilon(b - G_c) \sin(\omega x) e^{-\omega^* z} \quad (2.26)$$

$$T(x, z) - T_0 = \left( \frac{G_L D_{th}}{V} \right) \left( 1 - e^{-\left( \frac{Vz}{D_{th}} \right)} \right) + \varepsilon(a - G_L) \sin(\omega x) e^{-\omega_{th} z} \quad (2.27)$$

$$T'(x, z) - T_0 = \left( \frac{G_S D'_{th}}{V} \right) \left( 1 - e^{-\left( \frac{Vz}{D'_{th}} \right)} \right) + \varepsilon(a - G_S) \sin(\omega x) e^{-\omega'_{th} z} \quad (2.28)$$

Where  $T_0$  and  $C_0$  are the temperature and the concentration of the flat interface,  $G_c = -\frac{VC_S^*(1-k)}{kD_L}$  is the concentration gradient and  $G_S$  and  $G_L$  are the thermal gradients in the solid and the liquid respectively,  $C_S^*$  is the solid concentration at the interface,  $\omega^* = \frac{V}{2D_L} + \left[ \left( \frac{V}{2D_L} \right)^2 + \omega^2 \right]^{1/2}$ ,  $\omega_{th} = \frac{V}{2D_{th}} + \left[ \left( \frac{V}{2D_{th}} \right)^2 + \omega^2 \right]^{1/2}$ ,  $\omega'_{th} = \frac{V}{2D'_{th}} + \left[ \left( \frac{V}{2D'_{th}} \right)^2 + \omega^2 \right]^{1/2}$ , and  $a$  and  $b$  are the parameters that should be determined (the procedure is presented in [92]). Assuming that the velocity of the interface is  $V = \dot{\varepsilon} \sin(\omega x)$ , further manipulations (provided in [29]) leads to the following criterion for the stability of the interface which is known as MS criterion.

$$\frac{\dot{\varepsilon}}{\varepsilon} = \frac{V\omega \left[ -2T_m \Gamma_{SL} \omega^2 \left( \omega^* - \frac{Vl}{D_L} \right) - \left( \frac{K_S G_S + K_L G_L}{\bar{K}} \right) \left( \omega^* - \frac{Vl}{D_L} \right) + 2m_L G_c \left( \omega^* - \frac{V}{D_L} \right) \right]}{\left( \frac{K_S G_S - K_L G_L}{\bar{K}} \right) \left( \omega^* - \frac{Vl}{D_L} \right) + 2\omega m_L G_c} \quad (2.29)$$

Where  $\omega$  is the wave number of the perturbations,  $\bar{K} = (K_S + K_L)/2$  is the average thermal conductivity, and  $l = (1 - k)$ .

If the right hand side (RHS) of Equation 2.29 becomes positive, the perturbations will grow which leads to interface instability, and if the RHS becomes negative, the perturbations forming at the interface will decay, so the interface will remain stable.

### 2.5.3. Favier and Rouzaud Approach

In the MS criterion, convection is neglected. However, Favier and Rouzaud (FR) [93] included the effect of convection in their proposed criterion. By defining a deformable boundary layer which is also perturbed with the interface, the FR criterion for the stability is derived as

$$-\frac{V(K_L G_L + K_S G_S)}{2D_L \bar{K}} - \frac{4T_m \Gamma_{SL} V^2 \pi^2}{\Lambda^2 D_L^2} + \frac{k_{eff} m_L G_C}{k} \left\{ 1 - \frac{2k}{\xi} - \frac{H+Q}{\xi} \exp\left[\frac{-\Delta(1+Q)}{2}\right] \right\} < 0 \quad (2.30)$$

Where  $\Delta = \frac{\delta V}{D_L}$  is the non-dimensional wavelength,  $\Lambda = \frac{\lambda V}{D_L} = \frac{2\pi V}{\omega D_L}$  is the non-dimensional solute boundary layer,  $k_{eff} = \frac{k}{[k+(1-k)\exp(-\Delta)]}$  is the effective distribution coefficient, and the terms  $Q$ ,  $H$ , and  $\xi$  are defined as

$$Q = \left[ \frac{\Lambda^2 + 16\pi^2}{\Lambda^2} \right]^{1/2} \quad (2.31)$$

$$H = Q \coth\left(\frac{Q\Delta}{2}\right) \quad (2.32)$$

$$\xi = H + 2k - 1 \quad (2.33)$$

According to Equation 2.30, the FR criterion predicts that the stability of the interface increases with increase in the convection (reducing  $\delta$ ).

#### 2.5.4. Kinetic Stability

In the MS criterion, the interface is considered rough and isotropic which grows continuously. However, if the interface is faceted, as the case in most semiconducting crystals, atoms will preferentially attach to step ledges and kink sites due to anisotropic surface energy, and lateral growth will be dominated ( $V_{LG} \gg V_n$ ). Thus, steps from adjacent peaks of perturbation may spread into each other and decrease the overall height of the perturbations. The time it takes for steps from adjacent peaks, separated by  $\lambda$ , to spread into each other is

$$t_s = \frac{\lambda}{2V_{LG}} \quad (2.34)$$

For vicinal and tilted interfaces, spreading parallel to the interface will preferentially occur in one direction due to geometrical constraints, so  $t_s$  is

$$t_s = \frac{\lambda}{V_{LG}} \quad (2.35)$$

And as depicted in Figure 2.16, the lateral growth rate is calculated as

$$V_{LG} = V_L(\cos \theta) \quad (2.36)$$

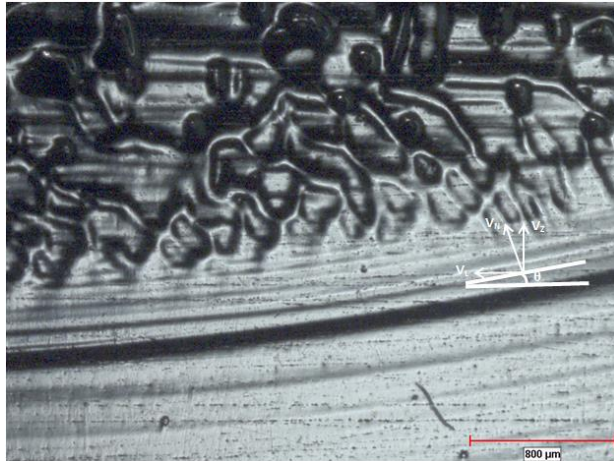


Figure 2.16. Striations at the onset of instability and the growth rate components.

Where  $R_L$  is the growth rate of the steps. Therefore,  $t_s$  can be written as

$$t_s = \frac{\lambda}{V_{LG}} = \frac{\lambda}{V_L(\cos \theta)} = \frac{\lambda(\sin \theta)}{V_z} \quad (2.37)$$

If  $t_s$  is shorter than the time required for the perturbation amplitude to double, the perturbation will decay. This concept can be written as kinetic stability (KS) criterion [21]

$$\frac{\dot{\varepsilon}}{\varepsilon} < \frac{V_z}{\lambda(\sin \theta)} \quad (2.38)$$

For more quantitative analysis, the KS parameter is defined as

$$KS = \frac{\frac{\dot{\varepsilon}}{\varepsilon} - \frac{V_z}{\lambda(\sin \theta)}}{\frac{V_z}{\lambda(\sin \theta)}} \quad (2.39)$$

Figure 2.17 [94] shows this KS parameter as a function of solute concentration for different vicinal angles. As  $\theta$  is decreasing (increasing  $V_{LG}/V_n$ ), KS turns into positive values at a higher solute concentration which expresses the increased stability.

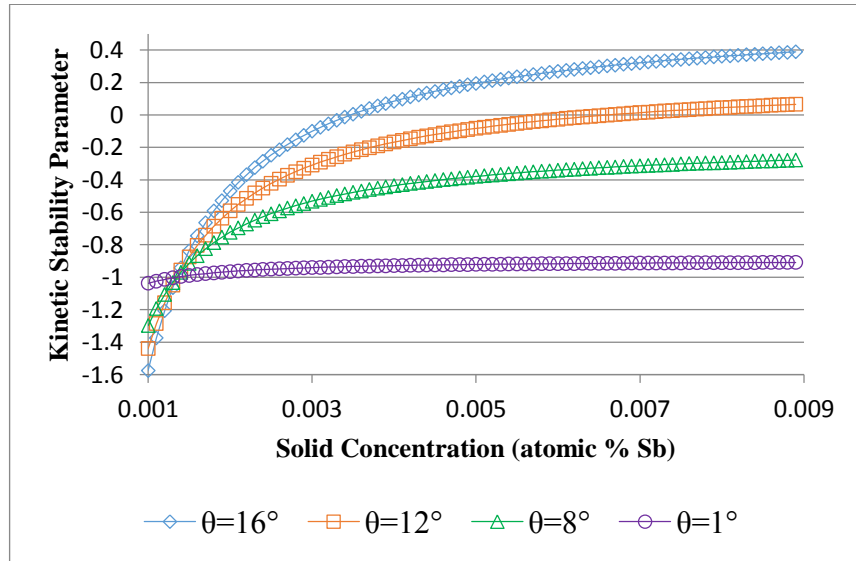


Figure 2.17. KS stability for different vicinal angles.



## 2.6. Solidification Modeling Methods

There are many numerical methods for modeling phase change problems including melting/solidification phenomenon. Generally, all these methods can be divided into two main approaches. The first approach is tracking the s/l interface explicitly (interface tracking method). In each time step, an extra equation for advection of the interface with an extra boundary condition on the interface (Stefan boundary condition) is required to be solved. Phase field [95-101] and Level set [102-107] methods are two well-known methods using this approach in order to model melting/solidification problems. On the other hand, in the second approach, the Stefan condition on the s/l interface is incorporated implicitly and explicit tracking of the interface is avoided. Methods using this approach are apparent heat capacity method [108, 109], effective capacity method [110-113], heat integration method [114-116], source based method [117, 118], and enthalpy-porosity method [119, 120]. Detailed explanations of these methods are presented in a review by H. Hu and S. A. Argropoulos [121]. Although apparent heat capacity method provides very simple solution for phase change problems, it suffers from small time step restrictions. Modifications in effective heat capacity methods to overcome this issue make this method numerically more expensive. While the heat integration method is computationally more economical, the accuracy in predicting the s/l interface is not satisfying. However, the enthalpy-porosity method is the simplest and most practical among other existing methods and gives accurate results. Therefore, ANSYS FLUENT uses enthalpy-porosity method for modeling melting/solidification problems.

In this study, ANSYS FLUENT is used to model the solidification of Ge-Sb. Simulations can be divided into two groups, global and local. While the geometry of the global simulations contains the whole solidification assembly including the furnace and the insulators, the geometry of the local simulations is restricted to the crucible, melt, and baffle inside the crucible. The details are explained in sections 4.2.1 and 4.2.2.

### 3. MOTIVATION AND OBJECTIVES

Available growth methods and their use for growing germanium single crystals are provided in Section 2.2.1. Presented literature in Section 2.2.1 infers that the AVC method may make it possible to produce quality crystals with a higher production yield. This inference is the motivation for the current dissertation study. Hence, among the mentioned methods in Section 2.2.1, the AVC method in the VB configuration is used in this Ph.D. study for growing Ge-Sb single crystals for the first time in the world. Partial results of this study are published in [21].

In this Ph.D. dissertation, antimony-doped germanium single crystal growth is investigated both experimentally and numerically to determine the effects of growth parameters on the quality of the grown crystals. Homogeneous solute redistribution and enhanced stability of the interface are the main challenges in the crystal growth. Natural convection arising from the radial temperature gradient in the VB method leads to inhomogeneous solute redistribution. Moreover, since the solute is rejected to the bulk fluid, most portion of the dopant is trapped into the poly crystalline region which is not going to be used in electronic devices. In order to overcome these handicaps, a baffle inserted to the melt to reduce the melt height and create forced convective flow in the AHP method. However, the pulling rate is still a major limitation which determines the time and cost of production. The current study investigates the vibration parameters in the AVC technique for the first time for Ge-Sb single crystal growth to increase the production yield by maintaining or improving the crystal quality. The main objectives of the study can be listed as follows:

- (i) Improve crystal quality and production yield.
- (ii) Grow crystals with three different methods, VB, AHP, and AVC.
- (iii) Investigate proper methods for sample preparation and metallographic analysis.
- (iv) Determine crystal quality with respect to single crystal length, solute uniformity, and dislocation density.

- (v) Simulate crystal growth process in global and local geometry to identify effect of growth parameters and to determine the most influential parameters.
- (vi) Investigate the influence of the growth parameters based on the growth methods.
- (vii) Make method suggestion for improved crystal quality and production yield.

## 4. MATERIALS AND METHODS

### 4.1. Experimental Apparatus and Procedures

#### 4.1.1. Crystal Growth Unit

As mentioned earlier, in order to postpone the instability of the interface and provide homogeneous solute distribution in the grown crystal, the growth parameters should be controlled accurately. This can be facilitated by a proper crystal growth method. In this study, the VB, AHP, and AVC methods are used and explained in the following subsections. Figure 4.1 shows the crystal growth unit, which is used in Bogazici University Single Crystal Growth Laboratory (BUSCG LAB). It contains a growth chamber, a vacuum enclosure, a translation mechanism, and a control system.

4.1.1.1. Growth Chamber. The growth chamber contains a cylindrical furnace made of alumina with 80 mm diameter and 450 mm height. In order to establish a desired axial temperature gradient, molybdenum wires, which are covered by alumina ceramics, are wrapped around the furnace with a certain separation. A graphite crucible with 40 mm inner diameter and 180 mm height is placed inside the furnace. The solidification takes place inside this crucible. There are several annular and axial grooves on the outer side of the crucible for positioning the thermocouples to record the temperature data along the crucible during the experiment. The top and bottom of the crucible are closed with a graphite cap and a graphite pedestal, respectively. There is a hole in the center of the cap for inserting the baffle in the AHP and AVC methods. The pedestal is connected to a molybdenum rod which can be translated vertically for moving the crucible through the furnace. The furnace and its ingredients are placed inside a cylindrical stainless steel enclosure. In order to provide a proper insulation and avoid heat loss of the furnace due to radiation, first two cylindrical molybdenum shields and then a three-layer graphite felt are placed between the furnace and the stainless steel enclosure. The baffle used in the AHP

and AVC methods is also made of graphite and has 39 mm diameter and 20 mm height to provide 0.5 mm annular gap for the melt flow. The schematic of the internal parts of the growth chamber is shown in Figure 4.2 [15].

4.1.1.2. Vacuum Enclosure. The stainless steel enclosure mentioned above is closed with two plates from bottom and top and the bottom plate is fixed on a stainless steel platform as shown in Figure 4.1. The enclosure is made double-wall for providing cooling by water circulation inside the walls of the enclosure. In order to avoid oxidization during heat up process, the system should be run under vacuum. To this end, Ilmvac mechanical vacuum pump and MRV100 multi range vacuum gauge with 1 digit resolution are used to evacuate the enclosure down to  $10^{-3}$  mbar. The evacuation continues until the system reaches  $500^{\circ}\text{C}$ . After this point, the system should continuously be purged with inert argon gas.

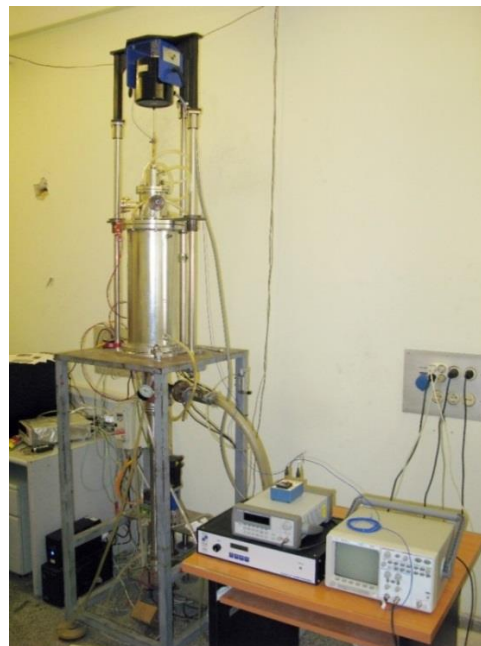


Figure 4.1. The crystal growth unit used in BUSCG LAB.

4.1.1.3. Translation Mechanism. In order to provide upward and downward motion of the crucible through the furnace, the molybdenum rod, which is connected to the pedestal from the top, is connected to the stainless steel shaft from the bottom. The bottom of the shaft is

closed with a flange. The thermocouple wires used inside the system are passing through the shaft and exit from the flange which is sealed with silicon O-ring. The flange is connected to a servo motor in order to move the shaft upward and downward.

4.1.1.4. Control System. In order to set the temperatures of the heaters, read temperature data from the thermocouples, pulling down and pushing up the crucible with a certain velocity, the crystal growth unit and its different components should be controlled with a data acquisition system. In this study, this is done by in-house developed software called LABVIEW. The thermocouples used on the crucible are handmade C-type thermocouples with 4.5 °C tolerance. These thermocouples consist of two wires (Tungsten-5% Rhenium and Tungsten-26% Rhenium) and the tips of the wires are welded. The wires are fed through double-hole ceramic beads to provide thermal and electrical. For the length of the wires that extends out of the furnace two fiber glass insulators with different colors (red and blue) are used. The electrical connections at the end of the wires are made by screw terminals in the boxes outside of the system which act as cold junction points. The connections between these boxes and the data acquisition system are done by copper wires.

For the accuracy of the temperature measurements, cold junction temperature in the terminal box should be measured via two K-type thermocouples, which has 2.2 °C tolerance, for cold junction compensation in the software.

The temperature data from the thermocouples are collected via a Keithley 7700 differential multiplexer module that is plugged into a Keithley 2700 data acquisition and switching system. The communication between the data acquisition system and the computer is done by an IEEE-488 (GPIB) interface. For monitoring the data, a software developed on the LABVIEW platform is used. The user interface of this platform consists of three pages, setup page, display page, and error page. In the setup page, the set temperatures and corresponding PID (Proportional Integral Derivative) values for each zone of the furnace, the velocity and the travel distance of the servomotor are determined. The system set the required output voltage to heat up the furnace zones either manually or

by PID control. A voltage range from 0 to 10 Volts sent to four Eurotherm single phase power thyristor (SCR) units using a Keithley PCI3130 analog output card. Then a current up to 60 A is sent by these thyristors to heat up the furnace zones. Also, for providing the rotation of the servomotor with a constant rate, the software sets a constant voltage rate.

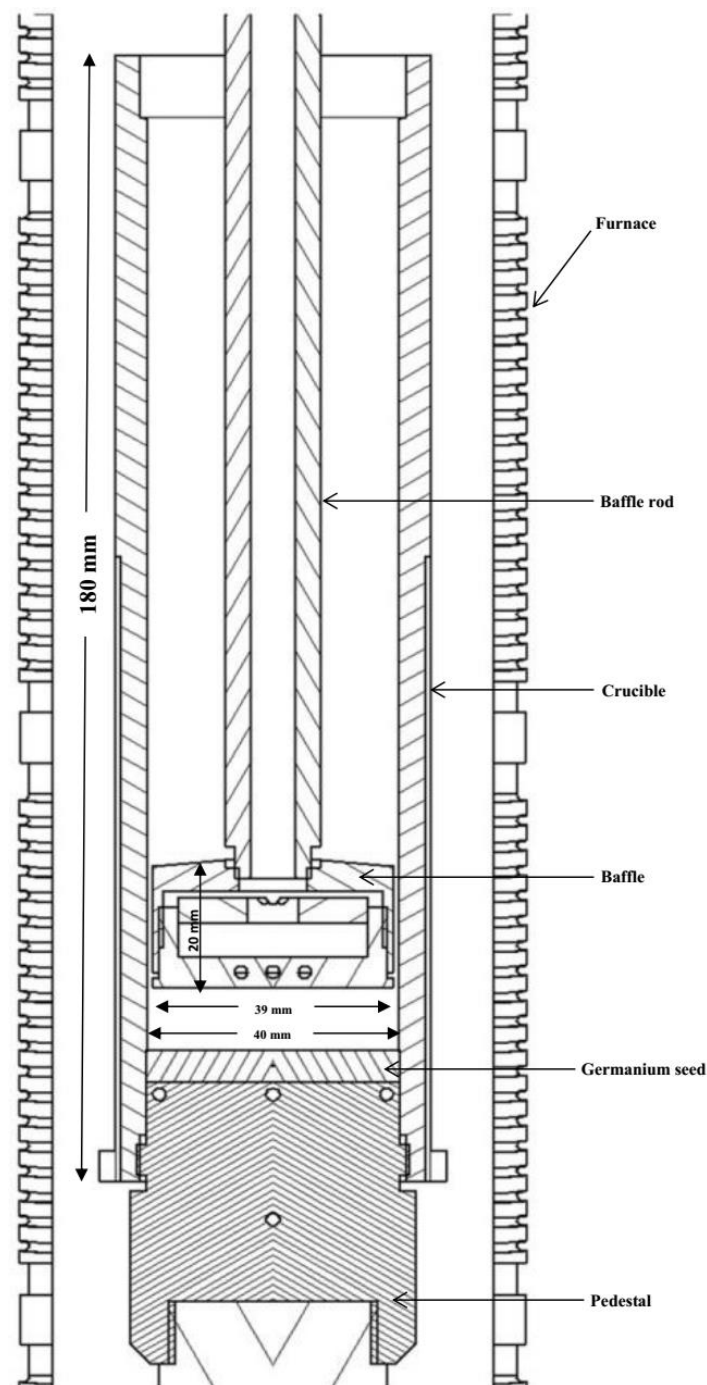


Figure 4.2. Internal parts of the growth chamber [15].

The display page provides a graph of temperature versus time and also the table consists of output voltages, thermocouple temperatures, set temperatures, position of the shaft, and the time which are recorded in an excel workbook. Whenever the software encounters a problem, the error is shown in the error page.

#### 4.1.2. Experimental Procedures

The schematic of the experimental setup is shown in Figure 2.9. All the crystals are grown in a 40 mm inner diameter graphite crucible in which a seed and germanium chunks are placed. In order to have flat isotherms and consequently promote a planar growth, the crucible is placed within the furnace appropriately. A highly pure single crystal germanium seed with 10 mm height and [111] orientation is placed at the bottom of the crucible. Since the melting temperature of the antimony ( $630^{\circ}\text{C}$ ) is much lower than that of the germanium ( $938.3^{\circ}\text{C}$ ), a master charge of a Ge-Sb alloy is prepared in vacuum and placed between the seed and germanium chunks to avoid vaporization of antimony during melting of the germanium chunks. Then, the polycrystalline germanium chunks are poured over the seed and the master charge. The concentration of the antimony in the master charge is set to obtain an overall  $10^{20}$  atoms/cc antimony concentration in the entire grown crystal. The total weight of the master charge is set to be approximately 10 g [29]. In order to obtain the  $C_{Sb} = 10^{20}$  atoms/cc, the weight of Sb and Ge chunks should be calculated. The calculation steps are as the following.

$C_{Sb} \left[ \frac{\text{atoms}}{\text{cc}} \right] = \frac{n_{sb}[\text{atoms}]}{V_T[\text{cc}]}$  with  $V_T = \pi \frac{D^2}{4} L$  Where,  $D$  is the diameter of the crystal and  $L$  is the length of the grown crystal except the length of the seed that is not melted. Then the weight of the required Sb can be calculated as

$$m_{sb}[\text{g}] = \frac{n_{sb}[\text{atoms}] \times M_{sb}[\frac{\text{g}}{\text{mol}}]}{N_A[\frac{\text{atoms}}{\text{mol}}]}$$



By converting the concentration of Sb from  $\frac{atoms}{cc}$  to  $wt\% = \frac{m_{sb}}{m_{sb}+m_{Ge}} \times 100$ , and knowing the weight of Sb ( $m_{sb}$ ), the weight of germanium is obtained. The weight of half of the seed and the weight of germanium used in the master charge should be subtracted from this value to obtain the weight of polycrystalline germanium chunks.

4.1.2.1. The Vertical Bridgman (VB) Method. In the VB method, after putting the seed, the master charge, and the germanium chunks inside the crucible, the system is closed but the bolts used in fastening the top and bottom plates to the vacuum enclosure are not tightened. Then, the mechanical vacuum pump is turned on to evacuate the system. When the inner pressure reaches to 10<sup>-3</sup> mbar, the bolts are tightened. Afterwards, the heaters of the furnace are set manually to reach 500°C. Up to this temperature, the system works under vacuum conditions to remove degassing impurities, and then the chamber has been argon purged three times. After this point, the heaters are heated up to their set temperatures with the PID control. The argon gas pressure inside the chamber is kept almost 1 atm above the ambient pressure during the experiment. The crucible is positioned in a way to melt all of the germanium chunks and half of the seed to establish the initial S/L interface. After waiting around 20 minutes for stabilization, the solidification process is started with rotating the servomotor and pulling down the shaft with a constant velocity. After the solidification is completed, the system is cooled down by the PID control until the heater temperatures reach 250°C. Up to this point, the argon gas feeding is continued in order to avoid oxidization.

4.1.2.2. The Axial Heat Processing (AHP) Method. The procedures described for the VB method are also followed in the AHP method. The only difference is that in the AHP method, a baffle of 39 mm diameter and 20 mm height is inserted into the melt via a 15 mm diameter graphite baffle shaft which is connected to a brass rod which is extended out of the vacuum enclosure. Moreover, three extra thermocouples (T1-T3 in Figure 2.9) are embedded inside the baffle to detect the temperature data in the melt close to the interface during the experiment. Since at the beginning of the experiment the germanium chunks have not been melted yet, the baffle should be positioned at its maximum position inside

the crucible. Similar to the VB method, the heaters reach to their set points and the crucible is positioned to melt half of the seed. Then, the baffle is pushed downward to touch the seed and pulled up to set the initial melt height before the solidification process begins. After setting the desired initial melt height and waiting for stabilization, the solidification process starts with pulling down the crucible with a desired constant velocity. The remaining procedures are the same as in the VB method.

4.1.2.3. The Axial Vibrational Control (AVC) Method. The AVC method is very similar to the AHP method and the same procedures for the AHP method are followed in the AVC method. The only contribution in this method is the axial vibration of the baffle during the solidification process. In order to supply this axial vibrational motion of the interface, a MODAL SHOP shaker model 2060E is assembled on top of the growth unit connected to the brass rod (Figure 4.1). This vibrator is powered by a SmartAmp power amplifier. An Agilent model 33220A signal generator is used to set the desired amplitude and frequency of the vibration which are monitored by an Agilent oscilloscope model 54621A during the crystal growth. The amplitude of the sinusoidal vibration is measured by a laser Doppler velocimeter. The vibration starts after the initial melt height is set and the system becomes stable.

### **4.1.3. Characterization**

After the solidification process has completed the grown crystal is taken out of the crucible. Each crystal is axially cut into two halves in order to study its characterizations. One of the halves is divided into radial slices with 10 mm interval along the axial direction (Figure 4.3). These slices are chemically etched to detect the dislocations. The other half of the grown crystals is used to determine the solute concentration and single crystallinity.

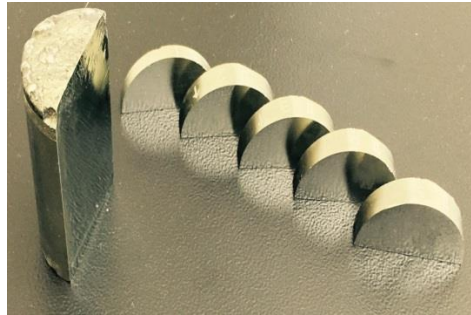


Figure 4.3. A crystal cut into two halves for revealing the characterization of the grown crystal.

4.1.3.1. Metallography. In order to prepare the surface of the crystal for resistivity measurement and revealing the striation lines, the standard metallography processes are applied. First, the surface is grinded with Beuhler SiC grinding papers from coarse (P-120 grit) to fine (P-2000 grit). Then, the ground surface is polished on Beuhler polishing cloths and a suspension of 5 $\mu$ m, 1  $\mu$ m, and 0.3 $\mu$ m Beuhler alumina powders, respectively.

4.1.3.2. Resistivity Measurement. After grinding and polishing the sample to achieve a mirror surface, the sample is ready for resistivity measurement. The measurement is done by four-point probe technique. The resistivity data have been collected axially starting from 5 mm above the seed base with 4 mm intervals upward. In the radial direction, the data have been collected up to 16 mm to the left and 16 mm to the right of the central axis with again 4 mm intervals (Figure 4.4). The probe tip has been kept 4 mm away from the sides to prevent edge effect.

For measuring the resistivity, the head of a JANDEL micro-position probe (provided by Jandel Engineering Ltd., UK) is lowered onto each grid point on the surface and the current is set to 30 mA. Then, the forward and reverse polarity voltages are taken from a JANDEL RM3 Nano voltmeter with 0.1% accuracy.

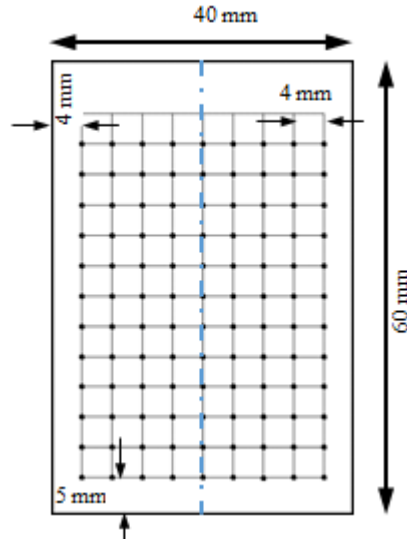


Figure 4.4. Four-point-probe schematic grid points.

These measurements are converted to resistivity via the following relationship [122]

$$Rs = 2\pi s V_r / I_r \quad (4.1)$$

Where  $Rs$  is the resistivity,  $s$  is the distance between the probe needles (0.72 mm in this case),  $I_r$  is the applied current, and  $V_r$  is the measured voltage. This resistivity is converted to dopant concentration [123] in order to obtain the axial and radial dopant distribution in each crystal.

4.1.3.3. Striations. After the 4-point probe measurement, the polished surface has been electrolytically etched in a solution of 150 mL  $H_2O$  and 1.9 g  $Na_2SO_3$  using a graphite cathode with 2A current [18] to reveal the single/poly crystalline regions as well as the striations that show the interface position and shape during the solidification.

4.1.3.4. Dislocations. In order to calculate the dislocation density, each semicircular surface is divided into 16 zones (Figure 4.5). Each region has four sub regions as seen in Figure 4.5. Then, the dislocation density for each region is calculated from average number of dislocations in each sub regions shown in Figure 4.5. In addition, the average

dislocation density for the seed, which is a pure single crystal, is calculated and it is  $1.23 \times 10^5 \text{ cm}^{-2}$ .

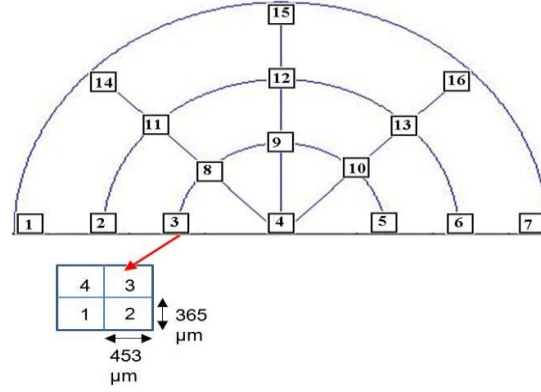


Figure 4.5. 16 zones where Dislocation densities are determined.

## 4.2. ANSYS Fluent Solidification/Melting Model

In order to prove our experimental observations and support our explanations for the experimental results, numerical models are developed using ANSYS Fluent software. There are many other commercial software packages for modeling the solidification and crystal growth such as CGSim [124], CrysVUn [125], CrysMAS [126], STHAMAS [127], ORCAN [128], and FEMAG [129]. However, providing robust and trusted solvers for fluid flow and presenting practical and user friendly solidification/melting module for the phase change problems make ANSYS Fluent preferred in this study. Among numerical methods used for solidification/melting phenomenon mentioned in section 2.6, ANSYS FLUENT uses enthalpy-porosity method [130]. In this method, instead of tracking the s/l interface, the interface is identified by liquid fraction ( $f_l$ ). In a completely solidified region  $f_l$  is equal to zero, in a completely liquid region  $f_l$  is equal to one, and in the mushy zone  $f_l$  differs between zero and one. The liquid fraction is calculated based on the liquidus and solidus temperatures of the solidifying material.

$$f_l = \begin{cases} 0 & T < T_S \\ \frac{T - T_S}{T_L - T_S} & T_S < T < T_L \\ 1 & T > T_L \end{cases} \quad (4.2)$$

The equations solved in ANSYS Fluent during the modeling of the solidification/melting problem are conservation of energy for updating the temperature field, conservation of mass (continuity) and momentum for updating the velocity field of the fluid flow, and conservation of species for updating the redistribution of the solute. In the following it is explained that how ANSYS Fluent treat these equations to model the solidification/melting phenomenon.

In solidification/melting problems, the conservation of energy equation is written in terms of enthalpy ( $H$ ) of the material which is calculated as sum of the sensible heat ( $h'$ ) and the latent heat ( $L$ ). The incorporation of the latent heat to the enthalpy is again provided by the liquid fraction. When the liquid fraction is zero (solid region), the amount of the enthalpy is just the sensible heat. When the liquid fraction is one (liquid region), the enthalpy is the sum of both the sensible and latent heats and in the mushy zone, fraction of the latent heat ( $\Delta H$ ) is added to the sensible heat.

$$\frac{\partial}{\partial t}(\rho H) + \nabla \cdot (\rho \vec{u} H) = \nabla \cdot (K \nabla T) \quad (4.3)$$

$$H = h' + \Delta H, \quad h = h_{ref} + \int_{T_{ref}}^T C dT, \quad \Delta H = f_l L \quad (4.4)$$

The momentum equation for the velocity components is discretized in the whole domain (solid and liquid) by adding a sink term ( $S_u$ ) to the momentum equations which forces the velocity components to be zero in solid regions. The amplitude of the velocity damping to zero is adjusted by mushy zone parameter ( $A_{mush}$ ). The higher the mushy zone parameter the steeper the transition of the velocity to zero as the material solidifies.

$$\nabla \cdot \vec{u} = 0 \quad (4.5)$$

$$\rho \frac{\partial \vec{u}}{\partial t} + \rho \vec{u} \cdot \nabla \vec{u} = \nabla \cdot (\mu \nabla \vec{u}) - \nabla p + S_u + S_b \quad (4.6)$$

$$S_u = A_{mush} \frac{(1 - f_l)^2}{f_l^3 + \epsilon} \quad (4.7)$$

Applying Boussinesq approximation, the body force term in the momentum equation ( $S_b$ ) can be written as:

$$S_b = \frac{\rho g \beta (h - h_{ref})}{c} \quad (4.8)$$

Where,  $\beta$  is the thermal expansion coefficient.

In the case of pure material, the solidus and liquidus temperatures are the same. However, for a binary alloy the liquidus and solidus temperatures are defined as

$$T_L = T_m + mY, \quad T_S = T_m + mY/k \quad (4.9)$$

Where  $m$  is the slope of the liquidus line, and  $Y$  is the mass fraction of the solute. In the case of binary alloy, the conservation of species equation should also be solved to achieve the solute redistribution. ANSYS fluent offers two alternatives, Lever and Scheil assumptions. If the Lever rule is applied, the species transport equation is written as

$$\frac{\partial}{\partial t}(\rho Y) + \nabla \cdot (\rho [f_l \vec{u} Y_{liq} + (1 - f_l) \vec{v}_p Y_{sol}]) = -\nabla \cdot \vec{J} \quad (4.10)$$

Where  $\vec{J} = -\rho [f_l D_{m,liq} \nabla Y_{liq} + (1 - f_l) D_{m,sol} \nabla Y_{sol}]$ ,  $Y_{liq}$  and  $Y_{sol}$  are concentration of solute in liquid and solid respectively and  $D_{m,liq}$  and  $D_{m,sol}$  are mass diffusion coefficient of solute in liquid and solid and  $\vec{v}_p$  is the pulling velocity.

On the other hand, if Scheil rule is applied, the species transport equation is solved for  $Y_{liq}$  as the dependent variable.

$$\begin{aligned} \frac{\partial}{\partial t}(\rho Y_{i,liq}) + \nabla \cdot (\rho [f_l \vec{u} Y_{liq} + (1 - f_l) \vec{v}_p Y_{sol}]) \\ = \nabla \cdot (\rho f_l D_{m,liq} \nabla Y_{liq}) - k Y_{liq} \frac{\partial}{\partial t}(\rho(1 - f_l)) \\ + \frac{\partial}{\partial t}(\rho(1 - f_l) Y_{liq}) \end{aligned} \quad (4.11)$$

### 4.2.1. Global Geometry

4.2.1.1. Geometry and Mesh Generation. Modeling the entire geometry enables us to achieve more precise data on the boundary of the solidifying region; therefore, the entire domain of the assembly is modeled. The simulated global geometry and its different parts are shown in Figure 4.6. This 2D axisymmetric geometry is meshed via GAMBIT software as shown in Figure 4.7. In order to distinguish several regions from each other, the software uses different colors separately for each region. The minimum cell size is  $0.015625 \text{ mm}^2$  and the maximum cell size is  $1 \text{ mm}^2$ . In the regions below the baffle, above the baffle and close to the baffle the cell size is  $0.03125 \text{ mm}^2$  and at the vicinity of the baffle (0.5 mm below and above the baffle) and the gap region between the baffle and the crucible the cell size is  $0.03125 \text{ mm}^2$ . The cell size in the crucible base is  $0.3 \text{ mm}^2$ , in the pedestal is  $0.54 \text{ mm}^2$ , in the crucible wall is  $0.2825 \text{ mm}^2$ , in the melt region above the baffle and far away the baffle is  $0.07 \text{ mm}^2$ , in the heaters is  $0.875 \text{ mm}^2$ , and in all other regions is  $1 \text{ mm}^2$ .



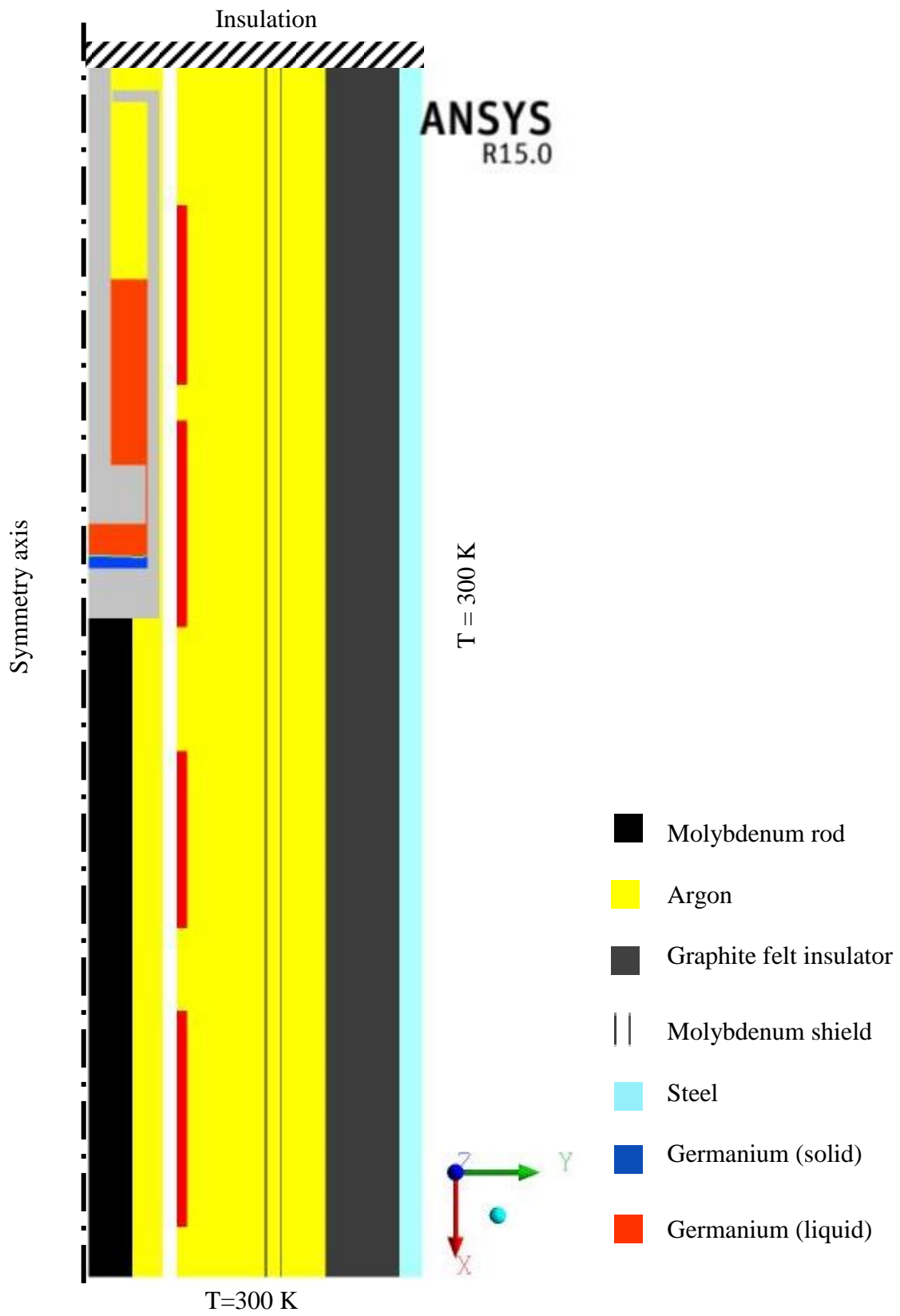


Figure 4.6. Global geometry.

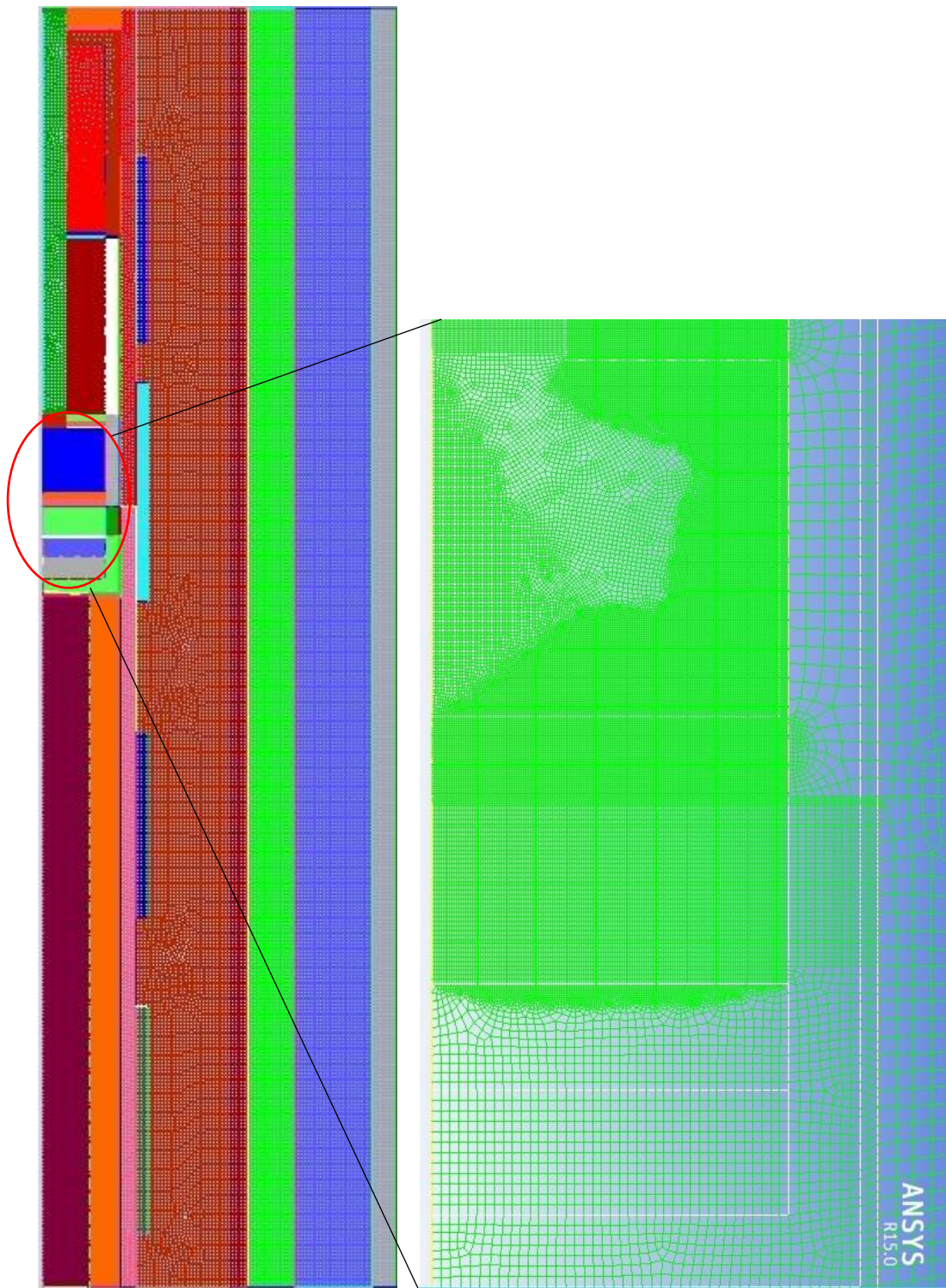


Figure 4.7. Mesh of the global geometry.

**4.2.1.2. Solidification/Melting Model.** The material properties used in the simulations are listed in Table 4.1. The solidification/melting module of ANSYS fluent is used. The  $A_{mush}$  parameter is recommended to set between  $1e4$  to  $1e7$  for most computations. While high values of  $A_{mush}$  lead to faster drop of the velocity to zero as the material solidifies, too large values lead to oscillation in the solution and divergence. In this study,  $A_{mush}$  parameter is set to  $1e6$ . When the solidification and melting module is activated, the energy module in the models dialog box of the ANSYS Fluent is turned on automatically. The flow is assumed to be viscous and laminar. While setting the density for germanium, the Boussinesq choice is selected to account for natural convection in the melt. In the cell zone conditions, the reference temperature is set to the highest temperature in the field. The SIMPLE scheme is used for the pressure-velocity coupling, the least square cell based is chosen for gradient spatial discretization, and the pressure spatial discretization is done by body force weighted method. The spatial discretization of momentum and energy equations are done by second order upwind method (in the case of convergence problem, first order upwind method is used) and the first order implicit method is used for transient formulations. The screen shots of ANSYS Fluent Graphical User Interface (GUI) of the relevant settings for solving the solidification/melting problem are provided in appendix A.

Table 4.1. Material properties.

Material	Germanium	Steel	Molybdenum	Graphite	Argon	Alumina
Density (kg/m <sup>3</sup> )	5500 [29]	8030 [131]	10280 [132]	2260 [133]	1.6228 [134]	3690 [135]
Specific heat (J/kg.K)	380 [29]	502.48 [131]	250 [132]	710 [136]	520.64 [134]	880 [135]
Thermal conductivity (W/mK)	39[29](liquid) 17 [29](solid)	16.27 [131]	138 [132]	70 [137]	0.0172 [134]	30 [135]
Viscosity (kg/m-s)	0.0073255 [29]					
Thermal expansion coefficient (1/K)	0.0001 [29]					
Melting heat (J/kg)	465000 [29]					
Solidus/Liquidus temperature (K)	1211 [29]					
Emissivity	0.2 [138]	0.45 [139]	0.3 [140]	0.8 [139]	0	0.4 [141]

**4.2.1.3. Heat Transfer.** The model contains different materials including solid insulators, liquid germanium, argon gas, solid baffle, crucible and pedestal. The heat transfer through all these materials involves conduction (solid, liquid, gas regions), convection (liquid and gas), and radiation (argon gas). For simplicity, the argon gas volume is also considered as solid and the only liquid volume is the germanium. The discrete ordinate (DO) model is used for the radiation. The emissivity of the materials is brought in Table 4.1. Also, all the surfaces are assumed opaque and diffused wall.

**4.2.1.4. Boundary Conditions.** At the top, insulation boundary condition is applied and fixed temperature value of 300 K is applied on the bottom and the side wall where there are water circulations. For all the walls no slip boundary condition is applied. In the heater zones, the temperature values of the heaters during the experiment are inserted as fixed values in the cell zone condition dialog box.

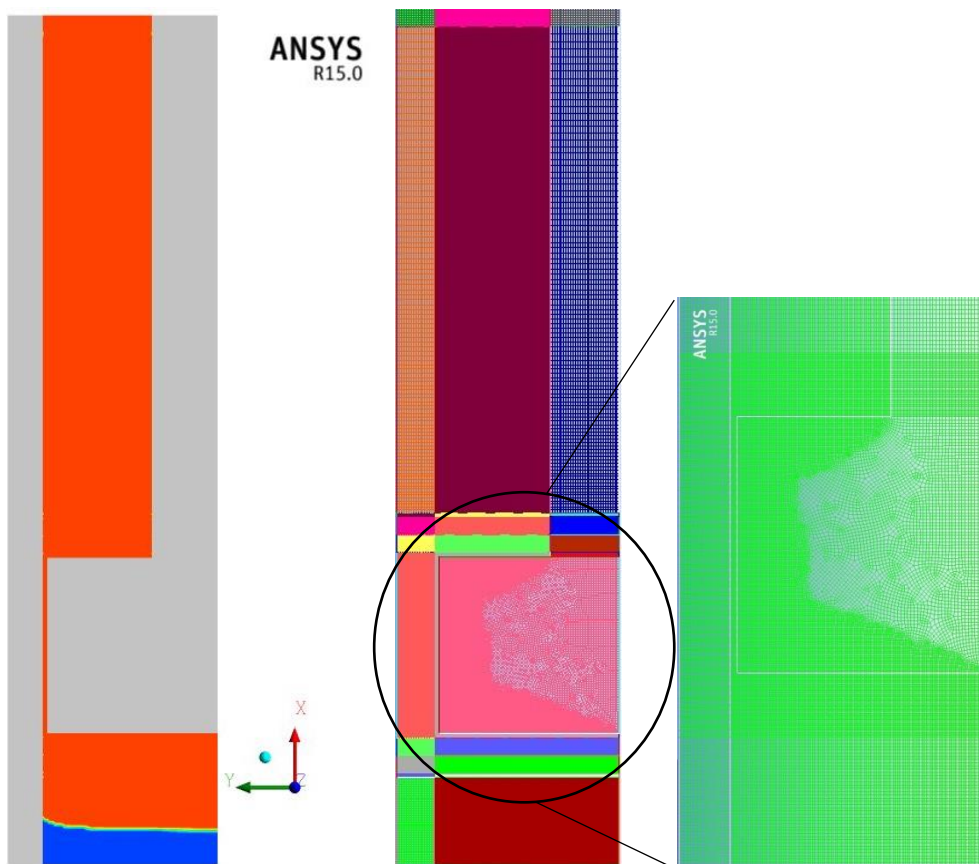


Figure 4.8. Local Geometry and the created mesh.

### 4.2.2. Local Geometry

4.2.2.1. Geometry and Mesh Generation. After obtaining the exact temperature gradient on the crucible wall from results of the global geometry simulations, the simulation geometry can be reduced in a way that only contains the inside of the crucible and its thickness. This local geometry and the generated mesh are shown in Figure 4.8. The minimum cell size is  $0.015625 \text{ mm}^2$  and the maximum cell size is  $0.1375 \text{ mm}^2$ . In the melt region around the baffle, where the reciprocating motion of the baffle is taking place, and below the baffle the cell size is  $0.015625 \text{ mm}^2$ . In the melt region above the baffle and far away from the baffle the cell size is  $0.06875 \text{ mm}^2$ , and in the baffle shaft and the crucible wall the cell size is  $0.1375 \text{ mm}^2$ . Since the local geometry does not contain argon volume, the radiation heat transfer is not considered. The heat transfer mechanisms are conduction and convection in the melt (germanium) and conduction in the crucible wall and the baffle (graphite).

4.2.2.2. Boundary Conditions. The temperature gradient on the outer side of the crucible wall which is obtained from the global geometry simulation is defined as a function of x-position along the crucible. Then, this x-position is updated according to the pulling velocity in the case of solidification. This temperature gradient is imposed on the bottom, side, and top boundaries of the local geometry. Moreover, no slip boundary condition is applied on all the walls.

4.2.2.3. Dynamic Mesh. In the local geometry, instead of pulling down the crucible, the temperature gradient on the crucible wall is pushed upward as mentioned above. In the case of AHP/AVC, the baffle is also moved upward with the pulling velocity. To this end, layering dynamic mesh of ANSYS Fluent is used. The domain, containing the baffle, is moved with the pulling velocity which is defined in the compiled user defined function (UDF). In the case of AVC, the sinusoidal motion is added to the translation motion of the baffle.

## 5. RESULTS

In this section, both experimental and numerical results are presented. In the experimental part, striations (interface shape), iso-concentration lines, radial and axial solute distribution, and dislocation density of each grown crystal are presented. In the numerical part, results for global and local simulations of the experimentally grown crystals are shown. For the global geometry, the problem is solved in steady state to get the temperature distribution profile along the crucible wall as the boundary condition for the local geometry. For the local geometry, while the flow pattern and the temperature field results are shown for the all experimentally grown crystals without considering the solute, the solute redistribution is solved for modeling the solidification of Ge-Sb alloy for VB20-58, AHP10-10, and AHP20-10. Finally, simulations including solute distribution during the solidification are presented.

### 5.1. Experimental Results

Seven crystals with 40 mm diameter have been grown with three different methods, the VB, AHP, and AVC, in order to investigate the homogeneity of the solute, stability of the interface, and the dislocation density in the grown single crystals with regards to the growth parameters such as the pulling velocity and temperature gradient which are common to all the methods, the effective melt height which is relevant to the AHP and AVC methods, and the amplitude and frequency of the vibrating baffle which is relevant to the AVC method. The growth parameters are given in Table 5.1. The samples are named as “mmm-ww-xx-yy-zz”, where mmm stands for the growth method (VB: Vertical Bridgman; AHP: Axial Heat Processing; AVC: Axial Vibrational Control), ww the pulling velocity in mm/h, xx the initial melt height in mm, yy the vibration amplitude in mm, and zz the vibration frequency in Hz.



Table 5.1 Grown crystals and their growth parameters.

Crystal Name	Parameters							
	$V_p$	h	A	f	$G_L$	$G_F$	H	$I \times 10^{-4}$
<b>VB20-58</b>	20	58			19	19	14	
<b>AHP10-10</b>	10	10			25	20	41.5	
<b>AHP20-5</b>	20	5			31	20	35	
<b>AHP20-14</b>	20	14			24	16	30.6	
<b>AVC20-20-0.25-1</b>	20	20	0.25	1.00	19	16	33.4	2.5
<b>AVC20-10-2-0.25</b>	20	10	2	0.25	27	19	39	1.25
<b>AVC20-15-0.25-25</b>	20	15	0.25	25.00	26	19	21.5	1562.5
$V_p$ : pulling velocity (mm/h), h: initial melt height in simulations (mm), A: amplitude of vibration (mm), f: frequency of vibration (Hz), $G_L$ : initial temperature gradient in melt ahead of the interface( $^{\circ}\text{C}/\text{cm}$ ), $G_F$ : furnace temperature gradient ( $^{\circ}\text{C}/\text{cm}$ ), H: single crystal length measured from initial interface to the last portion of the single crystal region at the center of the crystal (mm), I: vibration intensity parameter ( $\text{m}/\text{s}^2$ ).								

### 5.1.1. VB20-58

Sample VB20-58 is the only crystal grown with the VB method. The pulling rate is 20 mm/h and the furnace temperature gradient is 19  $^{\circ}\text{C}/\text{cm}$ . The shortest single crystal length, which is measured from the initial interface, is 14 mm. Figure 5.1a shows the etched half of the crystal in which revealed striations show the interface position during the growth. The contour plot of the Sb concentration data collected from the four-point probe test for this crystal is also shown in Figure 5.1b. The isoconcentration lines are just provided from 5 mm above the base of the seed up to 20 mm above the seed base, since after this height there is a polycrystalline region which makes it impossible to measure the resistivity and the solute concentration. The U-shape fringe pattern observed in the etched half is also observed in the isoconcentration lines. Radial and axial solute redistributions in this crystal are shown in Figures 5.2 and 5.3 respectively. The red dashed line shows where the single crystallinity is ended.

Taking a more careful look at Figure 5.1, it shows that at lower heights (up to 9mm) of the crystal the interface is smooth and planar and there is no severe concavity. In addition, there is relatively small solute segregation up to this height and the solute content in the crystal is not too high (Figure 5.2). However, the smooth and planar interface is broken down into cellular pattern at the higher levels (around 14mm) in the region between center and the side of the crystal and these cellular patterns from right and left side of the crystal grow toward the center of the crystal. On the other hand, the smoothness of the interface and singularity of the crystal are preserved almost to the end of the crystal at the sides where the solute has lower content compared to the central region.

The axial solute redistribution is also plotted in Figure 5.3. While the redistribution pattern is closer to the analytical diffusional mixing pattern in VB (VB-DM) at the center, the solute redistribution pattern at the sides is something between the two analytical formulations, complete mixing (Scheil) and VB-DM.

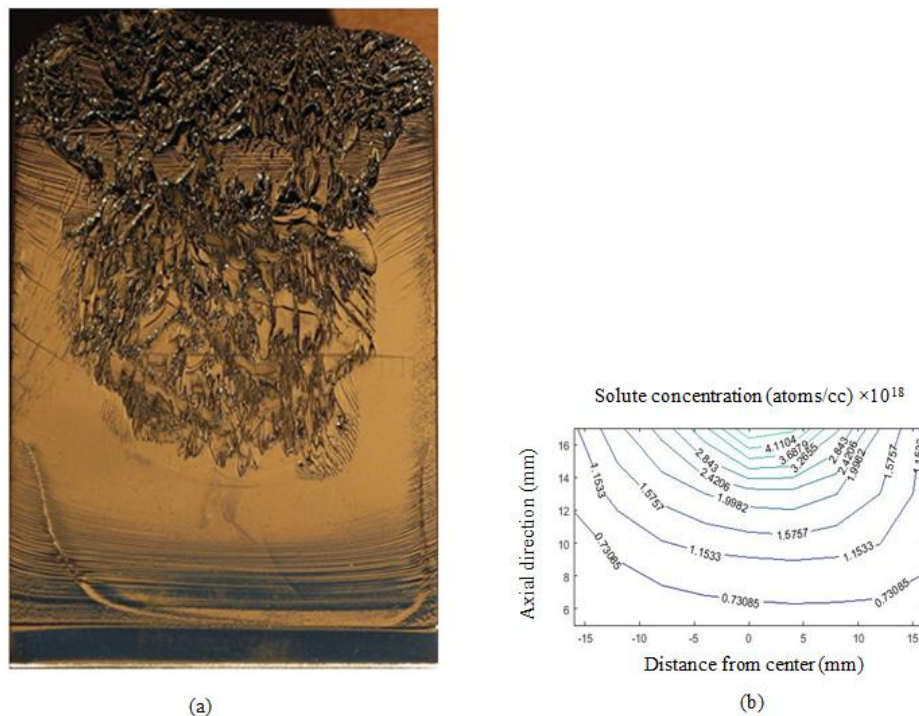


Figure 5.1. Striations (a) and isoconcentrations (b) of VB20-58.



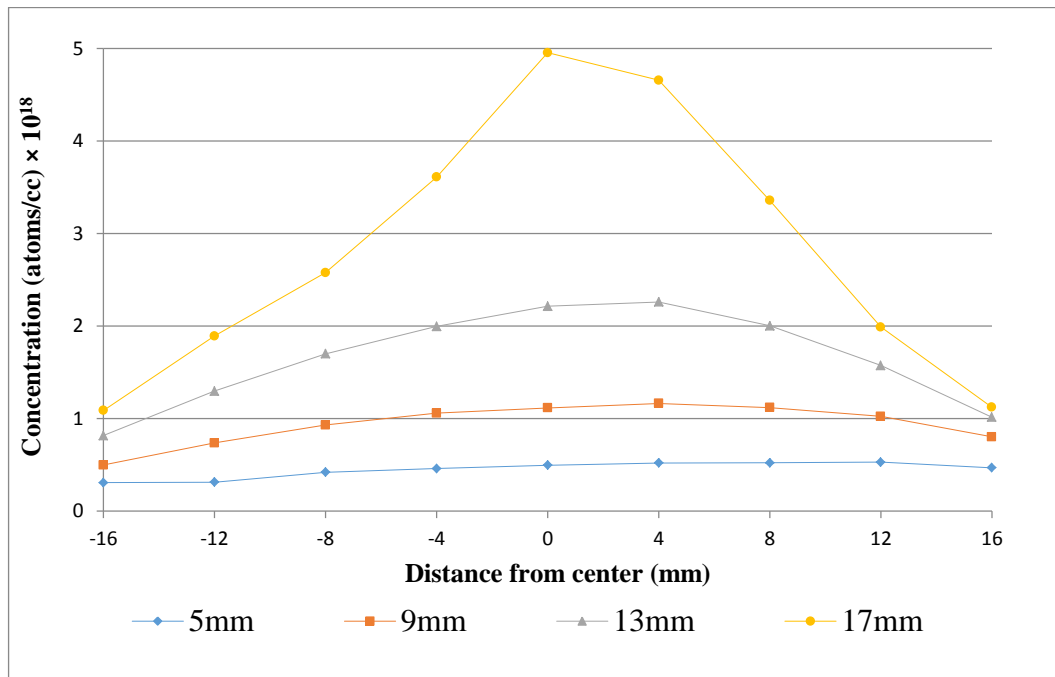


Figure 5.2. Radial solute redistribution of VB20-58.

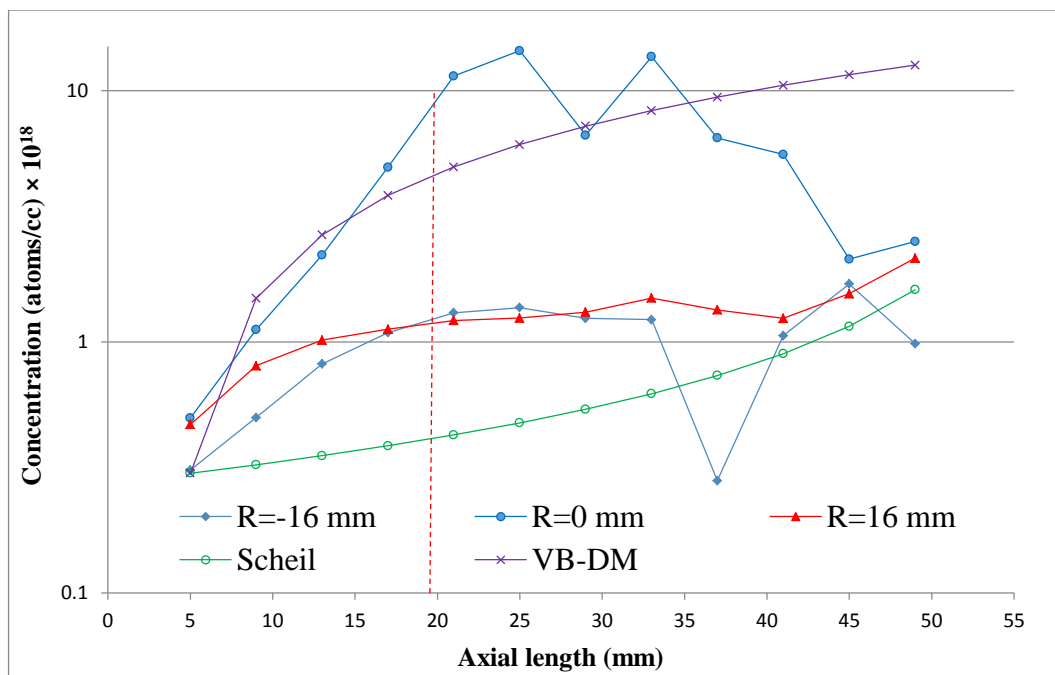


Figure 5.3. Axial solute redistribution of VB20-58. The red dashed line shows where the single crystallinity is ended.

### 5.1.2. AHP10-10

Sample AHP10-10 is grown with 10 mm/h pulling rate. The furnace gradient is 20 °C/cm and the baffle is set to achieve initial 10 mm melt height. The total single crystal length achieved with this method is 41.5 mm which is the highest length achieved since the pulling rate is the lowest among other grown crystals. The striations and isoconcentration lines are shown in Figures 5.4a and 5.4b respectively. The distance from bottom of the baffle to the bottom of the crystal ( $d_0$ ), The crystal height ( $H$ ), melt height ( $h$ ), temperature gradient in liquid ( $G_L$ ), and temperature gradient in solid ( $G_s$ ) during the growth are plotted in Figure 5.5. Radial and axial solute distributions in this crystal are shown in Figures 5.6 and 5.7 respectively.

The initial interface is not symmetric and the right side of the crystal is melted more. However, at the higher portion of the crystal the interface becomes symmetric. The interface shape is slightly concave and the morphology of the interface is not broken down almost in the entire crystal. The cellular patterns are appeared only at the end of the crystal. Moreover, as it is shown in Figure 5.6, the redistribution of the solute is relatively homogeneous and even at high levels of the crystal (45 mm), the solute content is relatively lower compared to the values in VB20-58 sample. Axial solute redistribution that is plotted in Figure 5.7 shows that the solute content values at the sides and the center are close to each other and the redistribution pattern is far from the analytical model for diffusional mixing in the AHP or AVC (AHP-DM), but it is closer to the complete mixing pattern (AHP-CM). Note that although the redistribution regime in both the AHP-CM and the Scheil is complete mixing, the solute concentration is higher in AHP-CM than in Scheil redistribution. The reason is the lower melt height above the interface in the AHP and AVC methods. According to Equations 2.12 and 2.16, since the area beneath the AHP-CM redistribution is smaller than that in the Scheil, the solute content at the interface should rise more rapidly (higher  $dC_L$  in Figure 2.13) in AHP-CM.

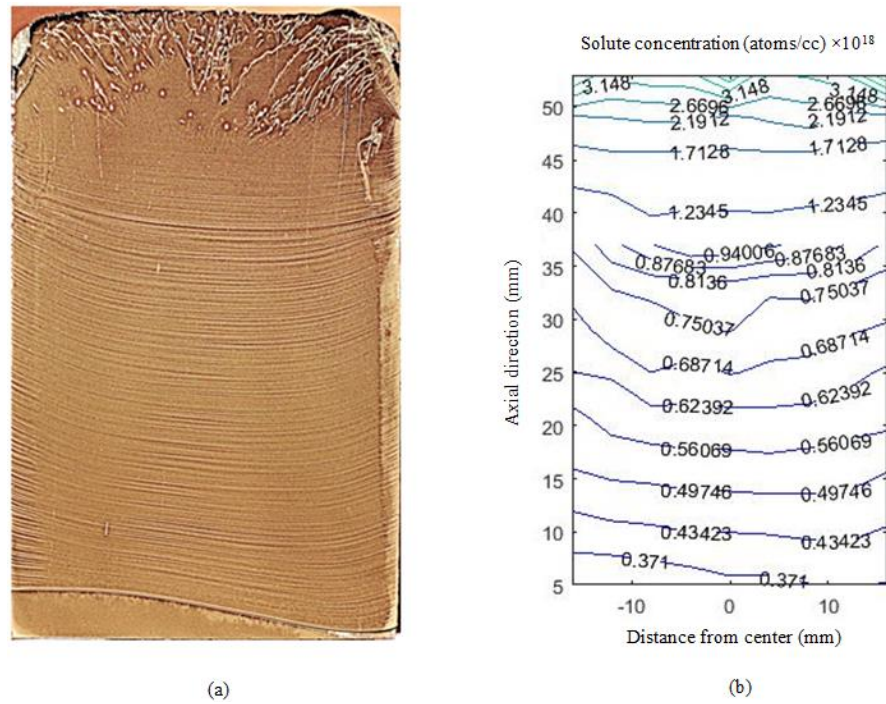


Figure 5.4. Striations (a) and isoconcentrations (b) of AHP10-10.

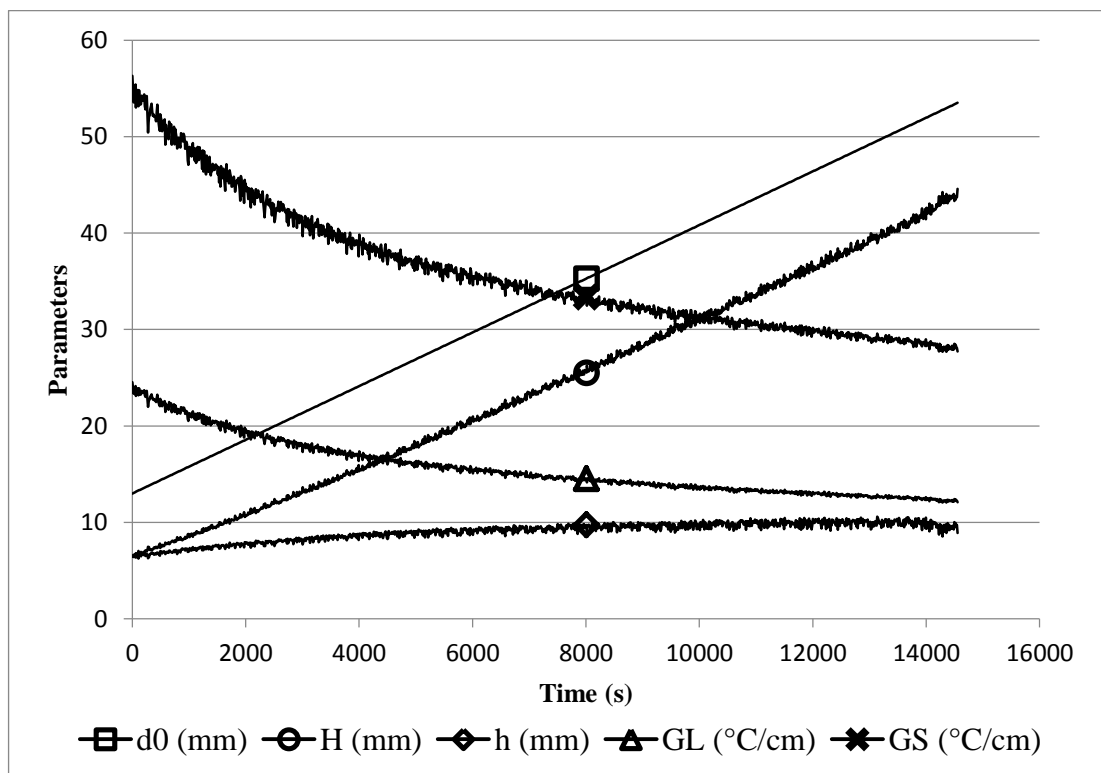


Figure 5.5. Solidification parameters during the growth for AHP10-10.

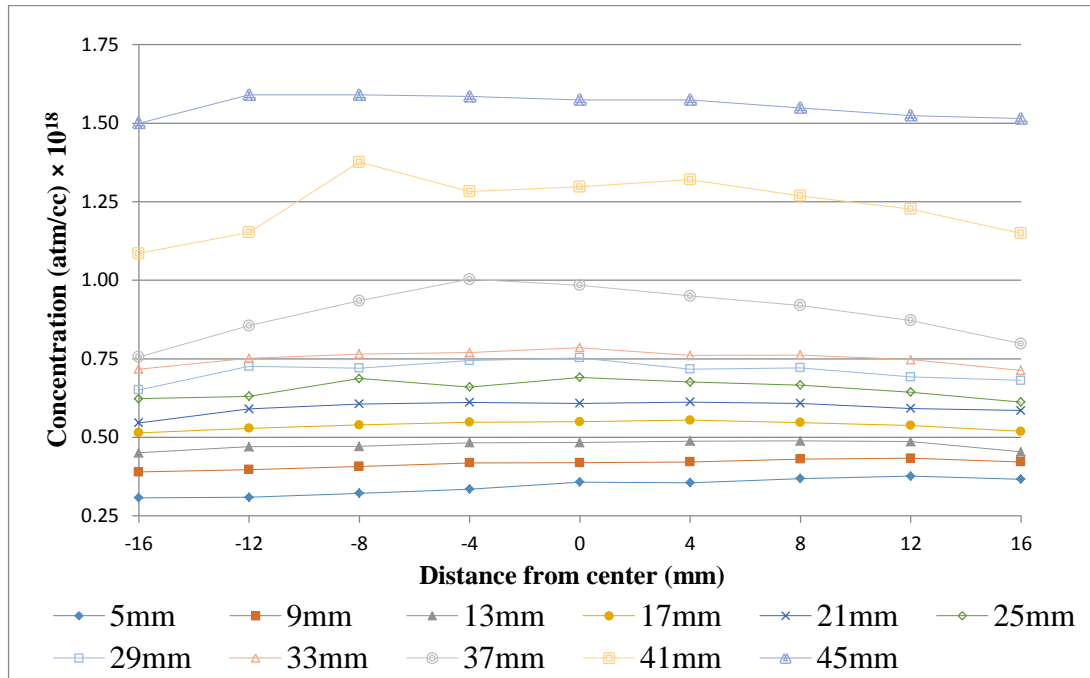


Figure 5.6. Radial solute redistribution of AHP10-10.

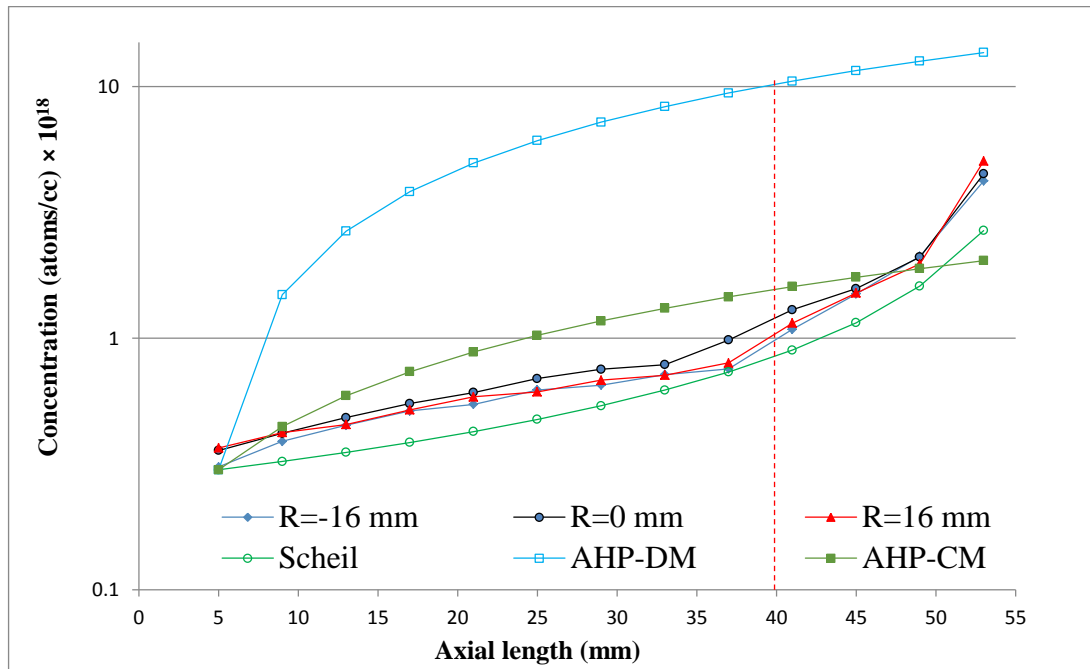


Figure 5.7. Axial solute redistribution of AHP10-10. The red dashed line shows where the single crystallinity is ended.

### 5.1.3. AHP20-14

Another crystal grown with the AHP method is AHP20-14 in which the pulling velocity is 20 mm/hr and the initial melt height is set to 14 mm. The temperature gradient of the furnace is 16 °C/cm and the total single crystal length achieved with this method is 30.6 mm. The striations and isoconcentration lines are shown in Figures 5.8a and 5.8b respectively. Figure 5.9 shows the distance from bottom of the baffle to the bottom of the crystal ( $d_0$ ), the crystal height ( $H$ ), melt height ( $h$ ), and temperature gradient in liquid and solid ( $G_L$  and  $G_S$ ). Radial and axial solute distributions in this crystal are shown in Figures 5.10 and 5.11 respectively.

Compared to AHP10-10, the interface is more concave and the cellular patterns are formed earlier. There are lineages at the left side of the crystal (Figure 5.8) which affect the solute redistribution at this region (Figure 5.10). This is also visible in the axial solute redistribution in Figure 5.11. Discrepancies observed in the radial and axial solute redistributions are due to the lineage formation in these regions. The axial solute redistributions at the sides and at the center are not close to each other as it was the case in AHP10-10. However, the values are still far from the analytical diffusional mixing model.

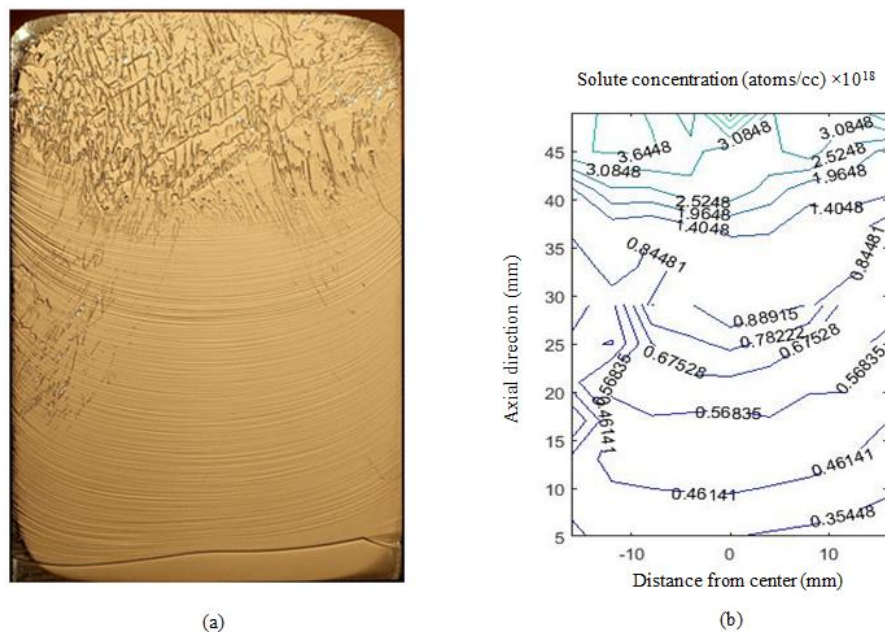


Figure 5.8. Striations (a) and isoconcentrations (b) of AHP20-14.

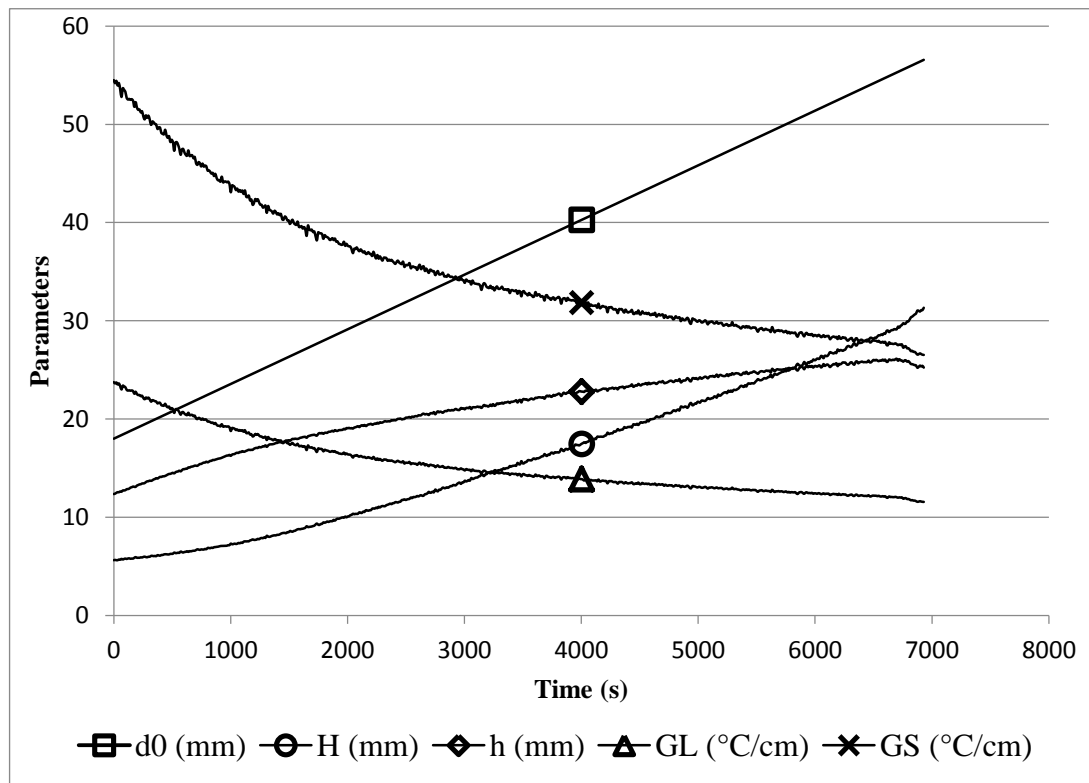


Figure 5.9. Solidification parameters during the growth for AHP20-14.

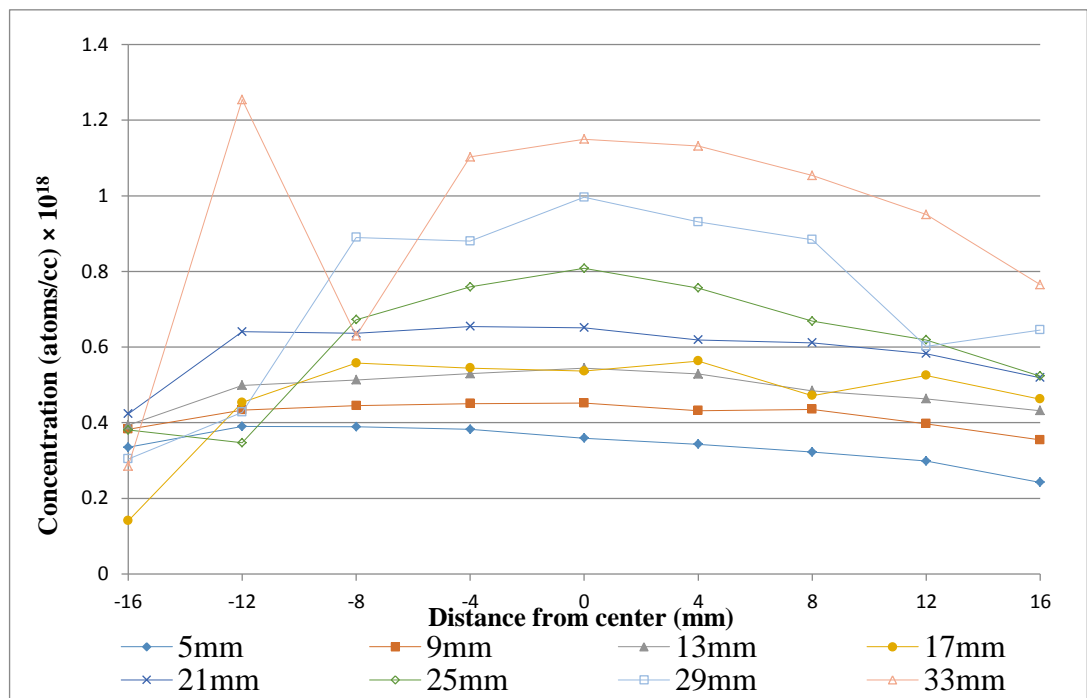


Figure 5.10. Radial solute redistribution of AHP20-14.

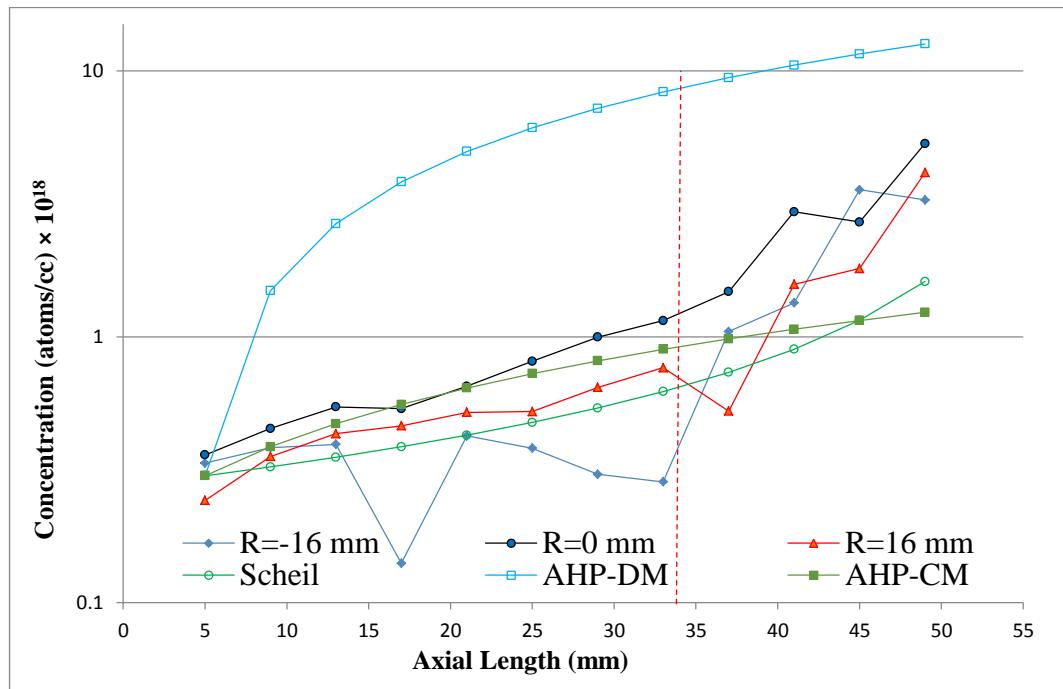


Figure 5.11. Axial solute redistribution of AHP20-14. The red dashed line shows where the single crystallinity is ended.

#### 5.1.4. AHP20-5

In the AHP20-5 sample, the initial melt height is reduced to 5mm while the pulling velocity is kept the same (20 mm/hr) and the temperature gradient of the furnace is 20 °C/cm. The achieved total single crystal length is 35 mm which is higher than that of the previous sample with higher initial melt height. Figures 5.12a and 5.12b show the striations and isoconcentration lines of this crystal.

Figure 5.13 shows the distance from bottom of the baffle to the bottom of the crystal ( $d_0$ ), the crystal height ( $H$ ), melt height ( $h$ ), and temperature gradient in liquid and solid ( $G_L$  and  $G_S$ ). Radial and axial solute distributions in this crystal are shown in Figures 5.14 and 5.15 respectively.

The interface shape is smooth and relatively less concave than that in AHP20-14. There is no lineage pattern observed in the crystal and the cellular pattern starts almost at the same height of the crystal through the radial direction.

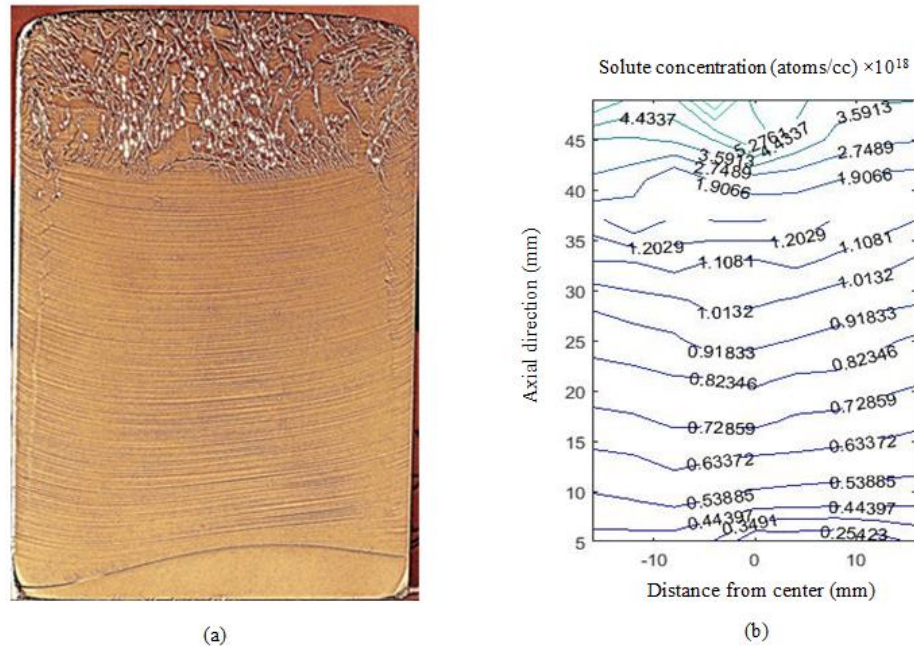


Figure 5.12. Striations (a) and isoconcentrations (b) of AHP20-5.

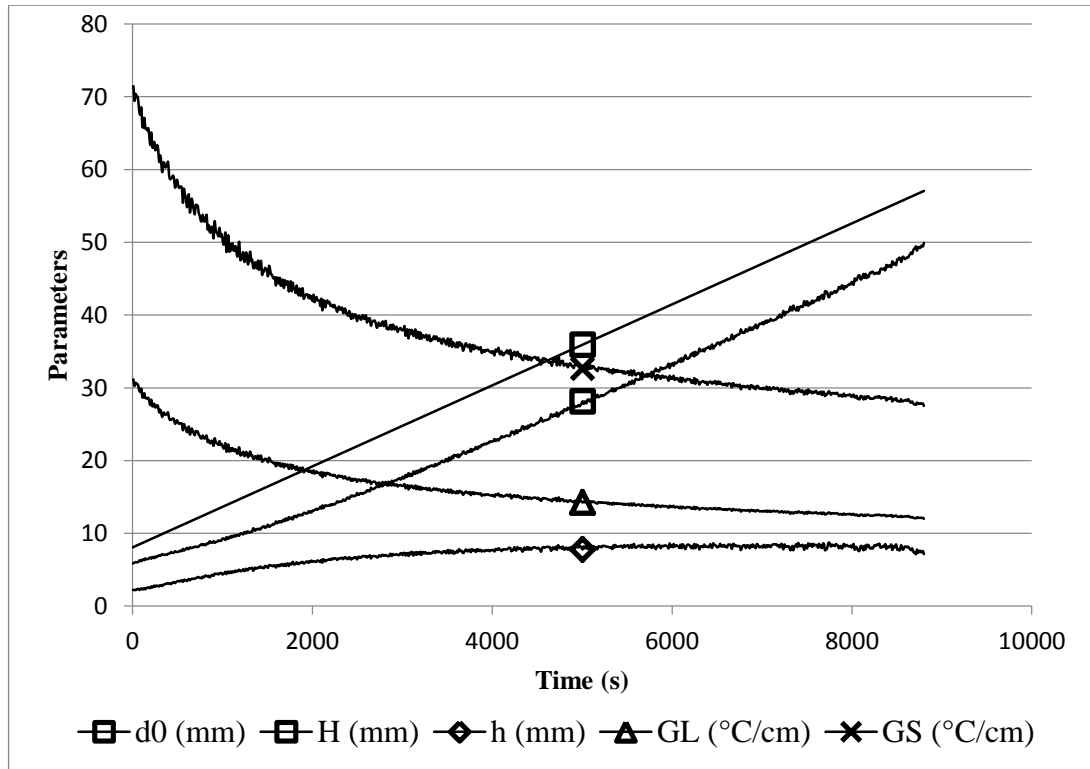


Figure 5.13. Solidification parameters during the growth for AHP20-5.



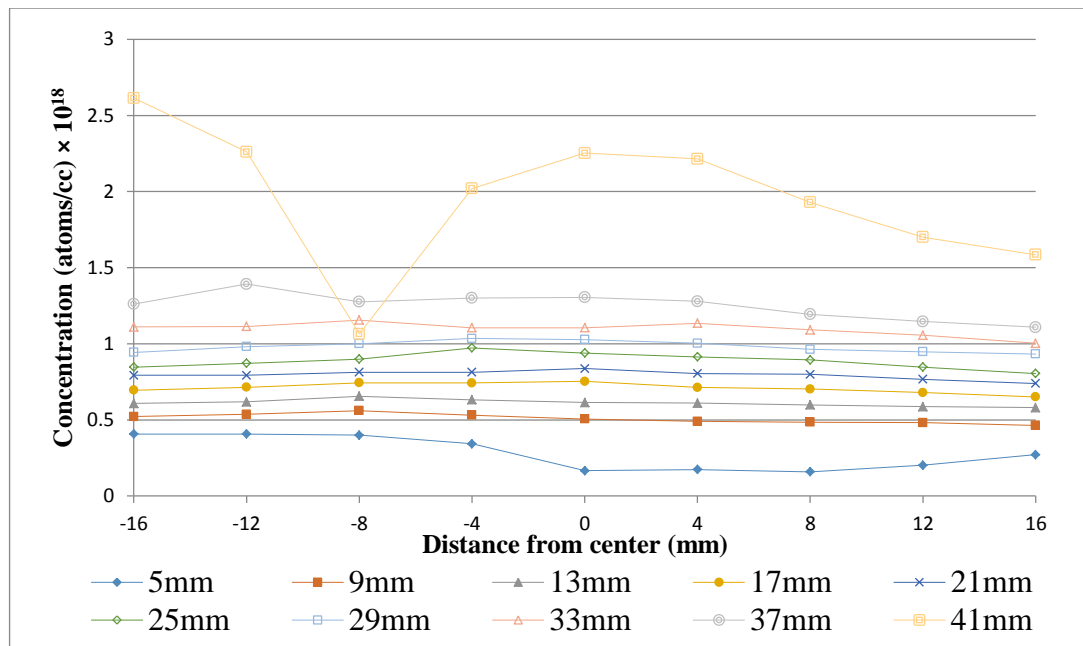


Figure 5.14 Radial solute redistribution of AHP20-5.

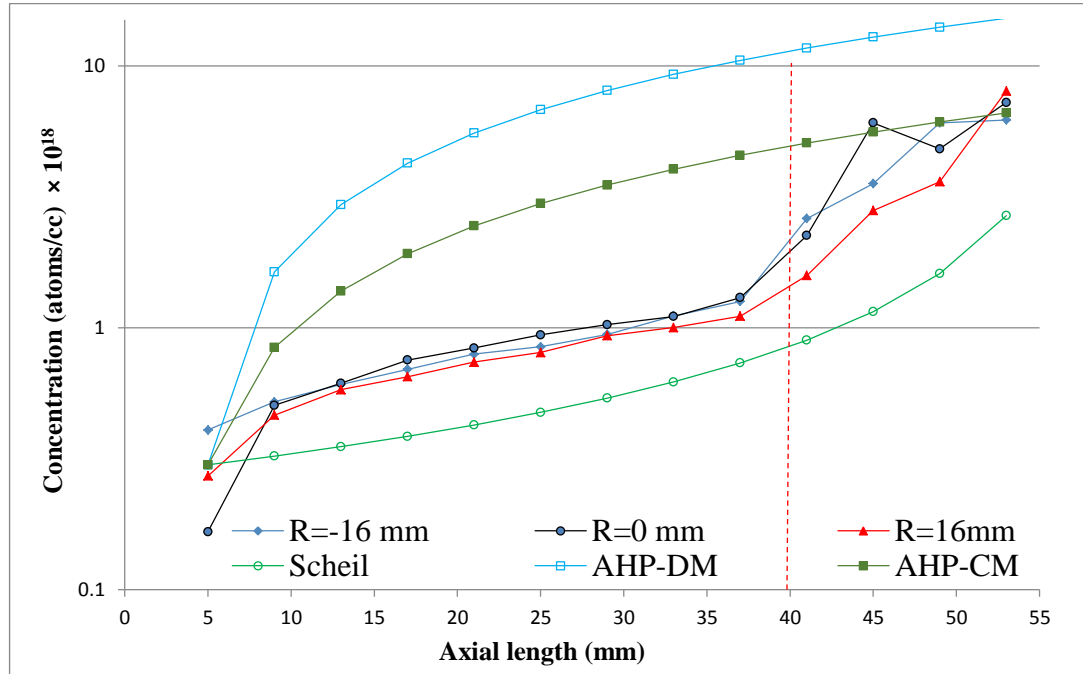


Figure 5.15. Axial solute redistribution of AHP20-5. The red dashed line shows where the single crystallinity is ended.

Also, Figure 5.14 shows that the solute is redistributed homogeneously in radial direction. This is also shown in Figure 5.15 of axial solute redistribution that the values at the sides and the center are close to each other.

#### **5.1.5. AVC20-15-0.25-25**

In the crystals grown with the AVC method, the effects of axial vibration of the baffle are investigated. The first AVC grown crystal is AVC20-15-0.5-25 in which the melt is mixed by high vibration of the melt (25 Hz). In order to avoid entire melting of the seed due to intense forced flow through the baffle gap arising from high frequency vibration of the baffle, the initial melt height is set to 15 mm. The temperature gradient of the furnace is 19 °C/cm and the total single crystal length achieved with this method is 21.5 mm. The striations and isoconcentration lines are shown in Figures 5.16a and 5.16b respectively. Initially, the interface is asymmetric and the concavity is high. But, at the last portion of the single crystal region, the interface becomes symmetric and the curvature is decreased. The isoconcentration lines follow the same pattern of the striation lines. The breaking down of the interface starts at the sides where the concavity is higher. Lineage patterns are also observed at the left side of the crystal.

Figure 5.17 shows the distance from bottom of the baffle to the bottom of the crystal ( $d_0$ ), the crystal height ( $H$ ), melt height ( $h$ ), and temperature gradient in liquid and solid ( $G_L$  and  $G_S$ ). Radial and axial solute distributions in this crystal are shown in Figures 5.18 and 5.19 respectively. The solute content is higher at the left side where there is more severe concavity. The axial solute redistributions at the sides and the center are far from each other and after passing the single crystallinity height, the solute redistribution at the center becomes closer to the analytical diffusional mixing regime.

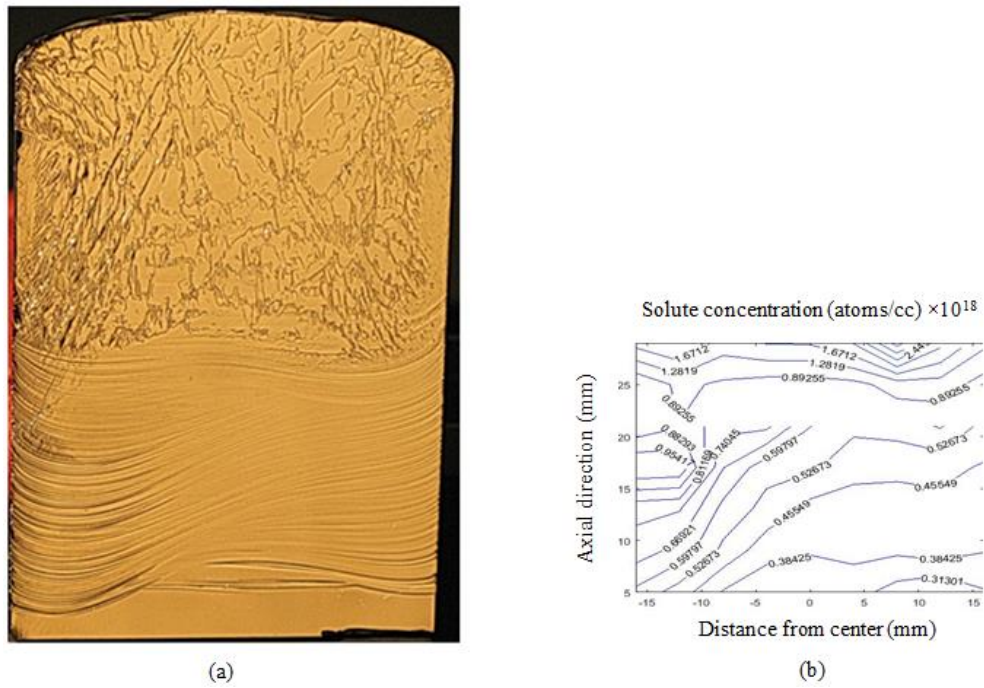


Figure 5.16. Striations (a) and isoconcentrations (b) of AVC20-15-0.25-25.

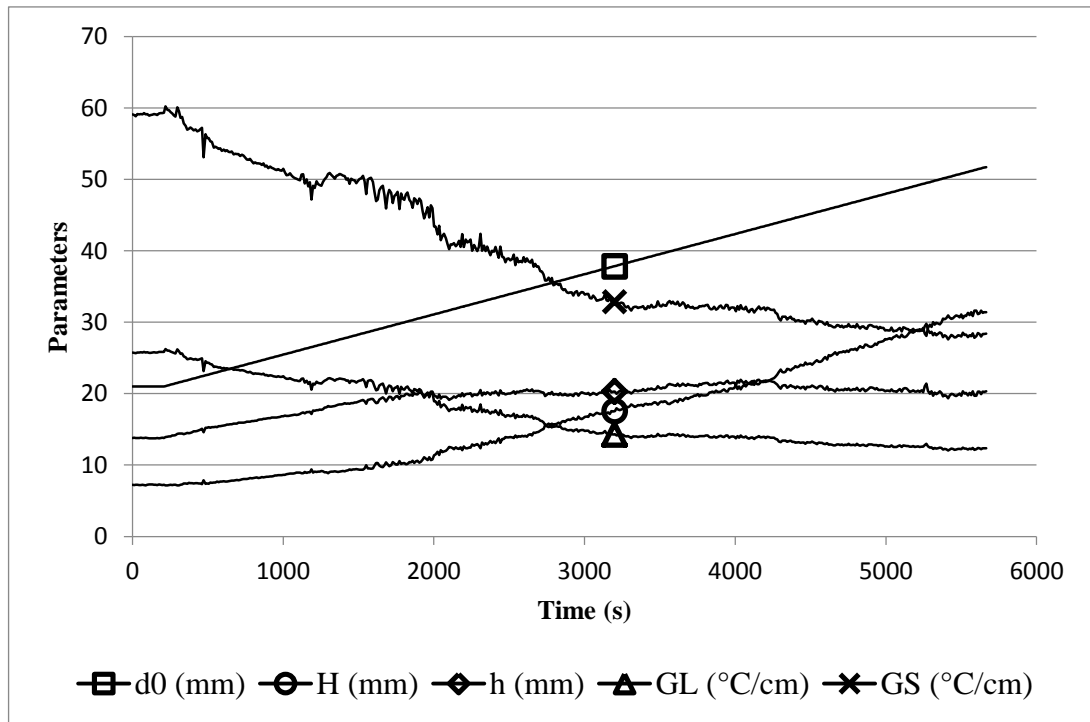


Figure 5.17. Solidification parameters during the growth for AVC20-15-0.25-25.

### 5.1.6. AVC20-20-0.25-1

In the second AVC grown crystal, the frequency of the vibration is decreased to 1 Hz and the initial melt height is increased to 20 mm. The temperature gradient of the furnace is  $16\text{ }^{\circ}\text{C/cm}$  and the total single crystal length is 33.4 mm. Striations and isoconcentration lines are shown in Figures 5.20 a and 5.20 b. The interface is symmetric and concave and the shape of the interface remains the same up to the end of single crystalline region. Figure 5.21 shows the distance from bottom of the baffle to the bottom of the crystal ( $d_0$ ), the crystal height ( $H$ ), melt height ( $h$ ), and temperature gradient in liquid and solid ( $G_L$  and  $G_S$ ). Radial and axial solute distributions in this crystal are shown in Figures 5.22 and 5.23 respectively.

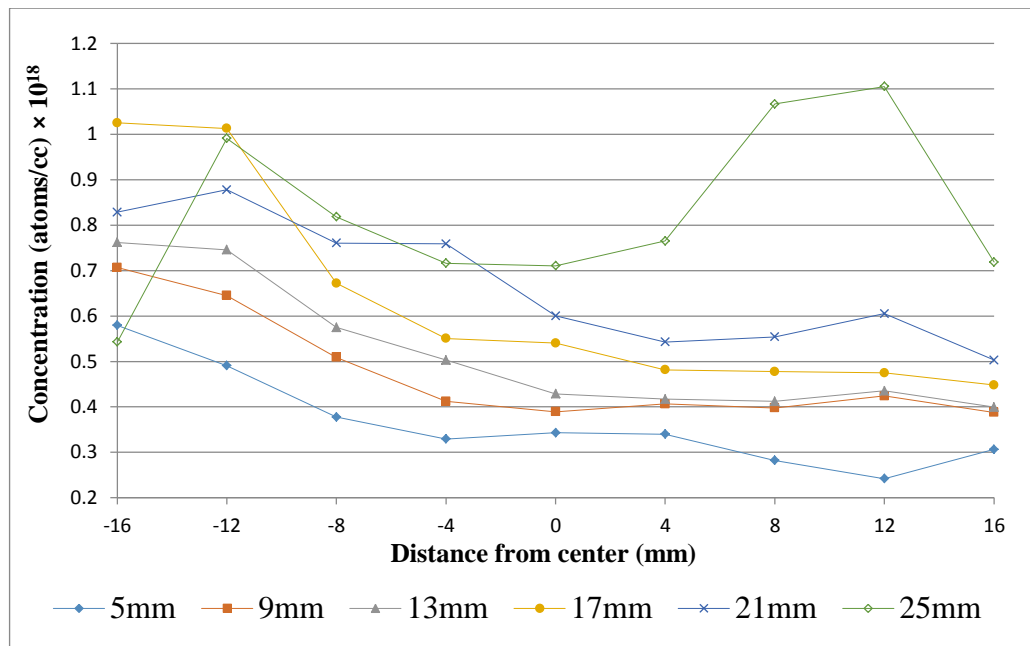


Figure 5.18. Radial solute redistribution of AVC20-15-0.25-25.

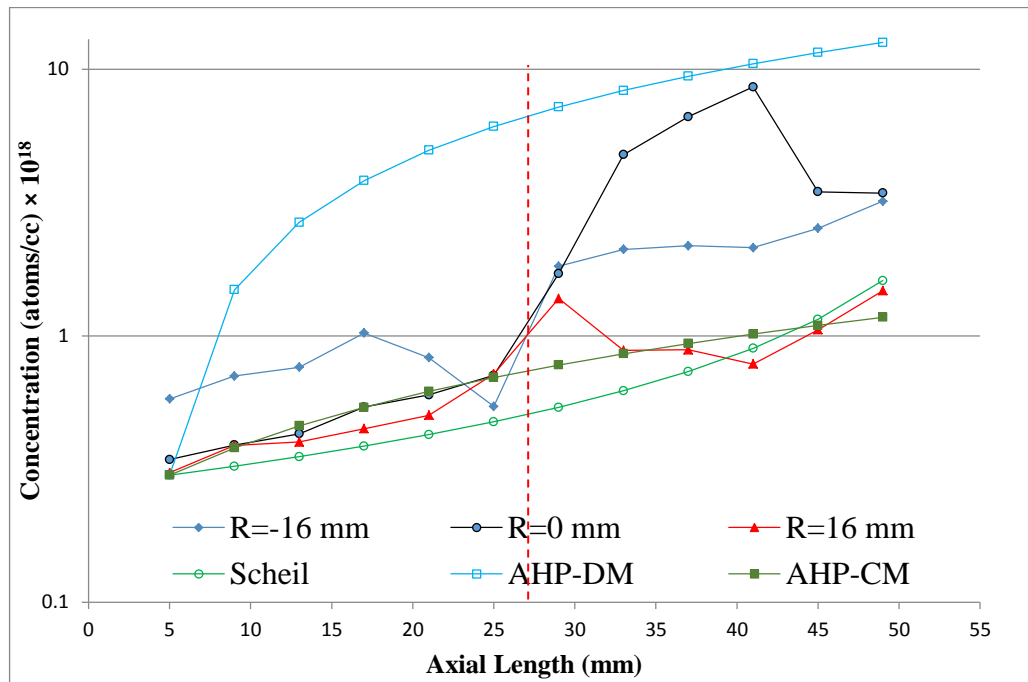


Figure 5.19. Axial solute redistribution of AVC20-15-0.25-25. The red dashed line shows where the single crystallinity is ended.

Like in AHP20-14, lineages are observed at the right side of the crystal (Figure 5.20) and affect the solute redistribution in this region (Figure 5.22). This is also reflected in the axial solute redistribution at the right side in Figure 5.23. Although the redistribution pattern is closer to the complete mixing at the sides rather than at the center, it is still far from the diffusional mixing pattern at the center.

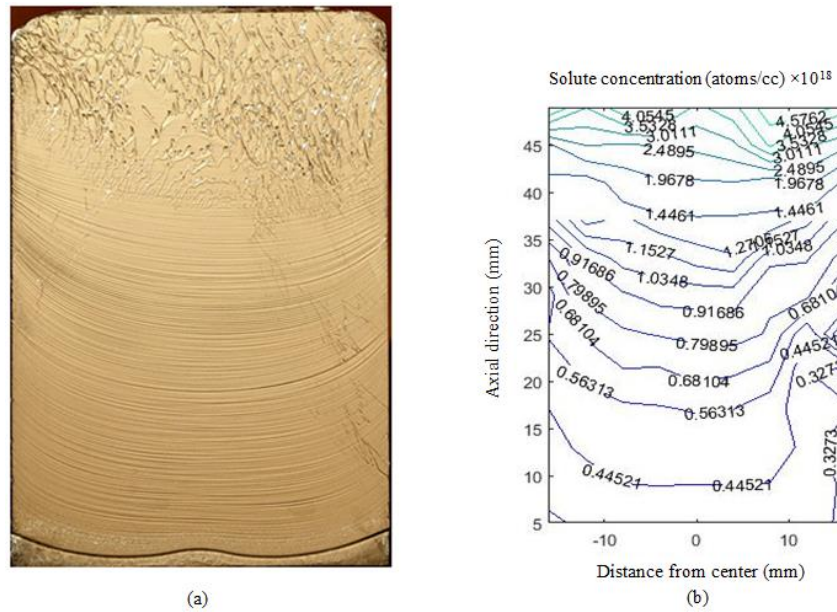


Figure 5.20. Striations (a) and isoconcentrations (b) of AVC20-20-0.25-1.

#### 5.1.7. AVC20-10-2-0.25

In the third AVC grown crystal, the melt is gently mixed with very low frequency (0.25 Hz) and relatively high amplitude (2mm). The temperature gradient of the furnace is  $19^{\circ}\text{C}/\text{cm}$  and the initial melt height is set to 10 mm. The total single crystal length is 39 mm which is the highest length achieved among other crystals grown with the same pulling rate (20 mm/hr).

The striations and isoconcentration lines are shown in Figures 5.24 (a) and 5.24 (b). The initial shape of the interface is maintained to the end of the single crystalline region. The polycrystalline region starts at the sides where the curvature of the interface is higher. At the center, the interface is almost flat and planar.

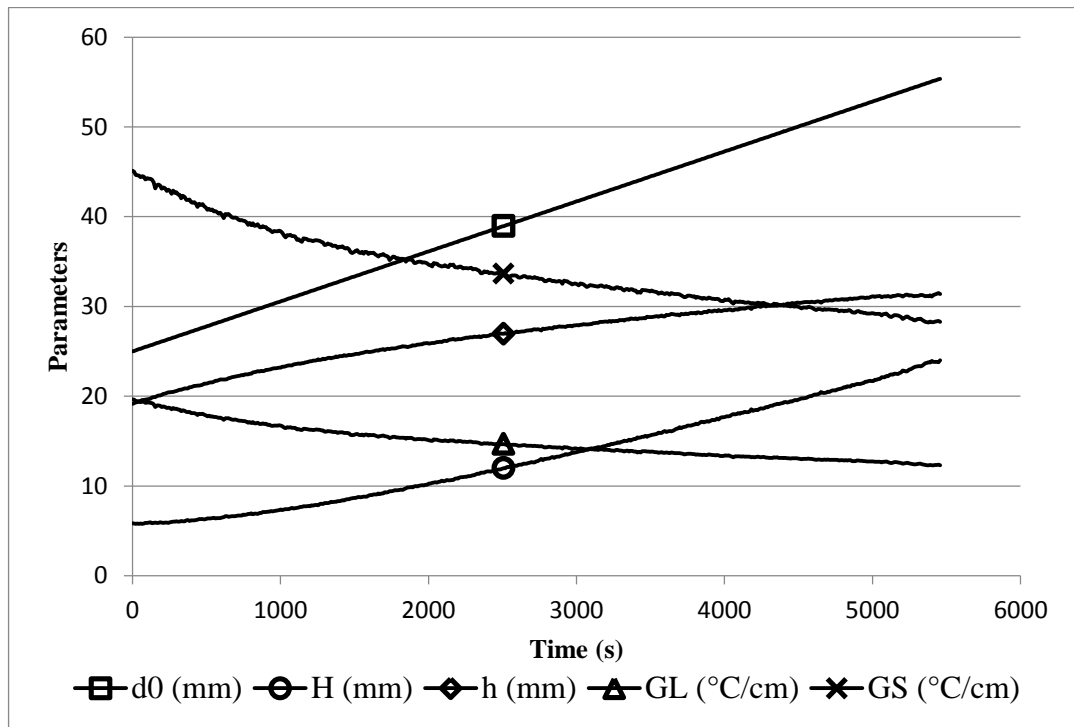


Figure 5.21. Solidification parameters during the growth for AVC20-20-0.25-1.

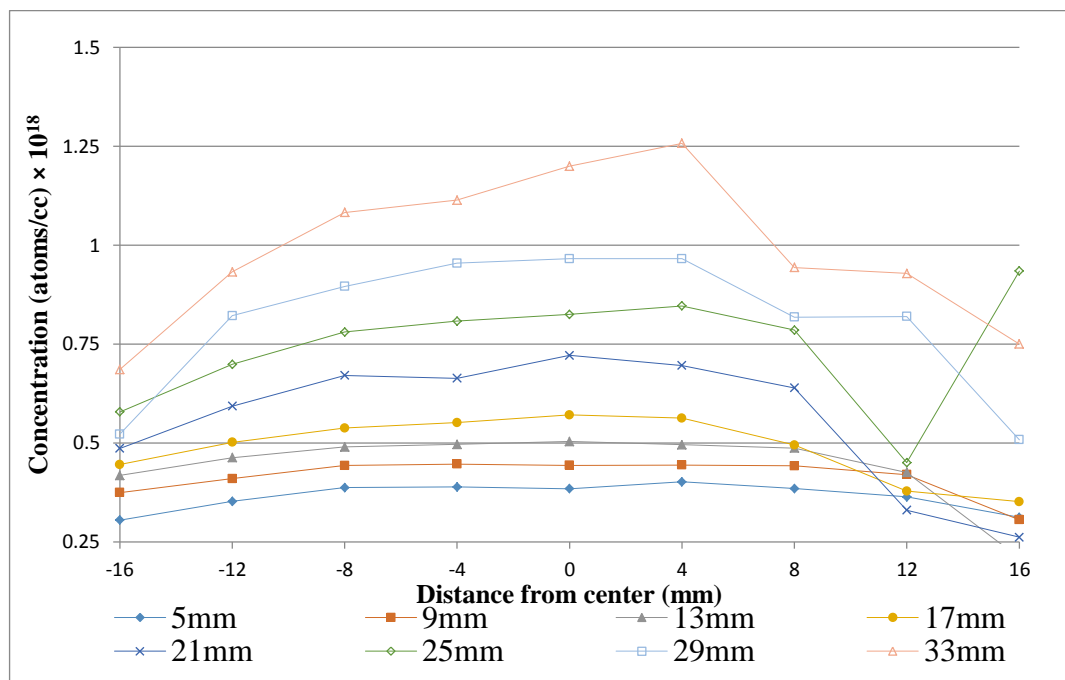


Figure 5.22. Radial solute redistribution of AVC20-20-0.25-1.

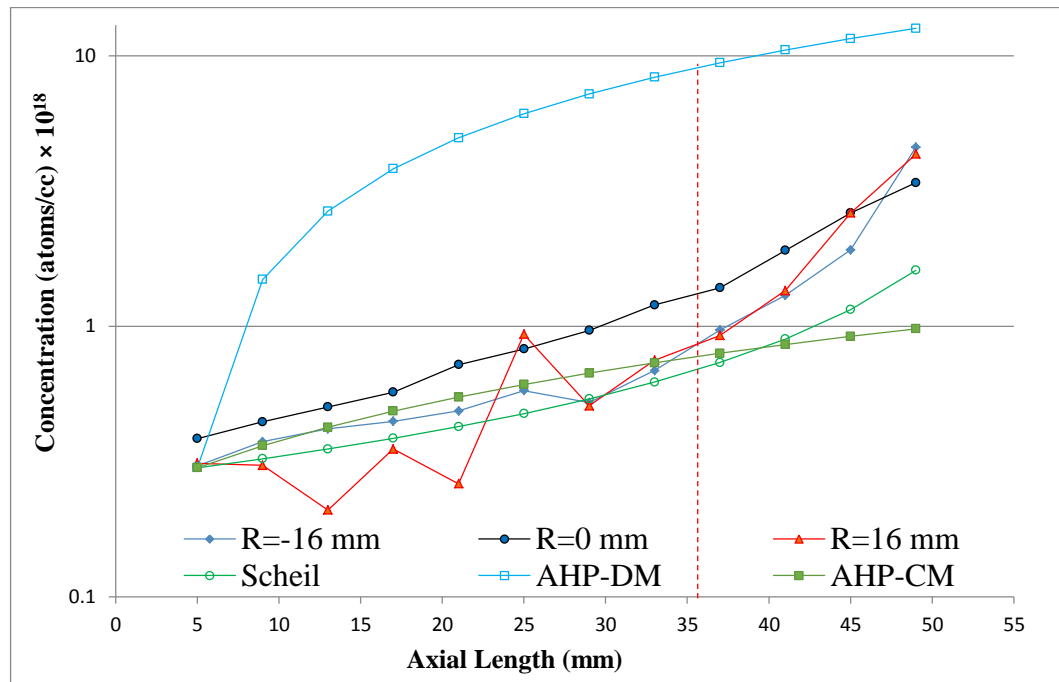


Figure 5.23. Axial solute redistribution of AVC20-20-0.25-1. The red dashed line shows where the single crystallinity is ended.

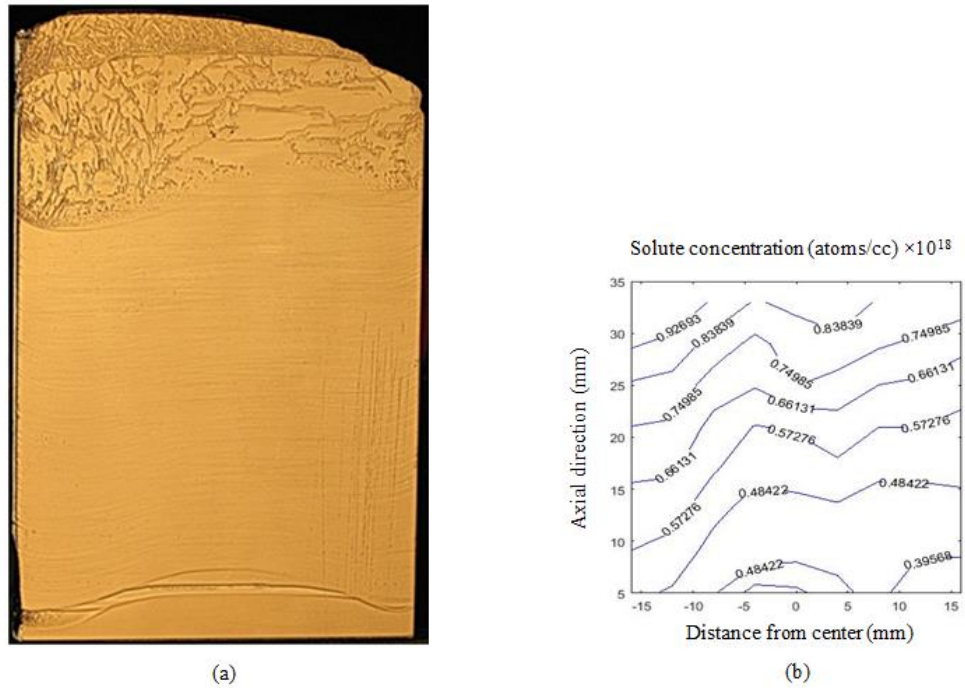


Figure 5.24. Striations (a) and isoconcentrations (b) of AVC20-10-2-0.25.



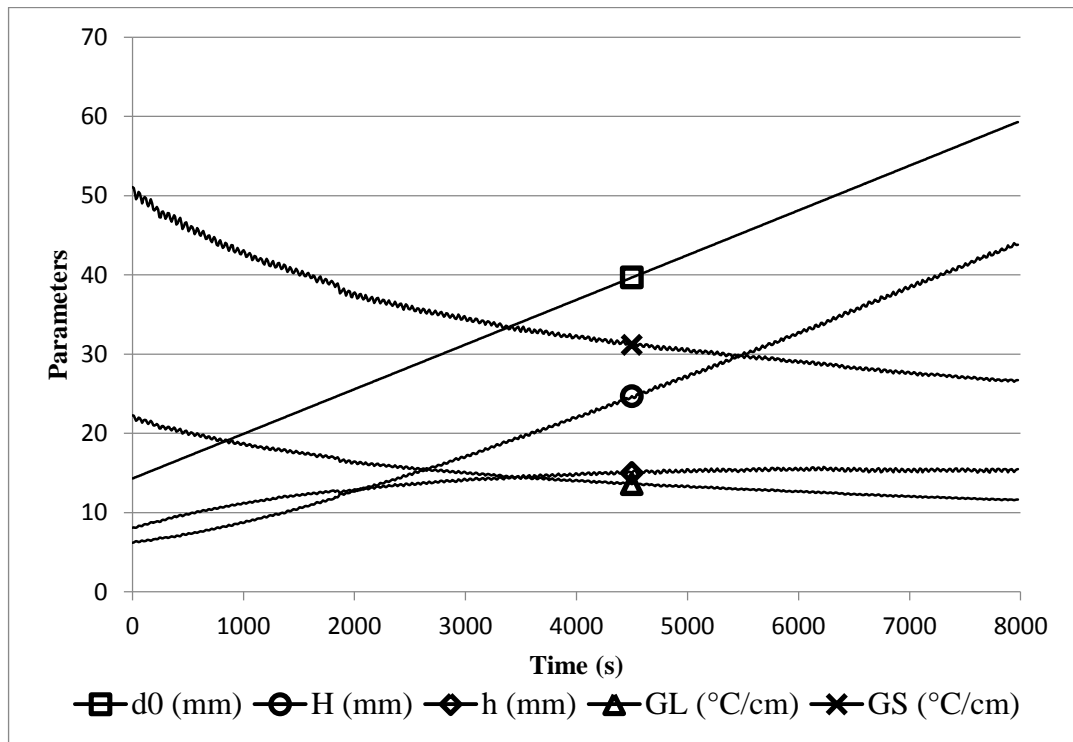


Figure 5.25. Solidification parameters during the growth for AVC20-10-2-0.25.

Figure 5.25 shows the distance from bottom of the baffle to the bottom of the crystal ( $d_0$ ), the crystal height ( $H$ ), melt height ( $h$ ), and temperature gradient in liquid and solid ( $G_L$  and  $G_S$ ). Radial and axial solute distributions in this crystal are shown in Figures 5.26 and 5.27 respectively. It is shown that the solute redistribution in radial direction is relatively homogeneous up to 37 mm height of the crystal. Then, there is a sudden increase in the solute content at the 41 mm height of the crystal at the left side where the interface is more concave and the cellular patterns begin to appear. Axial solute redistribution shows that both at the sides and the center the redistribution pattern is too far from the diffusional mixing regime and the solute content at the left side is higher than that at the center and the right side.

### 5.1.8. Dislocations

The microscope images of the chemically etched surface of each crystal in different radial and axial positions are shown in Appendix B. In the VB20-58 crystal, after the third layer ( $H=25$  mm), the formation of grains can be observed. The dislocations are coarser in the AHP grown crystals and finer in VB and AVC grown crystals. It is shown that generally, the dislocations are larger, more distinguishable, and with lower density at the lower levels of the crystal. At the higher levels of the crystal by approaching to the polycrystalline region, dislocations become finer and the density of the dislocation is increased. However, even at higher levels of the crystal ( $h=37$  mm), the dislocation density is remained relatively low in AHP10-10 and AHP20-5.

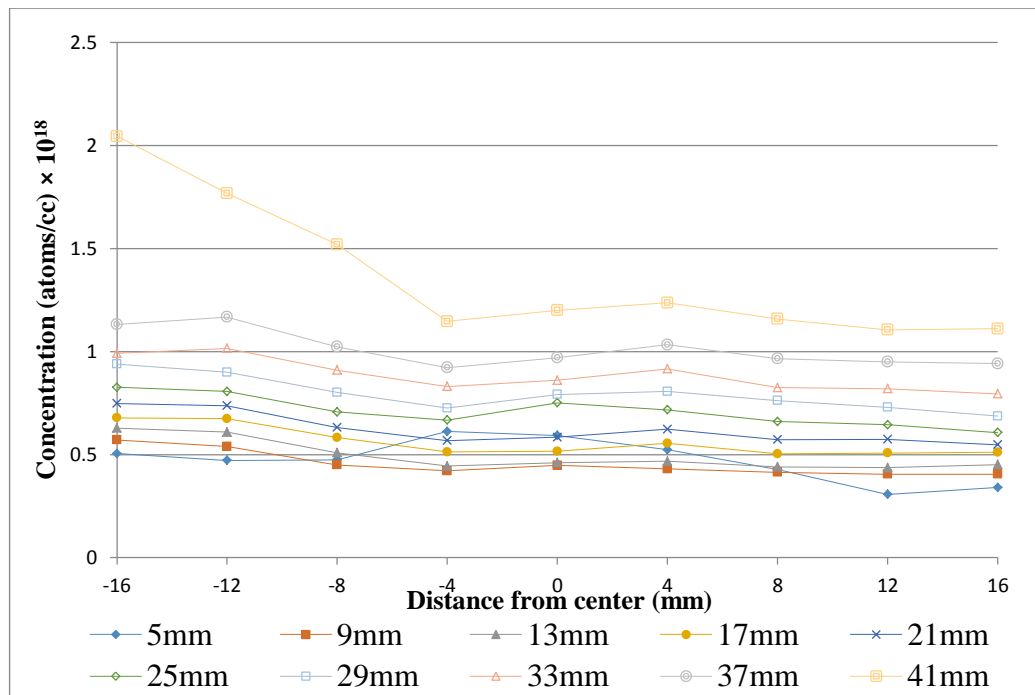


Figure 5.26. Radial solute redistribution of AVC20-10-2-0.25.

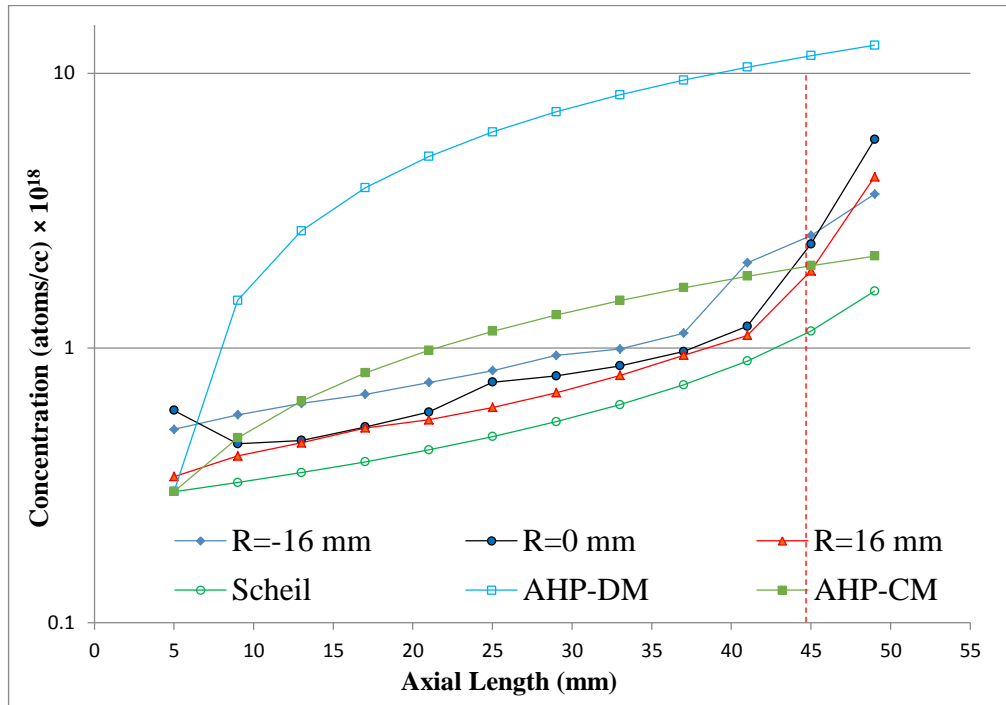


Figure 5.27. Axial solute redistribution of AVC20-10-2-0.25. The red dashed line shows where the single crystallinity is ended.

The radial distribution of the dislocation density is obtained by averaging the values on each arc (see Figure 4.5) and plotted for each crystal along the axial length from Figure 5.28 to Figure 5.33. It is observed that the dislocation density is higher close to the periphery and it is increasing along the axial direction except for the VB20-58 and AVC20-10-2-0.25 crystals for which the dislocation density is higher at the center. This also can be detected from the etched surface of the semicircular crystal cuts in Figure 5.28 and Figure 5.32. Although the sides are in single crystal region, the dislocation density in the VB20-58 is too high after  $h=15$  mm that it is not possible to calculate and show them in Figure 5.28.

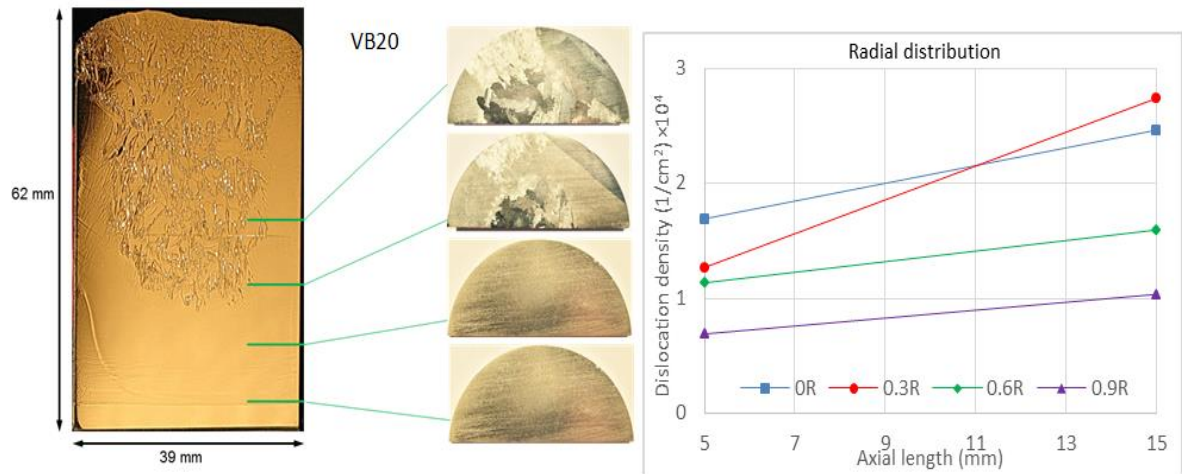


Figure 5.28. Radial distribution of dislocation densities of VB20-58 in 5 mm, 15 mm, 25 mm, and 35 mm axial heights.

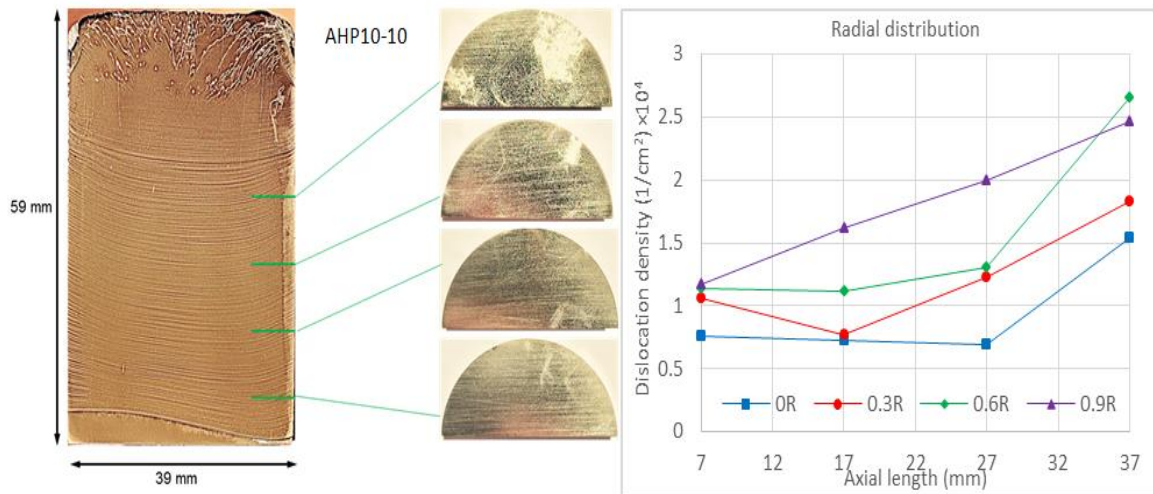


Figure 5.29. Radial distribution of dislocation densities of AHP10-10 in 7 mm, 17 mm, 27 mm, and 37 mm axial heights.

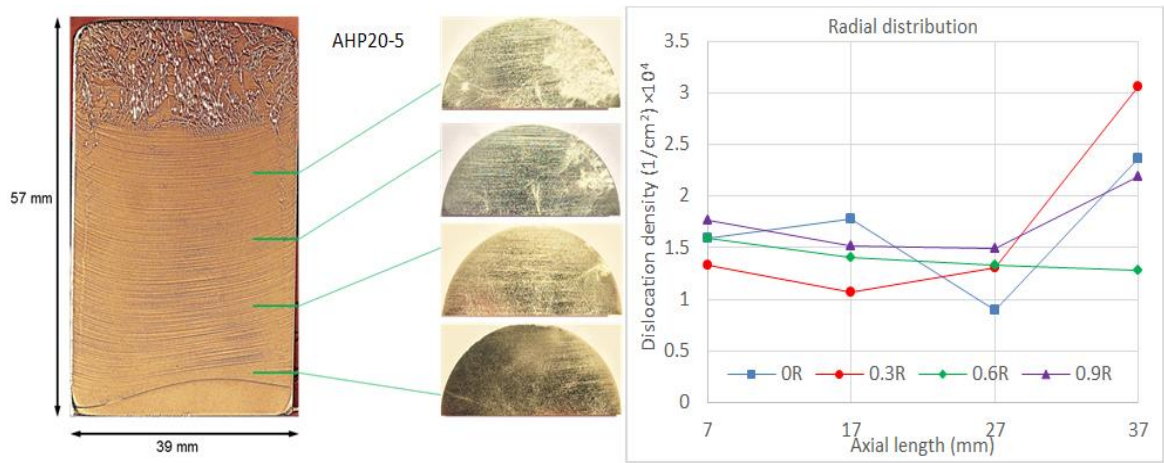


Figure 5.30. Radial distribution of dislocation densities of AHP20-5 in 7 mm, 17 mm, 27 mm, and 37 mm axial heights.

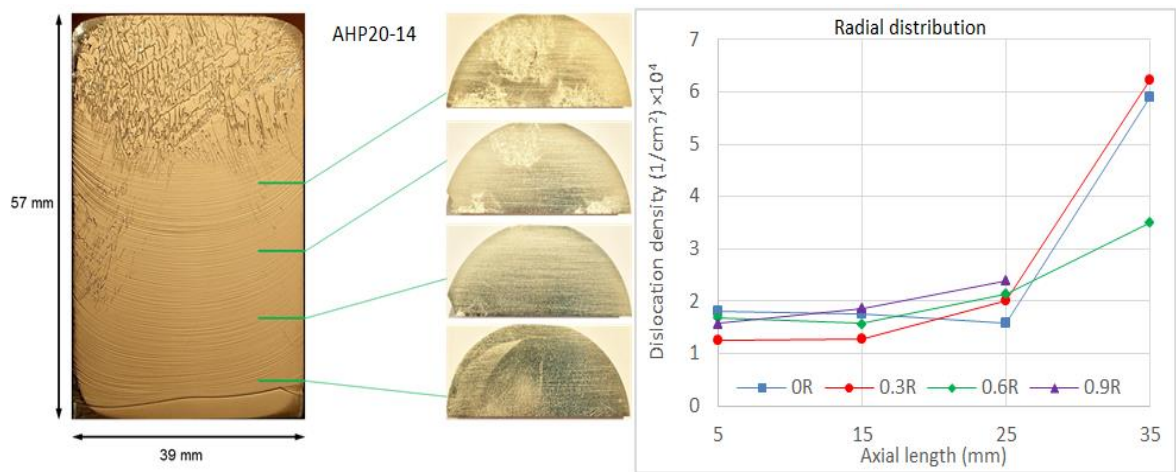


Figure 5.31. Radial distribution of dislocation densities of AHP20-14 in 5 mm, 15 mm, 25 mm, and 35 mm axial heights.

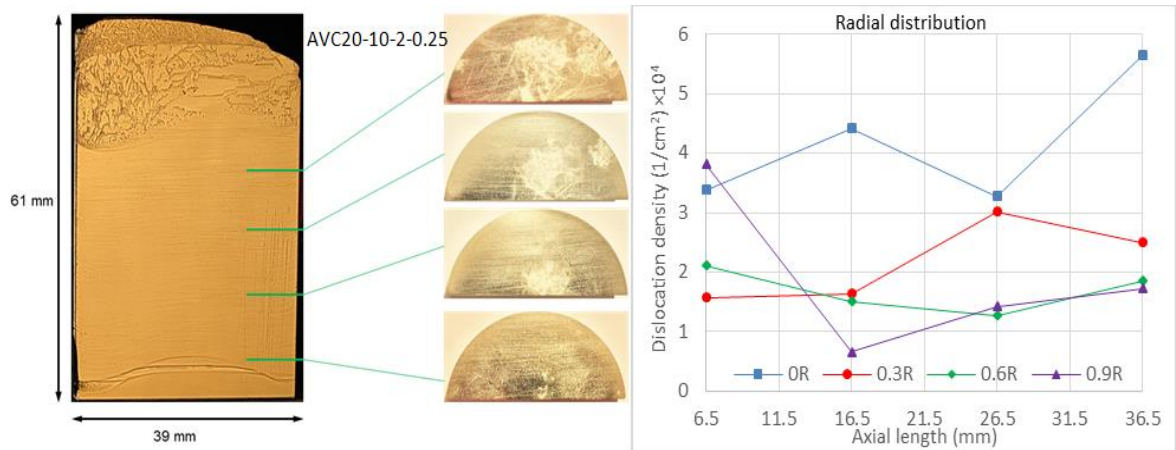


Figure 5.32. Radial distribution of dislocation densities of AVC20-10-2-0.25 in 6.5 mm, 16.5 mm, 26.5 mm, and 36.5 mm axial heights.

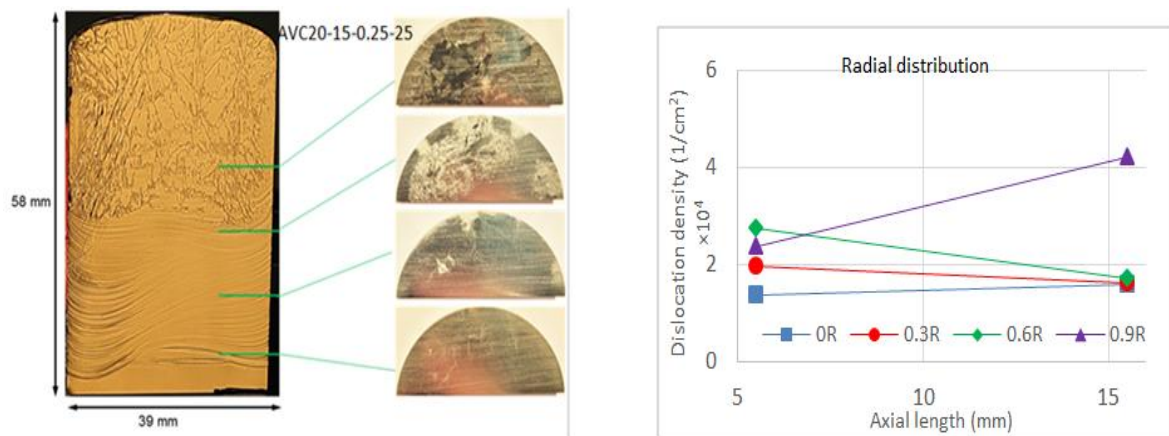


Figure 5.33. Radial distribution of dislocation densities of AVC20-15-0.25-25 in 5.5 mm, 15.5 mm, 25.5 mm, and 35.5 mm axial heights.

## 5.2. Numerical Simulations

### 5.2.1. Global Geometry

Before modeling the solidification phenomenon, first, the steady state thermal problem is solved in the global geometry. This provides the flow field in the melt, the

initial temperature distribution in the entire system and the initial shape of the s/l interface. The temperature profile on the outer surface of the crucible is used as a boundary condition in the local geometry simulations. The temperature distribution, the velocity contours, and the initial shape of the interface for VB20-58, AHP10-10 (AHP20-10), AHP20-5, and AHP20-14 are shown in Figure 5.34, Figure 5.35, Figure 5.36, and Figure 5.37, respectively. The temperature profiles on the outer side of the crucible are plotted in Figure 5.38, Figure 5.39, Figure 5.40, and Figure 5.41 for the VB20-58, AHP10-10 (AHP20-10, since the only difference is the pulling rate and the pulling rate is not considered in the steady state solution of the global geometry), AHP20-5, and AHP20-14, respectively.

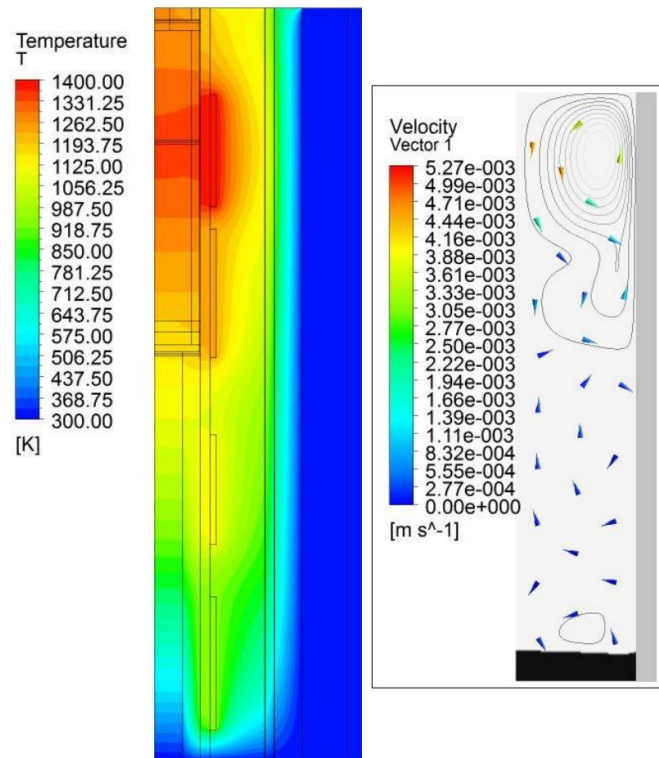


Figure 5.34. Temperature distribution (left) and velocity contours and the interface shape (right) for the global geometry of VB20-58.



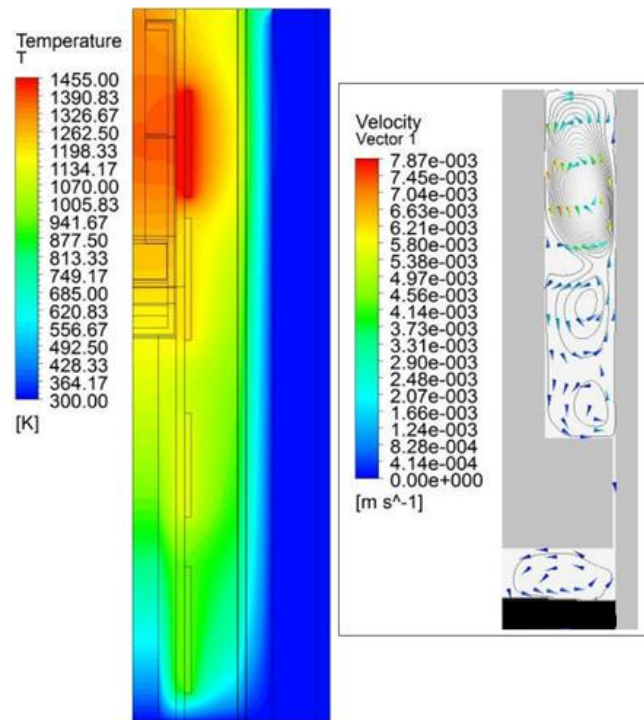


Figure 5.35. Temperature distribution (left) and velocity contours and the interface shape (right) for the global geometry of AHP10-10.

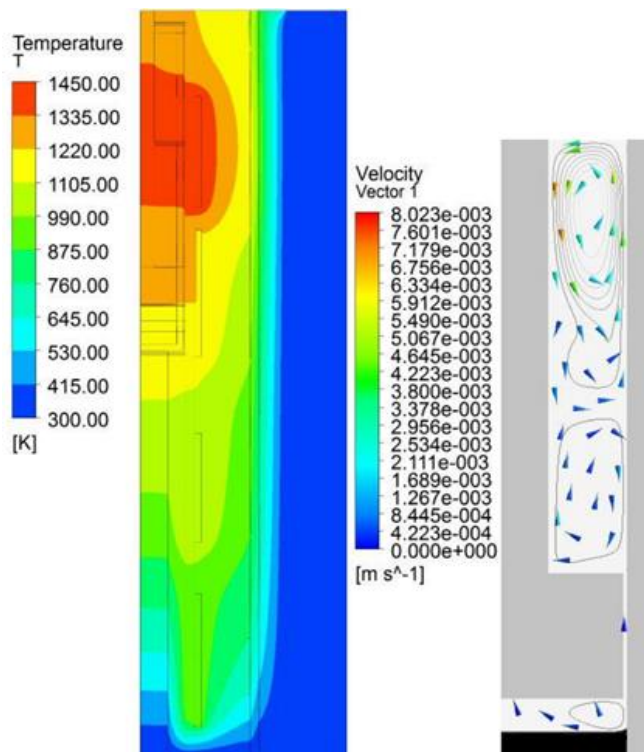


Figure 5.36. Temperature distribution (left) and velocity contours and the interface shape (right) for the global geometry of AHP20-5.



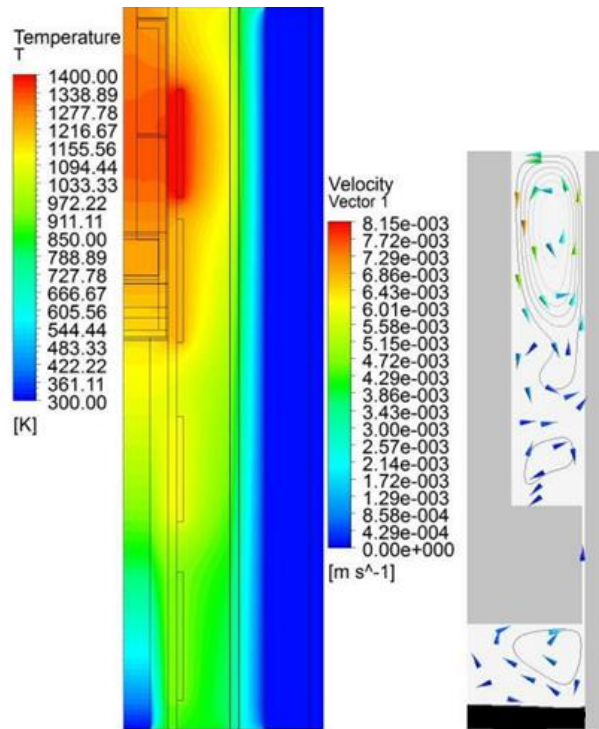


Figure 5.37. Temperature distribution (left) and velocity contours and the interface shape (right) for the global geometry of AHP20-14.

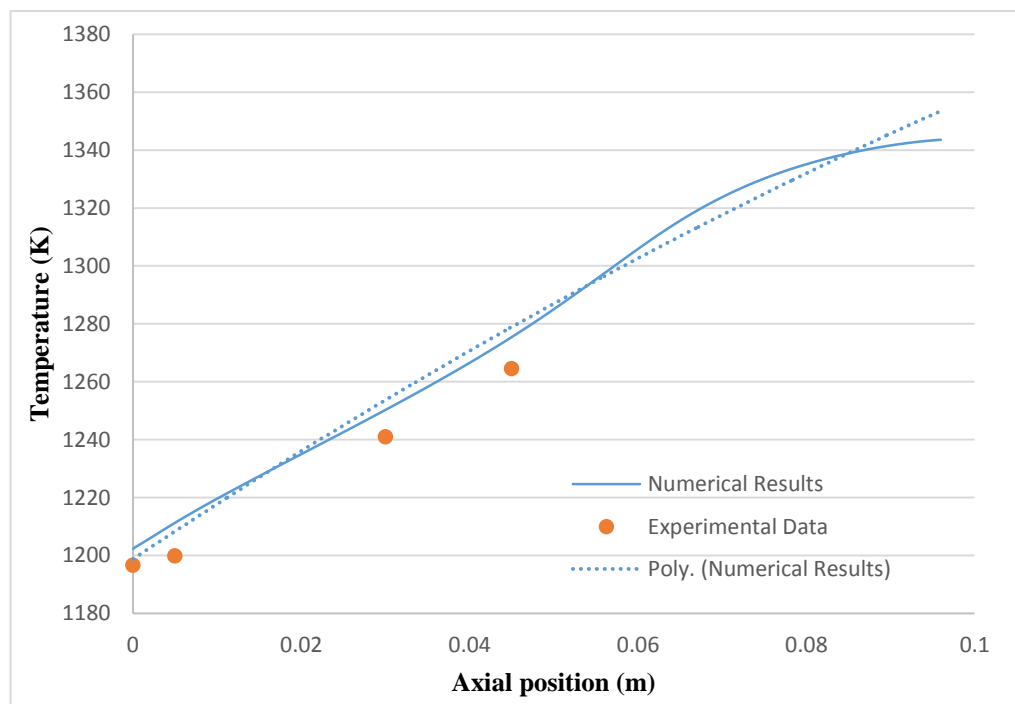


Figure 5.38. Temperature profile on the outer side of the crucible in global geometry of VB20-58.

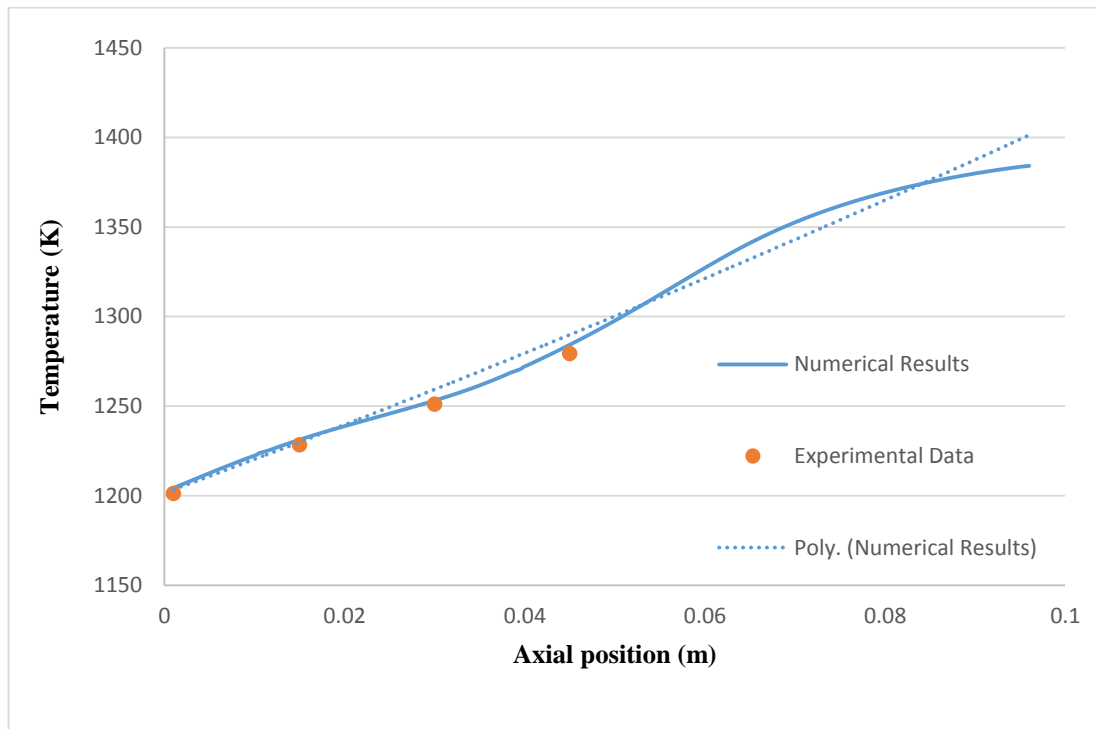


Figure 5.39. Temperature profile on the outer side of the crucible in global geometry of AHP10-10 (AHP20-10).

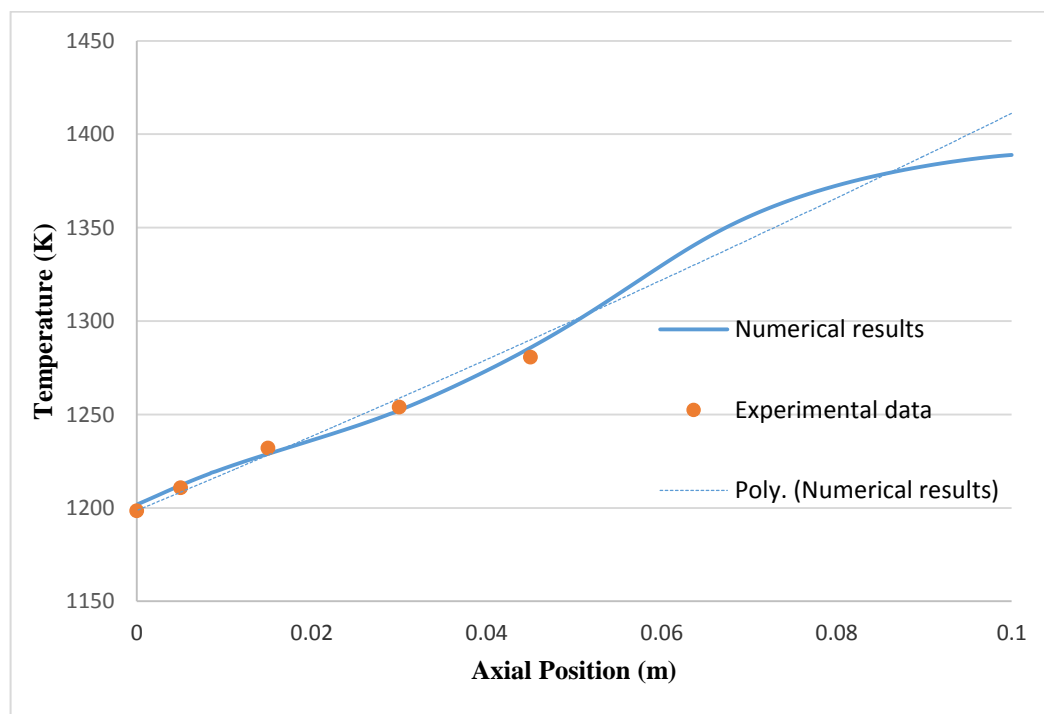


Figure 5.40. Temperature profile on the outer side of the crucible in global geometry of AHP20-5.

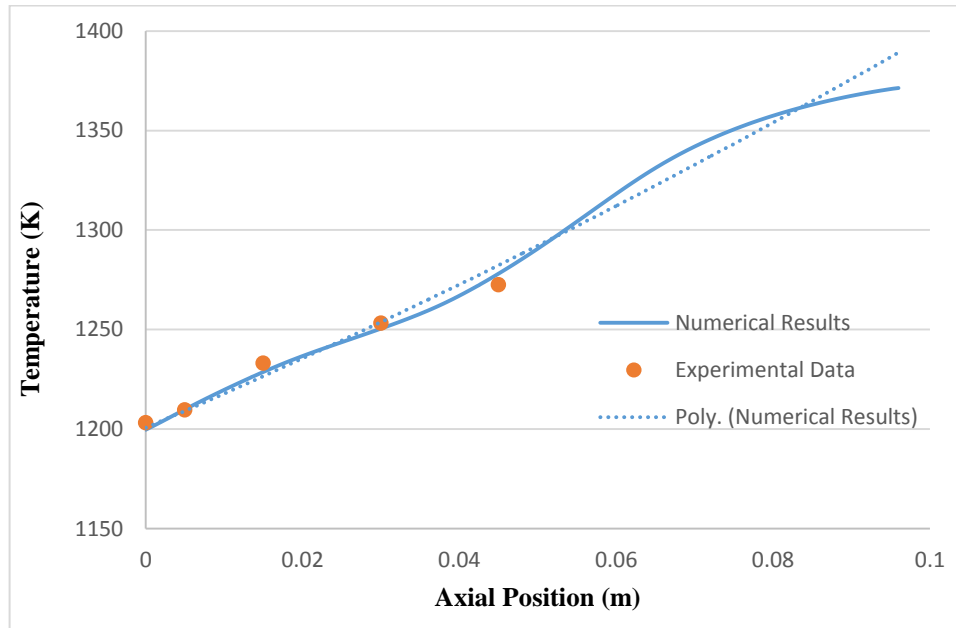


Figure 5.41. Temperature profile on the outer side of the crucible in global geometry of AHP20-14.

### 5.2.2. Local Geometry

The temperature data on the outer surface of the crucible which are achieved from the steady state solution of the global geometry are used as the boundary condition for the simulations in local geometry. The second order polynomials which are fitted to the temperature profile diagrams above are defined in a UDF (User Defined Function) in ANSYS Fluent. These second order polynomials (temperature profiles) are shifted upward by updating the vertical position ( $x$ ) via the specific pulling rate for each case. Also, the position of the baffle is updated with the same pulling rate. In the case of AVC, reciprocating motion is also added to the linear motion of the baffle. The size of the mesh is mentioned earlier in Section 4.2.2.1. It is shown that further mesh refinement does not influence the solution considerably. Figure 5.42 shows the velocity magnitude in radial direction at 5 mm height above the seed base of the steady state solution of AHP20-10 case. It is observed that the velocity magnitude does not change pretty much for further mesh refinement after  $0.015625 \text{ mm}^2$  cell size. For all the cases, the time step is initially set to 0.001 s up to 1 second and after that time the time step is adaptively changed with the

maximum time step of 0.1 s. However, in the AVC case lower time step is required for the convergence and avoiding negative cell formation during the motion of the baffle, so the maximum time step is set to 0.01 s.

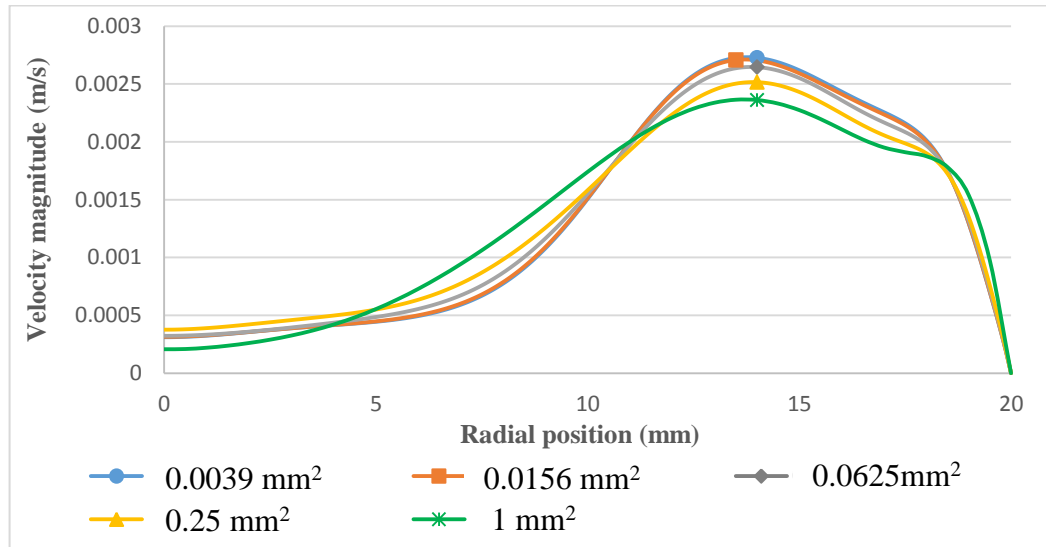


Figure 5.42. Velocity magnitude along the horizontal line 5mm above the seed base of the Steady state solution of AHP20-10.

In the following, results for the local geometry simulations are presented. The simulation results for the convective patterns in the melt for the local geometry are slightly different from those in the global geometry. However, the similarity in the flow direction and its intensity, both close to the interface and in the bulk fluid, shows that it is a good approach to use the local geometry instead of the global geometry and solving for the whole geometry and avoid increasing calculation time.

**5.2.2.1. VB20-58.** The temperature distribution, velocity magnitude, and the interface shape for the steady state solution (initial) and 2400 s after starting the solidification for the VB20-58 case are shown in Figure 5.43.

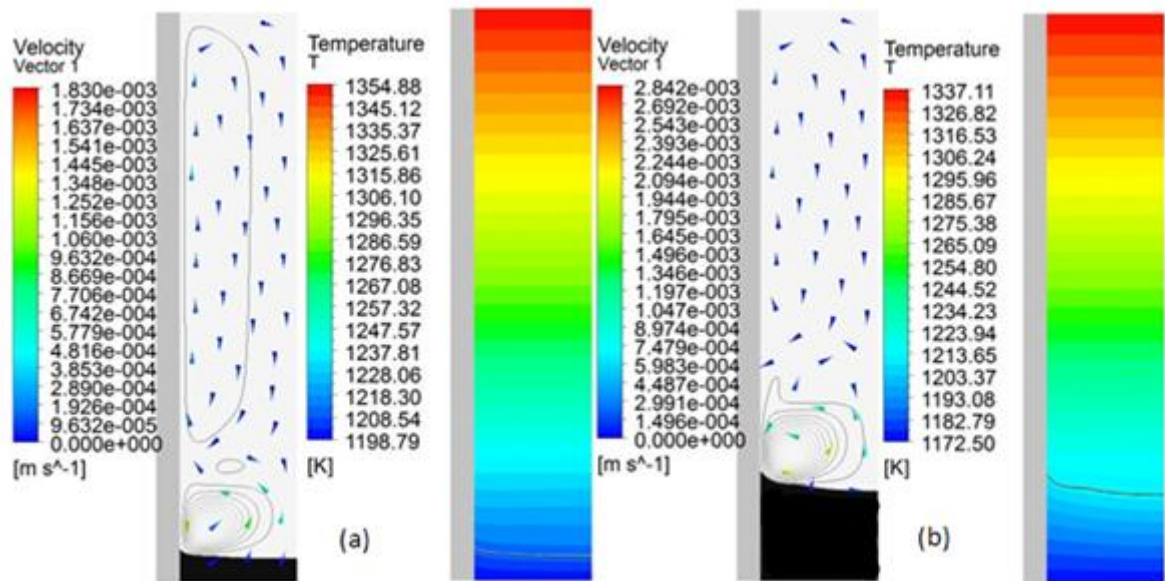


Figure 5.43. The temperature distribution, velocity magnitude, and the interface shape for initial (a) and 2400 s(b) for local geometry of VB20-58.

First, the problem is solved in steady state to achieve the initial s/l interface, temperature field and the convective flow pattern in the melt. While the initial interface is relatively flat, after starting the solidification by shifting upward the temperature gradient on the crucible, the rate of solidification at the side becomes more than that at the center and the interface becomes concave. Also, the fluid flow contours are concentrated at the sides and the flow field is not effective at the center close to the interface. Figure 5.44 shows the radial distribution of the temperature along a horizontal line 2 mm above the interface at the central axis of the crystal. In addition, the velocity magnitude values on the same line are plotted in Figure 5.45. The radial temperature gradient increases by time which shows the increased concavity of the interface during the growth. Since the concavity of the interface is increased, the more portion of the horizontal line (2mm above the interface) enters into the solid region, so more zero velocity magnitude is observed for data from higher time levels.

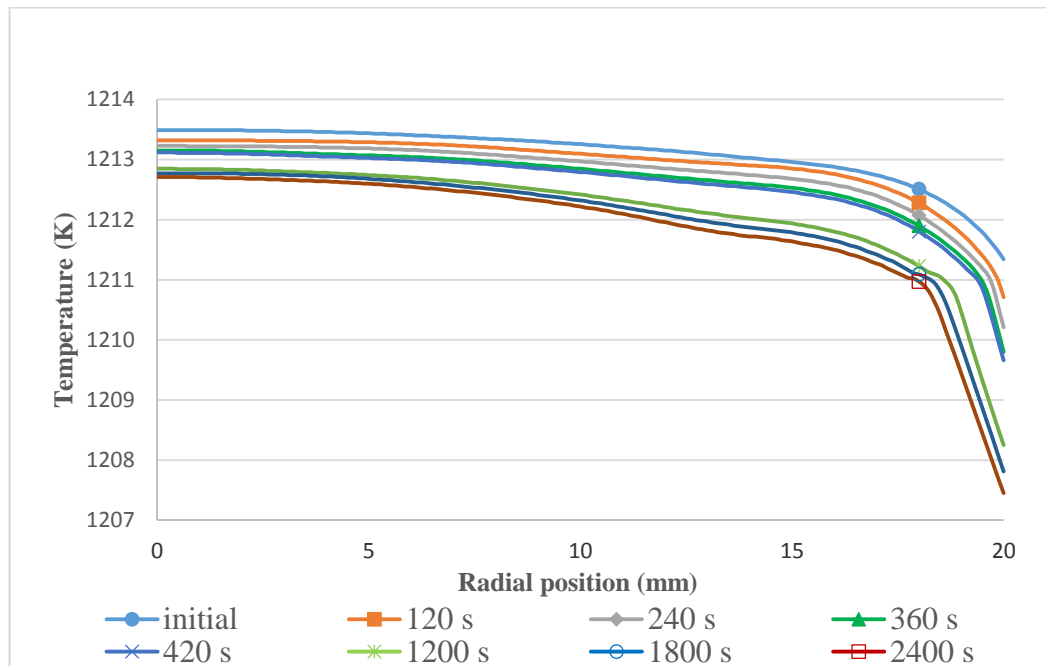


Figure 5.44. Radial temperature along the horizontal line 2mm above the interface in local geometry of VB20-58.

5.2.2.2. AHP10-10. The temperature distribution, velocity magnitude, and the interface shape for steady state solution (initial) and 2400s after starting the solidification for the AHP10-10 case are shown in Figure 5.46.

The interface almost preserves its initial flat shape and slightly becomes concave since the pulling velocity is relatively lower than in the VB20-58. Moreover, inserting the baffle, avoids concentration of the convective flow cell just at the side and the fluid flow covers the region below the baffle more effectively. Figure 5.47 shows the radial distribution of the temperature along a horizontal line 2 mm above the interface at the central axis of the crystal. Also, the velocity magnitude values on the same line are plotted in Figure 5.48. Same as the VB20-58 the radial temperature gradient has an increasing trend, but with much lower rate. Also, the concavity of the interface is much lower than that in the VB20-58 case. This is more obvious from the velocity magnitude plot (non-zero velocity magnitude close to the crucible wall).

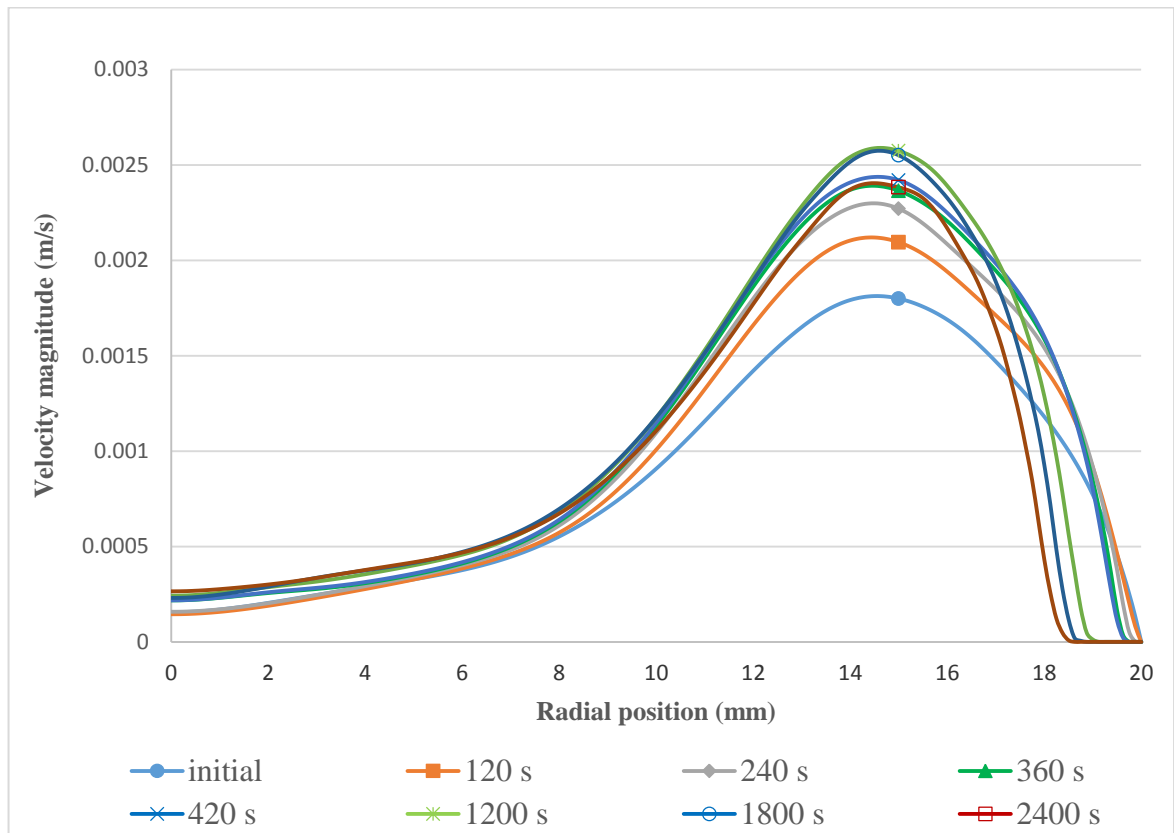


Figure 5.45. Velocity magnitude along the horizontal line 2mm above the interface in local geometry of VB20-58.

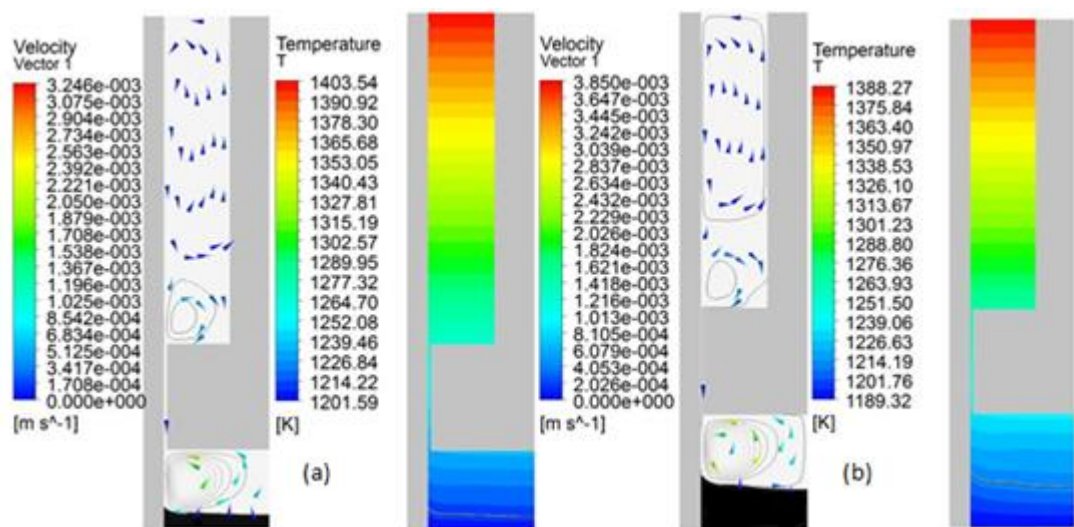


Figure 5.46. The temperature distribution, velocity magnitude, and the interface shape for initial (a) and 2400 s(b) for local geometry of AHP10-10.

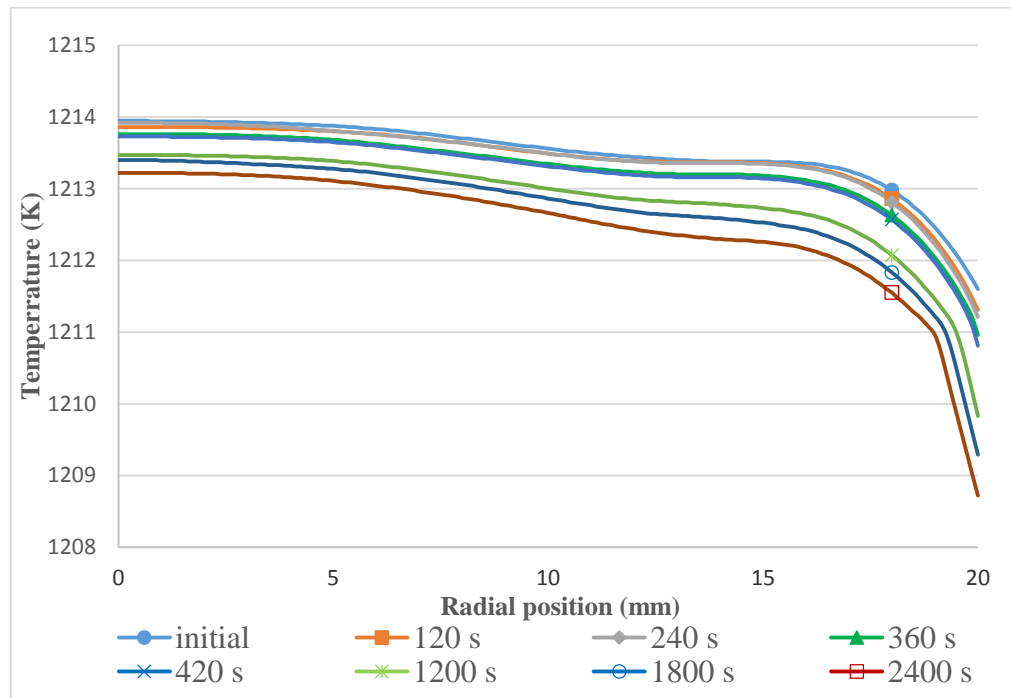


Figure 5.47. Radial temperature along the horizontal line 2mm above the interface in local geometry of AHP10-10.

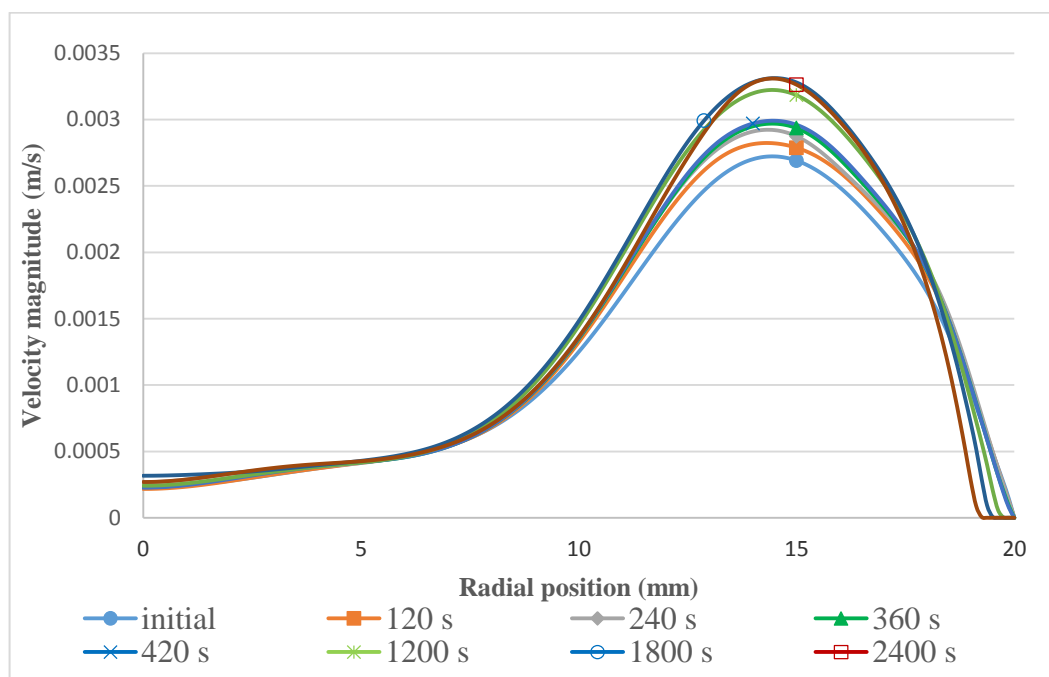


Figure 5.48. Velocity magnitude along the horizontal line 2mm above the interface in local geometry of AHP10-10.



**5.2.2.3. AHP20-10.** Since the initial melt height is the same as the AHP10-10, the same temperature gradient obtained from the steady state solution of the global geometry of the AHP10-10 case is applied on the outer side of the crucible as a boundary condition. The temperature distribution, velocity magnitude, and the interface shape for the steady state solution (initial) and 2400 s after starting the solidification for the AHP20-10 case are shown in Figure 5.49. Since the pulling velocity is high, just like in VB20-58, due to different solidification rates at the side and the center, the interface becomes concave but with less concavity comparing to the VB20-58. Also, the intensity of the flow below the baffle and close to the interface is more than that in the VB20-58 and the convective flow covers the region below the baffle more effectively. This is also concluded from comparing Figure 5.45 and Figure 5.51.

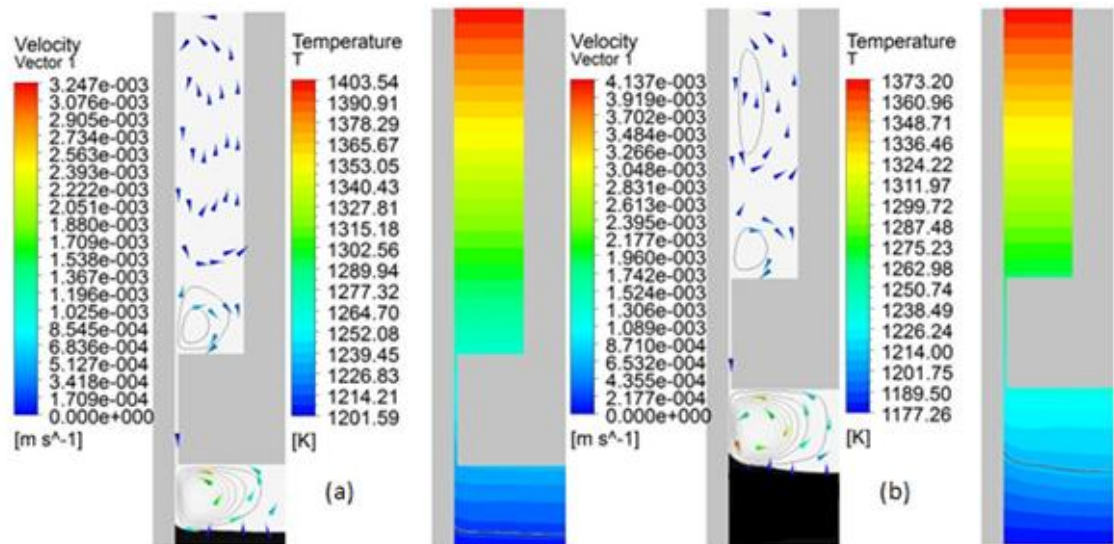


Figure 5.49. The temperature distribution, velocity magnitude, and the interface shape for initial (a) and 2400 s(b) for local geometry of AHP20-10.

Figure 5.50 shows the radial distribution of the temperature along a horizontal line 2 mm above the interface at the central axis of the crystal. Also, the velocity magnitude values on the same line are plotted in Figure 5.51. Since the pulling velocity is higher, the rate of increase in the radial temperature gradient is higher than the AHP10-10, but it is less than the VB20-58 with the same pulling velocity. Also, due to higher pulling rate the velocity magnitudes are higher than those in the AHP10-10.

5.2.2.4. AHP20-14. The temperature distribution, velocity magnitude, and the interface shape for steady state solution (initial) and 2400s after starting the solidification for the AHP20-14 case are shown in Figure 5.52.

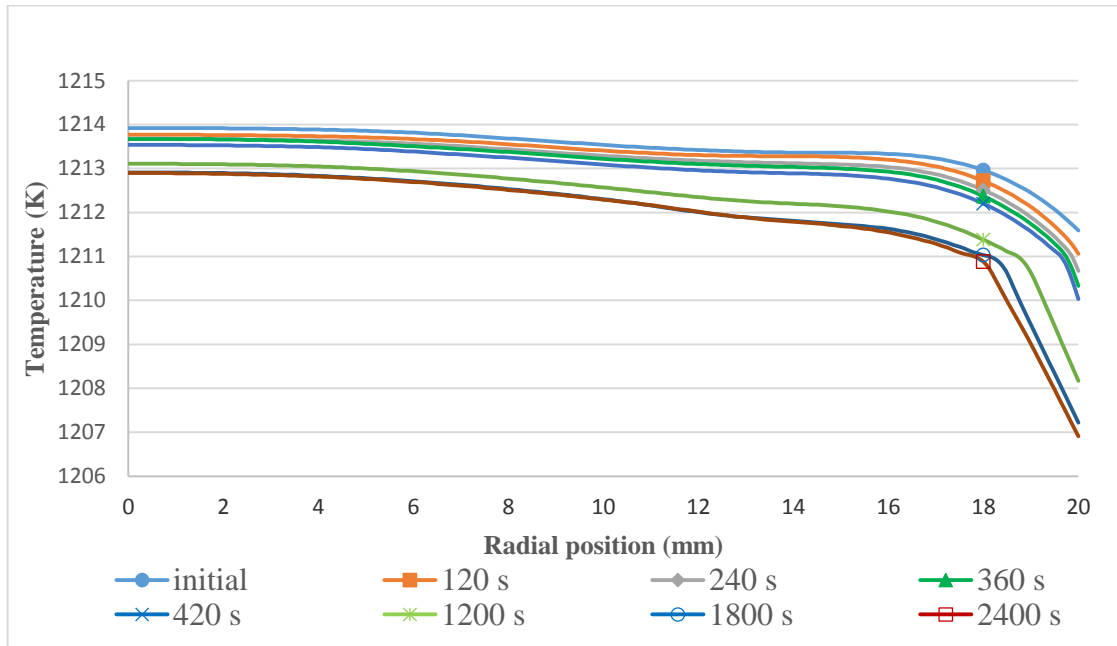


Figure 5.50. Radial temperature along the horizontal line 2mm above the interface in local geometry of AHP20-10.

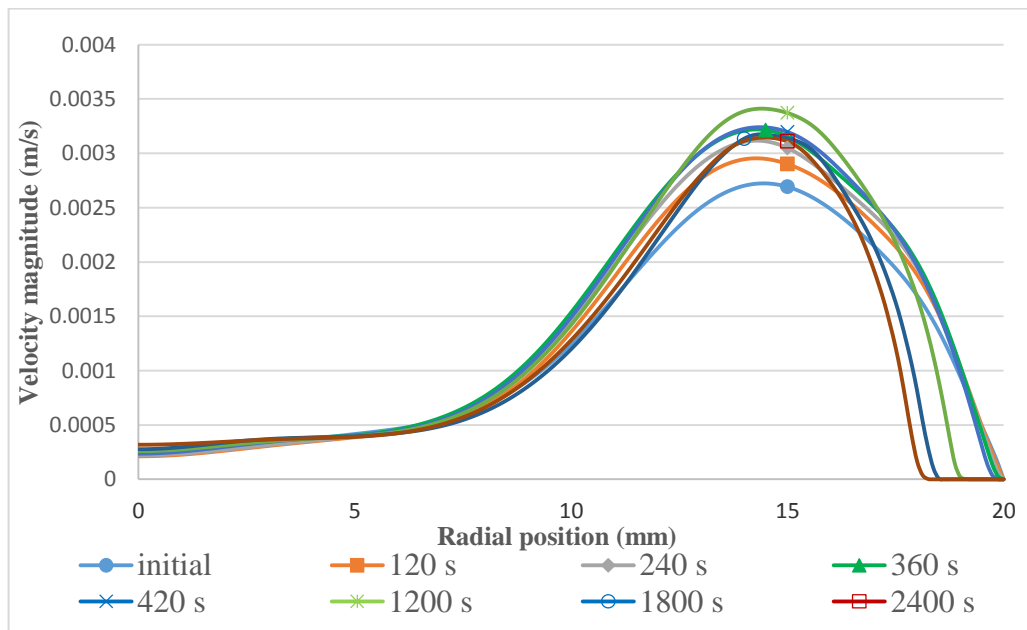


Figure 5.51. Velocity magnitude along the horizontal line 2mm above the interface in local geometry of AHP20-10.

Figure 5.53 shows the radial distribution of the temperature along a horizontal line 2 mm above the interface at the central axis of the crystal. Also, the velocity magnitude values on the same line are plotted in Figure 5.54. According to the higher melt height, the rate of increase in the radial temperature gradient is higher than the AHP20-10, which explains the more concavity of the interface rather than that in the AHP20-10. Also, the convective pattern close to the interface becomes elongated in the axial direction and the flow can cover the region below the baffle less effectively. Moreover, the intensity of the flow close to the interface is reduced (see velocity magnitudes in Figure 5.54).

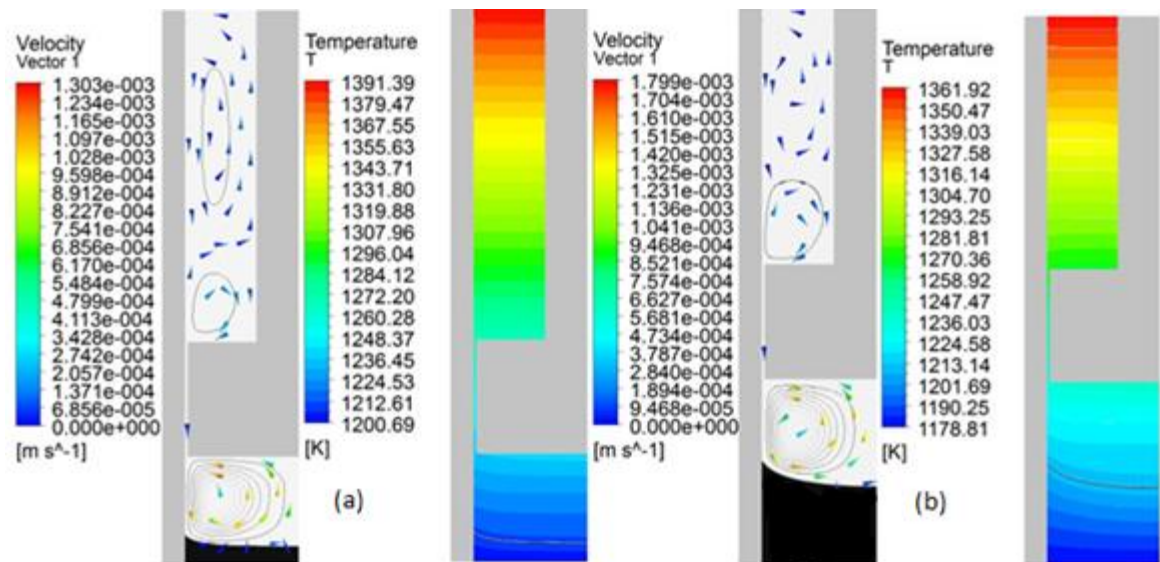


Figure 5.52. The temperature distribution, velocity magnitude, and the interface shape for initial (a) and 2400 s(b) for local geometry of AHP20-14.

5.2.2.5. AVC20-10-2-0.25. The temperature distribution, velocity magnitude, and the interface shape for steady state solution (initial) and 2400s after starting the solidification for the AVC20-10-2-0.25 case are shown in Figure 5.55.

Figure 5.56 shows the radial distribution of the temperature along a horizontal line 2 mm above the interface at the central axis of the crystal. Also, the velocity magnitude values on the same line are plotted in Figure 5.57.

Except regions close to the crucible wall, the interface is relatively flat. The concavity of the interface near the wall is due to the intense flow (see Figure 5.57) which brings the hot melt close to the interface and melts portion of the interface. This is also observed from Figure 5.56 which shows higher temperature values at the sides close to the crucible wall. However, this concavity is smoothed out in the later stages of the solidification.

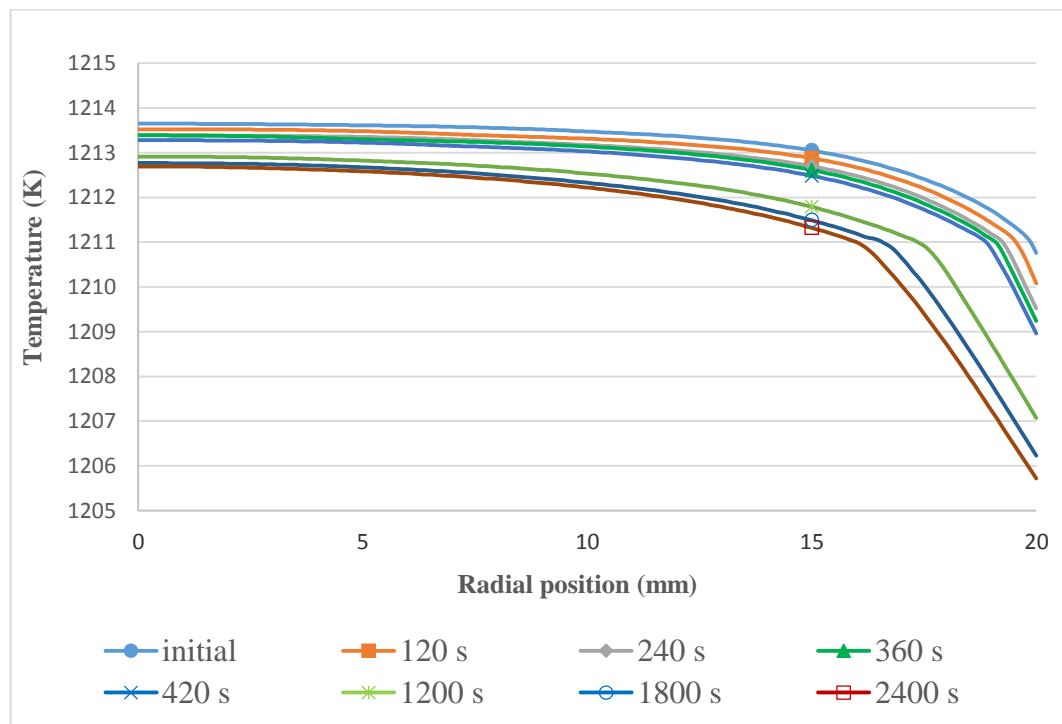


Figure 5.53. Radial temperature along the horizontal line 2mm above the interface in local geometry of AHP20-14.

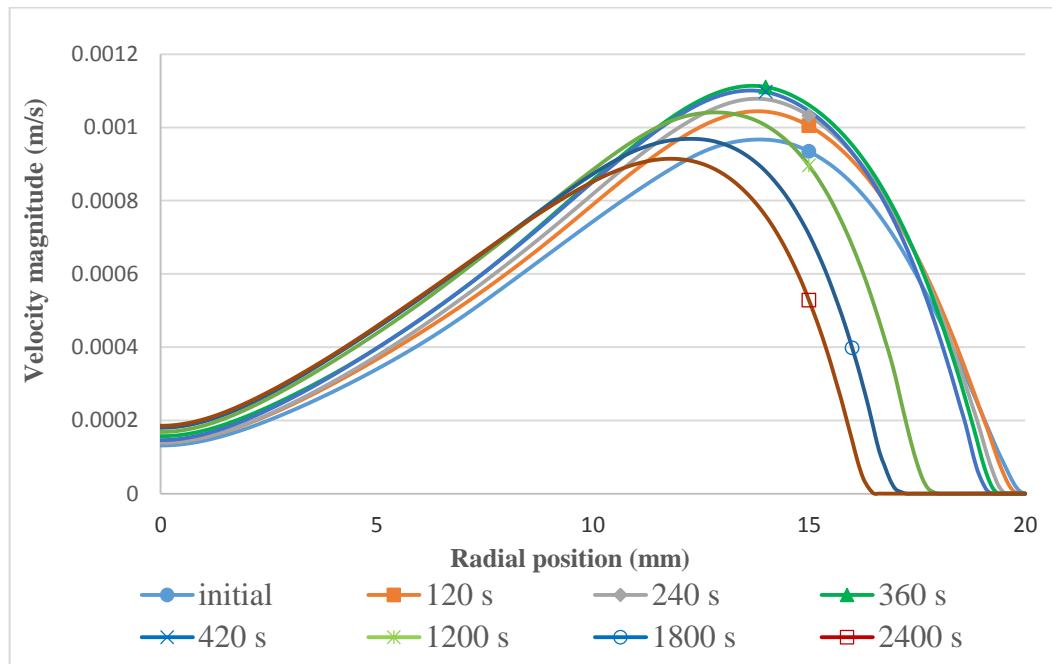


Figure 5.54. Velocity magnitude along the horizontal line 2mm above the interface in local geometry of AHP20-14.

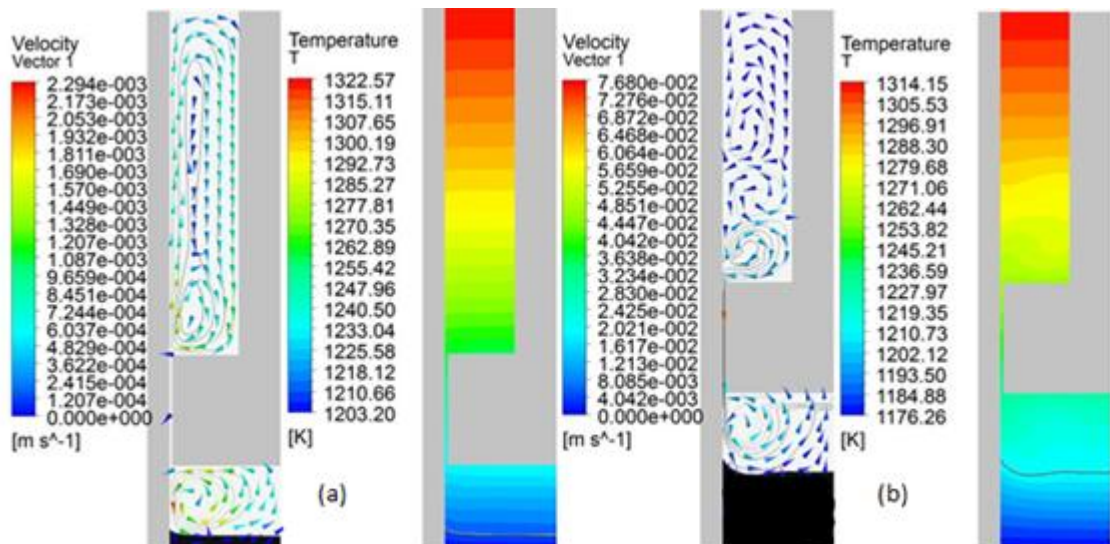


Figure 5.55. The temperature distribution, velocity magnitude, and the interface shape for initial (a) and 2400 s(b) for local geometry of AVC20-10-2-0.25.

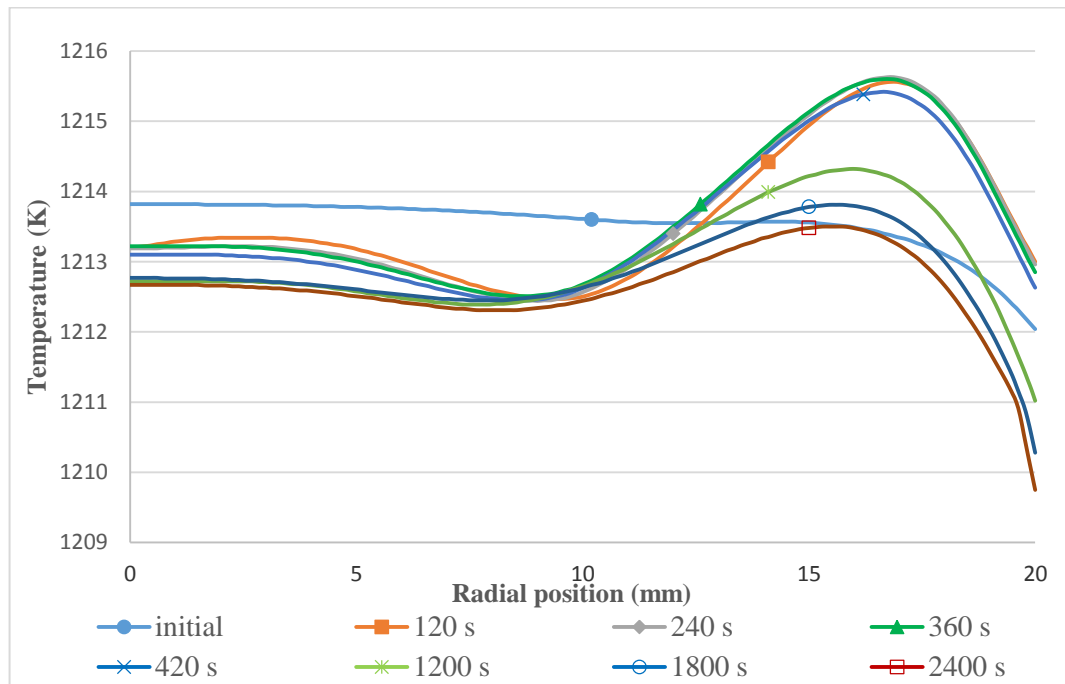


Figure 5.56. Radial temperature along the horizontal line 2mm above the interface in local geometry of AVC20-10-2-0.25.

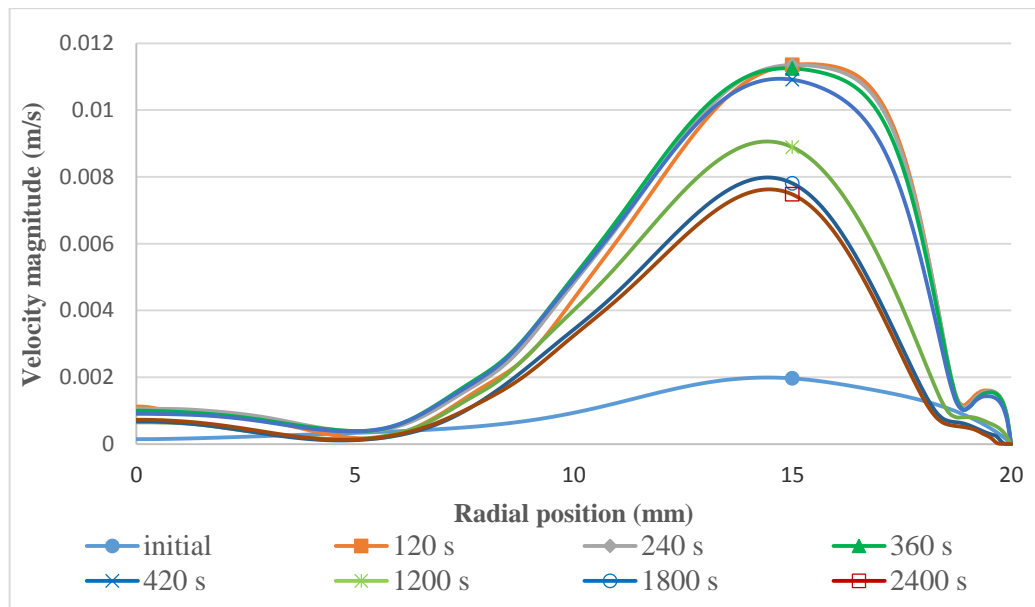


Figure 5.57. Velocity magnitude along the horizontal line 2mm above the interface in local geometry of AVC20-10-2-0.25.

The evolution of the interface during the growth is shown in Figure 5.58 for the VB20-58, AHP10-10, AHP20-10, AHP20-14, and AVC20-10-2-0.25 case. The interface shape obtained from the simulations nicely matches the striations observed in the samples. For comparison, numerical result of the AVC20-10-2-0.25 case (second from right) is shown beside the experimental observation (right most) of this sample. The simulations successfully shows the high concavity of the interface at the initial stages of the solidification due to intense forced convective flow through the baffle gap and gradual smoothing out of this concavity.

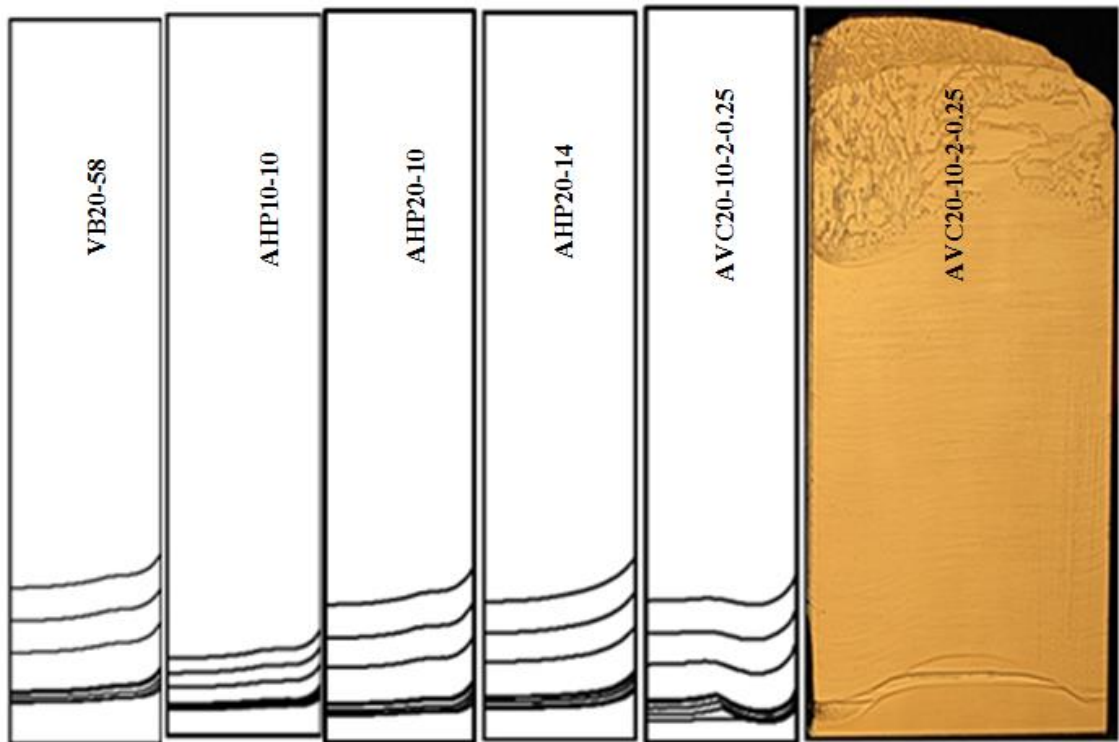


Figure 5.58. Numerical results for interface shape in VB20-58, AHP10-10, AHP20-10, AHP20-14, and AVC20-10-2-0.25 (from left to right) in 0, 120, 240, 360, 600, 1200, 1800, and 2400 seconds.

### 5.3. Species Transport

#### 5.3.1. Setup and Initialization

In order to model the solute distribution during the solidification, the species transport model of ANSYS Fluent is used. When this model is used, two options, Lever and Scheil, are automatically added to the solidification/Melting model of the ANSYS. In all of the simulations, Scheil model is used. Also, both thermal and solutal buoyancy are included to the model. When species transport model is activated, a mixture that contains both the solute and the solvent is also added to the material list box. The material properties are listed in Table 5.2.

For modeling solidification of binary alloy, it has been assumed that the solidification starts after the half of the 10 mm height seed is melted in all of the experiments. Therefore, first 5mm of the domain is considered as pure solid germanium and the conservation of species equation and the momentum equations are not solved in this region. For the initialization, 0.3795 wt% antimony is patched to the rest of the domain. The same temperature profile on the crucible wall, which is defined in the UDF as a boundary condition, is patched to the whole domain as the initial temperature distribution. The remaining steps of the simulation are the same as in the previous simulations (see appendix A).

The time step setting for AHP10-10 is the same for the local geometry of the pure germanium without considering solute distribution. However, for 20 mm/h pulling rate (VB20-58 and AHP20-10) using the same time step leads to decrease in the accuracy of the solution. The solver is not able to solve for the solute redistribution accurately which leads to accumulation of the solute at the center and consequently wider mushy zone at this region which affects the solution in the whole domain. Therefore a smaller time step is required for the solution convergence and increase the accuracy. The time step is reduced



from 0.1 s to 0.001 s and further decrease of the time step does not make any significant changes in the solution.

### 5.3.2. Solute redistribution results

In the following, simulation results for VB20-58, AHP10-10, and AHP20-10 are presented. Since the solutal buoyancy is also added to the simulations of the species transport, the convective flow pattern in the fluid becomes a little bit different from that in the pure germanium case. This difference is more obvious in the convective flow pattern in the bulk liquid in the VB20-58.

Table 5.2. Material properties of Germanium, Antimony, and the mixture [29].

Property	Ge	Sb	Mixture
Specific Heat [J/Kg.K]	210	380	
Thermal Conductivity [W/m.K]	Solid: 17 Liquid: 39	24.4	
Viscosity [Kg/m.s]	0.0131	0.00073255	
Molecular Weight [Kg/Kg mol]	121.76	76.64	
Pure solvent melting heat [J/Kg]	131000	465000	
Solidus Temperature of pure metal [K]	903.78	1211	
Liquidus Temperature of pure metal[K]	903.78	1211	
Density [Kg/m <sup>3</sup> ]			5500 (Boussinesq)
Slope of liquidus line [K]			-384.4
Partition coefficient			0.003
Thermal Expansion Coefficient [1/K]	0.0000109	0.00011	
Solutal Expansion Coefficient [1/wt%]	0.0035		
Mass diffusion coefficient [m <sup>2</sup> /s]			5.5e-9
Eutectic mass fraction			0.9
Eutectic temperature [K]			865
Pure solvent melting temperature[K]			1211

5.3.2.1. VB20-58. The solute distribution, velocity magnitude, and the interface shape for 600s and 2400s after starting the solidification for the VB20-58 case are shown in Figure 5.59.

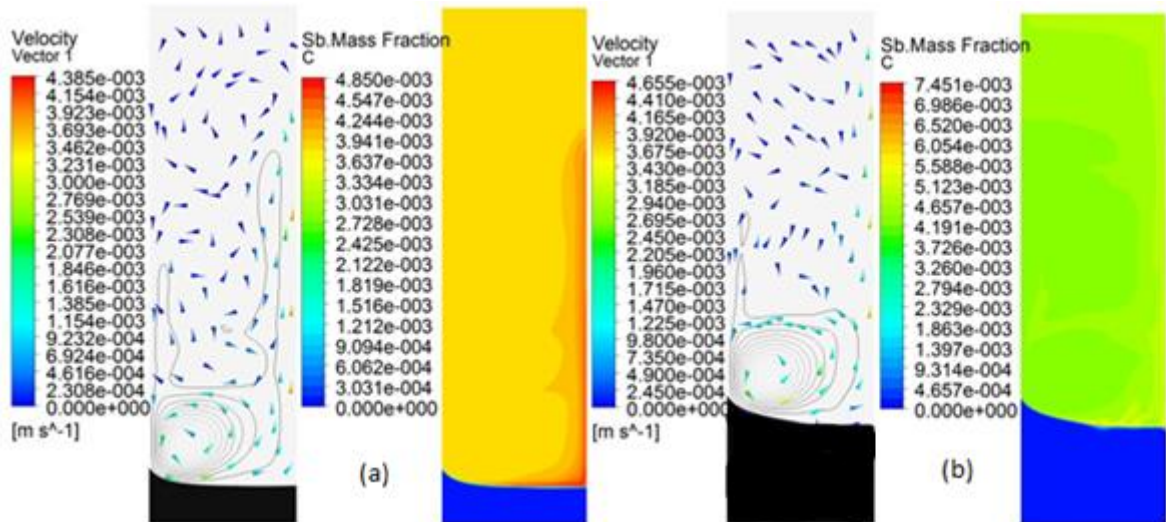


Figure 5.59. The solute distribution, velocity magnitude, and the interface shape for 600s (a) and 2400 s(b) for VB20-58.

The radial solute distribution is shown in Figure 5.60. The rejected solute is not redistributed homogeneously and the solute is accumulated near the interface. As shown in Figure 5.60 the crystal is solidifying with high solute content. Also, the solute content at the center is higher than that at the side.

The axial solute distribution along the central axis (0mm), 4mm, 8mm, 12mm, 16mm, and 20mm (the crucible wall) are plotted from Figure 5.61 to Figure 5.66. While the solute boundary layer forming ahead of the interface is more obvious at the center, the length of the boundary layer decreasing and it becomes vanishing by approaching to the side of the crystal. As it is shown in Figure 5.66, there is almost no solute boundary layer. Also, note that the solidification has not occurred yet at the center at the time 600 s, so no solute boundary is formed in the liquid (Figure 5.61).

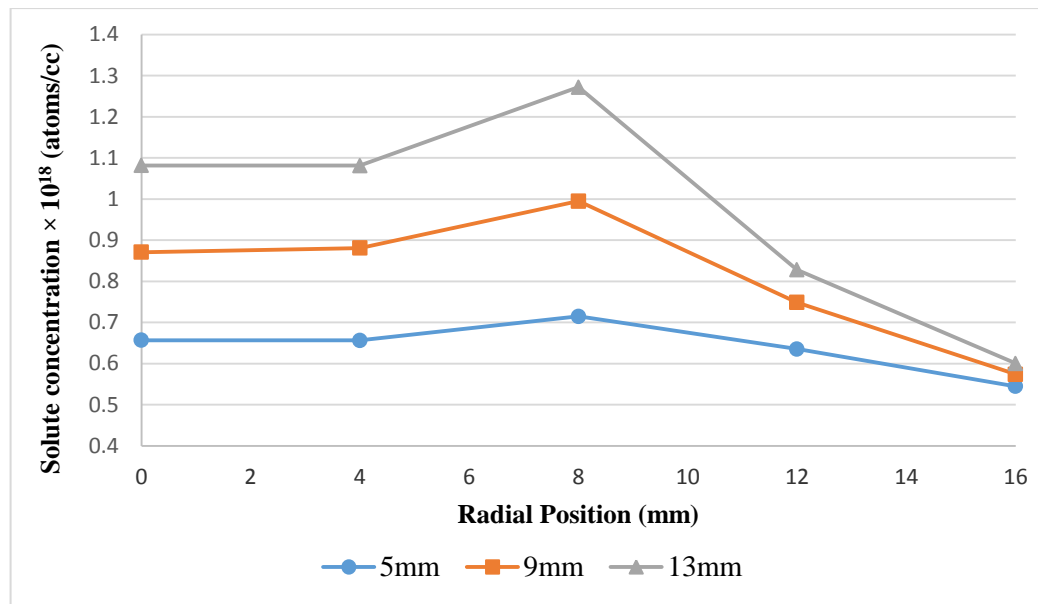


Figure 5.60. Simulated Radial solute distribution of VB20-58.

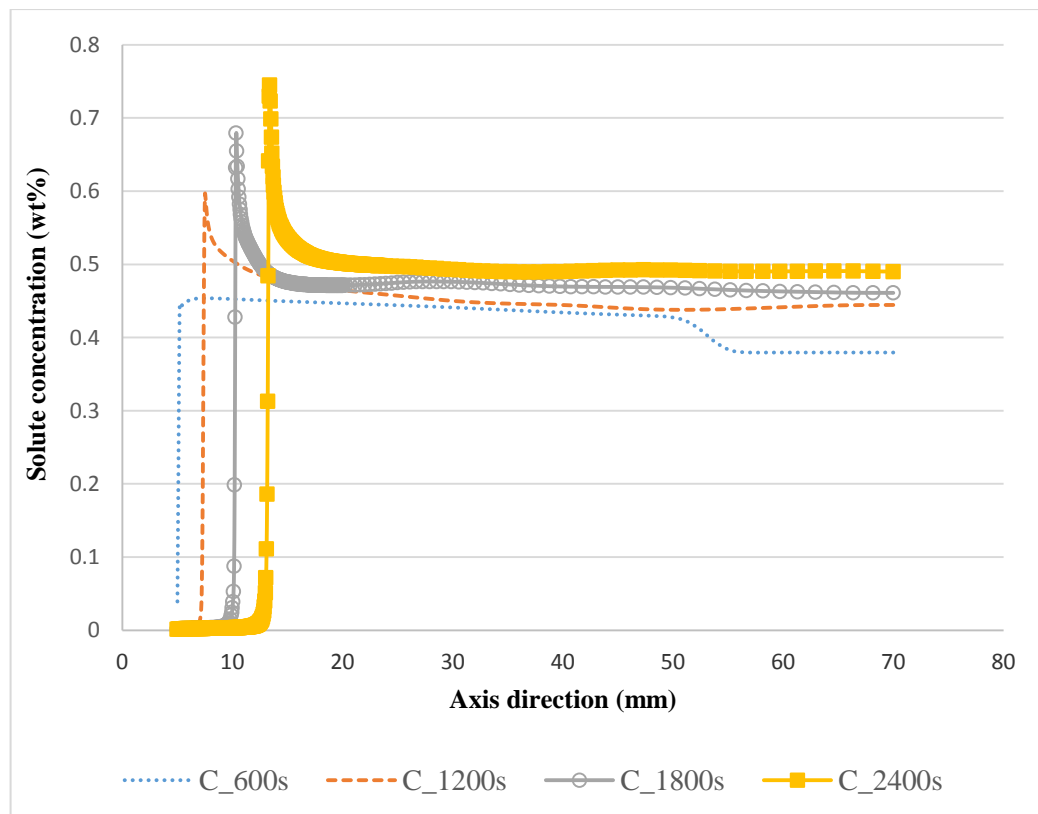


Figure 5.61. VB20-58 Axial Solute Distribution along 0mm Axis (center).

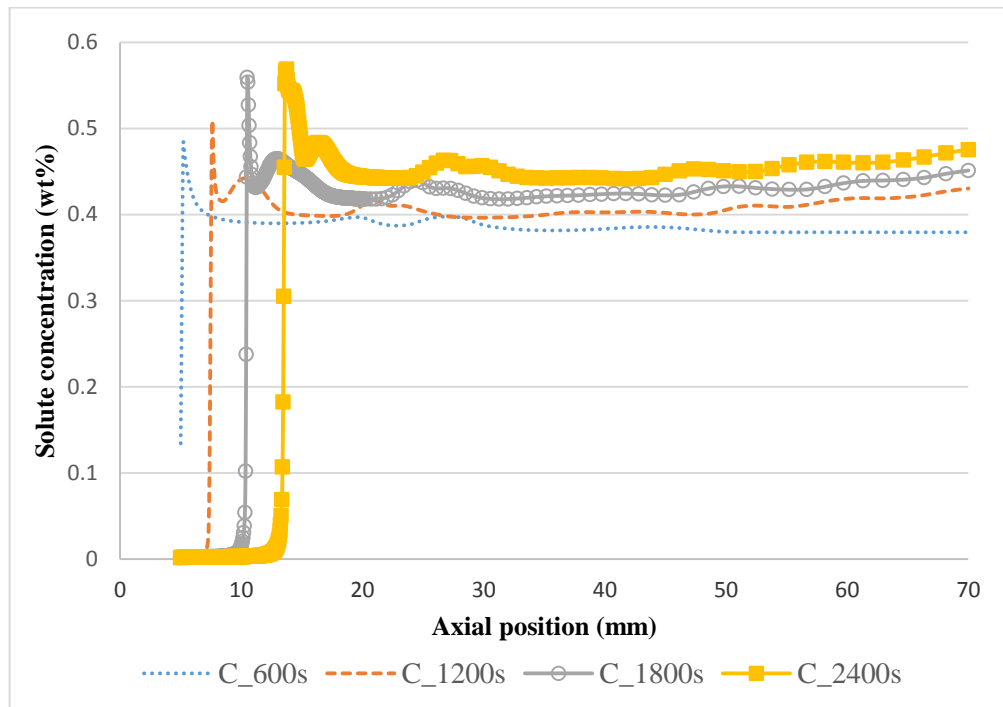


Figure 5.62. VB20-58 Axial Solute Distribution along 4mm Axis.

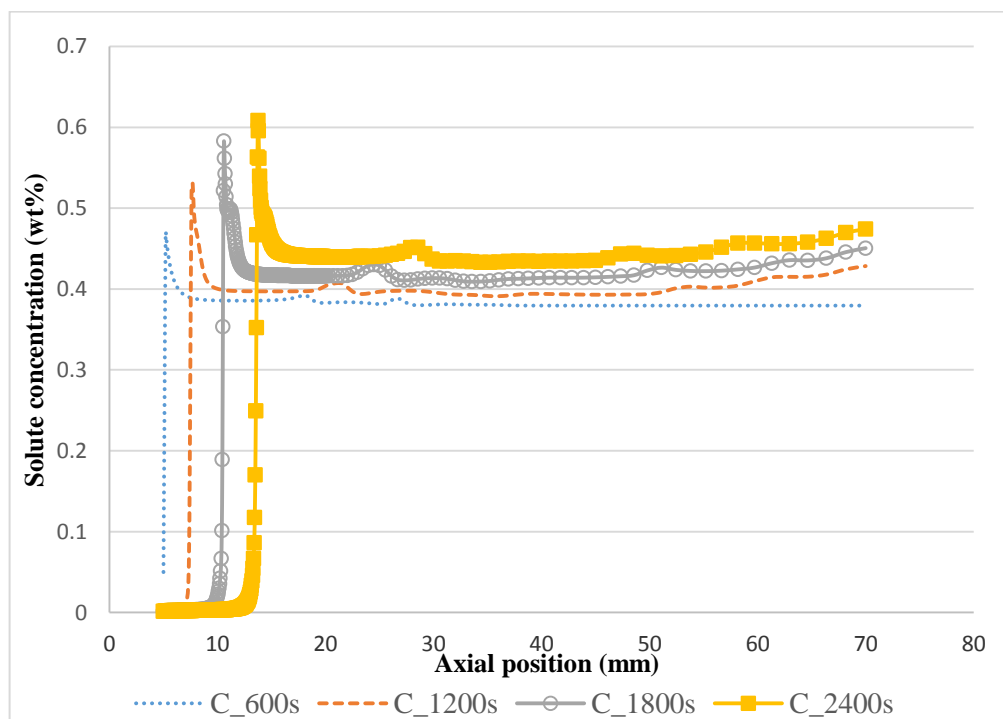


Figure 5.63. VB20-58 Axial Solute Distribution along 8mm Axis.

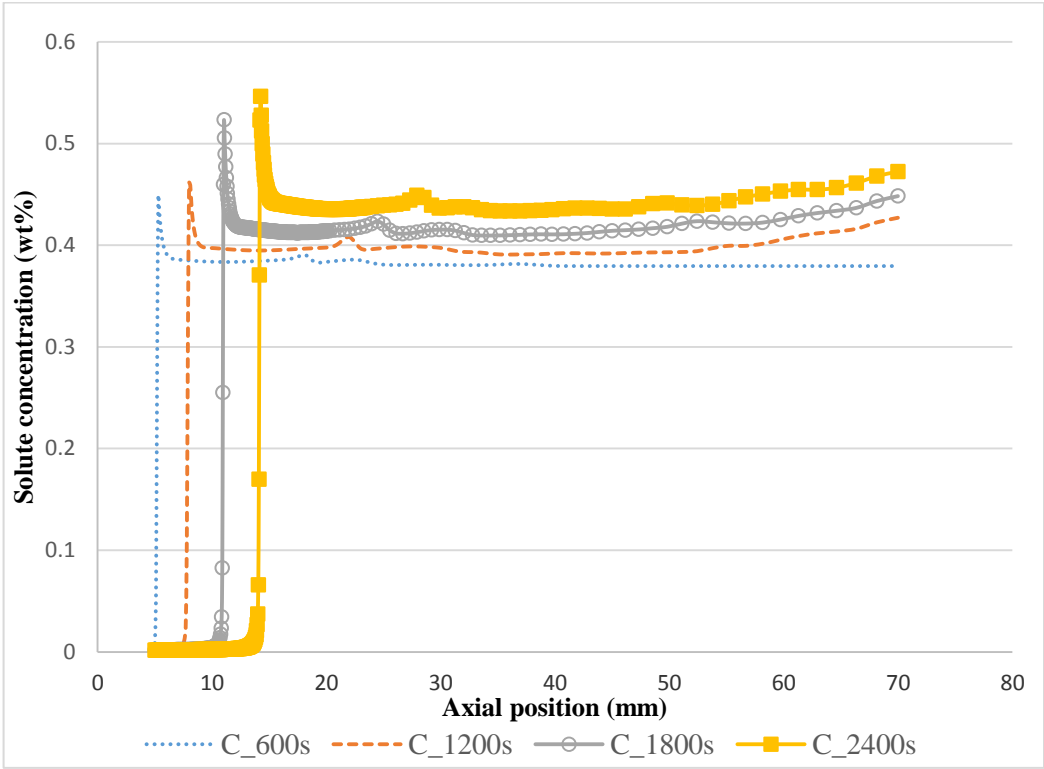


Figure 5.64. VB20-58 Axial Solute Distribution along 12mm Axis

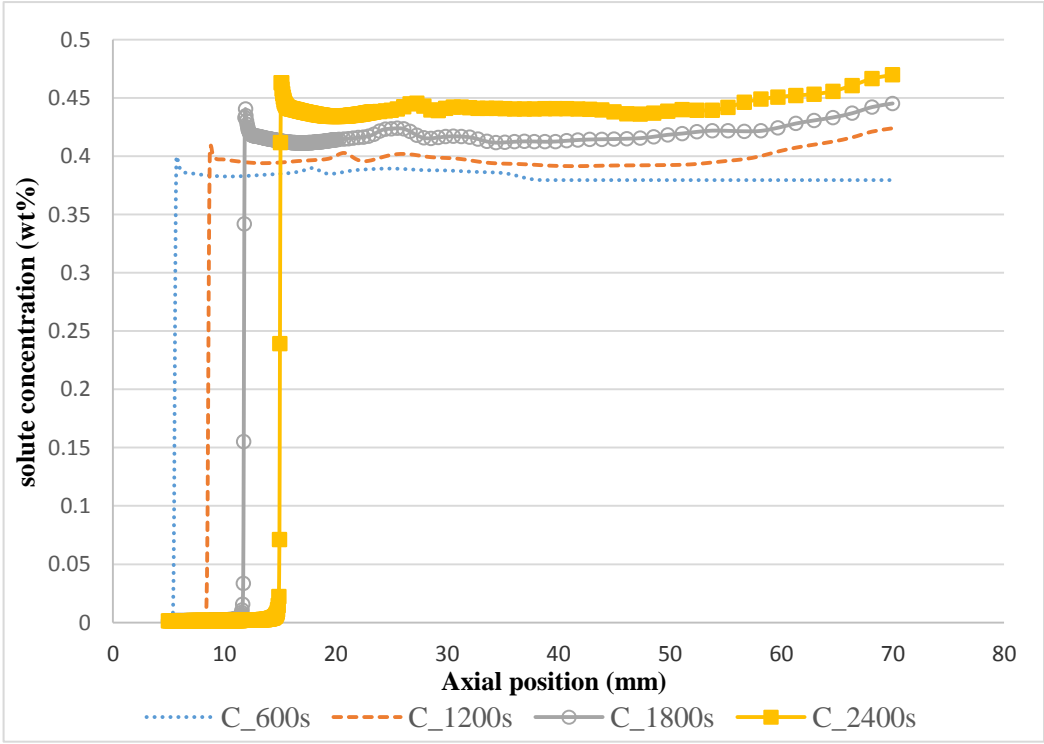


Figure 5.65. VB20-58 Axial Solute Distribution along 16mm Axis.

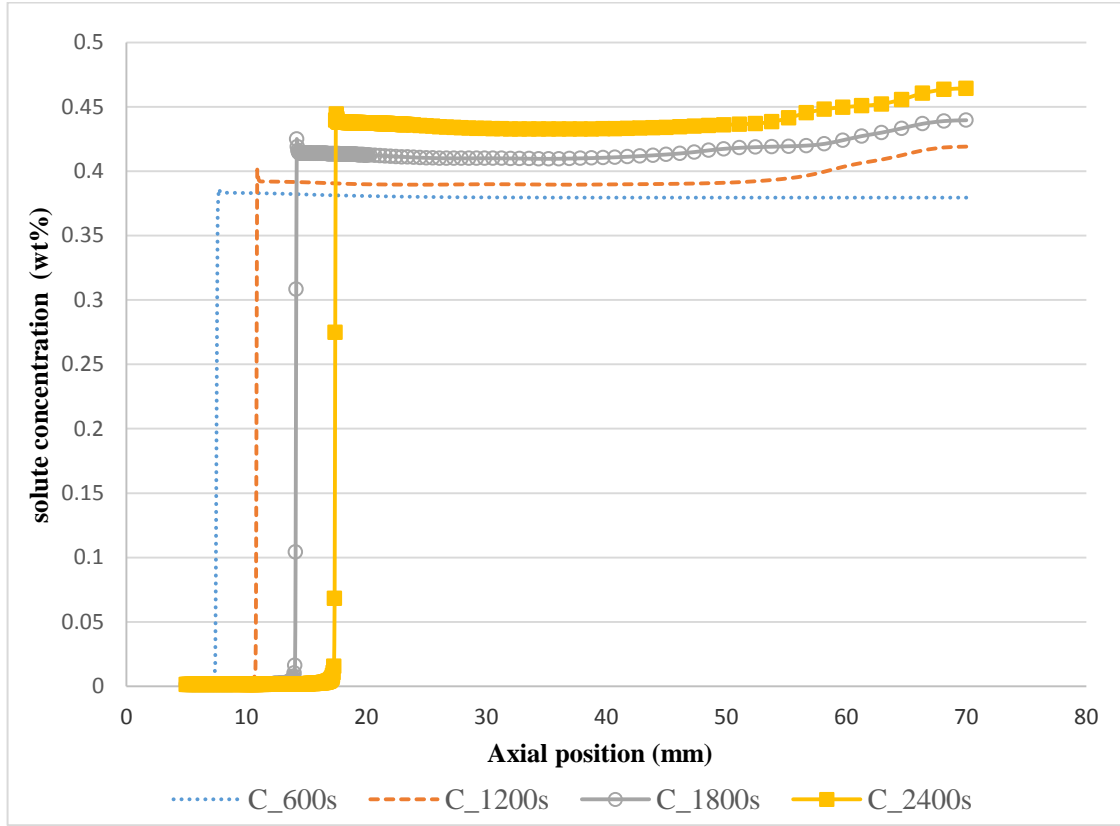


Figure 5.66. VB20-58 Axial Solute Distribution along 20mm Axis (wall).

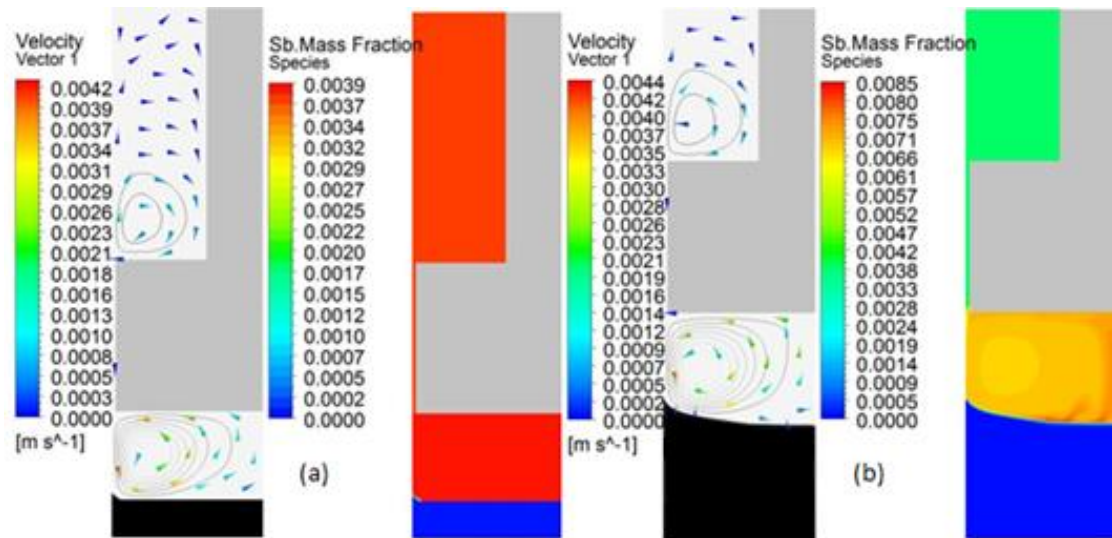


Figure 5.67. The solute distribution, velocity magnitude, and the interface shape for 600s (a) and 5400 s (b) for AHP10-10.

5.3.2.2. AHP10-10. The solute distribution, velocity magnitude, and the interface shape for 600s and 5400s after starting the solidification for the AHP10-10 case are shown in Figure 5.67.

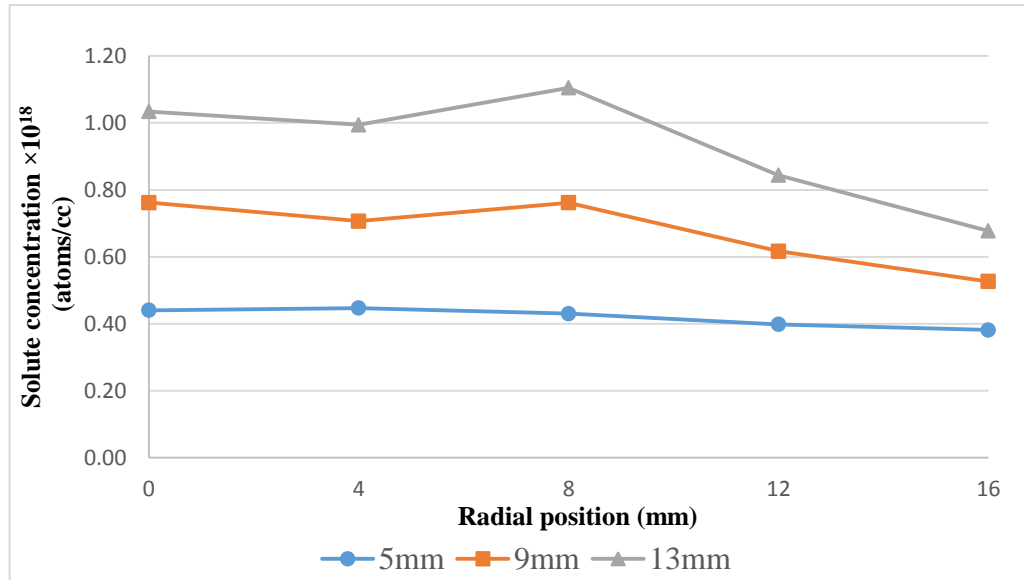


Figure 5.68. Radial solute distribution of AHP10-10.

The radial solute distribution is shown in Figure 5.68. Unlike in the VB20-58 that the solute is accumulated at the center, there is more homogeneous solute redistribution in the melt and the convective flow in the vicinity of the interface is more effective.

The axial solute distribution along the central axis (0mm), 4mm, 8mm, 12mm, 16mm, and 20mm (the crucible wall) are plotted in Figure 5.69 to Figure 5.74. Since up to 1200 seconds the solid is not formed yet above the 5mm pure solid seed at the center, the solute redistribution is not available for this region up to this time. The thickness of the solute boundary layer at the center is considerably less than that in the VB20-58. Again, the thickness of the solute boundary layer is vanishing from the center of the crystal toward the side.

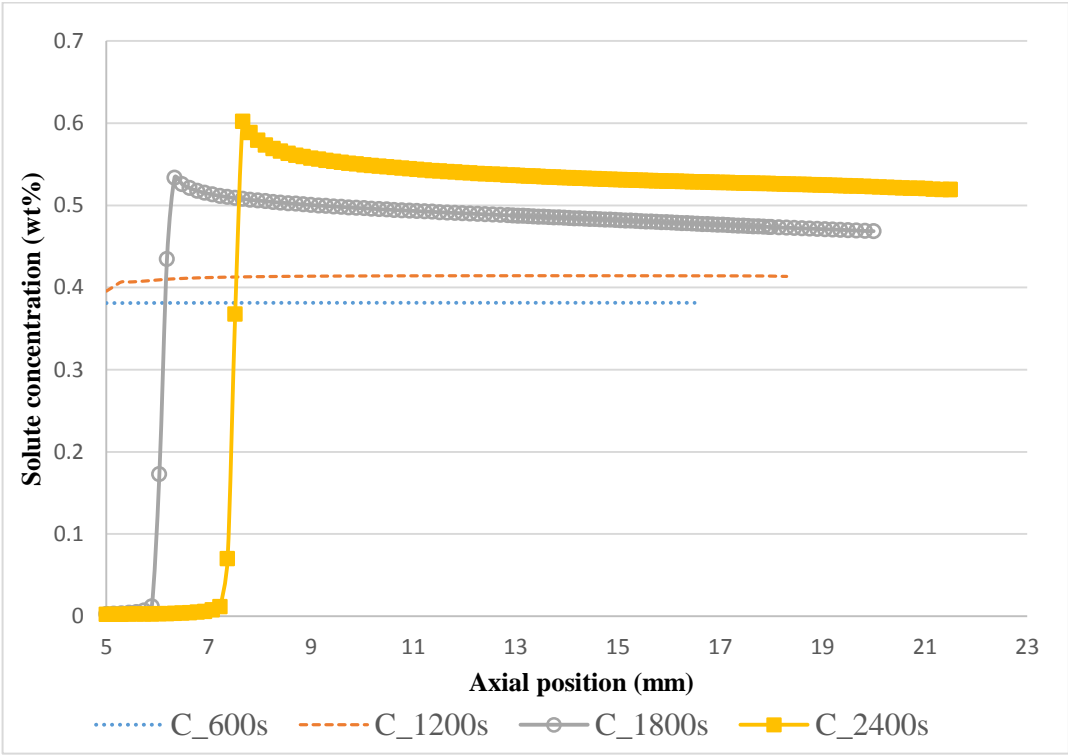


Figure 5.69. AHP10-10 Axial solute distribution at the center.

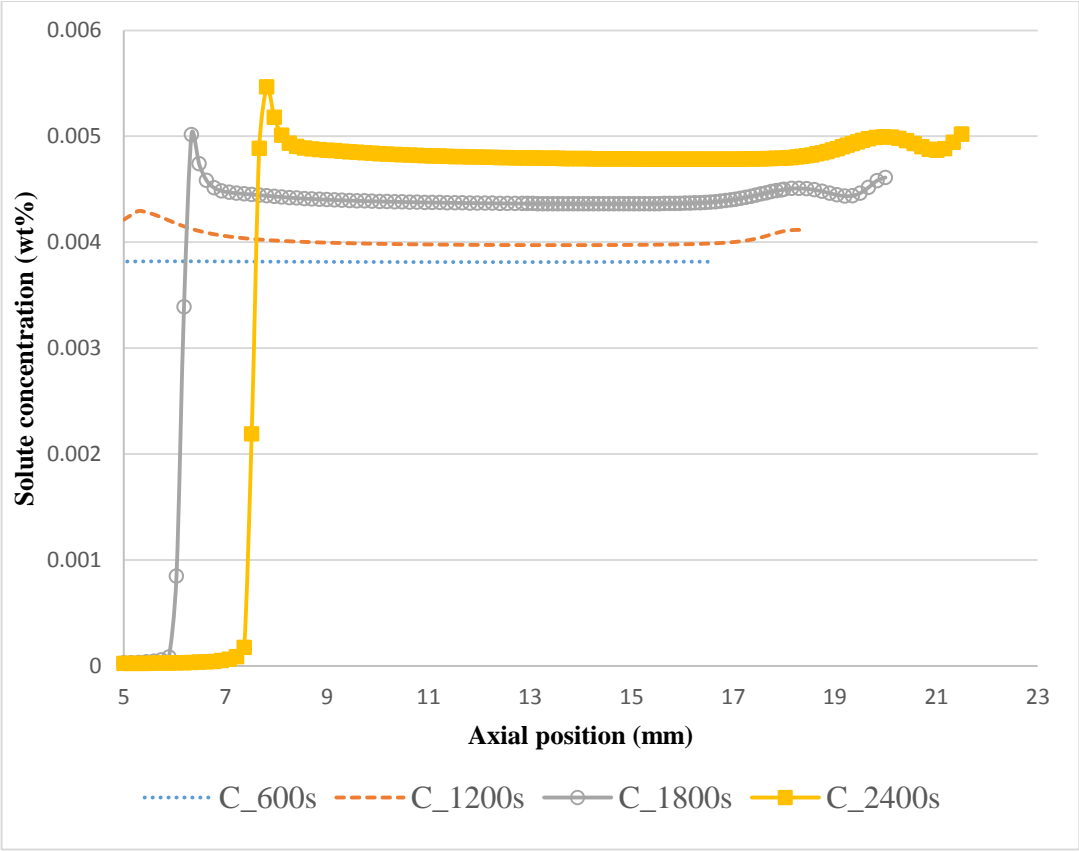


Figure 5.70. AHP10-10 Axial solute distribution at 4 mm from the center.



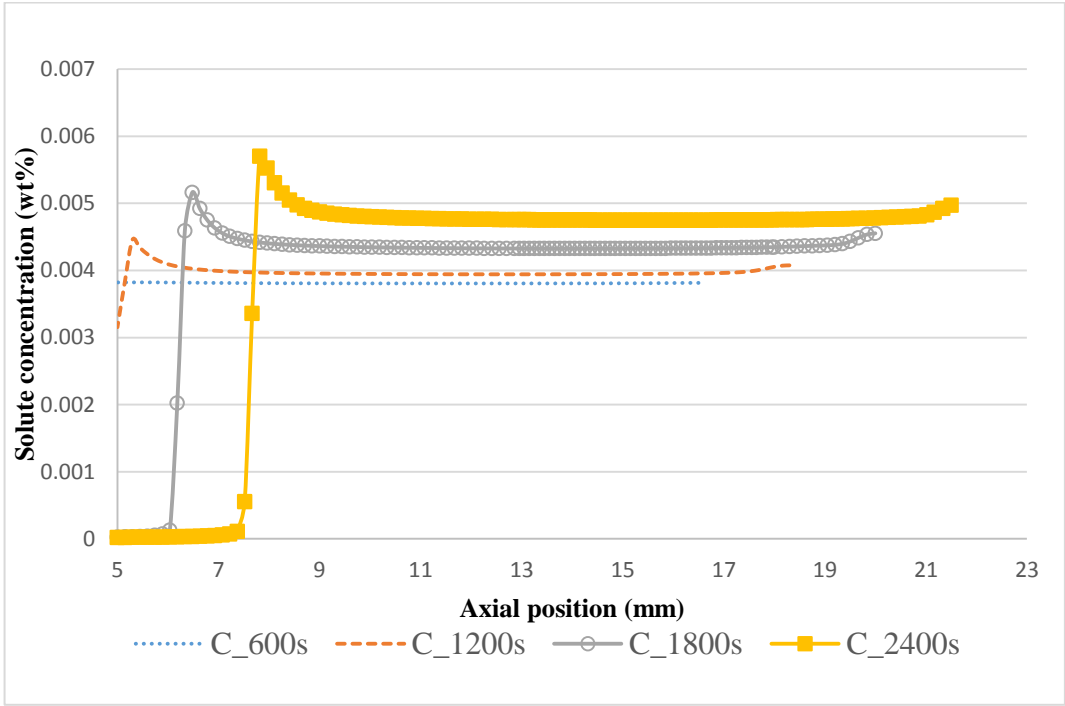


Figure 5.71. AHP10-10 Axial solute distribution at 8 mm from the center.

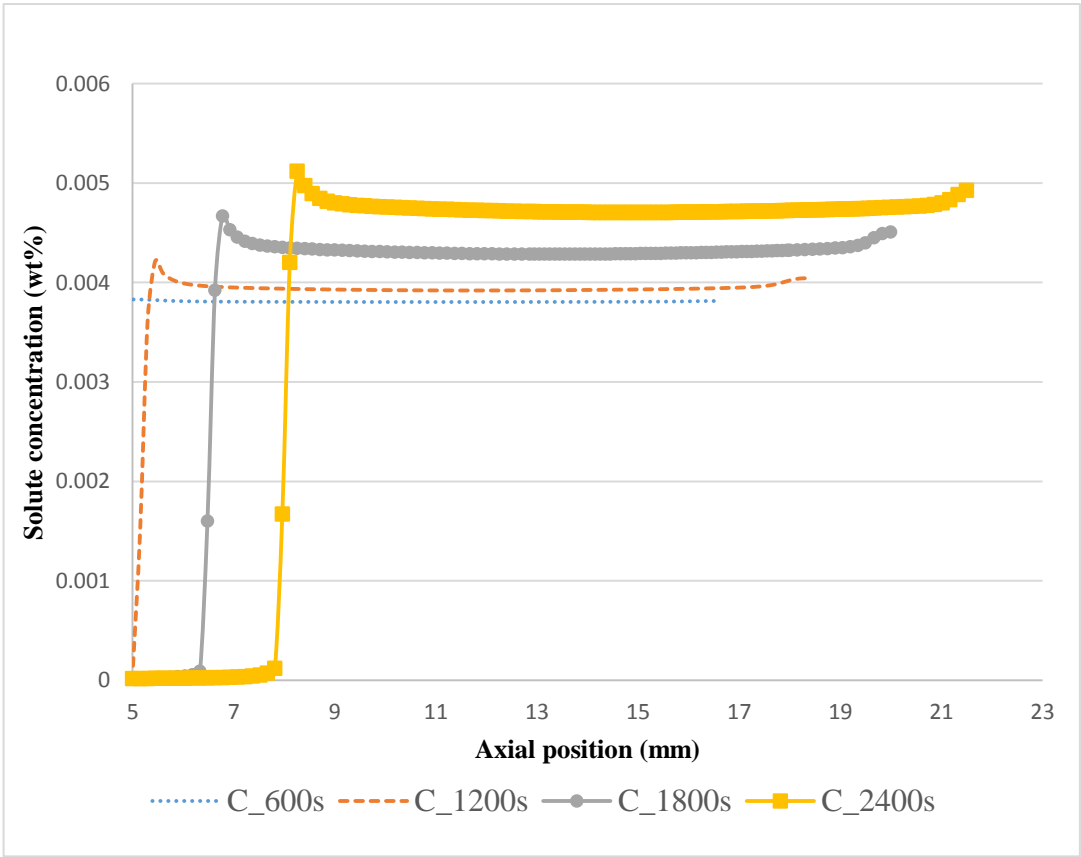


Figure 5.72. AHP10-10 Axial solute distribution at 12 mm from the center.

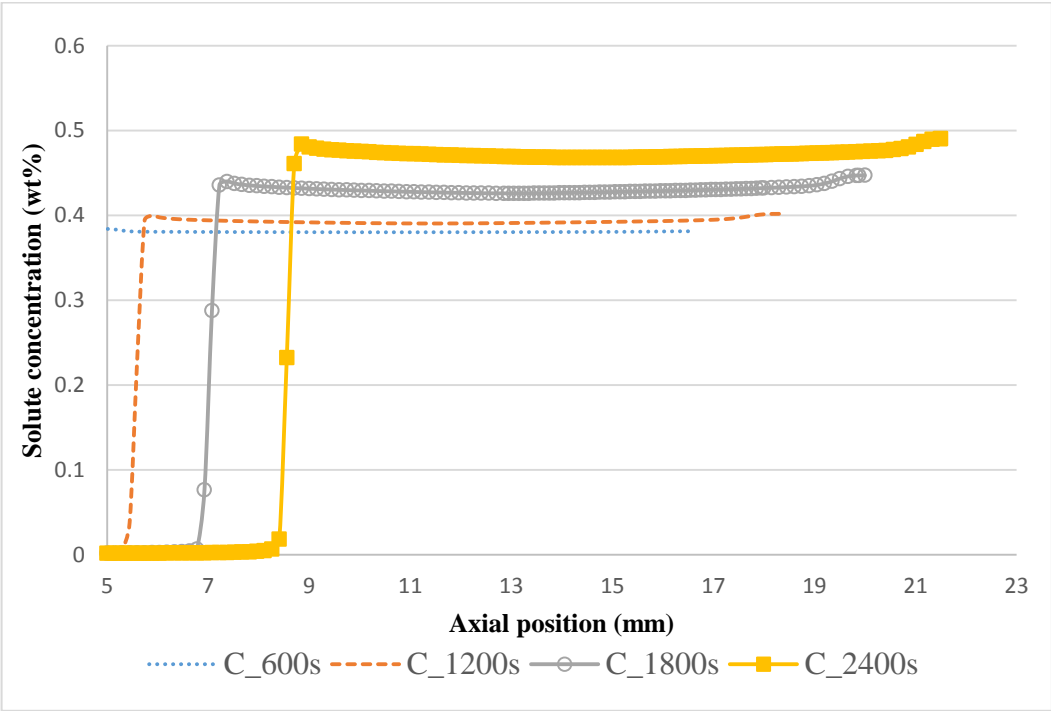


Figure 5.73. AHP10-10 Axial solute distribution at 16 mm from the center.

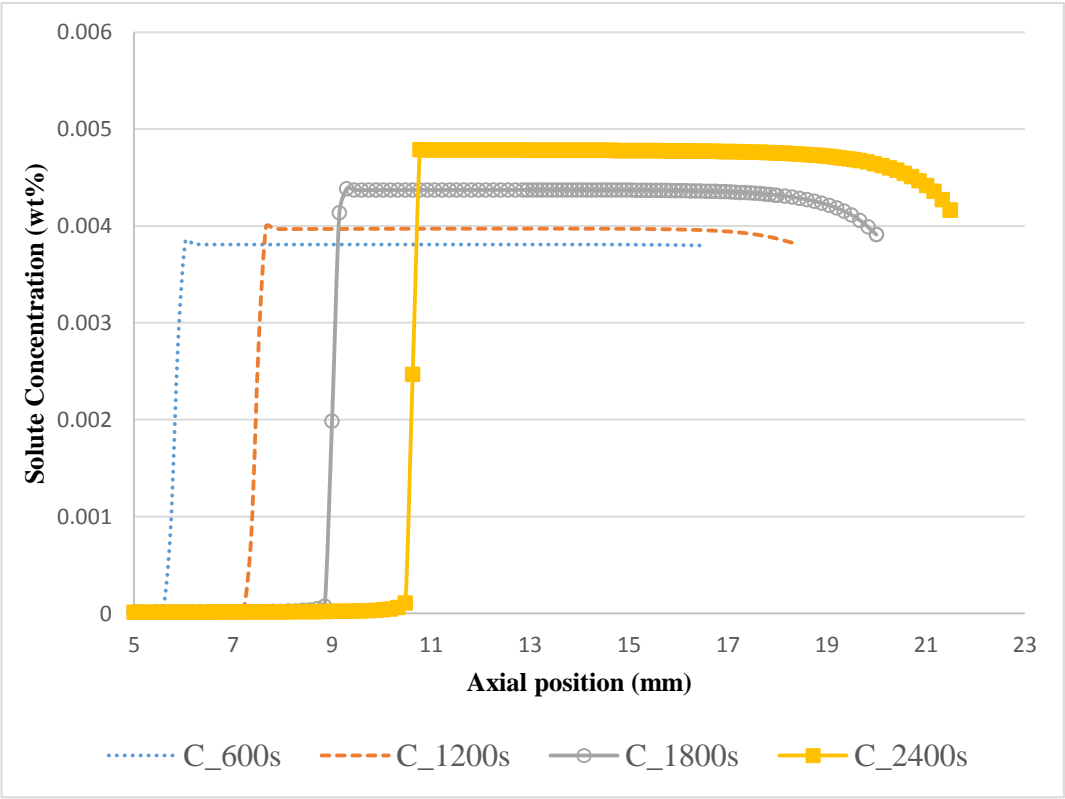


Figure 5.74. AHP10-10 Axial Solute Distribution along 20mm (wall).

5.3.2.2. AHP20-10. The solute distribution, velocity magnitude, and the interface shape for 600s and 2400s after starting the solidification for the AHP20-10 case are shown in Figure 5.75.

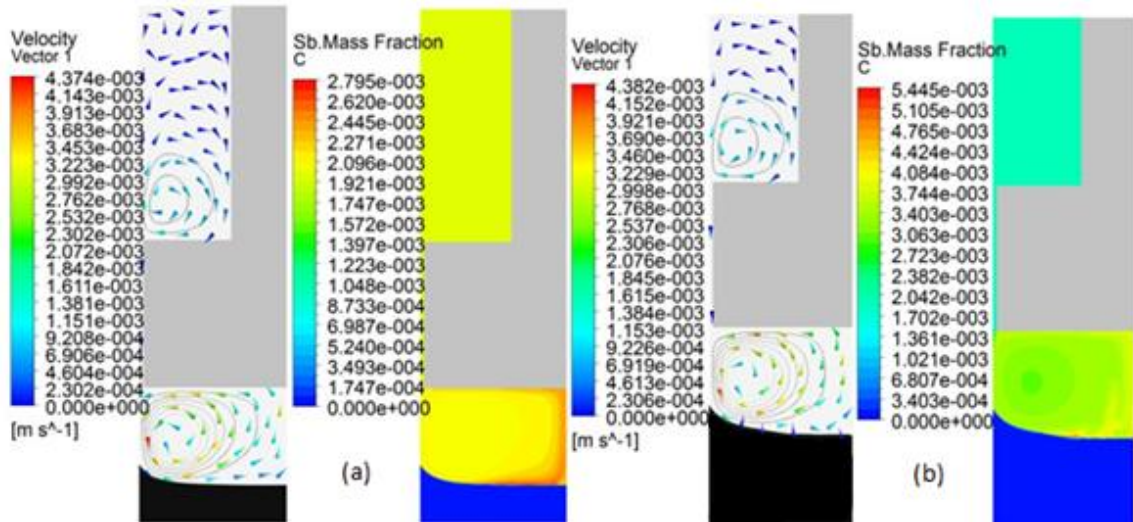


Figure 5.75. The solute distribution, velocity magnitude, and the interface shape for 600s(a) and 2400 s(b) for AHP20-10.

The radial solute distribution is shown in Figure 5.76. This figure shows that the solute has not been distributed homogeneously within the melt and the solute content is higher at the center.

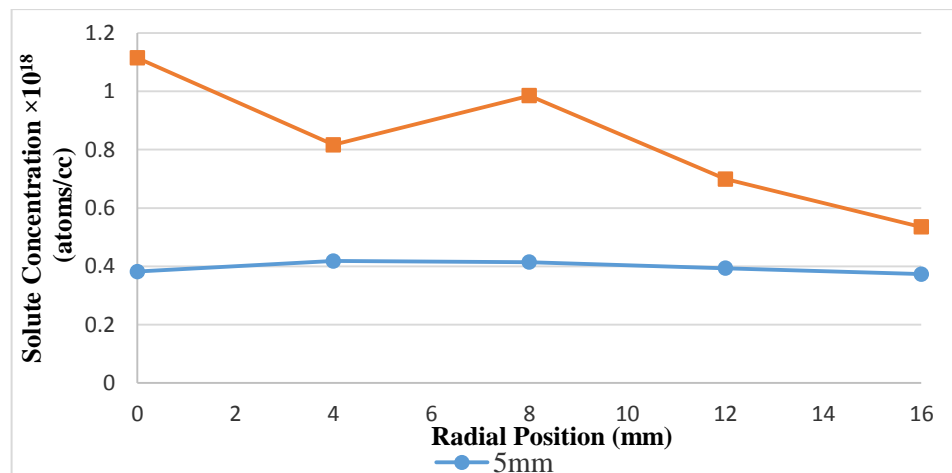


Figure 5.76. Radial solute distribution of AHP20-10.

The axial solute distribution along the central axis (0mm), 4mm, 8mm, 12mm, 16mm, and 20mm (the crucible wall) are plotted in Figure 5.77 to Figure 5.82. Comparing to AHP10-10, the solute boundary layer at the center is increased considerably.

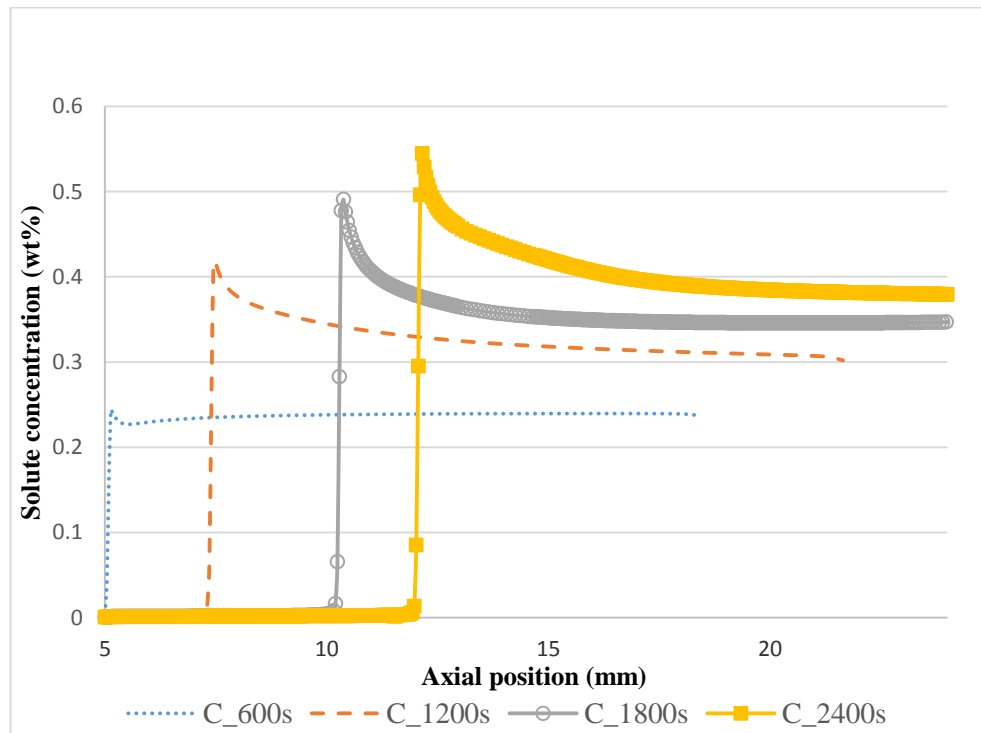


Figure 5.77. AHP20-10 Axial Solute Distribution along 0mm axis (center).

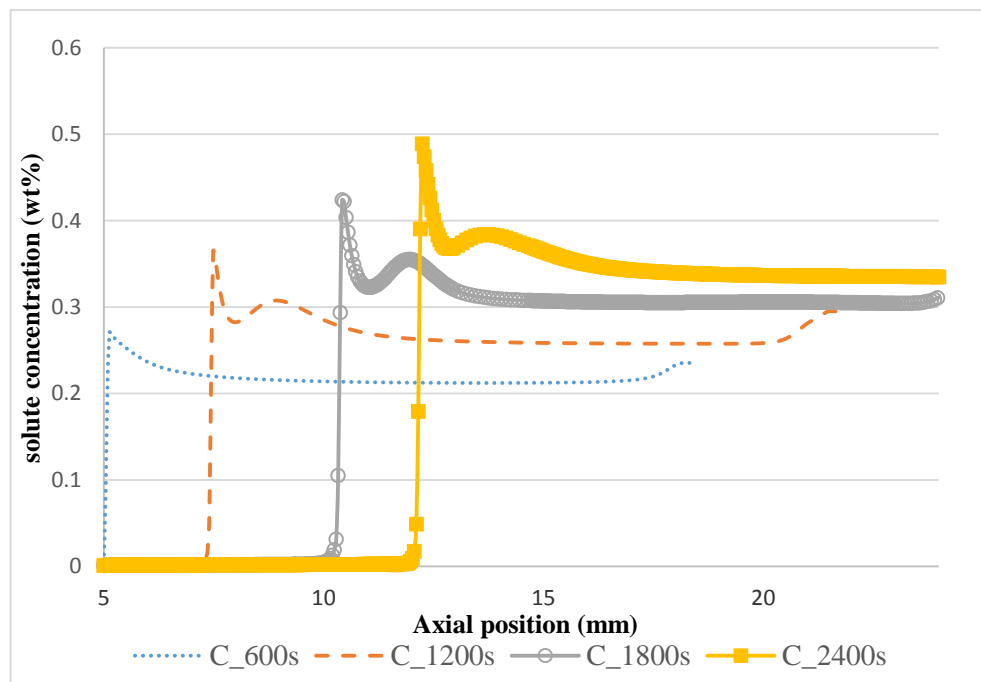


Figure 5.78. AHP20-10 Axial Solute Distribution along 4mm Axis.

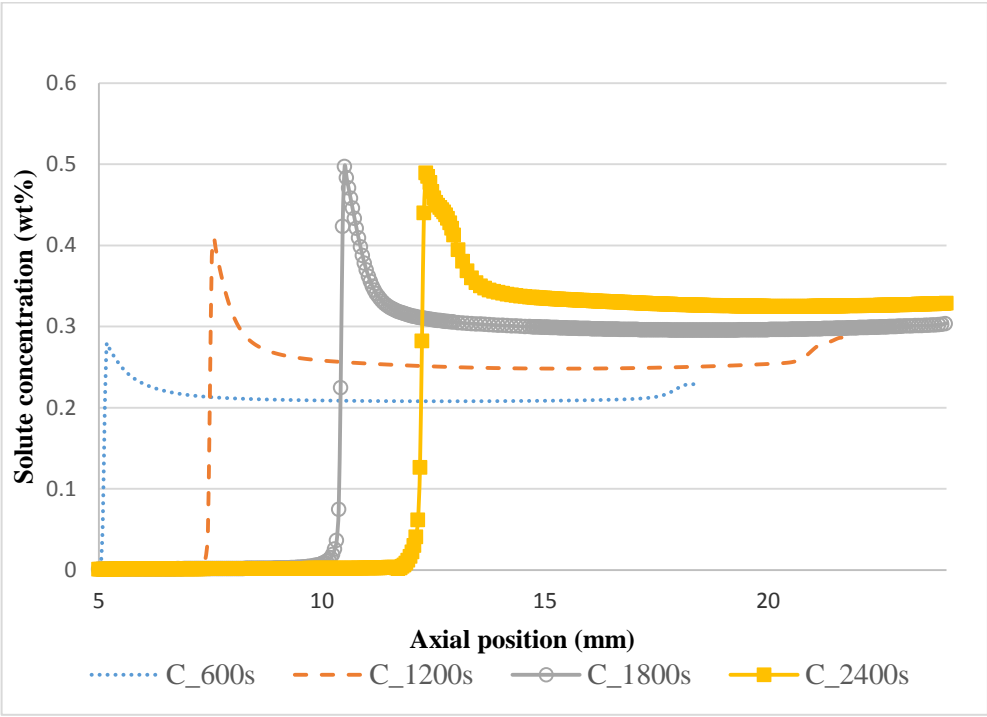


Figure 5.79. AHP20-10 Axial Solute Distribution along 8mm Axis.

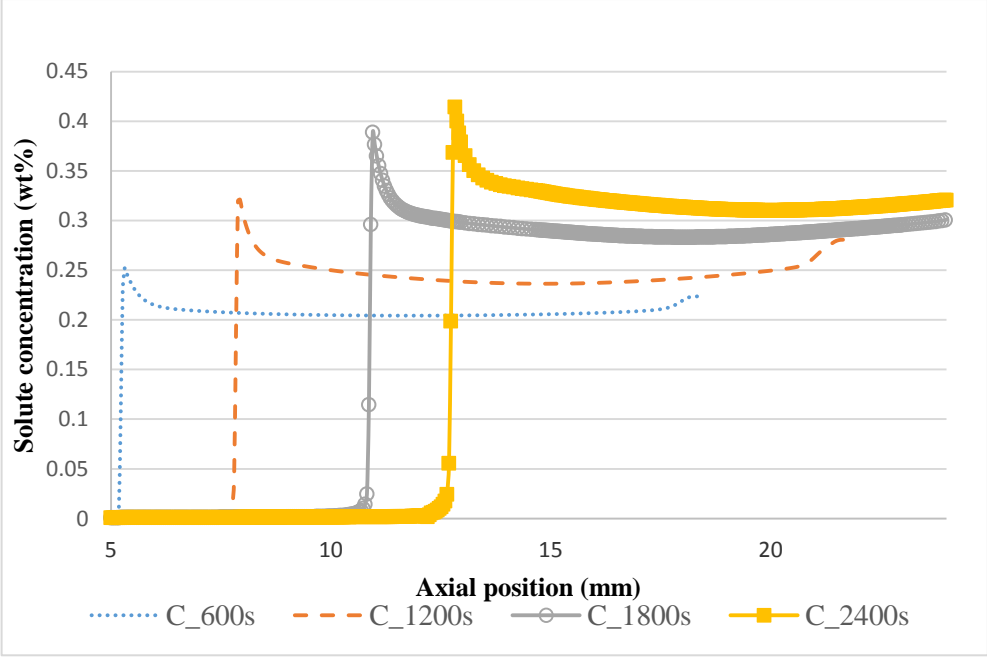


Figure 5.80. AHP20-10 Axial Solute Distribution along 12mm Axis.

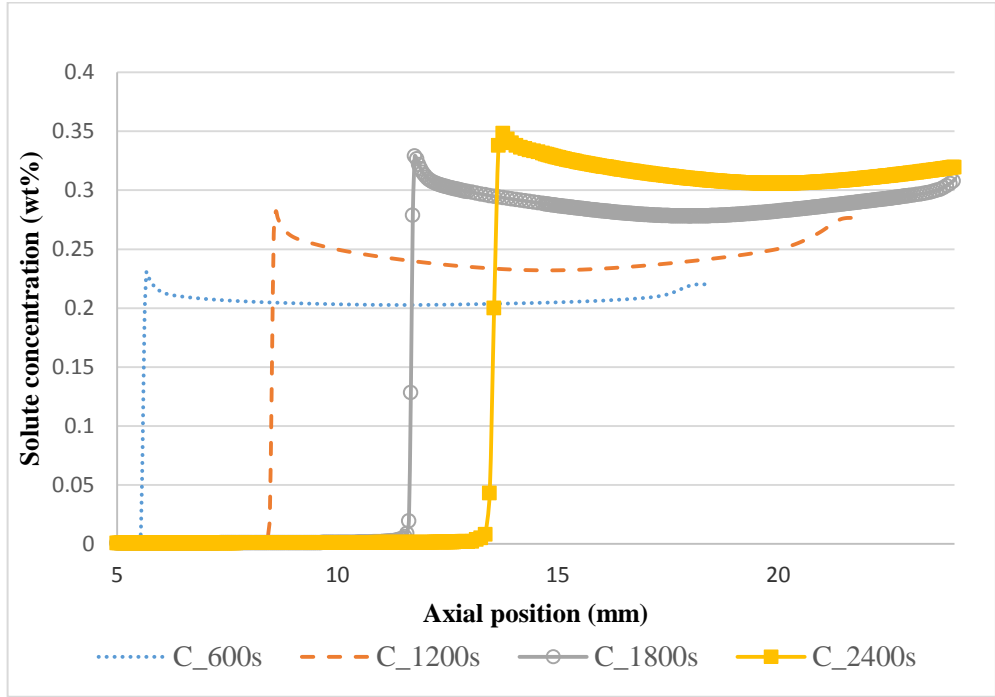


Figure 5.81. AHP20-10 Axial Solute Distribution along 16mm Axis.

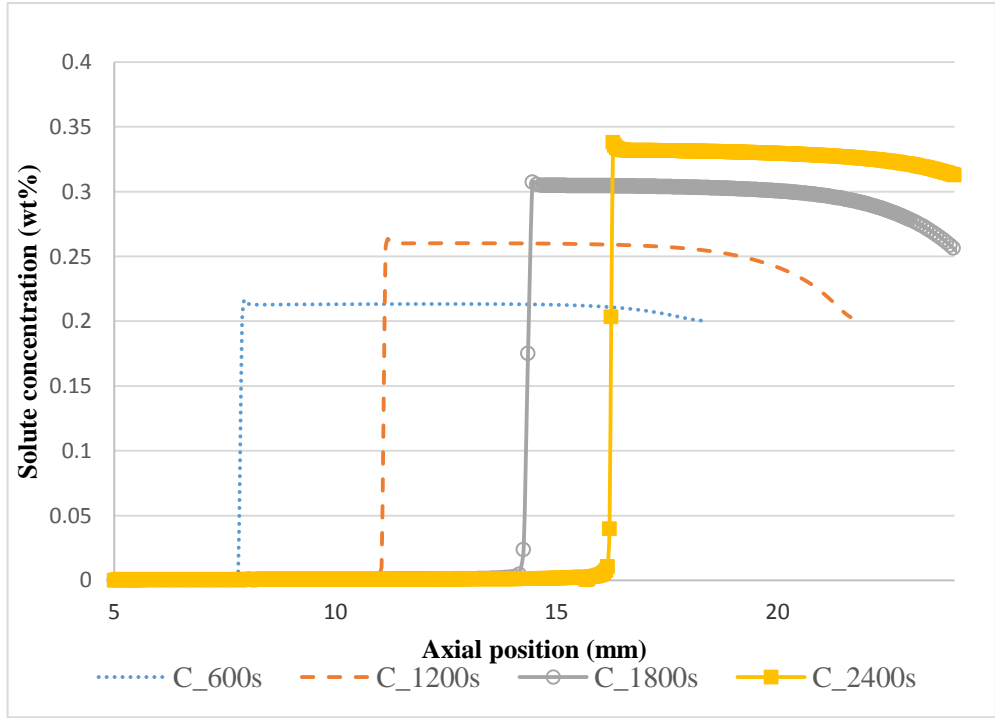


Figure 5.82. AHP20-10 Axial Solute Distribution along 20mm Axis (Wall).

## 6. DISCUSSION

### 6.1. Melt height

By comparing the experimentally grown crystals, it is shown that the reduction of the melt height above the s/l interface via inserting the baffle significantly enhances the total single crystal length and postpones morphological stabilities (see Figure 6.1). The effective melt height in the VB20-58 sample is the highest and the breakdown of the interface occurs earliest in the VB20-58 crystal compared to the other crystals grown in this study. When the melt height is reduced to 14 mm (AHP20-14) the single crystal length increases to 30.6 mm. A further reduction of the melt height to 5 mm (AHP20-5) increases the single crystal length to 35 mm. A similar trend is seen for the AVC crystals. Also, the radial solute segregation is less in the crystals grown with the lower initial melt heights (compare Figure 5.2, Figure 5.6, Figure 5.10, Figure 5.14, Figure 5.18, Figure 5.22, and Figure 5.26). Therefore, reducing the melt height has a positive effect on reducing the radial solute segregation and increasing the stability of the interface and consequently the total single crystal length. Thus, it is important to keep the melt height low during the growth.

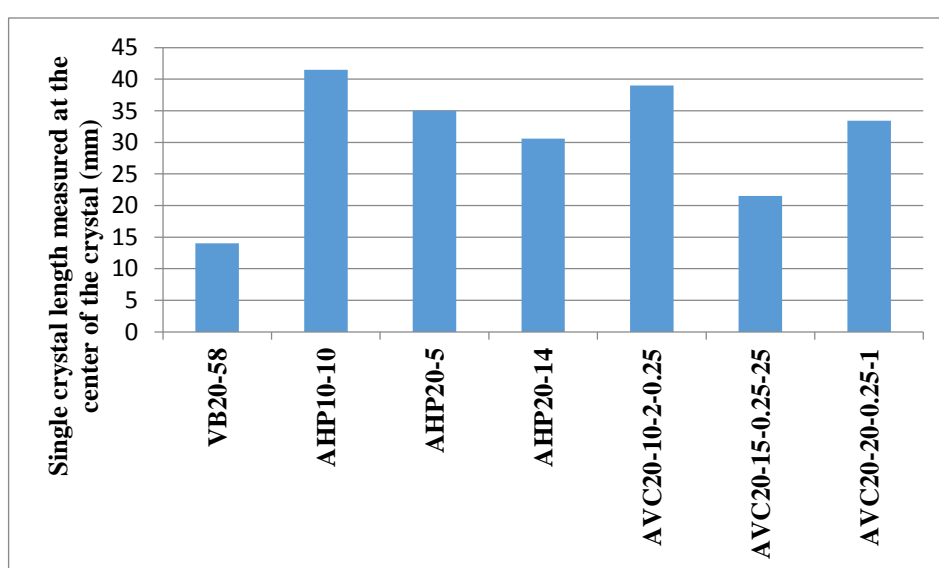


Figure 6.1. The single crystal length in the grown crystals.

The variation of the melt height during the growth, obtained from the experiments by using analytical formulations, is shown in Figure 6.2. Also, Figure 6.3 shows the melt height at different axial height of the crystal in different methods. This figure is constructed using data in Figure 6.2. In Figure 6.4, which is also constructed from Figure 6.2, the rate of change of the melt height for the first 10 mm height and from 10 mm height to the end are shown. Moreover, simulation results for the melt height variation are shown in Figure 6.5. The rate of change of the melt height is also shown in Figure 6.6. Although the analytical and numerical values do not match exactly, both results show a similar trend. Both show that there is an increase in the melt height during the growth. As it is shown in both figures, the change of the melt height is sharp in the beginning and declines as the crystals lengthen (see Figure 6.4). However, it is observed that for the first 10 mm, the rate of change of the melt height is significantly less in the crystal grown with 10 mm/h than the crystals grown with 20 mm/h. This could be due to a greater amount of the liberated heat of solidification at the interface and bringing more of the hotter liquid from above the baffle to below it with the high crucible pulling velocity. In order to avoid further increase of the melt height during the growth, the growth rate of the interface should not be deviated too much from the pulling rate. As it is shown in Figure 6.7, there is a greater deviation of the interface growth rate from the pulling velocity in crystals grown with 20 mm/h rather than those grown with 10 mm/h, especially at the first stages of the growth. However, as it is observed in Figure 6.4 and Figure 6.6, in the crystals grown with 20 mm/h the rate of change of melt height is decreased by decreasing the initial melt height. Moreover, Figure 6.5 shows lower melt height values in AVC20-10-2-0.25 comparing to AHP20-10 with the same pulling rate and initial melt height. Also, Figure 6.7 shows that vibration of the baffle is effective in stabilizing the growth rate of the interface and minimizing the deviation between growth velocity and the pulling rate. This implies the success of the AVC method in controlling the variation in the melt height during the growth (which is also observed in Figure 6.2) and the less change in the melt height in AVC20-10-2-0.25 rather than AHP20-10 (Figure 6.5) which leads to more stable interface during the growth.



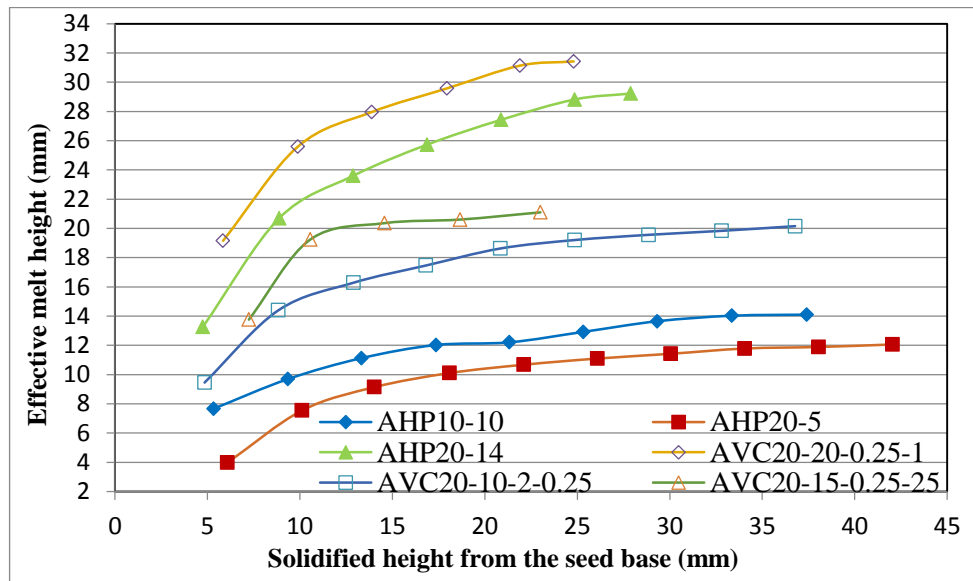


Figure 6.2. Variation of the effective melt height during the solidification process, experimental data.

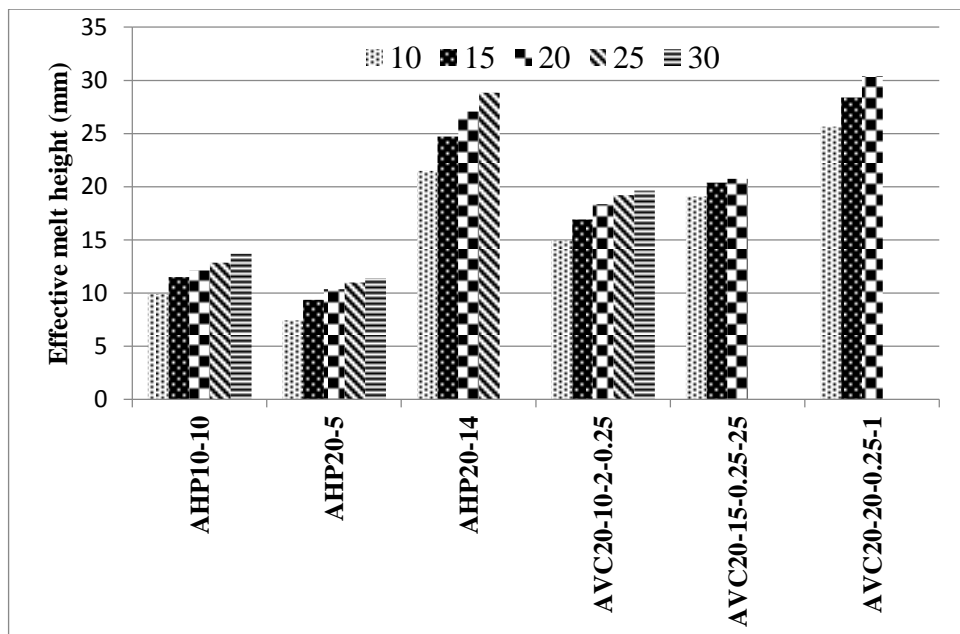


Figure 6.3. Comparison of the melt height at different axial heights of the crystals.

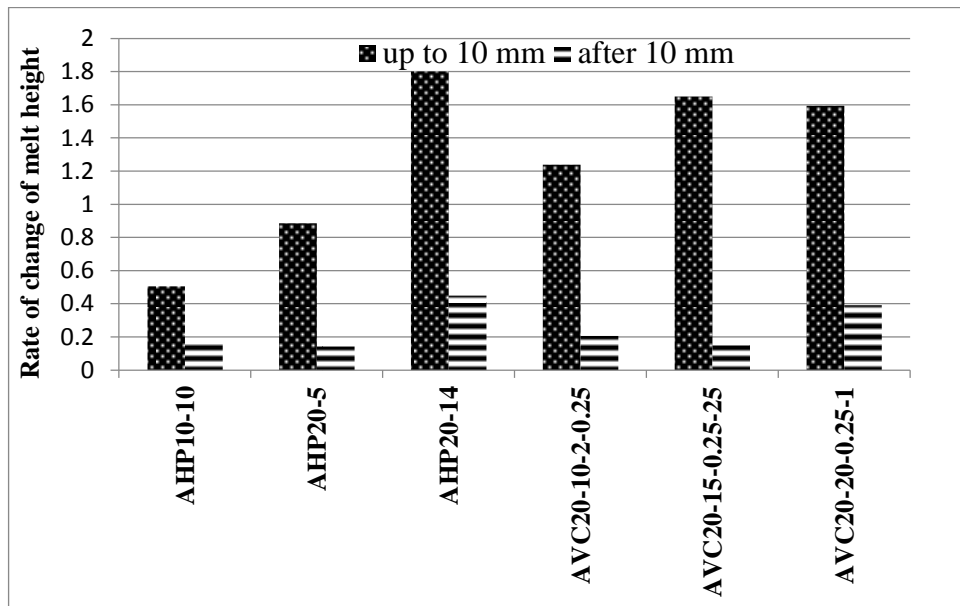


Figure 6.4. Rate of change of the melt height.

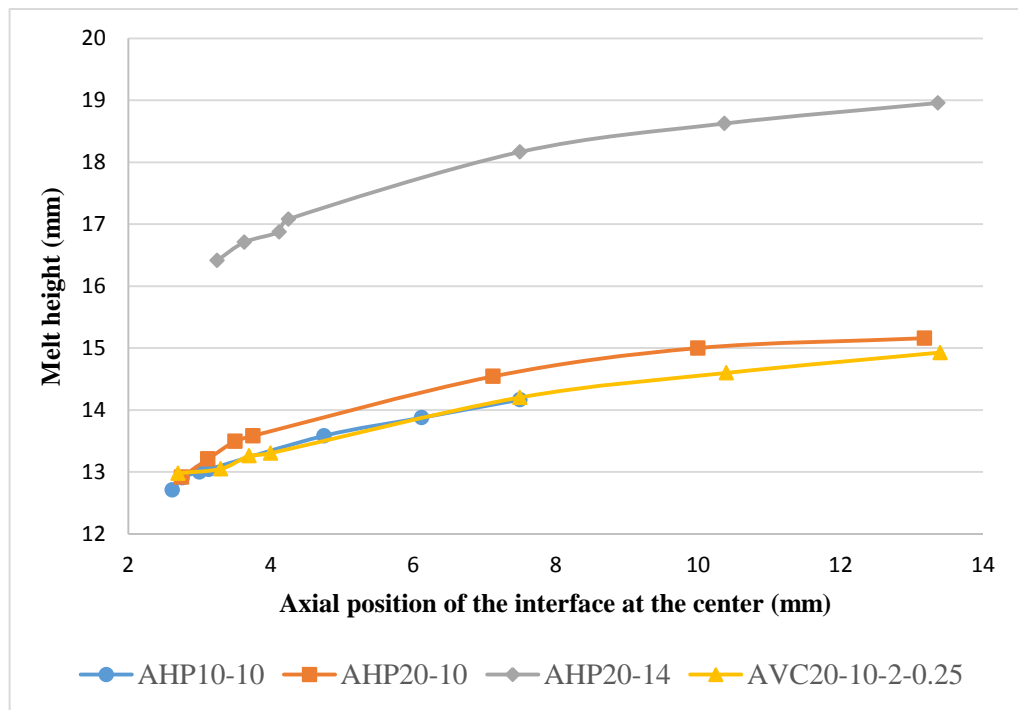


Figure 6.5. Local geometry simulation results for the melt height variation in AHP10-10, AHP20-10, AHP20-14, and AVC20-10-2-0.25.

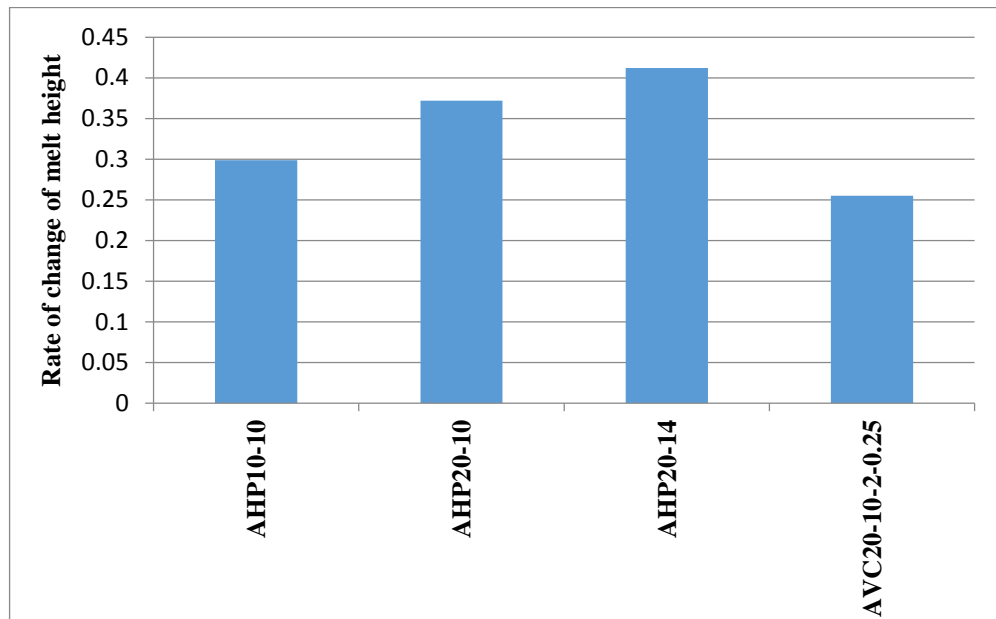


Figure 6.6. Rate of change of the melt height up to first 10 mm axial position according to the simulation results in Figure 6.5.

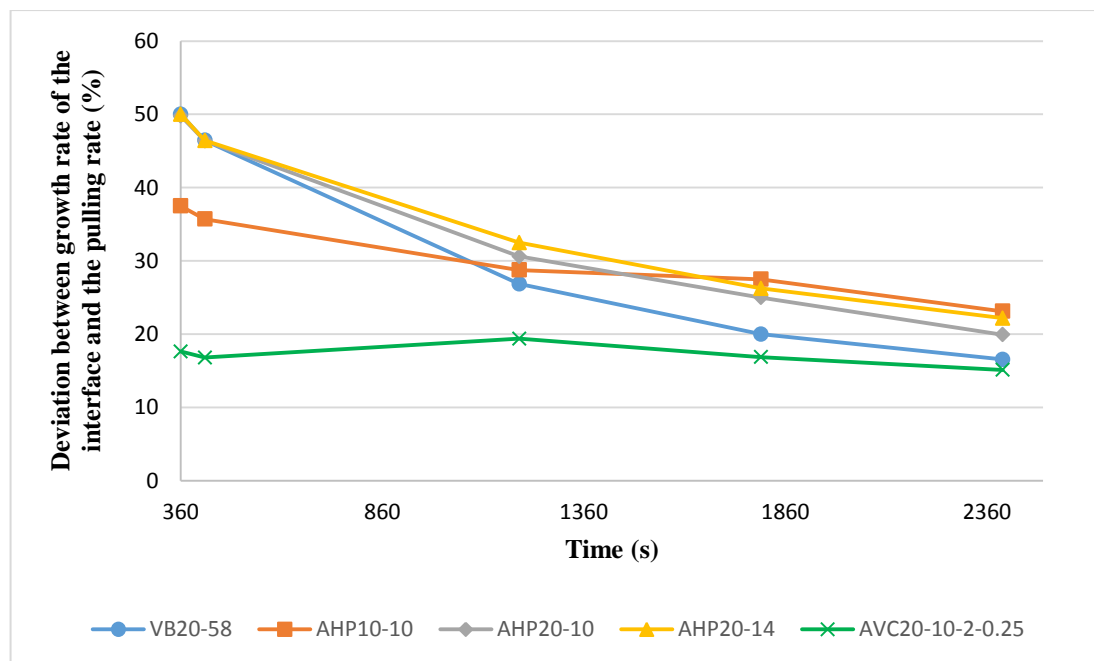


Figure 6.7. Simulation results for deviation between the pulling rate and the interface growth rate at the center radial position in the local geometry of VB20-58, AHP10-10, AHP20-10, AHP20-14, and AVC20-10-2-0.25.

## 6.2. Radial temperature gradient

It is believed that the insertion of the baffle is effective in reducing the radial temperature gradient close to the interface because of the high thermal conductivity of the baffle [16, 18]. However, Figure 6.8, which shows the simulated radial temperature gradient at different axial positions, demonstrates that except for AHP10-10, which has the lowest pulling rate, the radial temperature gradient is increased by inserting the baffle. Though, for the AHP method, decreasing the melt height leads to decrease in radial temperature gradient. However, the main advantage of the insertion of the baffle in the AHP method and its preference over the VB method is that it homogenizes the solute redistribution and avoids solute accumulation at the center which eventually postpones cellular formation and instability of the interface. On the other hand, reducing the pulling rate provides enough time for homogeneous distribution of the temperature, so for the same initial melt height the radial temperature gradient is less in AHP10-10 than that in AHP20-10. In order to overcome the problem of increasing radial temperature gradient due to insertion of the baffle, the melt should be gently mixed with low frequency vibration of the baffle in order to homogenize temperature distribution ahead of the interface. Figure 6.8 shows that the radial temperature gradient is successfully reduced in AVC20-10-2-0.25 at the central region. Note that since the temperature decrease is sharper at the sides, the radial temperature gradient is calculated according to the temperature difference between 0 mm and 15 mm radial positions. Moreover, for the AVC20-10-2-0.25, the radial distribution of the temperature is not continuous in radial direction due to vibration of the baffle. Therefore, three different zones (0-5 mm, 5-10 mm, and 10-15 mm) are considered for calculating the radial temperature gradient.

## 6.3. Convective flow

It is pointed out that the stability of the interface and the homogeneity of the solute redistribution are increased in the crystals grown with a lower melt height. The reason is the effect of the baffle insertion on changing the nature of the flow in the melt close to the interface. The flow behavior in the melt above the s/l interface is very influential in the

solute redistribution and in the single crystal length of a grown crystal. The melt may experience mixing due to a buoyancy-driven convection, which may arise from temperature and solute gradient inside the melt. A stabilizing, positive axial temperature gradient is applied during the growth of the crystals. In addition, since the density of the solute (Sb) is higher than the solvent (Ge) in the Sb-doped Ge crystals, the solute does not float. Thus, the system is thermally and solutally stable. Then, the convection in the melt should arise from the radial temperature gradient [142].

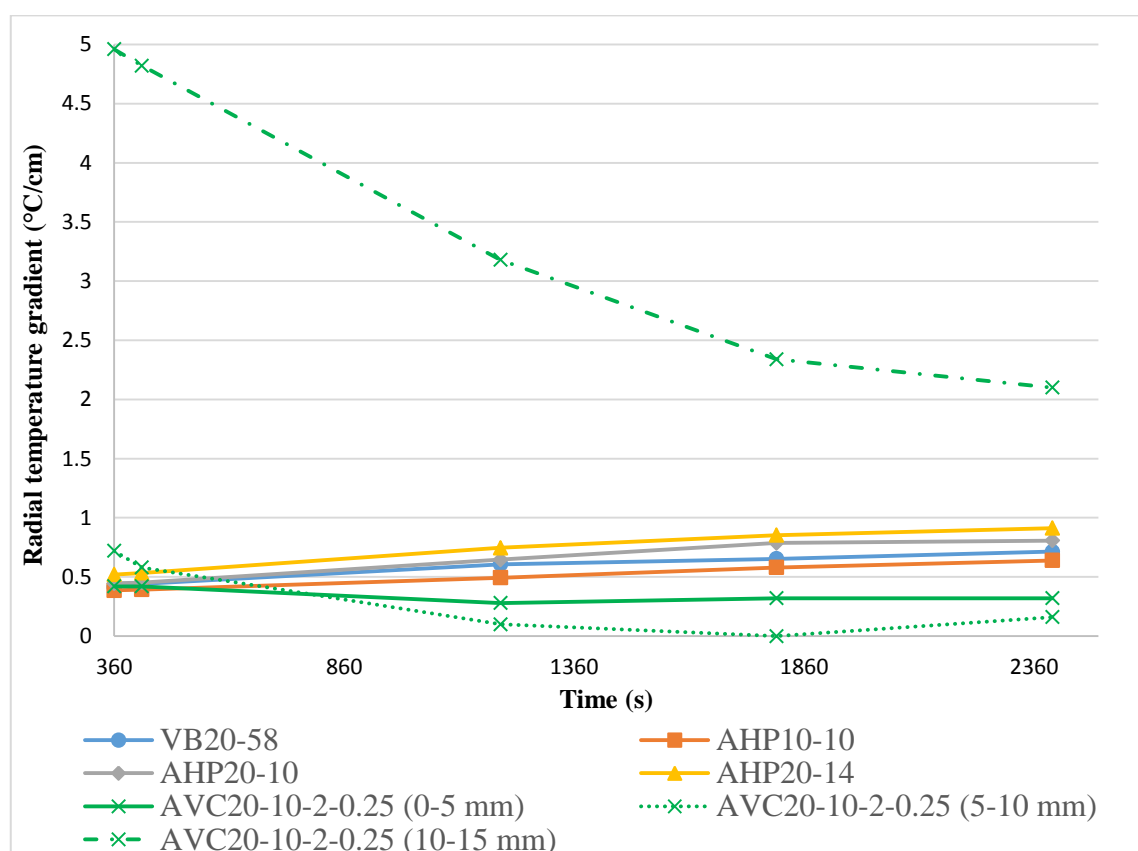


Figure 6.8. Simulation results for radial temperature gradients in the local geometry of VB20-58, AHP10-10, AHP20-10, AHP20-14, and AVC20-10-2-0.25.

This natural convection (VB case) is only concentrated at the sides near the crucible wall and does not mix the melt at the central regions. However, by inserting the baffle a forced flow due to relative motion between the baffle and the crucible is created in the melt. This forced flow makes the motion of the fluid toward the center axis and along the s/l interface more effectively and consequently provides better mixing in the melt at the

center. The suppression of the natural convection by this forced flow can be determined via Archimedes number (Ar) which is the ratio of the Grashof number to the square of Reynolds number.

$$Ar = \frac{\frac{g\beta\Delta TR^3}{\nu^2}}{\frac{V^2 R^2}{\nu^2}} = g\beta\Delta TR / V^2 \quad (6.1)$$

Where,  $R$  is the radius of the crucible and  $\Delta T$  is the radial temperature difference. If  $Ar$  becomes greater than unity, natural convection is dominant. Otherwise, if  $Ar$  becomes less than unity, natural convection is insignificant and the forced convection becomes dominant.  $Ar$  number for the maximum velocity magnitude at 2 mm above the interface at the center radial position for different times is shown in Figure 6.9.

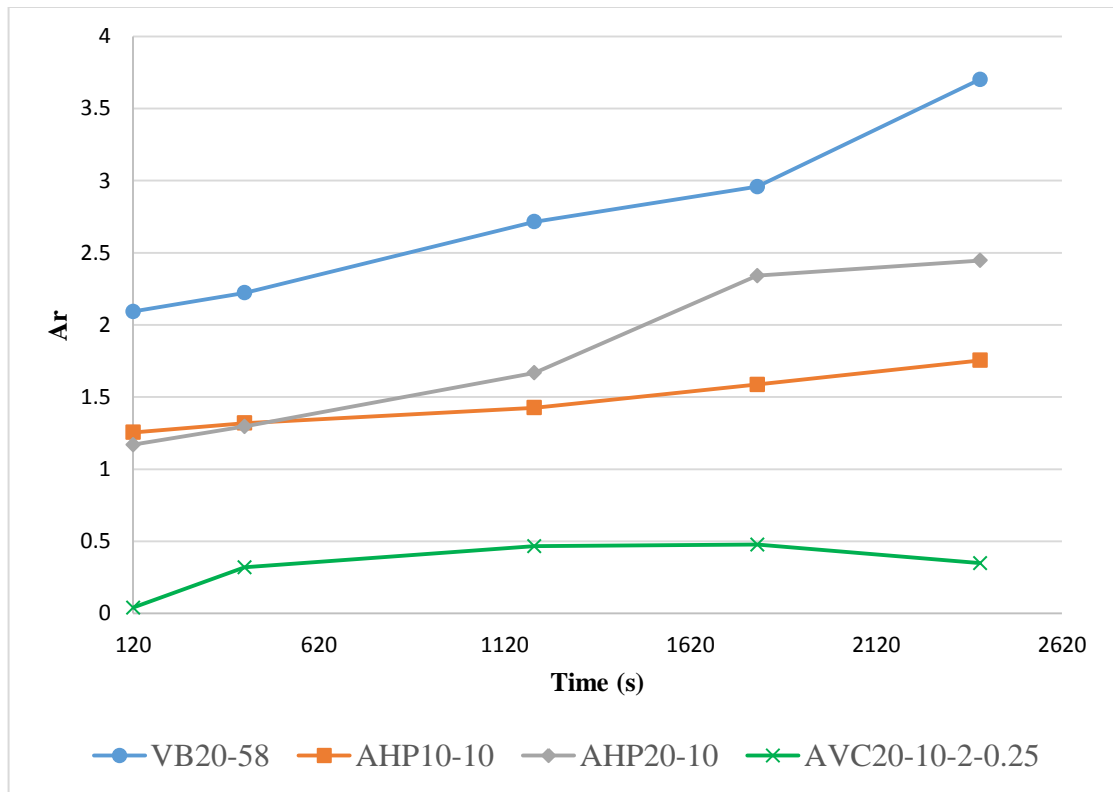


Figure 6.9. Archimedes number in different times.

Figure 6.9 shows that only in the AVC20-10-2-0.25 the Ar number falls below the unity, so the forced flow through the gap between the baffle and the crucible is not effective in suppressing the natural convection. However, decreasing the melt height in the AHP method leads to increased velocity magnitude of the flow close to the interface. Figure 6.10 shows the velocity magnitude along the horizontal line 2 mm above the interface position at the center after 2400 seconds for different crystals. It is shown that inserting the baffle increases the maximum velocity magnitude in the melt in AHP10-10 and AHP20-10. Also, the velocity magnitude is increased at the central region close to the axis. However, in AHP20-14 the velocity magnitude is reduced. This is due to the lowest axial temperature gradient of the furnace for this sample (Table 5.1). In addition, by increasing the distance from the baffle to the interface, the forced flow through the gap between the baffle and the crucible loses its effectiveness close to the interface. Moreover, Figure 6.10 shows that axial vibration of the baffle in AVC20-10-2-0.25 increases the velocity magnitude considerably. While the velocity magnitude in the annular gap between the baffle and the crucible wall is  $7.69 \times 10^{-2}$  m/s in AVC20-10-2-0.25, it is  $1.25 \times 10^{-4}$  m/s in the AHP20-10 and AHP20-14 and  $6.5 \times 10^{-5}$  m/s in AHP10-10. This increase in the velocity magnitude is not only restricted to the side close to the crucible wall, but the velocity magnitude is also increased at the central region in AVC20-10-2-0.25 as seen in the inset in Figure 6.10. Therefore, more effective mixing is provided and the convective flow is able to sweep away the solute close to the interface at the center and avoid solute accumulation in this region. The homogeneous radial solute redistribution in AVC20-10-2-0.25 crystal shown in Figure 5.26 proves this outcome.

#### 6.4. Solute redistribution

The buoyancy driven thermal convection in the melt redistributes the rejected solute from the solidifying interface into the bulk fluid. However, as it is shown in Figure 5.43 and Figure 5.59, a convective flow pattern is developed only at the sides, which does not effectively mix the melt to redistribute the solute uniformly. As it is shown in Figure 5.3, while the axial solute redistribution for the VB20-58 crystal at the center is close to the diffusional mixing, the solute concentration values at the sides are in between the Scheil

and VB-DM curves. This shows diffusional mixing at the center and partial mixing at the sides due to creation of a convective cell at each side that do not disturb the center appreciably. Formation of longer solute boundary layer in front of the interface at the center (Figure 5.61 to Figure 5.66) is another proof for this conclusion. Figure 6.11 compares the numerical results for solute redistribution with the analytical formulations in VB20-50, AHP10-10, and AHP20-10. In this figure, “mix” stands for complete mixing and “Diff” stands for diffusional mixing regimes. As it is expected, it is shown that at the sides the axial solute redistribution is closer to the complete mixing. Also, it is shown that even at the center the redistribution pattern becomes close to the complete mixing by reducing the melt height from 58 mm to 10 mm. It is also shown in Figure 5.2 that the solute concentration in VB20-58 is progressively higher at the center as solidification continues.

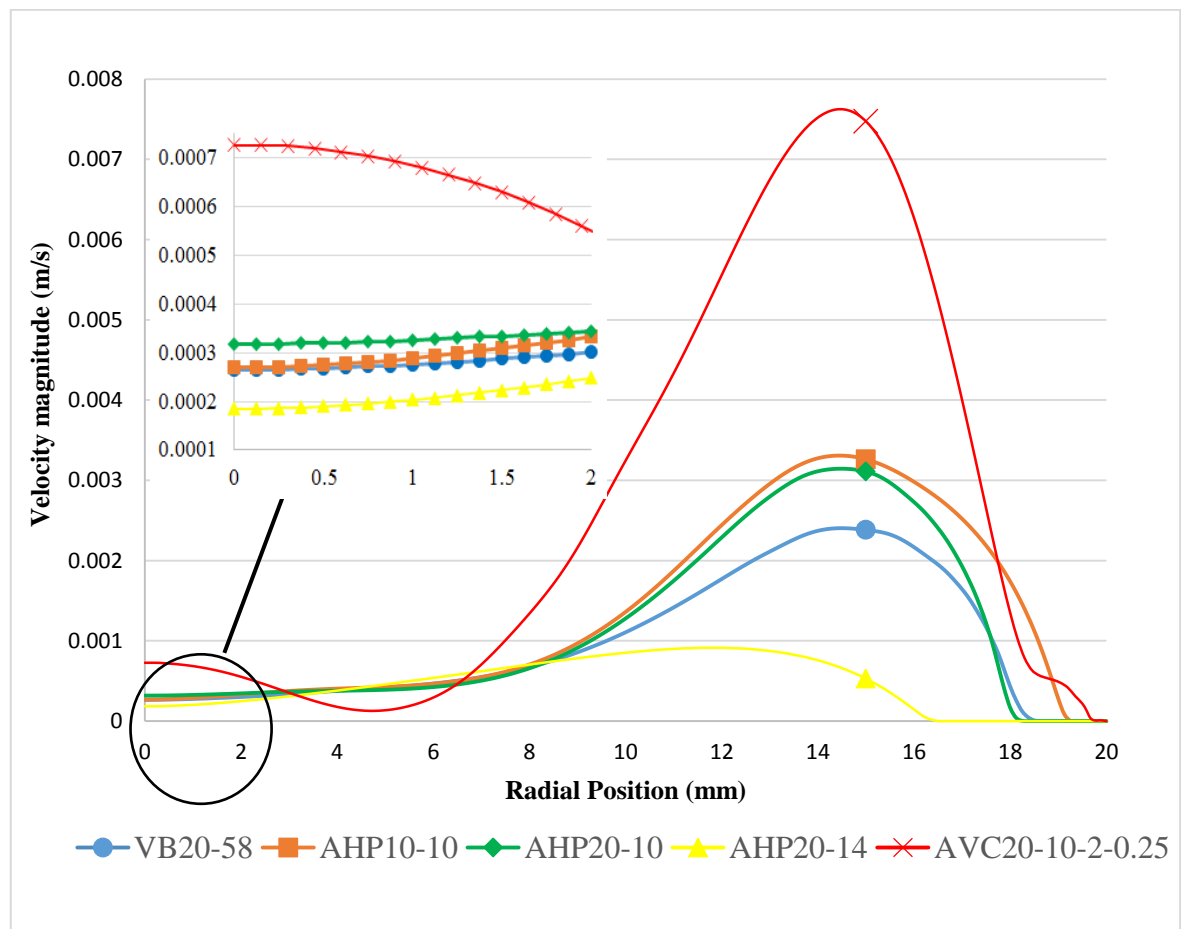


Figure 6.10. Velocity magnitude at 2400s for VB20-58, AHP10-10, AHP20-10, AHP20-14, and AVC20-10-2-0.25.



Due to a weak convection at the center, solute accumulates near the interface and the melt solidifies with a higher solute content, which leads to more radial solute segregation. In addition, by reducing the pulling rate to 10 mm/h and providing enough time for the convective flow to mix the melt properly, the redistribution pattern becomes closer to the complete mixing even at the center (Figure 6.11).

As it is mentioned earlier in section 5.1.2 and according to Equations 2.16, 2.17, and 2.19, by reducing the effective bulk melt volume below the baffle the crystal solidifies with a higher solute content. It is observed that in AHP20-5, which has the lowest melt height, the solute content is higher rather than other AHP-grown crystals at the same axial positions; compare AHP20-5 and AHP20-14 in Figure 5.14 and Figure 5.10 showing the radial solute redistribution. Actually, this argument is visibly substantiated by Figure 6.12 that plots the average solute concentration through the radial direction in each axial position for the AHP crystals [94]. The concentration is clearly higher in AHP20-5 than in AHP20-14.

This phenomenon is also observed in the numerical simulation results in Figure 6.13 that compares the average solute concentration between VB20-58 and AHP20-10. The amount of solute content is higher in the AHP20-10 in which the melt height is reduced by the baffle. Furthermore, solute incorporation in the solid normally becomes greater with increased solidification velocity. A similar outcome is seen in the radial segregation plots of these samples in Figure 6.14. This outcome is not observed for the other crystals (VB or AVC) probably because of a more rigorous melt flow in them. Also, the average radial solute segregation plots along the crystals given in Figure 6.15 show that the radial solute segregation is less in the crystals grown with a lower melt height, and the value of the segregation remains almost the same along the crystal. The same trend is observed for the segregation values of AVC20-10-2-0.25 crystal. This shows that both reducing the melt height and creating appropriate forced convection in the melt by axial vibration of the baffle promote convectional mixing in the melt and provide both radial and axial homogeneity in the grown crystals.

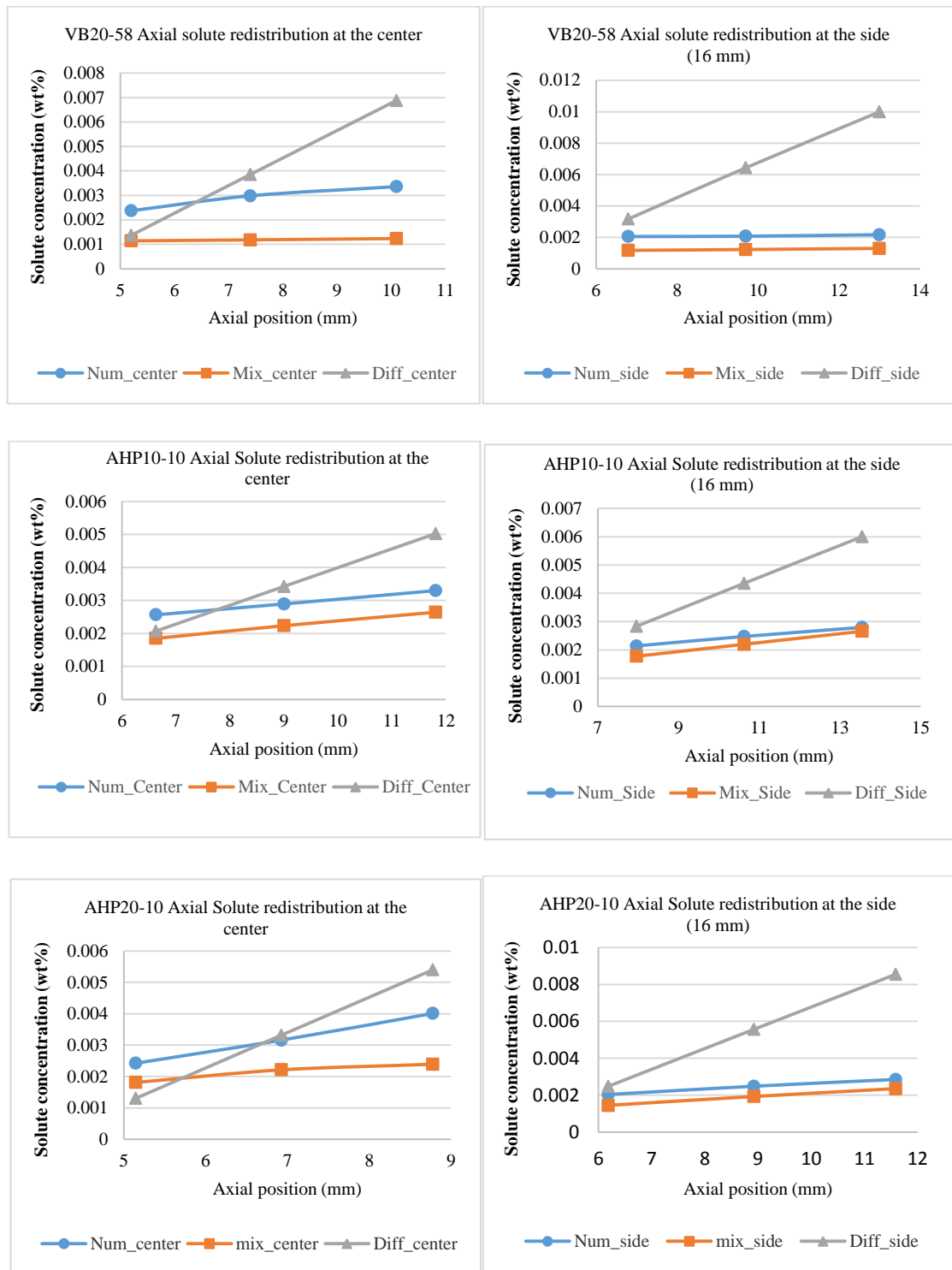


Figure 6.11. Axial solute redistribution at the center and at the side in VB20-58, AHP10-10, and AHP20-10.

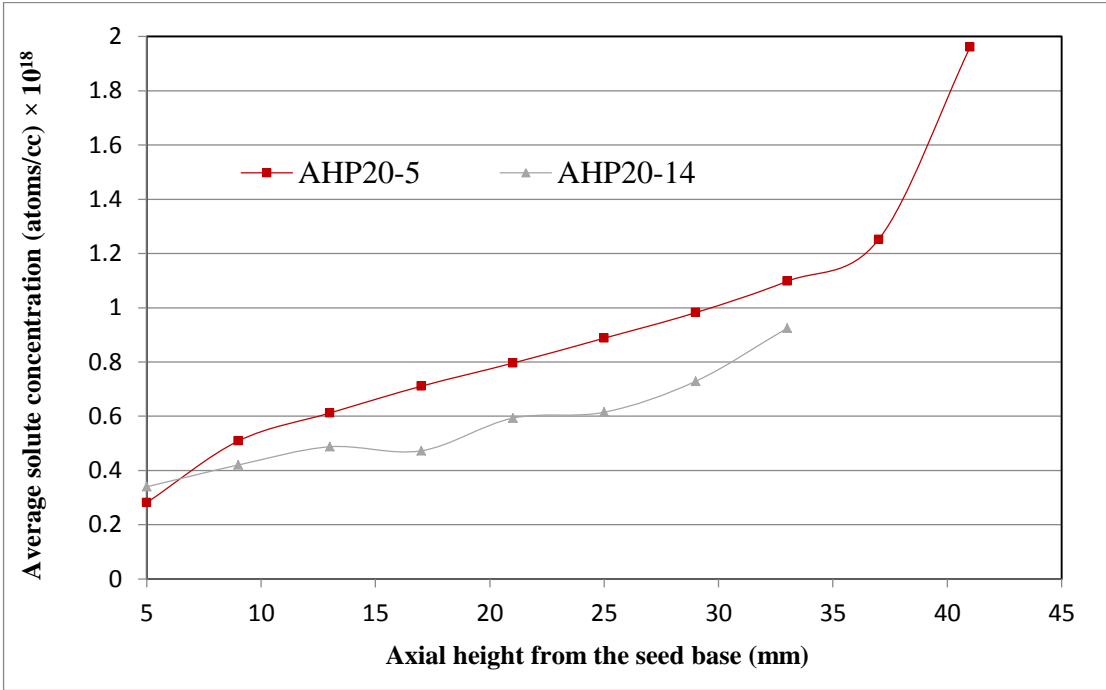


Figure 6.12. Average solute concentration (obtained from four-point probe test of the experimentally grown crystals) along the axial direction.

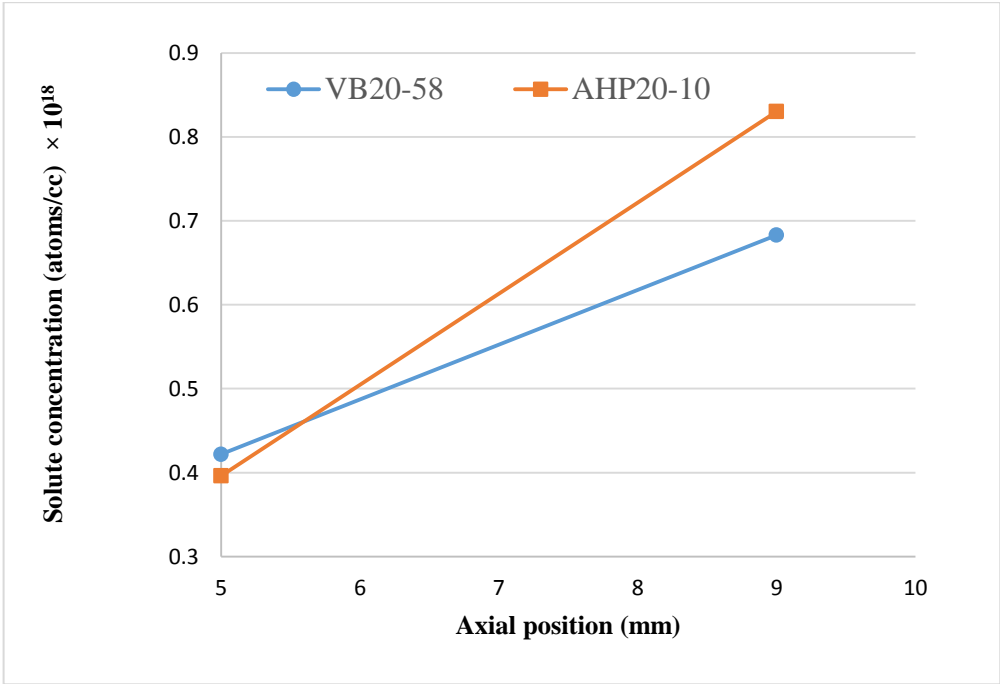


Figure 6.13. Numerical results for average solute concentration along the axial direction in VB20-58 and AHP20-10.

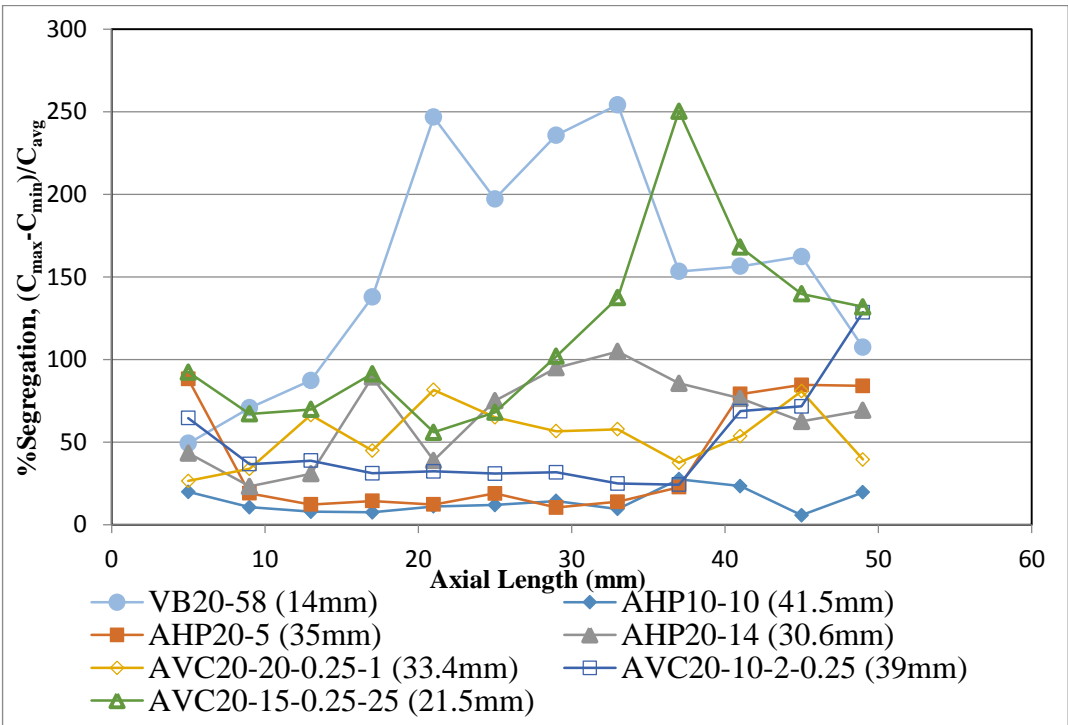


Figure 6.14. Averaged radial solute segregation along the crystals. The values in the parentheses are the single crystal lengths.

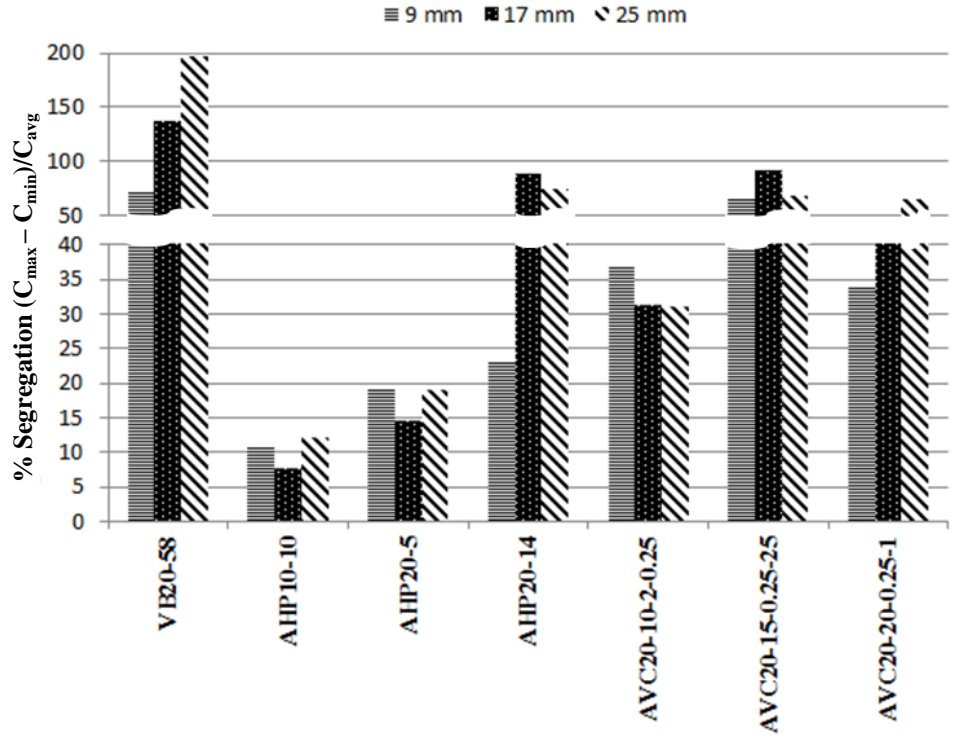


Figure 6.15. Comparison of solute segregation in the grown crystals.

### 6.5. Vibrational parameters

Earlier, it is mentioned that the convective flow in the melt plays a critical role in homogenizing the solute redistribution, stabilizing the interface, and enhancing the single crystal length. In the AHP method, it is tried to suppress the ineffective natural convection flow arising from the radial temperature gradient by inserting the baffle in the melt and creating forced flow through the gap between the baffle and the crucible [14-19, 143, 144]. Then by altering the position of the baffle inside the melt to adjust the melt height above the s/l interface, it is tried to control this forced flow in order to provide better mixing. Recently, it has been proved that creating forced flows close to the interface by oscillating the submerged baffle positioned properly in the melt affects the nature of the convective flow patterns in the melt, redistribution of the solute, the diffusion boundary layer ahead of the interface, the interface shape, the growth rate of the interface, and defects (dislocations) [23, 62, 145-151]. The influence of the vibrating baffle in controlling the buoyancy and the forced flow and homogenizing the solute redistribution is investigated by the crystals grown with the AVC technique in this study. A properly parameterized vibration can provide controlling of the flow in the melt during the growth. The controlling parameters in this study are amplitude and frequency of the vibrating baffle. The vibrational Reynolds number which is defined in Equation 6.2 [152] shows the character of vibrational vortices created under the baffle

$$Re_v = \frac{2\pi \cdot f \cdot A \cdot r}{\nu} \quad (6.2)$$

Where  $f$  is the frequency,  $A$  is the amplitude,  $r$  is the radius of the baffle, and  $\nu$  is the kinematic viscosity. For the higher vibrational Reynolds number, the vibrational vortices can suppress the natural convection and occupy the whole melt volume under the baffle. Therefore, according to Equation 6.2 high amplitude  $A$  and high frequency  $f$  are preferred. However, there is another parameter which characterizes the vibrational flow in the melt which is called vibration intensity parameter [24] ( $I = A \times f^2$ ) and is given in Table 5.1. If the frequency becomes too high, the vibrational flow becomes too intense and the forced flow through the annular gap brings the hot liquid close to the interface and deflects it toward the crystal. Thus the interface becomes concave at the sides and solute segregation

is increased there (see Figure 5.16 and Figure 5.18). On the other hand, applying high amplitude with a low frequency mix the melt gently, avoids intensity increase, and provides more flat interface with more homogeneous solute redistribution. Another parameter that determines the effect of the vibration on the nature of the convective flow in the melt is the viscous dissipation rate ( $W = \mu S^2$  [153]). Where,  $\mu$  is the viscosity and  $S = \sqrt{2u_x^2 + 2v_y^2 + 2w_z^2 + (u_z + w_x)^2 + (u_y + v_x)^2 + (w_y + v_z)^2}$  is the strain rate and  $u, v$ , and  $w$  are the velocity components in  $x, y$ , and  $z$  directions in the general 3D case. Viscous dissipation rate determines the rate at which the kinetic energy of the flow transforms to the internal energy (heating up) by means of the viscosity. Since it is assumed that the viscosity in the melt is constant, just the strain rate for the VB, AHP, and AVC cases is shown in Figure 6.16 for comparison. The strain rate in the melt region below the baffle is considerably higher in the AVC20-10-2-0.25 than that in the other crystals. Therefore, more heat is supplied to the melt region close to the interface and as it is also shown in Figure 6.8, the radial temperature gradient is reduced and more homogenized temperature field is provided in front of the interface, which promotes the flat interface shape at the center in AVC20-10-2-0.25. The flat interface at the center of the crystal, which is observed in both experimental and numerical results in Figure 5.24 and Figure 5.55 respectively, supports this hypothesis. Although the concavity of the interface at the sides due to the intense melt flow from the gap to the interface needs improvement in the AVC20-10-2-0.25, the flattening of the interface at the center contributes homogeneity of solute redistribution and postpones morphological instabilities. Also, it is believed [153] that the increased intensity in the melt leads to redistribution of the viscous dissipation rate in the melt and consequently dissociates the melt and destroys cluster formations in the melt.

Figure 6.17 shows the convective patterns in different positions of the baffle in AVC20-10-2-0.25. The intense convective flow created in the vicinity of the interface at the side in the top position of the baffle, which makes the interface concave, is not persistent. This flow is replaced by moderate convective patterns in the middle and bottom positions of the baffle, so increasing the concavity of the interface at the side is avoided.

Moreover, by reciprocating motion of the baffle, the rejected solute can be mixed effectively with the bulk liquid (see the change in direction of the flow in the gap in Figure 6.17), so the solute build up can be reduced in front of the interface. It should be noticed here that mixing between the regions below and above the baffle is more significant in the AVC than the AHP [15].

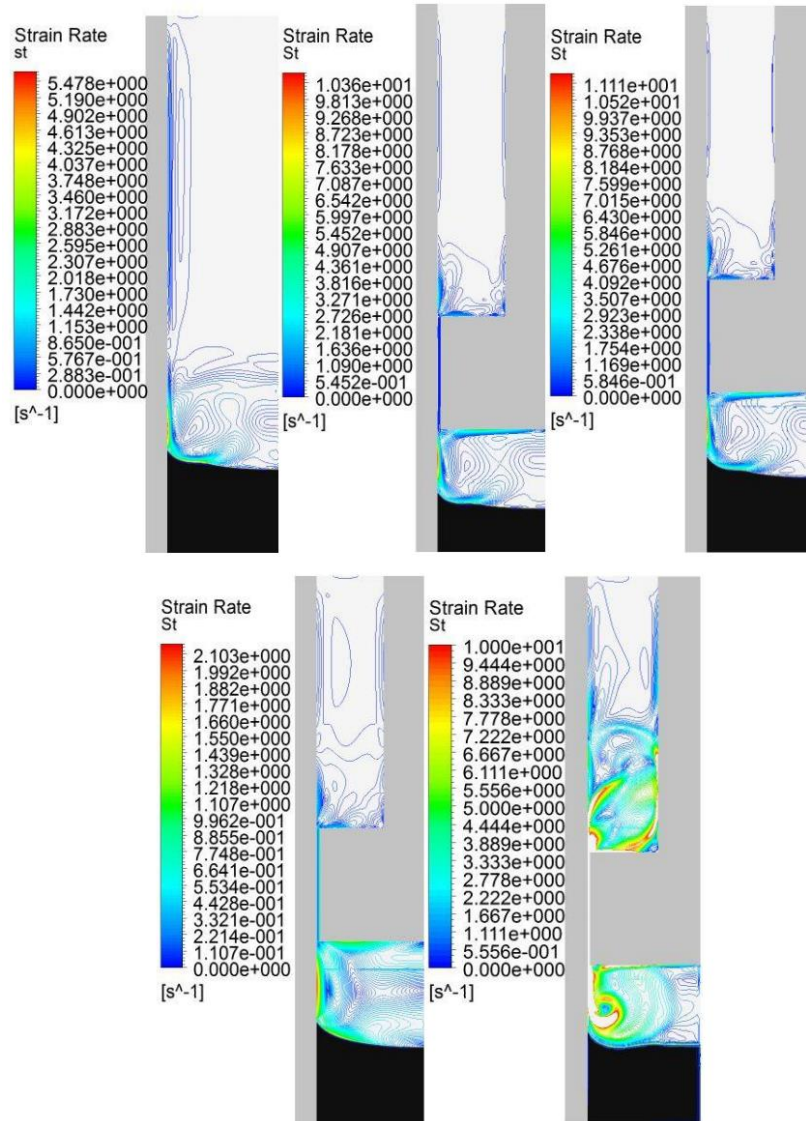


Figure 6.16. Numerical results for strain rate in VB20-58, AHP10-10, AHP20-10, AHP20-14, and AVC20-10-2-0.25 (from left to right) at 2400 s

Therefore, by controlling the forced convective flow with the appropriate amplitude and frequency, a single crystal length close to that in AHP10-10 can be achieved in AVC20-10-2-0.25, even though the pulling rate is doubled in the latter.

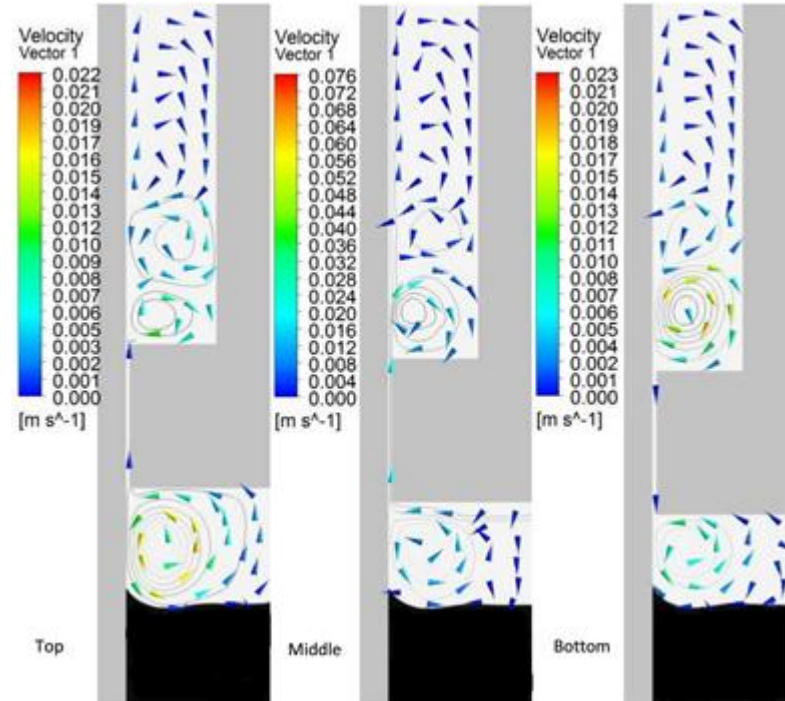


Figure 6.17. Convective cells inside the melt during the vibrational motion of the baffle in AVC20-10-2-0.25

## 6.6. Dislocations

Another effective parameter in the quality assessment of a grown crystal is the existence of dislocations. Dislocations may arise from solute segregation and thermal and mechanical stresses induced in the crystal that exceed the critical resolved shear stress [154, 155]. Radial temperature gradient which leads to concavity of the interface is known as the main source of the thermal stresses [10]. As the seed is snugly fit into the crucible at room temperature and thermal expansion coefficient of the graphite crucible is larger than that of the Ge, any constrained stress is not expected in the seed before the solidification. However, contractions of both Ge and graphite during the cooling down process induce the thermo-mechanical stresses in the crystal because of squeezing



germanium crystal by the graphite that has higher thermal expansion (contraction) coefficient. Obviously, higher temperature differences initiate higher thermal stress ( $\sigma = E\alpha\Delta T$ ) and consequently increase the probability of dislocations generation. Figure 6.18 shows the temperature variation of the same position on the crucible wall (thermocouple T10 in Figure 2.9) from the temperatures slightly above the melting temperature (around 945° C) to the lower temperatures far from the melting temperature in the same time period for different grown crystals, except for AHP10-10 that the time period is twice the others since the pulling rate is half of the others. Figure 6.19 compares the temperature gradient during the cooling process in different grown crystals according to T10 thermocouple data. While AVC20-15-0.25-25 has the highest temperature gradient, the lowest temperature gradient at T10 position is obtained in AHP10-10 which has the lowest growth rate. Therefore, it is expected to have the lowest dislocation density in AHP10-10 and the highest dislocation density in AVC20-15-0.25-25. In addition, comparing the AHP-grown crystals with the same pulling rate (20 mm/h), the temperature gradient is less in AHP20-5 than in AHP20-14 for the same time period. Thus, it is expected to have lower dislocation density in AHP20-5. This outcome is shown in Figure 6.20 which shows the average dislocation density in the grown crystals.

As mentioned in Section 2.4.1, dislocations can also propagate into the crystal from the seed. The dislocation density in the seed before the solidification process is determined to be  $9.0 \times 10^3 \text{ 1/cm}^2$ . The average dislocation density along the crystals after the solidification is presented in Figure 6.20. The average value given for each axial position is the average dislocation density calculated in each 16 sub-region of a radial plane shown in Figure 4.5. This average dislocation density together with the maximum and minimum dislocation density of a radial plane in each axial position are reported in Table 6.1. It is seen that the dislocation density at the seed base increases from its before-growth value in all crystals. Thus, there should be other sources for the dislocation increase in addition to the contraction during cooling.

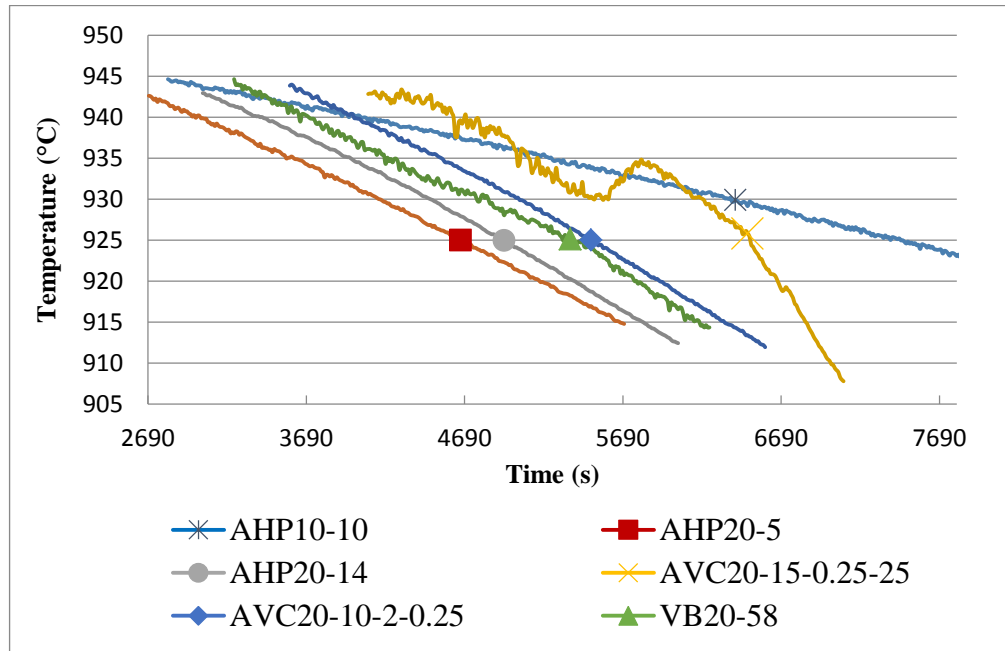


Figure 6.18. Temperature variations of the grown crystals at T10 thermocouple position during the solidification.

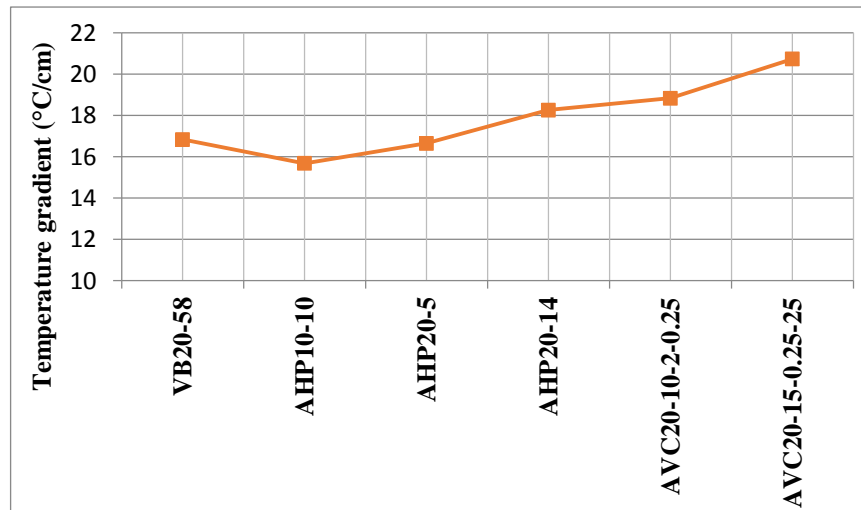


Figure 6.19. Axial temperature gradient in crystals during growth, calculated using data measured by T10 thermocouple as shown in Figure 6.18.

A reason for the additional dislocation generation in the seed may be due to holding the seed close to the melting temperature while waiting for stabilization of the interface before pulling down the crucible [156]. For example, the increase in dislocation density in

the AVC seeds is noteworthy. Post analysis of the thermal data during heating of the crystals for melting has revealed that several heat-cool cycles and/or sudden temperature changes have occurred in the AVC crystals. This oscillatory thermal input has generated a high number of dislocations in the seeds of the AVC crystals. Also the waiting time for stabilizing the interface was more in the AVC grown crystals rather than that in the other crystals.

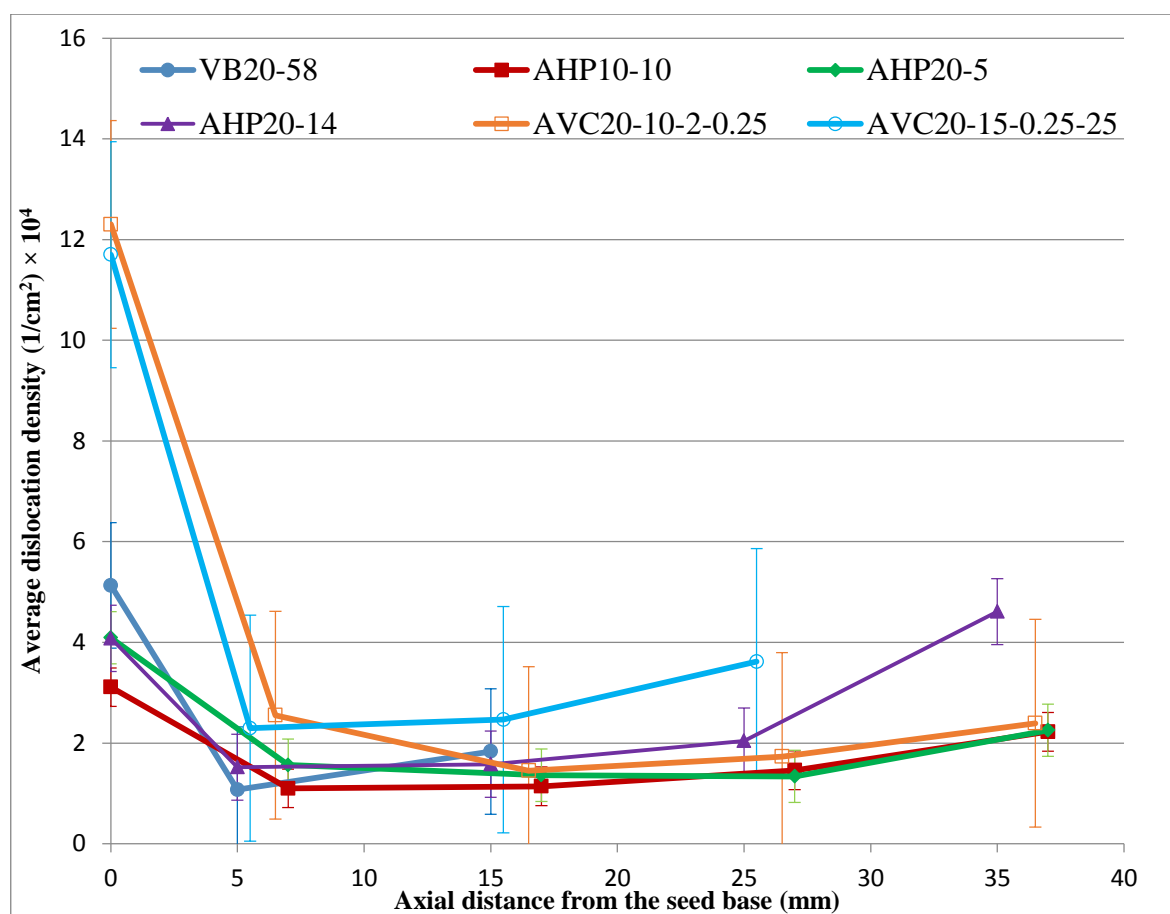


Figure 6.20. Average dislocation densities of the grown crystals up to the point where the single crystallinity is lost.

Table 6.1. Dislocation density in radial planes at given axial positions starting from the seed base.

DISLOCATION DENSITY ( $1/\text{cm}^2$ ) $\times 10^4$				
Method	Axial Height	Min	Max	Av.
VB20-58	0	2.01	9.27	5.13
	5	0.18	1.87	1.07
	15	0.06	3.61	1.83
AHP10-10	0	1.53	4.19	3.11
	7	0.62	1.74	1.1
	17	0.63	2.04	1.14
	27	0.6	2.55	1.46
	37	0.9	3.49	2.22
AHP20-5	0	1.8	7.73	4.09
	7	0.71	2.63	1.56
	17	0.48	2.16	1.36
	27	0.78	2.19	1.34
	37	0.71	3.16	2.25
AHP20-14	0	1.39	5.47	4.08
	5	0.86	2.27	1.52
	15	0.79	2.34	1.58
	25	1.01	3.2	2.04
	35	1.17	8.24	4.61
AVC20-10-2-0.25	0	5.28	27.9	12.3
	6.5	0.42	4.22	2.55
	16.5	0.06	4.01	1.45
	26.5	0.26	4.84	1.73
	36.5	0.36	3.76	2.39
AVC20-15-0.25-25	0	3.99	24.7	11.7
	5.5	1.27	3.52	2.29
	15.5	0.65	8.35	2.46
	25.5	2.64	6.49	3.62

Moreover, Figure 6.20 shows the reduction of dislocation density from its value in the seed for all the crystals. In the work of Taishi et al. [157], it is concluded that the melt back of the interface can eliminate the dislocations generated in the seed. Figure 6.20 shows a remarkable improvement in the dislocation density in the AVC grown crystals, around %80 reduction in AVC and %60 reduction in the others. This significant reduction

in the density may be because of the more severe melt back of the interface due to intense convective flow in the melt at the sides (Figure 5.24) arising from the axial vibration of the baffle in the AVC method. An observation of Figure 5.32 shows that dislocation density is lower at sides in AVC20-10-2-0.25. Also, as it is pointed out in the previous section and in the work of Avetissov and Zharikov [24], the vibration of the baffle prevents premature cluster formation at the interface and reduces crystal defects by increasing the intensity of the flow and redistributing the viscous dissipation rate effectively in the melt region below the baffle and close to the interface.

In fact, a similar clustering has been noticed in solidifying Ge as a change in the Seebeck signal [158] near the melting temperature. This might be a sign for clustering in molten Ge in the absence of the vibration. Moreover, the effect of vibration in reducing the radial temperature gradient (Figure 6.8), which is the main source of thermal stresses and dislocation generation, is noteworthy.

Since it is expected that the thermal stress is higher at the periphery of the crystal and the dislocations preferentially nucleate at the periphery, it is expected to have higher dislocation density at the periphery rather than the center of the crystal. Dislocation density of the grown crystals is shown in Figure 5.28 to Figure 5.33 in Section 4.4.8. As it is expected, the dislocation density is higher at the periphery except for VB20-58 and AVC20-10-2-0.25 crystals in which the dislocation density is higher at the center. To show this in a more sensible way dislocation densities at the center and the periphery for a certain axial height (15 mm for instance) are shown in Figure 6.21. The low dislocation density at the sides in AVC20-10-2-0.25 is explained above. The higher density at the center may be due to the fact that the interface shape does not change much and stays planar, so the pre-existing dislocations in the seed can propagate with the interface. However, the interface is changed considerably at the sides that impede the propagation of the dislocations in the seed. As mentioned earlier in section 2.1.2, intersection of dislocations with the interface contributes the lateral growth by providing preferential sites at the interface for atomic attachments. The planar faceted interface observed at the center

of the AVC20-10-2-0.25 crystal and higher growth rate of the interface in this sample (Figure 6.7) prove this outcome.

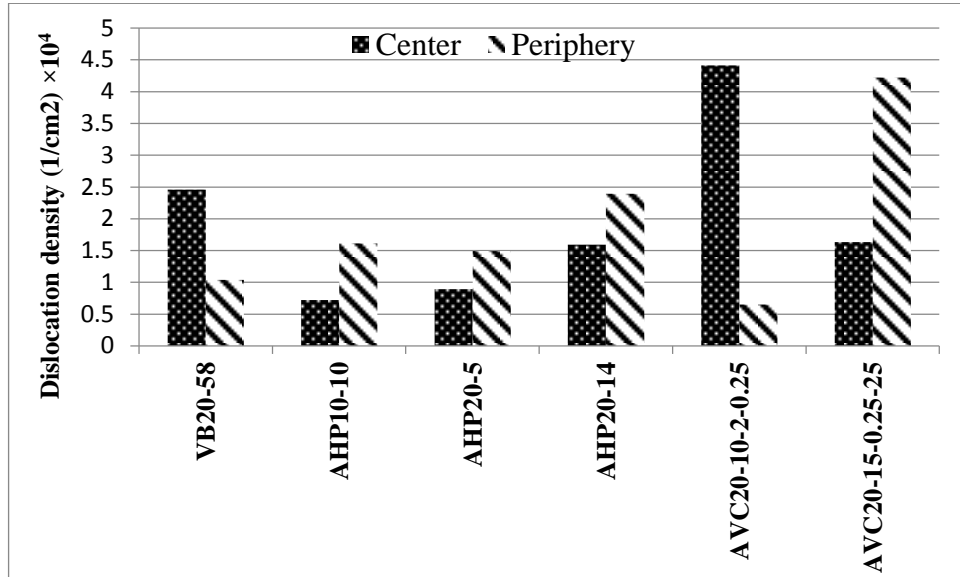


Figure 6.21. Dislocation density at the center and periphery of the crystals at 15 mm axial height from the seed base.

On the other hand, by comparing Figure 6.14 and Figure 6.20, it is seen that the crystals with a greater radial solute segregation have a higher dislocation density. It is shown in [159] that increasing solute segregation on the faceted steps of the interface increases the possibility of the elimination of the strain filed by introduction of the dislocations. Therefore, the dislocation density at the center is higher than the sides in the VB20-58 because of higher solute content at the center.

The lowest dislocation density is achieved in the crystal grown with the lowest pulling rate (AHP10-10). It is observed in [160] that the dislocation density increases with higher growth rate. Low pulling rate provides enough time for uniform growth rate of the interface across the radial section of the crystal and avoid severe concavity and radial solute and temperature gradient. However, increasing the pulling rate leads to increased concavity due to faster growth rate at the sides close to the crucible wall. Concavity of the interface can be controlled by adjusting the melt height. Moreover, by reducing the melt

volume below the baffle, the forced flow can sweep the rejected solute in front of the interface more effectively and reduce the radial solute segregation. Therefore, increasing the melt height contributes both the solute segregation and the concavity of the interface (radial temperature gradient) which both promote dislocation generation. Thereby, as it is shown in Figure 6.20, AHP20-5, with the lowest melt height, has the lowest dislocation density among the crystals grown with 20 mm/h. In addition, the melt height affects the size of the generated dislocations in the grown crystals. For the initial melt height up to 10 mm, the size of the dislocations is almost the same through the axial direction for each radial position (see Figure B.2, Figure B.3, and Figure B.5 for dislocations in AHP10-10, AHP20-5, and AVC20-10-2-0.25 respectively). In our observations, it is seen that the dislocations are smaller at the sides than at the central regions in all of the crystals. There might be several reasons for the emergence of the dislocations with different sizes. It is pointed out in [161] that the size of dislocations may be dependent to the length of the singular line of dislocation just below the interface. When an edge-type dislocation is changed into screw-type, the length of the singular line of dislocation may vary which may leads to appearance of smaller dislocations. Also, it is mentioned in [161] that the variation of the size in the etch pits may be related to the angle between the dislocation line and the s/l interface. By increasing the concavity of the interface, the emergent dislocations become smaller in size. Since the concavity of the interface is higher at the sides, it is expected to have smaller dislocations in these regions. However, for the melt height equal to or higher than 14 mm, the size of the dislocations is also reduced in the axial direction (see Figure B.1, Figure B.4, and Figure B.6 for dislocations in VB20-58, AHP20-14, and AVC20-15-0.25-25 respectively). This is due to the increased concavity of the interface, leading to a higher angle between the local interface plane and the global growth plane which is (111). Thus, the reduction in the size of the dislocations is more abrupt in the VB20-58.

## 6.7. Interface shape and Morphological Instability

The stability of the interface has been treated by Constitutional Super cooling (CS), Mullins and Sekerka (MS), and Favier and Rouzaud (FR) criteria which are reformulated

[21] to be solvable for the critical value of solid concentration at the onset of instability,  $C_s^*$ . Measured concentration values in at/cc given so far have been converted to at% using Equation 6.3 and used in the below stability treatments.

$$at\% = \frac{100 \times \left(\frac{atoms}{cc}\right)}{\left(\frac{atoms}{cc}\right) + \frac{\rho_{Ge} \times N_A}{M_{Ge}} - \left(\frac{atoms}{cc}\right) \left(\frac{M_{Sb} \times \rho_{Ge}}{M_{Ge} \times \rho_{Sb}}\right)} \quad (6.3)$$

Where at% and  $\frac{atoms}{cc}$  are concentration of Sb,  $\rho_{Ge}$  is the density of Ge in g/cm<sup>3</sup>,  $\rho_{Sb}$  is the density of Sb in g/cm<sup>3</sup>,  $M_{Ge}$  is the atomic weight of Ge,  $M_{Sb}$  is the atomic weight of Sb, and  $N_A$  is the Avogadro's number.

Accordingly, The CS criterion proposed by Tiller and Jackson is directly solvable for  $C_s^*$  as

$$C_s^* = \frac{kD_L G_L}{m_L V (k-1)} \quad (6.4)$$

On the other hand, for the MS criterion the marginal stability criterion for the critical parameter  $C_s^*$  can be achieved as shown in Equation (6.5) by setting Equation (2.29) to zero.

$$C_s^* = \frac{D_L k \left[ 2T_m \Gamma_{SL} \omega^2 + \left( \frac{K_S G_S + K_L G_L}{K} \right) \right] \left( \omega^* - \frac{V(1-k)}{D_L} \right)}{2m_L V (k-1) \left( \omega^* - \frac{V}{D_L} \right)} \quad (6.5)$$

The predicted  $C_s^*$  for both the MS and CS criteria together with the measured  $C_s^*$  for the grown crystals at the center ( $r = 0$ ), right side ( $r = 12$  mm), and left side ( $r = -12$  mm) are presented in Table 6.2. The stability ratios, which are the ratio of the measured critical concentration to the predicted value for these criteria, are also presented in the same table (MS-ratio and CS-ratio). Although the MS criterion provides a better prediction than the CS, the experimentally measured  $C_s^*$  values are greater than the predictions of the either criterion.



Also, the FR criterion given in Equation (2.30) for the critical parameter  $C_S^*$  reduces to

$$C_S^* = \frac{k^2 \left[ \frac{D_L(K_L G_L + K_S G_S)}{2V\bar{K}} + \frac{4T_m \Gamma_{SL} V \pi^2}{\Lambda^2 D_L} \right]}{k_{eff} m_L (k - 1) \left\{ 1 - \frac{2k}{\zeta} - \frac{H + Q}{\zeta} \exp \left[ \frac{-\Delta(1 + Q)}{2} \right] \right\}} \quad (6.6)$$

The extent of the solute boundary layer,  $\delta$ , is unknown due to presence of convection. Thus,  $\delta$  is adjusted in Equation (6.6) to match the calculated  $C_S^*$  with the critical concentrations measured experimentally from the crystals that are provided in Table 6.3. If there is no convection in the melt, the rejected solute at the interface will diffuse down to the bulk concentration and a diffusion boundary layer of thickness  $D_L/V$  will be formed ahead of the interface. Presented results in Table 6.3 shows that the predicted values for  $\delta$  are several orders of magnitude below the diffusion boundary layer in the absence of convection ( $D_L/V$ ) which supports the presence of convection in the melt. Moreover, it shows that increasing the vibration amplitude makes the effective distribution coefficient ( $k_{eff}$ ) approach to the equilibrium value,  $k = 0.003$ . The convective mixing removes the rejected solute from the interface, so a smaller boundary layer is expected. Numerical results shown in Figure 6.22 support this opinion. In this figure, it is shown that the solute boundary layer at the center where the convective motion is not effective is longer than that at the sides where there is more effective mixing in the melt. Moreover, even at the center, the solute boundary layer is less in the AHP10-10 comparing to the other two samples in Figure 6.22. That is why the AHP10-10 is most stable case, and the highest single crystal length is achieved in this case. Also, since the pulling rate in the VB20-58 is twice the pulling rate in AHP10-10, the difference of the solute concentration at the interface from the solute concentration at the bulk liquid is higher in VB20-58 than in AHP10-10. This is also expected according to the analytical formula for the solute redistribution in transient region for diffusional mixing given in Equation 2.13. Moreover, Figure 6.22 shows that the formation of solute boundary layer in front of the interface is more distinct in the VB20-58 than in AHP20-10. Therefore, the accumulation of the solute close to the interface is avoided better and consequently it is expected to have more stable

interface in AHP20-10 than in VB20-58 which is the case in our experimental observations.

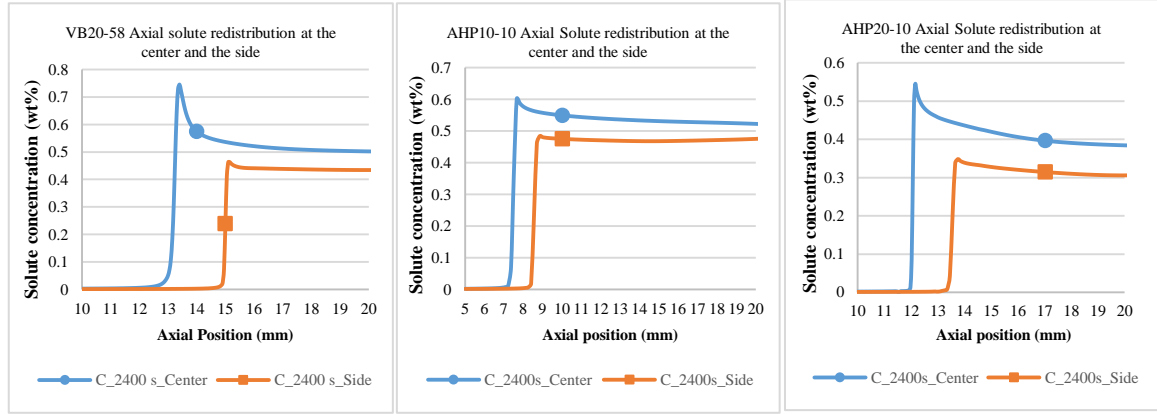


Figure 6.22. Numerical results of the axial solute redistribution inside the melt at the center and at the sides in VB20-58, AHP10-10, and AHP20-10.

As mentioned in section 2.5.4 and shown in Figure 2.17, interfaces with a low vicinal angle are kinetically stabilized. By setting Equation 2.33 to zero, the critical concentration values,  $C_S^*$ , are determined and presented in Table 6.3. The measured and predicted critical concentrations are compared by the stability ratio. As mentioned earlier, according to the KS criterion the interfaces with  $\theta < 10^\circ$  are kinetically stabilized, so the KS stability ratio is not available for these cases. While for high vicinal angles the KS provides a better prediction, for low vicinal angles the MS is still a better predictor.

Table 6.2. CS and MS stability criteria.

Sample	$C_s^*$ -measured (at%)	$C_s^*$ (MS) (at%)	MS-ratio $[\frac{C_s^*}{C_s^*(MS)}]$	$C_s^*$ (CS) (at%)	CS-ratio $[\frac{C_s^*}{C_s^*(CS)}]$
AHP10-10-center	$3.7 \times 10^{-3}$	$3.0 \times 10^{-3}$	1.18	$2.0 \times 10^{-3}$	1.90
AHP10-10-Left	$5.3 \times 10^{-3}$	$5.8 \times 10^{-3}$	0.90	$4.0 \times 10^{-3}$	1.31
AHP10-10-Right	$4.8 \times 10^{-3}$	$5.0 \times 10^{-3}$	0.95	$3.40 \times 10^{-3}$	1.39
AHP20-5-center	$5.4 \times 10^{-3}$	$1.5 \times 10^{-3}$	3.63	$0.90 \times 10^{-3}$	5.83
AHP20-5-Left	$5.4 \times 10^{-3}$	$1.7 \times 10^{-3}$	3.18	$1.10 \times 10^{-3}$	4.98
AHP20-5-Right	$4.0 \times 10^{-3}$	$1.2 \times 10^{-3}$	3.30	$0.75 \times 10^{-3}$	5.28
AHP20-14-center	$2.7 \times 10^{-3}$	$1.3 \times 10^{-3}$	2.08	$0.83 \times 10^{-3}$	3.32
AHP20-14-Left	$6.0 \times 10^{-3}$	$1.4 \times 10^{-3}$	4.40	$0.94 \times 10^{-3}$	6.40
AHP20-14-Right	$2.6 \times 10^{-3}$	$0.4 \times 10^{-3}$	6.21	$0.29 \times 10^{-3}$	8.83
AVC20-20-0.25-1-center	$3.3 \times 10^{-3}$	$1.3 \times 10^{-3}$	2.45	$0.85 \times 10^{-3}$	3.91
AVC20-20-0.25-1-Left	$2.9 \times 10^{-3}$	$1.9 \times 10^{-3}$	1.54	$1.30 \times 10^{-3}$	2.19
AVC20-20-0.25-1-Right	$2.8 \times 10^{-3}$	$1.8 \times 10^{-3}$	1.59	$1.1 \times 10^{-3}$	2.51
AVC20-10-2-0.25-center	$5.7 \times 10^{-3}$	$1.4 \times 10^{-3}$	4.05	$0.90 \times 10^{-3}$	6.49
AVC20-10-2-0.25-Left	$4.2 \times 10^{-3}$	$2.6 \times 10^{-3}$	1.59	$1.60 \times 10^{-3}$	2.57
AVC20-10-2-0.25-Right	$5.3 \times 10^{-3}$	$2.3 \times 10^{-3}$	2.28	$1.50 \times 10^{-3}$	3.42
AVC20-15-0.25-25-center	$1.8 \times 10^{-3}$	$1.5 \times 10^{-3}$	1.17	$0.90 \times 10^{-3}$	2.03
AVC20-15-0.25-25-Right	$1.5 \times 10^{-3}$	$1.5 \times 10^{-3}$	1.04	$0.97 \times 10^{-3}$	1.59



## 7. CONCLUSIONS

Germanium crystals have been grown by conventional vertical Bridgman (VB) method and novel Axial Heat Processing (AHP) and Axial Vibrational Control (AVC) methods. The growth processes have been also numerically simulated to have a better insight into the role of growth parameters on the crystal quality and production yield. It is seen that the highest solute segregation and the shortest single crystal length are achieved by the VB method that has the highest melt height. However, the single crystal length is increased in the crystals by decreasing the initial melt height via inserting the baffle. Insertion of the baffle leads to formation of forced convective motion arising from relative motion between the baffle and the crucible. Although only in the AVC20-10-2-0.25 forced convective flow suppresses the natural convection, simulation results show that the magnitude of the flow velocity is increased at the vicinity of the interface in the AHP and AVC methods compared to the VB method. Decreasing the melt height increases the effectiveness of this forced flow in mixing the melt close to the interface. Therefore, homogeneity of the solute redistribution is improved by decreasing the melt height and the solute segregation is decreased both radially and axially. Both experimental and simulation results show that by decreasing the melt height, the solute redistribution pattern becomes closer to the analytical complete mixing pattern. In addition, it is observed both numerically and experimentally that the crystals grown with a lower initial melt height solidify with a higher solute content. For instance, in the VB20-58 which has the highest melt height, the most portion of the solute content is trapped into the poly crystalline region that is not going to be used in the electronic applications. Therefore, the doping process in the crystals grown with a lower initial melt height is done more effectively.

Analytical and simulation results for the variation of the melt height during the growth show that the melt height gradually increases during the growth. It means that there is a deviation between the crucible pulling rate and the growth rate of the interface. The gradual increase in the melt height may nullify the intended effect of the baffle. It is observed that for the first stages of the growth, the deviation is the lowest with the lowest crucible pulling rate. However, both experimental and simulation results show that further

increase of the melt height during the growth can be controlled by decreasing the initial melt height. In addition, the low pulling rate provides enough time for the melt flow to homogenize both the temperature and the solute redistribution close to the interface that results in enhanced stability of the interface. As such, the highest single crystal length is achieved in the AHP10-10, which has the lowest pulling rate.

However, low pulling rate increases the time and the cost of the production. In order to increase the production yield without any loss in crystal quality, the AVC method is adopted. It has been observed that the forced convective flow arising from vibrational motion of the baffle is effective in suppressing the natural convection and the velocity magnitude is increased considerably at the vicinity of the interface. Also, the forced vibrational flow leads to more viscous dissipation rate which supplies heat close to the interface and reduces the radial temperature gradient more effectively. However, vibrational parameters, amplitude and frequency of the vibration, should be adjusted carefully. High frequency leads to very intense flow that melts the interface at the sides and brings more concavity that eventually breaks down the stability of the interface. Proper setting of the vibrational parameters provides homogeneous distribution of both the temperature and the solute at the vicinity of the interface which enhances the stability of the interface. In consequence, vibration of the baffle in the AVC method effectively improved the total single crystal length even with the higher pulling rate, 20 mm/h.

Dislocation density is another important parameter that determines the quality of the grown crystals. There are many sources for dislocation generation in the crystals. One of them is the thermal compression on crystals due to different thermal expansion coefficients of the crucible and the crystal during the cooling process. During the cooling, the temperature gradient in the crystal with the lowest pulling rate (AHP10-10) is the least and in the AVC20-15-0.25-25 is the highest. Thus, while the AHP10-10 attains the lowest dislocation density, the AVC20-15-0.25-25 has the highest dislocation density. Also, dislocations can propagate into the crystal from the seed. It is observed that the dislocation density in the seed is increased from its before growth value in all the grown crystals. The reason may be due to long waiting time for stabilization of the initial interface. However,

dislocation density is decreased in higher portions of the crystal above the seed. The reason may be due to melt back of the interface. According to more intense convective flow in the AVC-grown crystals, the melt back of the interface and consequently the reduction of the dislocation density is more sensible in these crystals. Moreover, forced convective flow arising from the vibrating baffle destroys cluster formations that may lead to dislocation generation. Since dislocations preferentially nucleate at the side, it is expected to have higher dislocation density at the sides. Except for the VB20-58 and AVC20-10-2-0.25, experimental observations support this expectation. Since the interface shape at the center in the AVC20-10-2-0.25 remains almost flat without any distortion, the dislocations in the seed can easily propagate beneath the interface through the crystal. However, as it is mentioned earlier, forced convective flow melts back the interface at the sides and avoids the increase in the dislocation density. On the other hand, the solute segregation is highest in the VB20-58 and the solute accumulates at the center due to weak convective mixing in the melt. Increasing the solute content at the center may increase the strain field in this region which increases the probability of dislocation formation. Another outcome of our observations is that the dislocations are finer at the sides of the grown crystals and if the initial melt height exceeds the 10 mm, the dislocation size immediately reduces at the higher axial length of the crystal. However, for the crystals grown with initial melt height less than or equal to 10 mm, the dislocation size almost remains the same through the whole crystal. The reason is higher concavity of the interface at the sides and increased concavity by increasing the effective melt height above the interface. By increasing the concavity, the angle between the dislocation line and the interface is reduced and the emergent dislocation appears smaller in size. Generally, since the low pulling rates decrease the solute segregation and radial temperature gradient, the lowest dislocation density is observed in the crystal grown with the lowest pulling rate. However, applying appropriate amplitude and frequency of the vibrating baffle in the AVC method is effective in homogenizing the solutal and thermal fields, avoiding cluster formation in front of the interface, and improving the quality of the crystal by enhancing the interface stability and reducing the dislocation density. Hence, the AVC method shows promising advantages over the other methods in germanium single crystal growth.

## 8. FUTURE WORK

It has been mentioned that the vibrational flow in the melt region below the baffle in the AVC method is effective in homogenizing the solute and the temperature distribution in front of the interface. However, the intense forced flow through the gap melts the interface and cause concavity of the interface. Therefore, further investigations should be done on the setting the vibrational parameters to avoid severe melt flow into the interface. A change in the shape of the baffle base can be a remedy for this problem. A proper change in the shape of the baffle base may change the flow direction below the baffle and prevent melting of the interface at the sides. In addition, increasing the gap size between the baffle and the crucible may contribute to reduce the intensity of the forced flow and melting the interface at the sides. Also, a heater can be placed inside the baffle for further reduction of the radial temperature gradient close to the interface.



## REFERENCES

1. Derluyn, J., Dessein, K., Flamand, G., Mols, Y., Poortmans, J., Borghs, G. and Moerman, I., “*Comparison of MOVPE grown GaAs solar cells using different substrates and group-V precursors*”. Journal of crystal growth. **247**(3-4): pp. 237-244, 2003.
2. Thomas, S.G., Johnson, E.S., Tracy, C., Maniar, P., Li, X., Roof, B., Hartmann, Q. and Ahmari, D.A., “*Fabrication and characterization of InGaP/GaAs heterojunction bipolar transistors on GOI substrates*”. IEEE electron device letters. **26**(7): pp. 438-440, 2005.
3. D'Hondt, M., Yu, Z.-Q., Depreter, B., Sys, C., Moerman, I., Demeester, P. and Mijlemans, P., “*High quality InGaAs/AlGaAs lasers grown on Ge substrates*”. Journal of crystal growth. **195**(1-4): pp. 655-659, 1998.
4. Saraswat, K.C., Chui, C.O., Krishnamohan, T., Nayfeh, A. and McIntyre, P., “*Ge based high performance nanoscale MOSFETs*”. Microelectronic Engineering. **80**: pp. 15-21, 2005.
5. Wang, J. and Lee, S., “*Ge-photodetectors for Si-based optoelectronic integration*”. Sensors. **11**(1): pp. 696-718, 2011.
6. Franke, A., Bilic, D., Chang, D., Jones, P., King, T.-J., Howe, R. and Johnson, G. *Post-CMOS integration of germanium microstructures*. in *Micro Electro Mechanical Systems, 1999. MEMS'99. Twelfth IEEE International Conference on*. 1999. IEEE.
7. Shang, H., Jeong, M., Chu, J.O. and Guarini, K.W., *Integration of strained Ge into advanced CMOS technology*, Google Patents, 2007.
8. Yurasov, D., Antonov, A., Drozdov, M., Schmagin, V., Spirin, K. and Novikov, A., “*Antimony segregation in Ge and formation of n-type selectively doped Ge films in molecular beam epitaxy*”. Journal of Applied Physics. **118**(14): pp. 145701, 2015.

9. Ismail, K., Meyerson, B., Rishton, S., Chu, J., Nelson, S. and Nocera, J., “*High-transconductance n-type Si/SiGe modulation-doped field-effect transistors*”. IEEE electron device letters. **13**(5): pp. 229-231, 1992.
10. Depuydt, B., Theuwis, A. and Romandic, I., “*Germanium: From the first application of Czochralski crystal growth to large diameter dislocation-free wafers*”. Materials Science in Semiconductor Processing. **9**(4-5): pp. 437-443, 2006.
11. Artemyev, V., Smirnov, A., Kalaev, V., Mamedov, V., Sidko, A., Podkopaev, O., Kravtsova, E. and Shimansky, A., “*Modeling of dislocation dynamics in germanium Czochralski growth*”. Journal of Crystal Growth. **468**: pp. 443-447, 2017.
12. Golyshev, V., Gonik, M. and Tsvetovskii, V., “*In situ measurement of interface supercooling during growth of Bi<sub>4</sub>Ge<sub>3</sub>O<sub>12</sub> single crystals from melt*”. Instruments and experimental techniques. **41**(5): pp. 735-738, 1998.
13. Golyshev, V., Gonik, M. and Tsvetovsky, V., “*Problems of Bi<sub>4</sub>Ge<sub>3</sub>O<sub>12</sub> and Li<sub>2</sub>B<sub>4</sub>O<sub>7</sub> single crystal growth by crucibleless variant of AHP method*”. Journal of crystal growth. **198**: pp. 501-506, 1999.
14. Dario, A., Sicim, H.O. and Balikci, E., “*Germanium–silicon single crystal growth by the axial heat processing (AHP) technique*”. Journal of Crystal Growth. **318**(1): pp. 1057-1061, 2011.
15. Dario, A., Sicim, H.O. and Balikci, E., “*A new approach for dopant distribution and morphological stability in crystals grown by the axial heat processing (AHP) technique*”. Journal of Crystal Growth. **337**(1): pp. 65-71, 2011.
16. Dario, A., Sicim, H.O. and Balikci, E., “*A comparative study on the growth of germanium–silicon single crystals grown by the vertical Bridgman and axial heat processing techniques*”. Journal of Crystal Growth. **351**(1): pp. 1-8, 2012.
17. Balikci, E., Deal, A. and Abbaschian, R., “*Detached crystal growth from melt by the axial heat processing technique*”. Journal of crystal growth. **271**(1-2): pp. 37-45, 2004.

18. Balikci, E., Deal, A. and Abbaschian, R., “*Antimony-doped germanium single crystals grown from the melt by the axial heat processing (AHP) technique*”. Journal of Crystal Growth. **262**(1-4): pp. 581-593, 2004.
19. Balikci, E., Deal, A., Abbaschian, R., Bykova, S.V., Golyshev, V.D., Gonik, M.A., Tsvetovsky, V.B., Marchenko, M.P. and Frjazinov, I.V., “*A study on the morphological stability of faceted interfaces in antimony-doped germanium single crystals grown by the axial heat processing method*”. Crystal growth & design. **4**(2): pp. 377-381, 2004.
20. Bykova, S.V., Golyshev, V.D., Gonik, M.A., Tsvetovsky, V.B., Balikci, E., Deal, A., Abbaschian, R., Marchenko, M.P., Frjazinov, I.V. and Vlasov, V.N., “*The experimental–numerical investigation of instability of faceted Ge doped by Sb growth on the base of AHP method*”. Journal of Crystal Growth. **275**(1-2): pp. e229-e236, 2005.
21. Deal, A., Balikci, E. and Abbaschian, R., “*Enhanced morphological stability in Sb-doped Ge*”. Metallurgical and Materials Transactions A. **38**(1): pp. 100-115, 2007.
22. Avetissov, I.C., Sadovskii, A., Sukhanova, E. and Zharikov, E., “*Single crystal growth by axial vibrational control technique in Czochralski configuration*”. Journal of Crystal Growth. **318**(1): pp. 979-982, 2011.
23. Avetissov, I.C., Sadovskii, A., Sukhanova, E., Zharikov, E., Belogorokhov, A. and Levonovich, B., “*Czochralski crystal growth assisted by axial vibrational control technique*”. Journal of Crystal Growth. **312**(8): pp. 1104-1108, 2010.
24. Avetissov, I.C., Sadovskiy, A., Sukhanova, E., Orlova, G.Y., Belogorokhov, I. and Zharikov, E., “*Perfection of NaNO<sub>3</sub> single crystals grown by axial vibrational control technique in Czochralski configuration*”. Journal of Crystal Growth. **360**: pp. 167-171, 2012.
25. Avetissov, I.C., Sukhanova, E., Khomyakov, A., Zinovjev, A.Y., Kostikov, V. and Zharikov, E., “*Simulation and crystal growth of CdTe by axial vibration control technique in Bridgman configuration*”. Journal of Crystal Growth. **318**(1): pp. 528-532, 2011.

26. Avetissov, I.C., Sukhanova, E., Sadovskii, A., Kostikov, V. and Zharikov, E., “*Experimental and numerical modeling of Czochralski crystal growth under axial vibrational control of the melt*”. Journal of Crystal Growth. **312**(8): pp. 1429-1433, 2010.
27. Avetisov, I.K., Mel'kov, A.Y., Zinov'ev, A.Y. and Zharikov, E., “*Growth of nonstoichiometric PbTe crystals by the vertical Bridgman method using the axial-vibration control technique*”. Crystallography Reports. **50**(1): pp. S124-S129, 2005.
28. Fedyushkin, A., Bourago, N., Polezhaev, V. and Zharikov, E., “*The influence of vibration on hydrodynamics and heat-mass transfer during crystal growth*”. Journal of Crystal Growth. **275**(1-2): pp. e1557-e1563, 2005.
29. Deal, A., *Enhanced morphological stability in Sb-doped Ge single crystals*, University of Florida, 2004.
30. Stefanescu, D.M., *Science and engineering of casting solidification*: Springer, 2015.
31. Porter, D.A., Easterling, K.E. and Sherif, M., *Phase Transformations in Metals and Alloys, (Revised Reprint)*: CRC press, 2009.
32. Olesinski, R. and Abbaschian, G., “*The Ge– Sb (Germanium-Antimony) system*”. Bulletin of Alloy Phase Diagrams. **7**(3): pp. 219-222, 1986.
33. Kaiser, N., Cröll, A., Szofran, F., Cobb, S. and Benz, K., “*Wetting angle and surface tension of germanium melts on different substrate materials*”. Journal of Crystal Growth. **231**(4): pp. 448-457, 2001.
34. Turnbull, D., “*Thermodynamics in metallurgy*”. ASM, Metals Park, Ohio. pp. 282, 1949.
35. Knrpnrncr, R.J., “*Crystal growth from the melt: a review*”. Am Mineral. **60**: pp. 798-814, 1975.
36. Frank, F., “*The influence of dislocations on crystal growth*”. Discussions of the Faraday Society. **5**: pp. 48-54, 1949.

37. Hillig, W. and Turnbull, D., "*Theory of crystal growth in undercooled pure liquids*". The Journal of Chemical Physics. **24**(4): pp. 914-914, 1956.
38. Cahn, J.W., Hillig, W.B. and Sears, G., "*The molecular mechanism of solidification*". Acta Metallurgica. **12**(12): pp. 1421-1439, 1964.
39. Czochralski, J., "*Ein neues verfahren zur messung der kristallisationsgeschwindigkeit der metalle*". Zeitschrift für physikalische Chemie. **92**(1): pp. 219-221, 1918.
40. Teal, G., "*GK Teal and JB Little, Phys. Rev. 78, 647 (1950)*". Phys. Rev. **78**: pp. 647, 1950.
41. Cittadino, G., Volpi, A., Di Lieto, A. and Tonelli, M., "*Czochralski crystal growth for laser cooling*". Optical Engineering. **56**(1): pp. 011107, 2016.
42. Pfann, W.G. and Theuerer, H.C., *Semiconductor translating device*, Google Patents, 1955.
43. Keck, P.H. and Golay, M.J., "*Crystallization of silicon from a floating liquid zone*". Physical Review. **89**(6): pp. 1297, 1953.
44. Emeis, R., "*Tiegelfreies Ziehen von Silicium-Einkristallen*". Zeitschrift für Naturforschung A. **9**(1): pp. 67-68, 1954.
45. MOTOHIRA, N., KUWAHARA, K., HASEGAWA, T., KISHIO, K. and KITAZAWA, K., "*Single crystal growth of  $\text{Bi}_2\text{Sr}_2\text{Ca}_{n-1}\text{Cu}_n\text{O}_y$  superconductors by the floating zone method*". Journal of the Ceramic Society of Japan. **97**(1130): pp. 1009-1014, 1989.
46. Kimura, S. and Shindo, I., "*Single crystal growth of YIG by the floating zone method*". Journal of Crystal Growth. **41**(2): pp. 192-198, 1977.
47. Takekawa, S., Nozaki, H., Umezono, A., Kosuda, K. and Kobayashi, M., "*Single crystal growth of the superconductor  $\text{Bi}_{2.0}(\text{Bi}_{0.2}\text{Sr}_{1.8}\text{Ca}_{1.0})\text{Cu}_{2.0}\text{O}_8$* ". Journal of crystal growth. **92**(3-4): pp. 687-690, 1988.

48. Takeya, H., Hirano, T. and Kadowaki, K., “*Single crystal growth of quaternary superconductor YNi<sub>2</sub>B<sub>2</sub>C by a floating zone method*”. Physica C: Superconductivity. **256**(3-4): pp. 220-226, 1996.
49. Lal, K. and Bhagavannarayana, G., “*A high-resolution diffuse X-ray scattering study of defects in dislocation-free silicon crystals grown by the float-zone method and comparison with Czochralski-grown crystals*”. Journal of Applied Crystallography. **22**(3): pp. 209-215, 1989.
50. Campbell, T., Schweizer, M., Dold, P., Cröll, A. and Benz, K., “*Float zone growth and characterization of Ge<sub>1-x</sub>Si<sub>x</sub> ( $x \leq 10$  at%) single crystals*”. Journal of Crystal Growth. **226**(2-3): pp. 231-239, 2001.
51. Shonai, T., Higuchi, M., Kodaira, K., Ogawa, T., Wada, S. and Machida, H., “*Float zone growth and laser performance of Nd: GdVO<sub>4</sub> single crystals*”. Journal of crystal growth. **241**(1-2): pp. 159-164, 2002.
52. Wünscher, M., Lüdge, A. and Riemann, H., “*Crucible-free pulling of germanium crystals*”. Journal of Crystal Growth. **318**(1): pp. 1039-1042, 2011.
53. Capper, P., *Bulk Crystal Growth—Methods and Materials*, in *Springer Handbook of Electronic and Photonic Materials*. 2006, Springer. p. 231-254.
54. Bridgman, P. *Various Physical Properties of Rubidium and Caesium and the Resistance of Potassium Under Pressure*. in *Proceedings of the American Academy of Arts and Sciences*. 1925. JSTOR.
55. Koai, K., Sonnenberg, K. and Wenzl, H., “*Influence of crucible support and radial heating on the interface shape during vertical Bridgman GaAs growth*”. Journal of crystal growth. **137**(1-2): pp. 59-63, 1994.
56. Helmers, L., Schilz, J., Bähr, G. and Kaysser, W., “*Macrosegregation during Bridgman growth of Ge<sub>1-x</sub>Si<sub>x</sub> mixed crystals*”. Journal of crystal growth. **154**(1-2): pp. 60-67, 1995.

57. Chen, H., Li, R., Ge, C., Ge, X. and Xu, W., “*Growth of bismuth tellurite crystals by vertical Bridgman method*”. Journal of crystal growth. **281**(2-4): pp. 303-309, 2005.
58. Xiao, H., Chen, H., Xu, F., Jiang, C. and Yang, P., “*Bridgman growth of CdWO<sub>4</sub> single crystals*”. Journal of Crystal Growth. **310**(3): pp. 521-524, 2008.
59. Ma, D., Wang, F., Wu, Q., Bogner, S. and Bührig-Polaczek, A. *Innovations in Casting Techniques for Single Crystal Turbine Blades of Superalloys*. in *Superalloys 2016: Proceedings of the 13th International Symposium of Superalloys*. 2016. Wiley Online Library.
60. Ma, D., “*Novel casting processes for single-crystal turbine blades of superalloys*”. Frontiers of Mechanical Engineering. **13**(1): pp. 3-16, 2018.
61. Montakhab, M., Bacak, M. and Balikci, E., “*Low Melt Height Solidification of Superalloys*”. Metallurgical and Materials Transactions A. **47**(6): pp. 3031-3039, 2016.
62. Zharikov, E., Prihod'ko, L. and Storozhev, N., “*Fluid flow formation resulting from forced vibration of a growing crystal*”. Journal of Crystal Growth. **99**(1-4): pp. 910-914, 1990.
63. Gulliver, G., “*The quantitative effect of rapid cooling upon the constitution of binary alloys*”. J. Inst. Met. **9**(1): pp. 120-157, 1913.
64. Scheil, E., “*Bemerkungen zur schichtkristallbildung*”. Zeitschrift für Metallkunde. **34**(3): pp. 70-72, 1942.
65. Smith, V.G., Tiller, W.A. and Rutter, J., “*A mathematical analysis of solute redistribution during solidification*”. Canadian Journal of Physics. **33**(12): pp. 723-745, 1955.
66. Tiller, W., Jackson, K., Rutter, J. and Chalmers, B., “*The redistribution of solute atoms during the solidification of metals*”. Acta metallurgica. **1**(4): pp. 428-437, 1953.

67. Burton, J., Prim, R. and Slichter, W., "*The distribution of solute in crystals grown from the melt. Part I. Theoretical*". The journal of chemical physics. **21**(11): pp. 1987-1991, 1953.
68. Pfann, W.G., "*Zone melting*". Metallurgical Reviews. **2**(1): pp. 29-76, 1957.
69. Billig, E., "*Some defects in crystals grown from the melt-I. Defects caused by thermal stresses*". Proc. R. Soc. Lond. A. **235**(1200): pp. 37-55, 1956.
70. Bennett, D. and Sawyer, B., "*Single crystals of exceptional perfection and uniformity by zone leveling*". Bell Labs Technical Journal. **35**(3): pp. 637-660, 1956.
71. Cressell, I. and Powell, J., "*Progress in Semiconductors*". II (London, 1956). pp. 137-164, 1957.
72. Penning, P., "*Generation of imperfections in germanium crystals by thermal strain*". Philips' Research Reports. **13**: pp. 79, 1958.
73. Rosi, F., "*Effect of crystal growth variables on electrical and structural properties of germanium*". RCA REVIEW. **19**(3): pp. 349-387, 1958.
74. Belyaev, A., Vasilevskaya, V. and Miselyuk, E., "*Investigation of The Effect of Certain Factors on Formation of Dislocations During Crystallization And on The Dislocation States In Germanium Monocrystals*". Soviet Physics-Solid State. **2**(2): pp. 208-214, 1960.
75. Klapper, H., "*Generation and propagation of dislocations during crystal growth*". Materials chemistry and physics. **66**(2-3): pp. 101-109, 2000.
76. Rittenhouse, T.L., *Single crystal growth and characterization of silicon germanium alloys*, Massachusetts Inst of Tech Cambridge Dept of Materials Science and Engineering, 1999.
77. Goss, A., Benson, K. and Pfann, W., "*Dislocations at compositional fluctuations in germanium-silicon alloys*". Acta Metallurgica. **4**(3): pp. 332-333, 1956.



78. Brock, G. and Aliotta, C., "*Direct Observation of Dislocation Loops in Arsenic-Doped Germanium [Letter to the Editor]*". IBM Journal of Research and Development. **6**(3): pp. 372-374, 1962.
79. Mitchell, J.W., "*Equilibration of Lattice Defects in Real Crystals*". Journal of Applied Physics. **33**(1): pp. 406-413, 1962.
80. Hull, D. and Bacon, D.J., *Introduction to dislocations*: Butterworth-Heinemann, 2001.
81. Claeys, C. and Simoen, E., *Fundamental and technological aspects of extended defects in Germanium*: Springer, 2008.
82. McKelvey, J. and Longini, R., "*Volume and surface recombination rates for injected carriers in germanium*". Journal of Applied Physics. **25**(5): pp. 634-641, 1954.
83. Ellis, S., "*Dislocations in germanium*". Journal of Applied Physics. **26**(9): pp. 1140-1146, 1955.
84. Allen, J. and Smith, K., "*XLVII. Electron Microscopy of Etched Germanium Surfaces*". International Journal Of Electronics. **1**(4): pp. 439-443, 1956.
85. Pfann, W. and Vogel Jr, F., "*Observations on the dislocation structure of germanium crystals*". Acta Metallurgica. **5**(7): pp. 377-384, 1957.
86. Bell, R., "*The Crystalline Perfection of Some Semiconductor Single Crystals*". INTERNATIONAL JOURNAL OF ELECTRONICS. **3**(5): pp. 487-493, 1957.
87. Bardsley, W., Bell, R. and Straughan, B., "*Dislocation Etch Pits in Germanium*". International Journal Of Electronics. **5**(1): pp. 19-28, 1958.
88. Trakhtenberg, A. and Fainshtein, S., "*EXPOSURE OF DISLOCATIONS IN GERMANIUM AND SILICON BY ETCHING*". SOVIET PHYSICS-SOLID STATE. **1**(3): pp. 335-340, 1959.
89. Pugh, E. and Samuels, L., "*A Metallographic Investigation of the Damaged Layer in Abraded Germanium Surfaces*". Journal of The Electrochemical Society. **108**(11): pp. 1043-1047, 1961.

90. Vasilevskaya, V. and Miselyuk, E., "*The Problem of Visualization of Dislocations in Germanium by Etching*". SOVIET PHYSICS-SOLID STATE. **3**(2): pp. 313-318, 1961.
91. Rutter, J.W. and Chalmers, B., "*A prismatic substructure formed during solidification of metals*". Canadian Journal of Physics. **31**(1): pp. 15-39, 1953.
92. Mullins, W.W. and Sekerka, R., *Stability of a planar interface during solidification of a dilute binary alloy*, in *Dynamics of Curved Fronts*. 1988, Elsevier. p. 345-352.
93. Favier, J. and Rouzaud, A., "*Morphological stability of the solidification interface under convective conditions*". Journal of crystal growth. **64**(2): pp. 367-379, 1983.
94. Sheikhi, A., Yousefi L, P. and Balikci, E., "*Growing Single Crystals with a Low Melt Height and an Axial Vibration*". Crystal Growth & Design. **16**(4): pp. 2429-2440, 2016.
95. Karma, A. and Rappel, W.-J., "*Phase-field method for computationally efficient modeling of solidification with arbitrary interface kinetics*". Physical Review E. **53**(4): pp. R3017, 1996.
96. Wang, S.-L., Sekerka, R., Wheeler, A., Murray, B., Coriell, S., Braun, R. and McFadden, G., "*Thermodynamically-consistent phase-field models for solidification*". Physica D: Nonlinear Phenomena. **69**(1-2): pp. 189-200, 1993.
97. Boettinger, W.J., Warren, J.A., Beckermann, C. and Karma, A., "*Phase-field simulation of solidification*". Annual review of materials research. **32**(1): pp. 163-194, 2002.
98. Karma, A., "*Phase-field formulation for quantitative modeling of alloy solidification*". Physical Review Letters. **87**(11): pp. 115701, 2001.
99. Beckermann, C., Diepers, H.-J., Steinbach, I., Karma, A. and Tong, X., "*Modeling melt convection in phase-field simulations of solidification*". Journal of Computational Physics. **154**(2): pp. 468-496, 1999.
100. Wheeler, A.A., Boettinger, W.J. and McFadden, G.B., "*Phase-field model of solute trapping during solidification*". Physical Review E. **47**(3): pp. 1893, 1993.

101. Echebarria, B., Folch, R., Karma, A. and Plapp, M., “*Quantitative phase-field model of alloy solidification*”. Physical Review E. **70**(6): pp. 061604, 2004.
102. Chen, S., Merriman, B., Osher, S. and Smereka, P., “*A simple level set method for solving Stefan problems*”. Journal of Computational Physics. **135**(1): pp. 8-29, 1997.
103. Kim, Y.-T., Goldenfeld, N. and Dantzig, J., “*Computation of dendritic microstructures using a level set method*”. Physical Review E. **62**(2): pp. 2471, 2000.
104. Gibou, F., Fedkiw, R., Caflisch, R. and Osher, S., “*A level set approach for the numerical simulation of dendritic growth*”. Journal of Scientific Computing. **19**(1-3): pp. 183-199, 2003.
105. Sethian, J.A. and Straint, J., “*Crystal growth and dendritic solidification*”. Journal of Computational Physics. **98**(2): pp. 231-253, 1992.
106. Chen, S., Merriman, B., Kang, M., Caflisch, R.E., Ratsch, C., Cheng, L.-T., Gyure, M., Fedkiw, R.P., Anderson, C. and Osher, S., “*A level set method for thin film epitaxial growth*”. Journal of Computational Physics. **167**(2): pp. 475-500, 2001.
107. Zhang, H., Zheng, L., Prasad, V. and Hou, T., “*A curvilinear level set formulation for highly deformable free surface problems with application to solidification*”. Numerical Heat Transfer, Part B. **34**(1): pp. 1-30, 1998.
108. Yao, M. and Chait, A., “*An alternative formulation of the apparent heat capacity method for phase-change problems*”. Numerical Heat Transfer, Part B Fundamentals. **24**(3): pp. 279-300, 1993.
109. Civan, F. *Limitation in the apparent heat capacity formulation for heat transfer with phase change*. in *Proceedings of the Oklahoma Academy of Science*. 1987.
110. Basak, T. and Ayappa, K., “*Analysis of microwave thawing of slabs with effective heat capacity method*”. AIChE Journal. **43**(7): pp. 1662-1674, 1997.

111. Lamberg, P., Lehtiniemi, R. and Henell, A.-M., "*Numerical and experimental investigation of melting and freezing processes in phase change material storage*". International Journal of Thermal Sciences. **43**(3): pp. 277-287, 2004.
112. Salcudean, M. and Abdullah, Z., "*On the numerical modelling of heat transfer during solidification processes*". International journal for numerical methods in engineering. **25**(2): pp. 445-473, 1988.
113. Yang, H. and He, Y., "*Solving heat transfer problems with phase change via smoothed effective heat capacity and element-free Galerkin methods*". International Communications in Heat and Mass Transfer. **37**(4): pp. 385-392, 2010.
114. Rolph, W.D. and Bathe, K.J., "*An efficient algorithm for analysis of nonlinear heat transfer with phase changes*". International Journal for Numerical Methods in Engineering. **18**(1): pp. 119-134, 1982.
115. Argyropoulos, S. and Guthrie, R., "*The Exothermic Dissolution of 50 wt.% Ferro-Silicon in Molten Steel*". Canadian Metallurgical Quarterly. **18**(3): pp. 267-281, 1979.
116. Argyropoulos, S.A. and Guthrie, R.I., "*The dissolution of titanium in liquid steel*". Metallurgical Transactions B. **15**(1): pp. 47-58, 1984.
117. Voller, V. and Swaminathan, C., "*ERAL Source-based method for solidification phase change*". Numerical Heat Transfer, Part B Fundamentals. **19**(2): pp. 175-189, 1991.
118. Voller, V., Swaminathan, C. and Thomas, B.G., "*Fixed grid techniques for phase change problems: a review*". International Journal for Numerical Methods in Engineering. **30**(4): pp. 875-898, 1990.
119. Voller, V., Cross, M. and Markatos, N., "*An enthalpy method for convection/diffusion phase change*". International journal for numerical methods in engineering. **24**(1): pp. 271-284, 1987.
120. Voller, V.R. and Prakash, C., "*A fixed grid numerical modelling methodology for convection-diffusion mushy region phase-change problems*". International Journal of Heat and Mass Transfer. **30**(8): pp. 1709-1719, 1987.

121. Hu, H. and Argyropoulos, S.A., “*Mathematical modelling of solidification and melting: a review*”. Modelling and Simulation in Materials Science and Engineering. **4**(4): pp. 371, 1996.
122. Valdes, L.B., “*Resistivity measurements on germanium for transistors*”. Proceedings of the IRE. **42**(2): pp. 420-427, 1954.
123. Sze, S. and Irvin, J., “*Resistivity, mobility and impurity levels in GaAs, Ge, and Si at 300 K*”. Solid-State Electronics. **11**(6): pp. 599-602, 1968.
124. Group, S., “*CGSim Flow Module Theory Manual, v. 8.12*”. St. Petersburg, Russia, 17th July. 2009.
125. Friedrich, J., “*CrysVun Flyer: Modeling of Crystal Growth*”. Fraunhofer Institute of Integrated Systems and Device Technology. 2007.
126. Fainberg, J., Vizman, D., Friedrich, J. and Mueller, G., “*A new hybrid method for the global modeling of convection in CZ crystal growth configurations*”. Journal of Crystal Growth. **303**(1): pp. 124-134, 2007.
127. Fainberg, J., Leister, H.-J. and Müller, G., “*Numerical simulation of the LEC-growth of GaAs crystals with account of high-pressure gas convection*”. Journal of crystal growth. **180**(3-4): pp. 517-523, 1997.
128. Treibig, J., Berler, S. and Rüde, U. *ORCAN: A platform for complex parallel simulation software*. in *ARCS Workshops*. 2006.
129. Dupret, F., Nicodeme, P., Ryckmans, Y., Wouters, P. and Crochet, M., “*Global modelling of heat transfer in crystal growth furnaces*”. International Journal of Heat and Mass Transfer. **33**(9): pp. 1849-1871, 1990.
130. Fluent, A., “*ANSYS fluent theory guide 15.0*”. Inc, Canonsburg, PA. 2013.
131. Mazur, D., Gołębiowski, M. and Korkosz, M., *Analysis and Simulation of Electrical and Computer Systems*: Springer, 2018.

132. *Tools and Basic Information for Design, Engineering and Construction of Technical Applications*, 2001, <https://www.engineeringtoolbox.com/>, accessed at June 2016.
133. Davis, R.F., Palmour, H. and Porter, R.L., *Emergent process methods for high-technology ceramics*: Springer Science & Business Media, Vol. 17. 2012.
134. Guo, K., Liu, C., Chen, S., Li, J. and Fu, Q. *Effect of atomization pressure on the flow field distribution of TC4 alloy powder prepared by EIGA*. in *IOP Conference Series: Materials Science and Engineering*. 2017. IOP Publishing.
135. Accuratus, *Aluminum Oxide, Al<sub>2</sub>O<sub>3</sub> Ceramic Properties*, 2013, <http://accuratus.com/alumox.html>, accessed at July 2016.
136. Potenza, M., Cataldo, A., Bovesecchi, G., Corasaniti, S., Coppa, P. and Bellucci, S., “*Graphene nanoplatelets: Thermal diffusivity and thermal conductivity by the flash method*”. *AIP Advances*. **7**(7): pp. 075214, 2017.
137. Sheppard, R., Mathes, D. and Bray, D., “*Properties and characteristics of graphite for the semiconductor industry*”. Poco Graphire Inc. 2001.
138. Takasuka, E., Tokizaki, E., Terashima, K. and Kimura, S., “*Emissivity of liquid germanium in visible and near infrared region*”. *Journal of applied physics*. **82**(5): pp. 2590-2594, 1997.
139. Dornberger, E., Tomzig, E., Seidl, A., Schmitt, S., Leister, H.-J., Schmitt, C. and Müller, G., “*Thermal simulation of the Czochralski silicon growth process by three different models and comparison with experimental results*”. *Journal of crystal growth*. **180**(3-4): pp. 461-467, 1997.
140. Allen, R.D., Glasier Jr, L.F. and Jordan, P.L., “*Spectral emissivity, total emissivity, and thermal conductivity of molybdenum, tantalum, and tungsten above 2300 K*”. *Journal of Applied Physics*. **31**(8): pp. 1382-1387, 1960.
141. Omega, *Table of Total Emissivity*, 2003, <https://www.omega.com/temperature/z/pdf/z088-089.pdf>, accessed at June 2016.

142. Trivedi, R., Karma, A., Lo, T., Mazumder, P., Park, J. and Plapp, M. *Dynamic pattern formation in the two-phase region of peritectic systems*. in *2nd Workshop on Solidification Microstructures*. 1998.
143. Meyer, S. and Ostrogorsky, A., “*Forced convection in vertical Bridgman configuration with the submerged heater*”. *Journal of crystal growth*. **171**(3-4): pp. 566-576, 1997.
144. Golyshev, V. and Gonik, M., “*Terrestrial experimental research of new method features of large single crystal growth*”. *Proc. Microgravity sci. and applications session, Int. Aerospace Congr., Moscow*. pp. 167-171, 1994.
145. Fedyushkin, A. and Bourago, N. *Impurity distribution in submerged heater method with and without rotation*. in *Proceedings of the Int. Conf. on Computational Heat and Mass Transfer*. 1999.
146. Avetisov, I., Bourago, N., Fedyushkin, A., Polezhev, V., Skorenko, A. and Zharikov, E. *The heat and mass transfer during direct crystallization under the vibrational influence*. in *Third Int. Conference “Single crystal growth, strength problem, and heat mass transfer”*. Obninsk. 1999.
147. Lyubimov, D., Lyubimova, T., Meradji, S. and Roux, B., “*Vibrational control of crystal growth from liquid phase*”. *Journal of crystal growth*. **180**(3-4): pp. 648-659, 1997.
148. Ivanova, A., Kozlov, V., Liubimov, D., Liubimova, T., Meragy, S. and Roux, B., “*Structure of averaged flow driven by a vibrating body with a large-curvature edge*”. *Fluid dynamics*. **33**(5): pp. 659-666, 1998.
149. Fedyushkin, A. and Bourago, N. *Influence of vibrations on boundary layers in Bridgman crystal growth*. in *Proceedings of 2 nd Pan Pacific Basin Workshop on Microgravity Sciences*. 2001.
150. Fedyushkin, A., Bourago, N., Polezhaev, V. and Zharikov, E. *Influence of vibration on heat and mass transfer during crystal growth in ground-based and microgravity environments*. in *2nd Pan Pacific Basin Workshop on Microgravity Sciences*. 2001.

151. Avetisov, I.C. *Axial vibrational control: the novel method for crystal growth from liquid phase*/I. Ch. Avetisov, A. Yu. Zinovjev, MV Romanenkov, LV Romanenkova, EV Zharikov. in *II France– Russia Seminar «New achievements in materials science»: Book of Abstracts.*– M.(Russia). 2005.
152. Zharikov, E.V., “*Advanced Technologies of Crystal Growth from Melt Using Vibrational Influence*”. Crystal Growth Technology: Semiconductors and Dielectrics. 2010.
153. Avetissov, I., Sadovskiy, A., Belov, S., Khomyakov, A., Rekunov, K., Kostikov, V. and Sukhanova, E., “*Thermodynamic features of axial vibrational control technique for crystal growth from the melt*”. CrystEngComm. **15**(12): pp. 2213-2219, 2013.
154. Claeys, C. and Simoen, E., *Germanium-based technologies: from materials to devices*: elsevier, 2011.
155. Indenbom, V., “*Ein Beitrag zur Entstehung von Spannungen und Versetzungen beim Kristallwachstum*”. Crystal Research and Technology. **14**(5): pp. 493-507, 1979.
156. Matsumoto, F., Okano, Y., Yonenaga, I., Hoshikawa, K., Rudolph, P. and Fukuda, T. *Growth of < 100> InP single crystals by the liquid encapsulated vertical Bridgman method using a flat-bottom crucible.* in *Indium Phosphide and Related Materials, 1994. Conference Proceedings., Sixth International Conference on.* 1994. IEEE.
157. Taishi, T., Huang, X., Wang, T., Yonenaga, I. and Hoshikawa, K., “*Behavior of dislocations due to thermal shock in B-doped Si seed in Czochralski Si crystal growth*”. Journal of crystal growth. **241**(3): pp. 277-282, 2002.
158. Balikci, E. and Abbaschian, R., “*The Seebeck coefficient of the solid and liquid germanium*”. Journal of materials science. **40**(6): pp. 1475-1479, 2005.
159. Tiller, W., “*Production of dislocations during growth from the melt*”. Journal of Applied Physics. **29**(4): pp. 611-618, 1958.
160. Dash, W.C., “*Growth of silicon crystals free from dislocations*”. Journal of Applied Physics. **30**(4): pp. 459-474, 1959.



161. Kurtz, A., Kulin, S. and Averbach, B., “*Effect of dislocations on the minority carrier lifetime in semiconductors*”. Physical Review. **101**(4): pp. 1285, 1956.

## APPENDIX A: FLUENT GRAPHICAL USER INTERFACE (GUI) FIGURES

The figures of different settings of ANSYS Fluent solver for solving the solidification/melting problem of a pure metal without species (mentioned in Section 4.2.1.2) are presented in Figure A.1 to Figure A.6. Also the differences made for the solution of solidification/melting of a binary alloy with species that are mentioned in Section 5.3.1 are in Figure A.7 to Figure A.9.

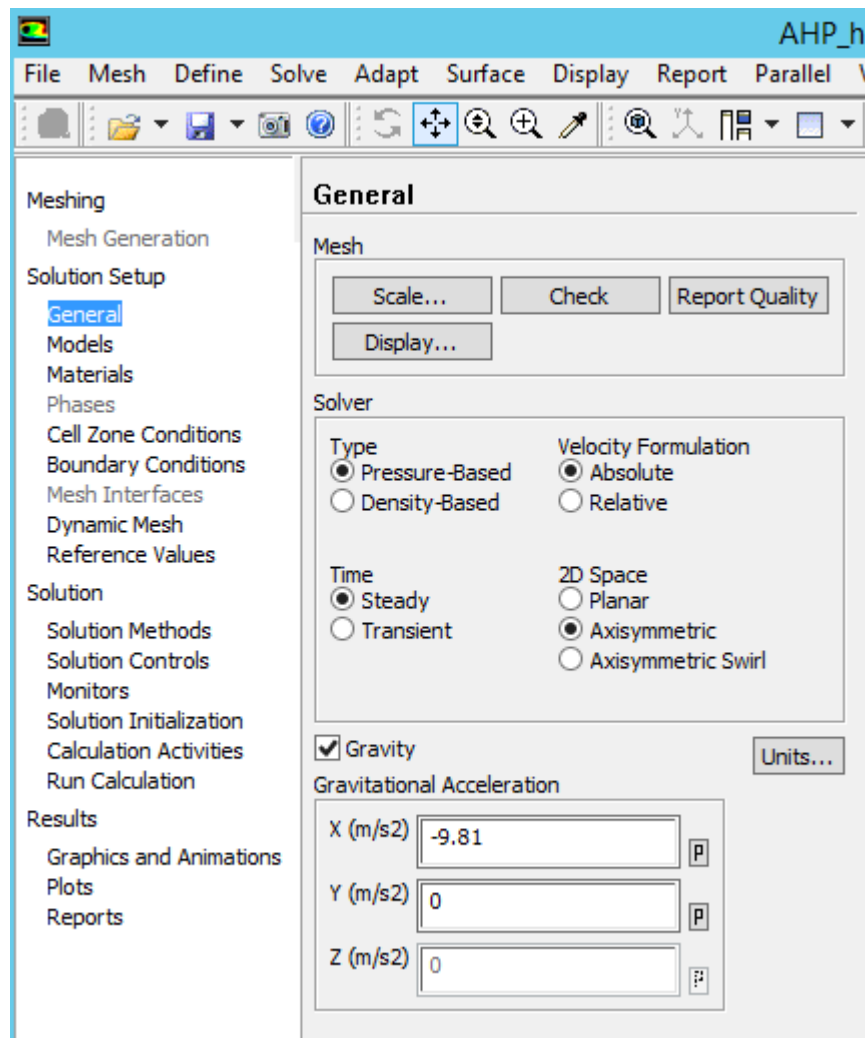


Figure A.1. Solver selection.

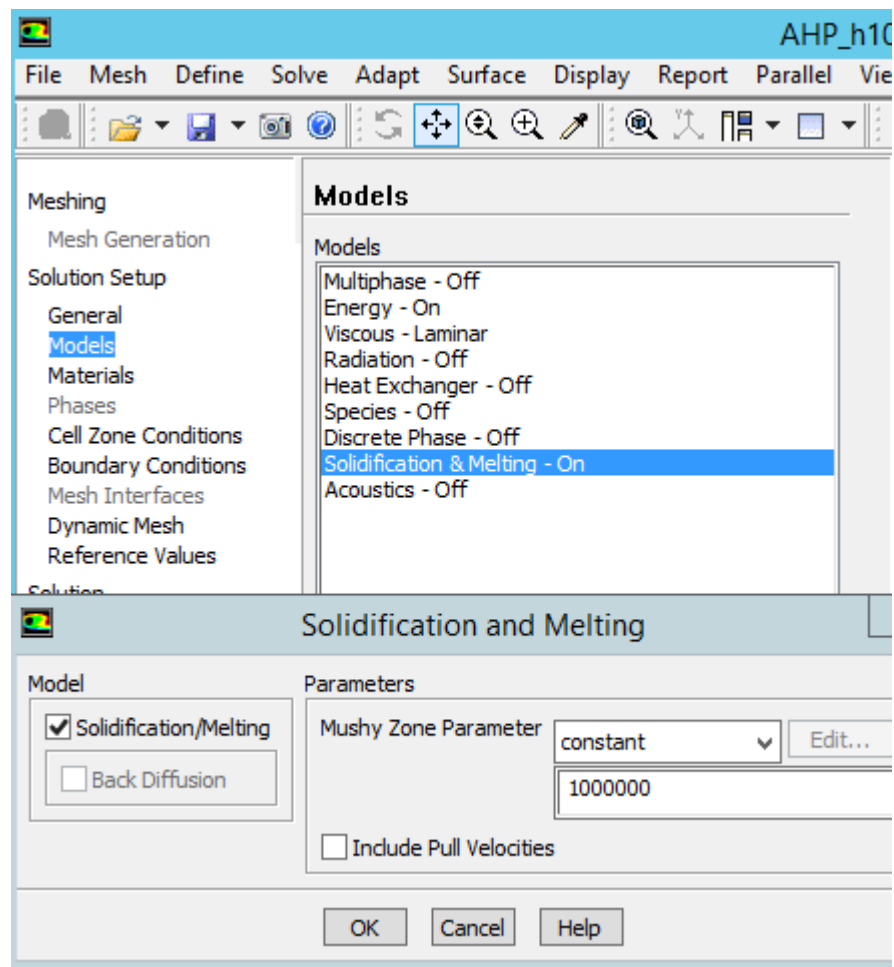


Figure A.2. Solidification and Melting model parameters.

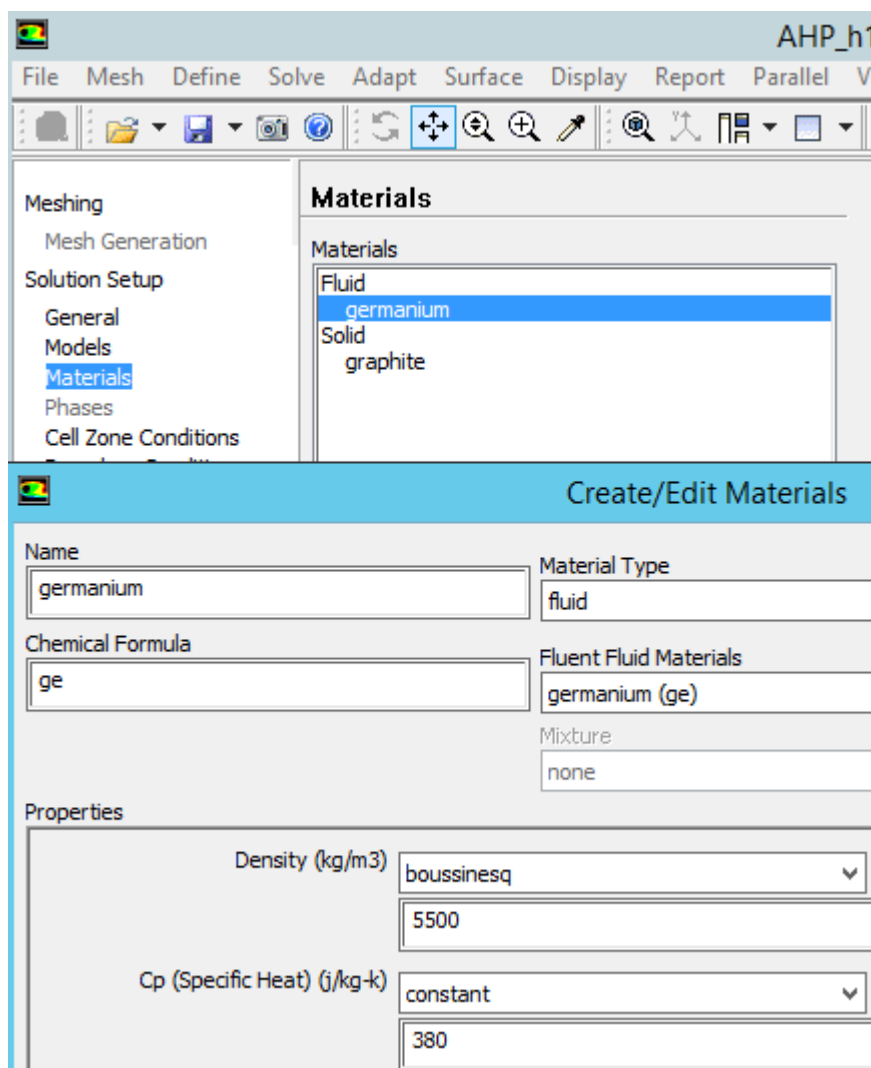


Figure A.3. Selecting Boussinesq option for density of germanium.

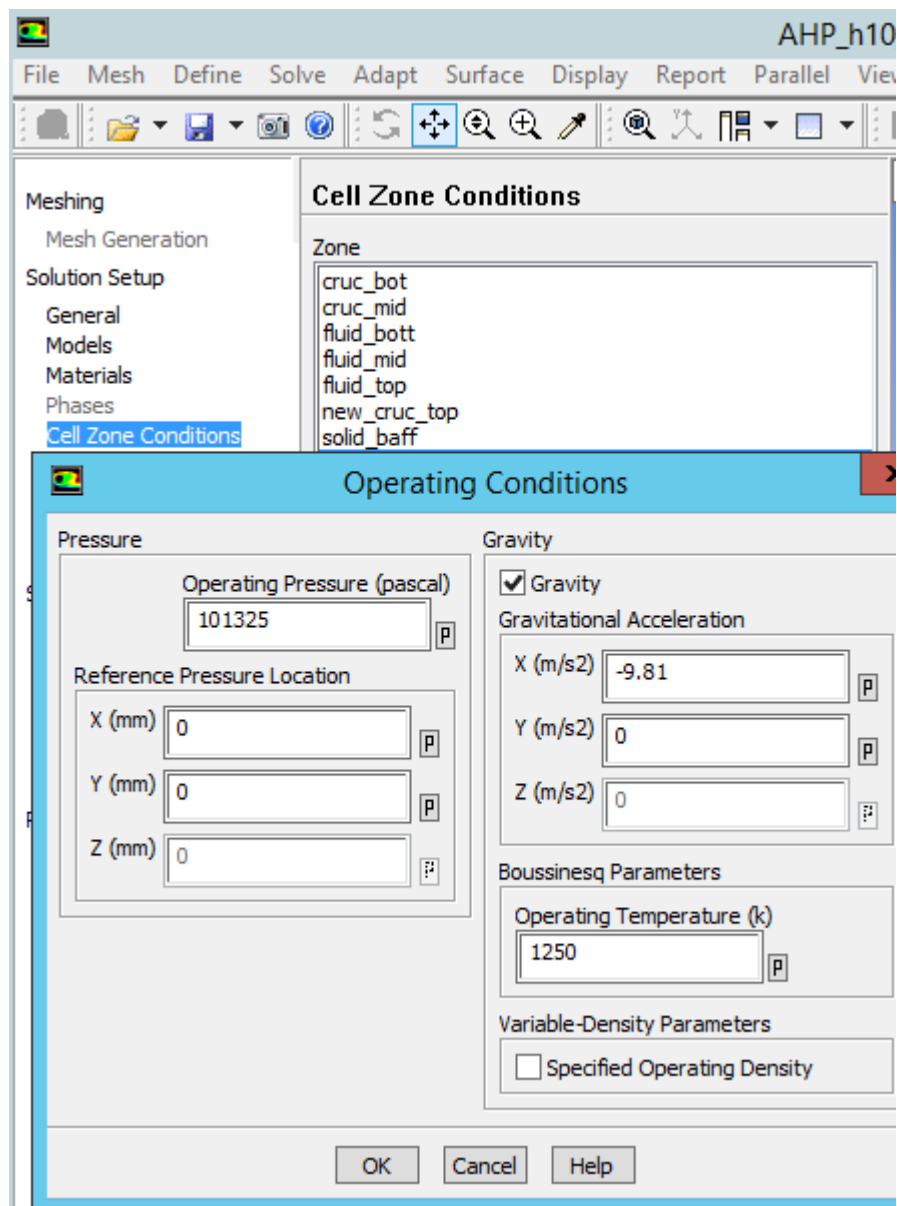


Figure A.4. Operating conditions.

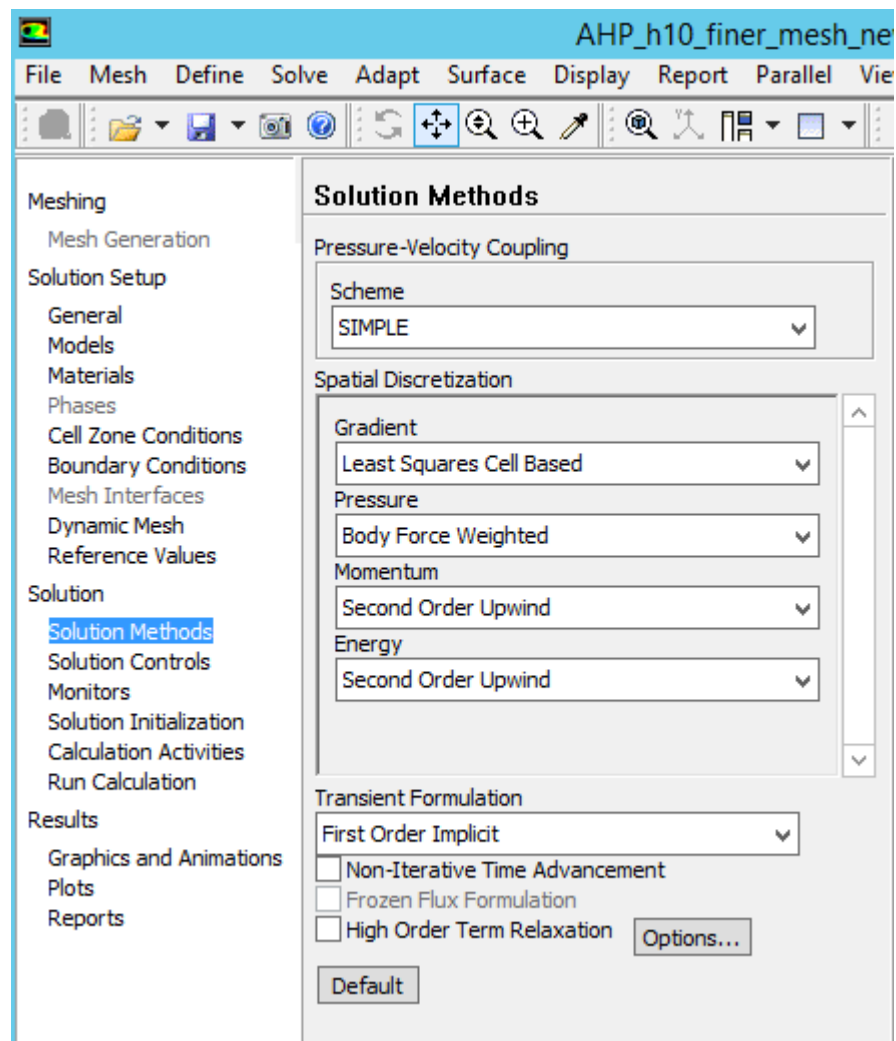


Figure A.5. Solution methods.

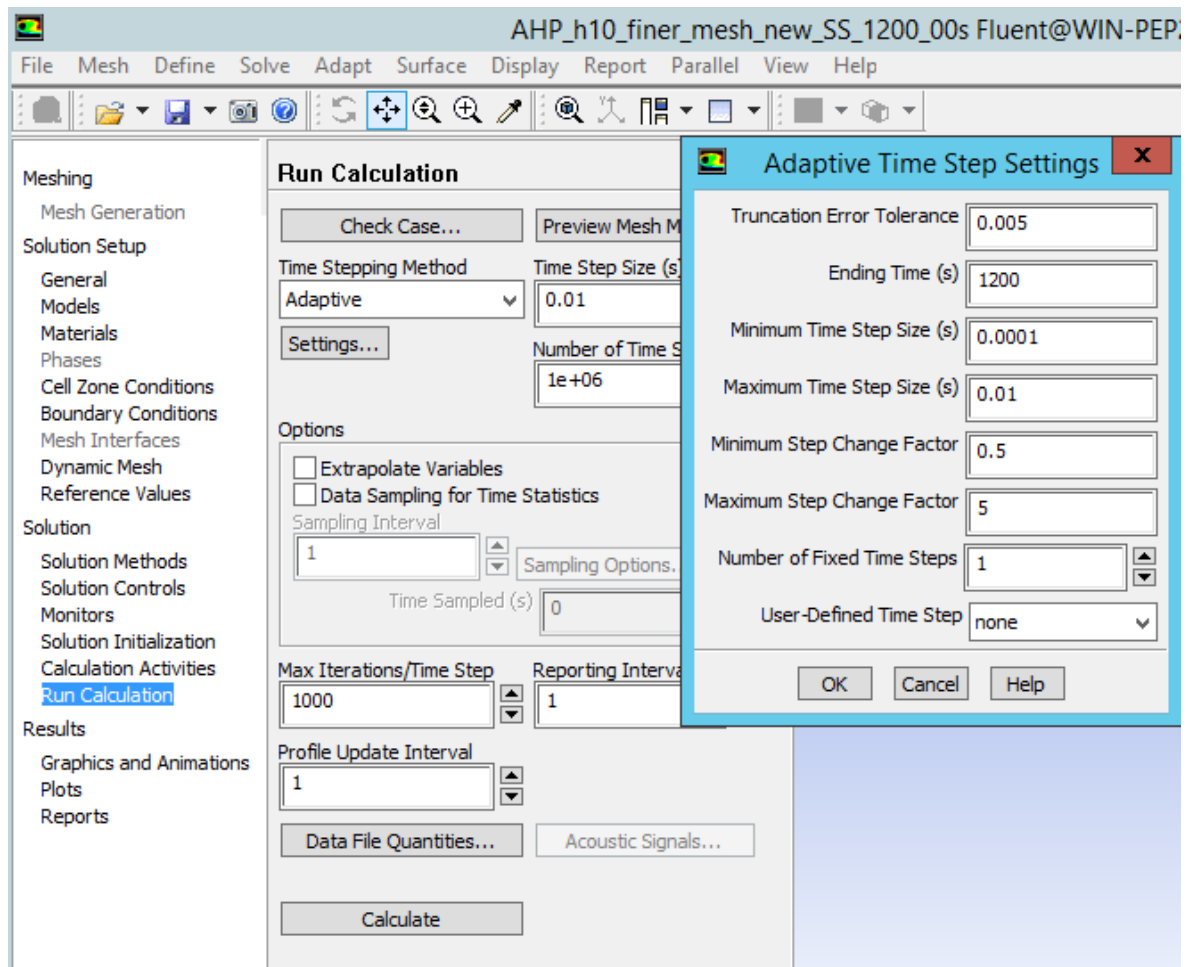


Figure A.6. Time step settings.

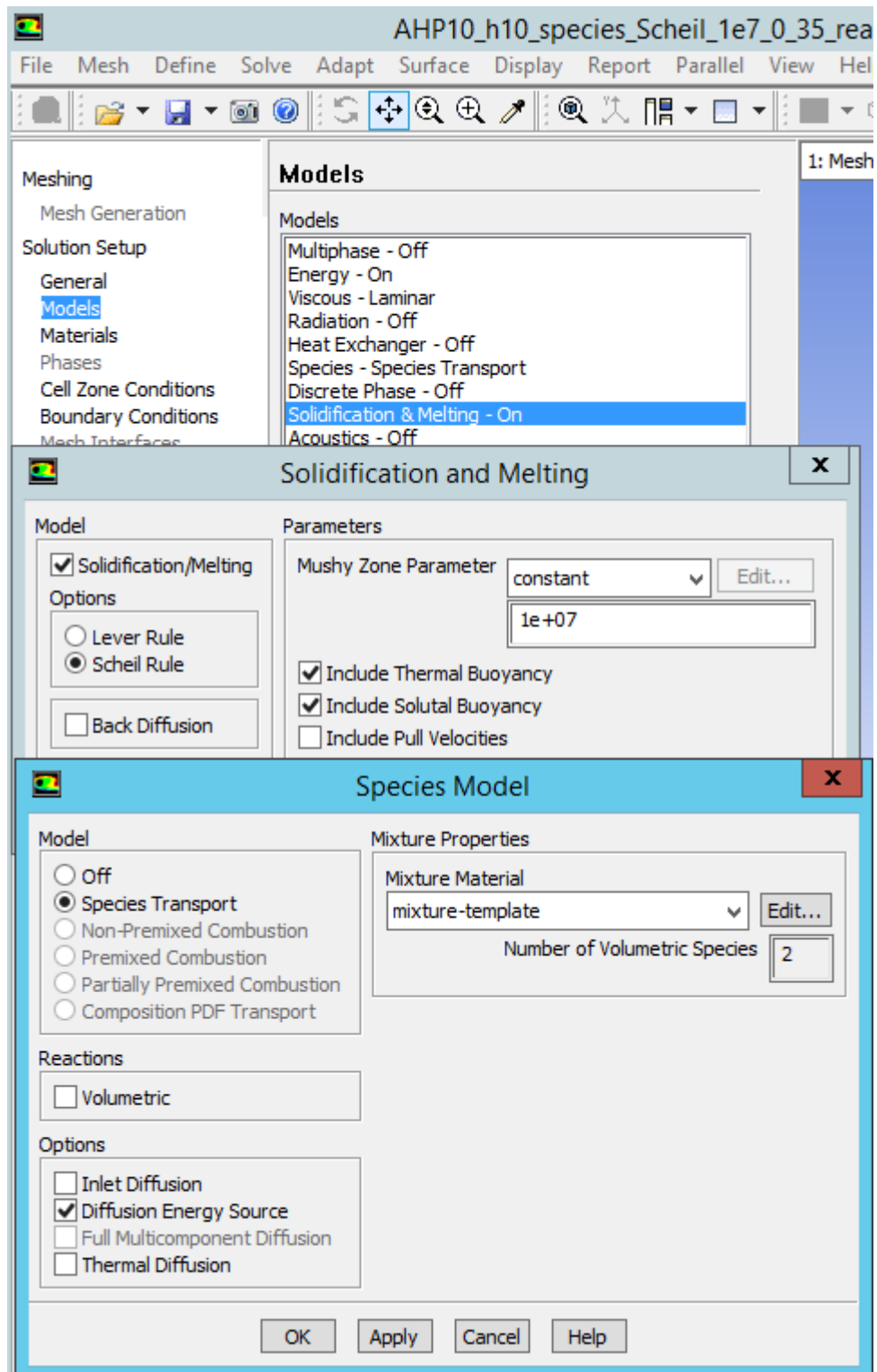


Figure A.7. Species model.



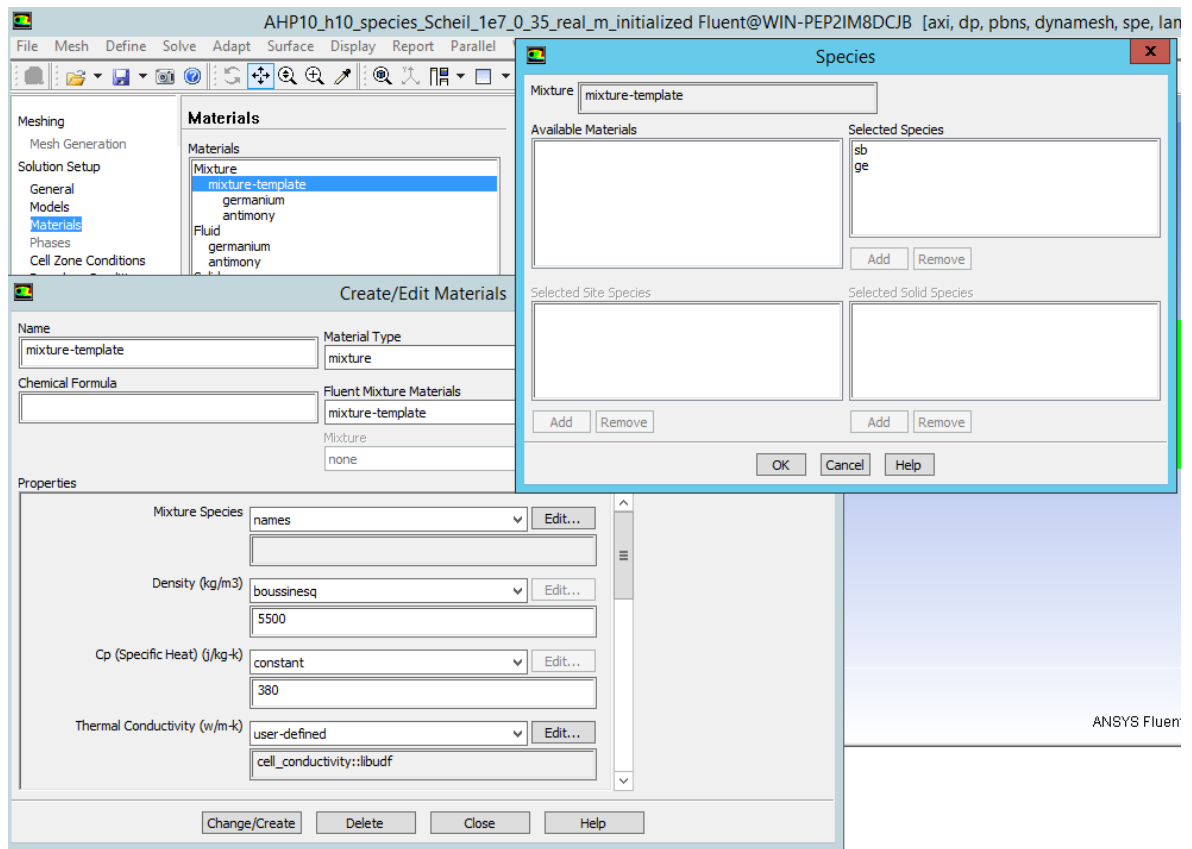


Figure A.8. Mixture setting.

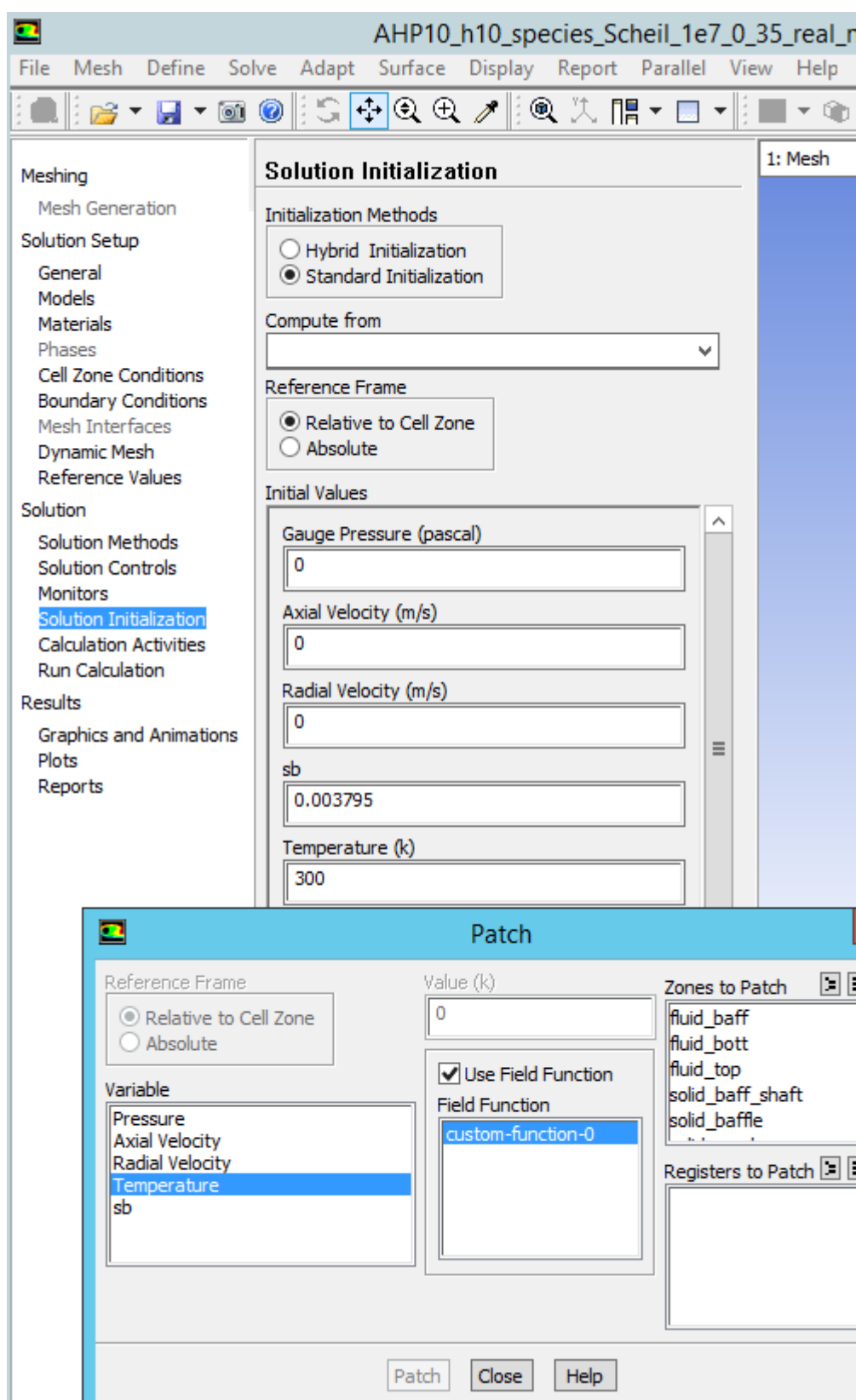


Figure A.9. Initialization and patching the solute and temperature fields.

## APPENDIX B: DISLOCATION FIGURES

Dislocations at different radial and axial positions of the grown crystals are shown in the following figures.

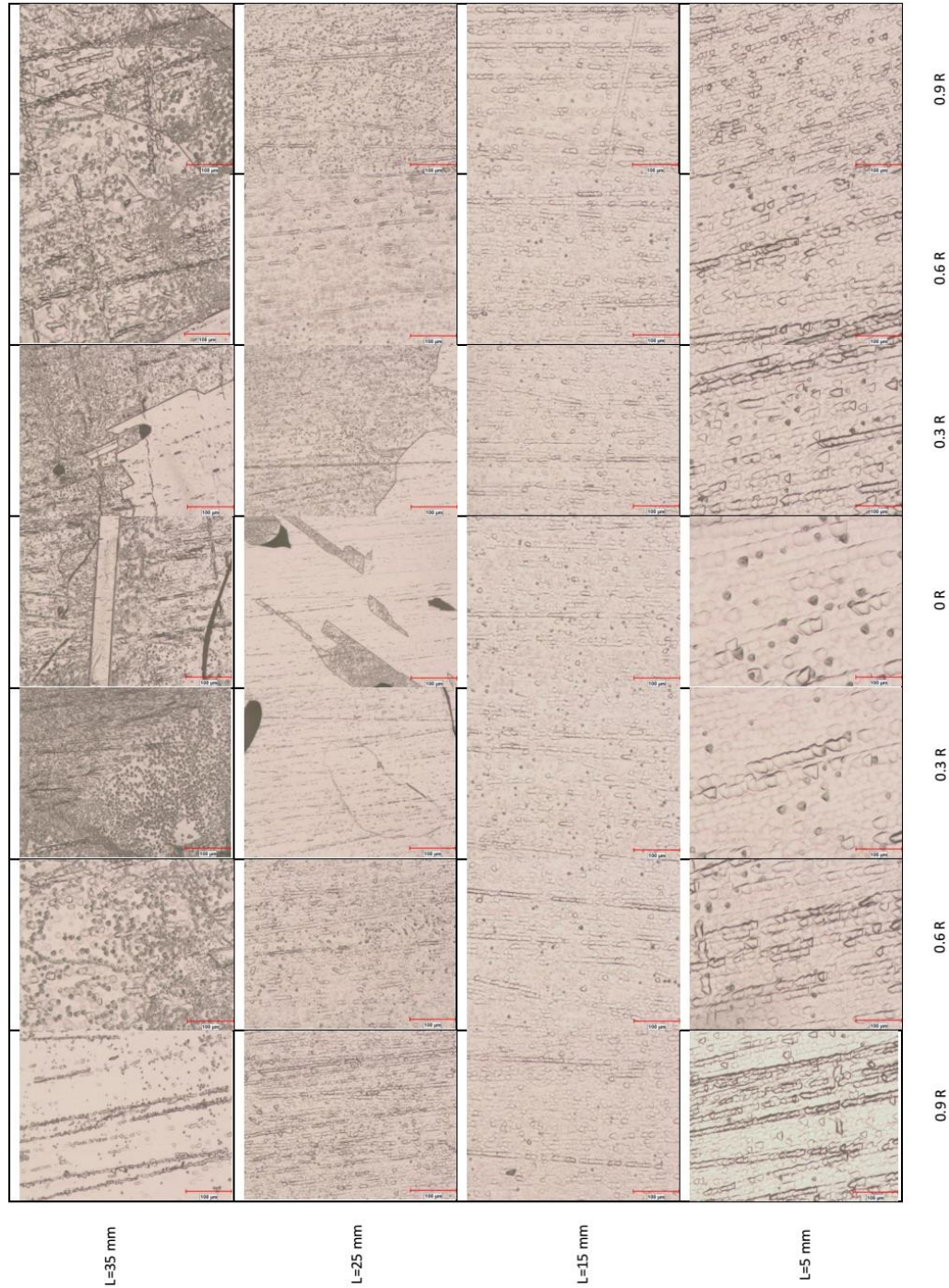


Figure B.1. Dislocations at different radial and axial positions in VB20-58.



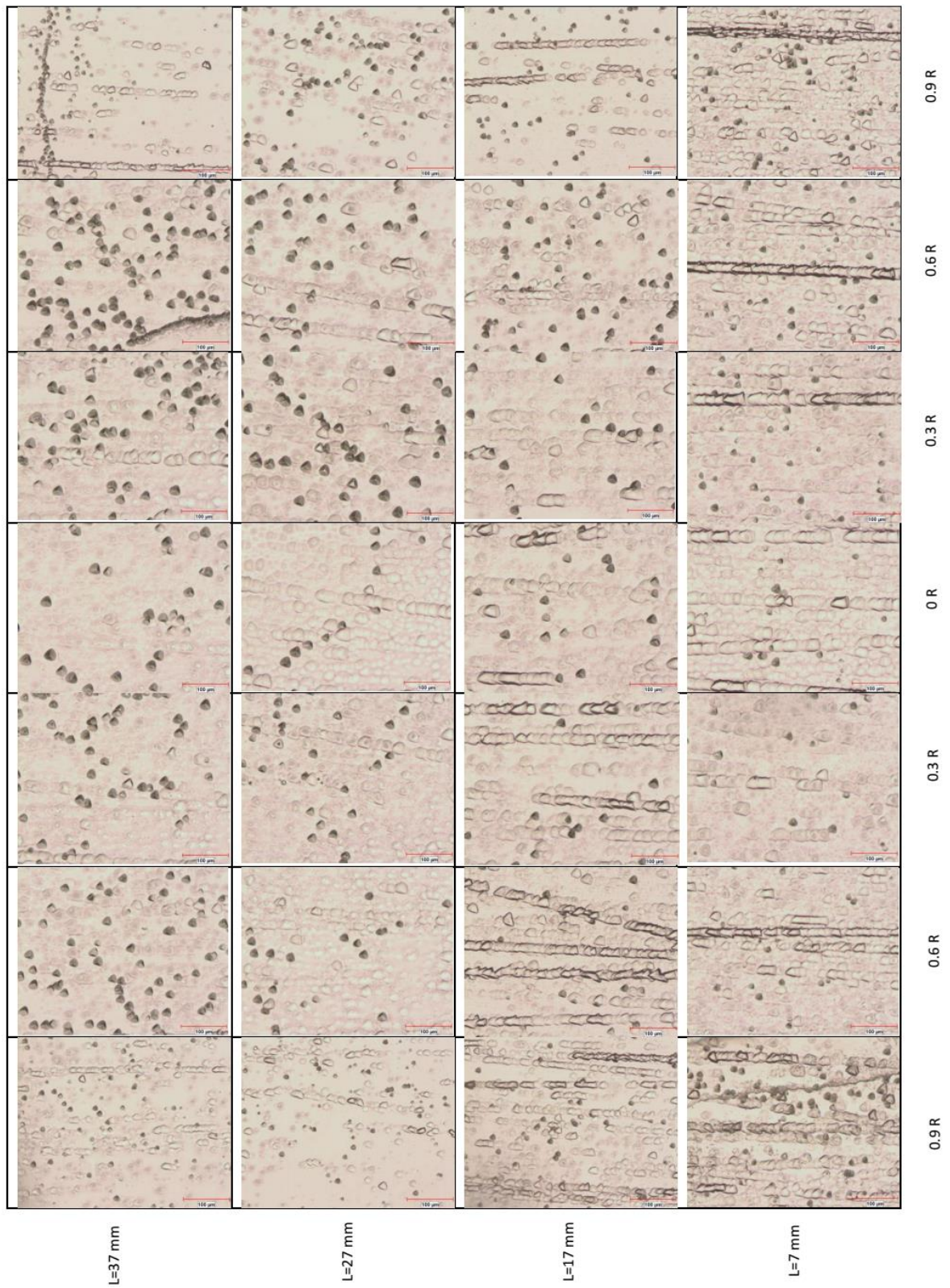


Figure B.2. Dislocations at different radial and axial positions in AHP10-10.



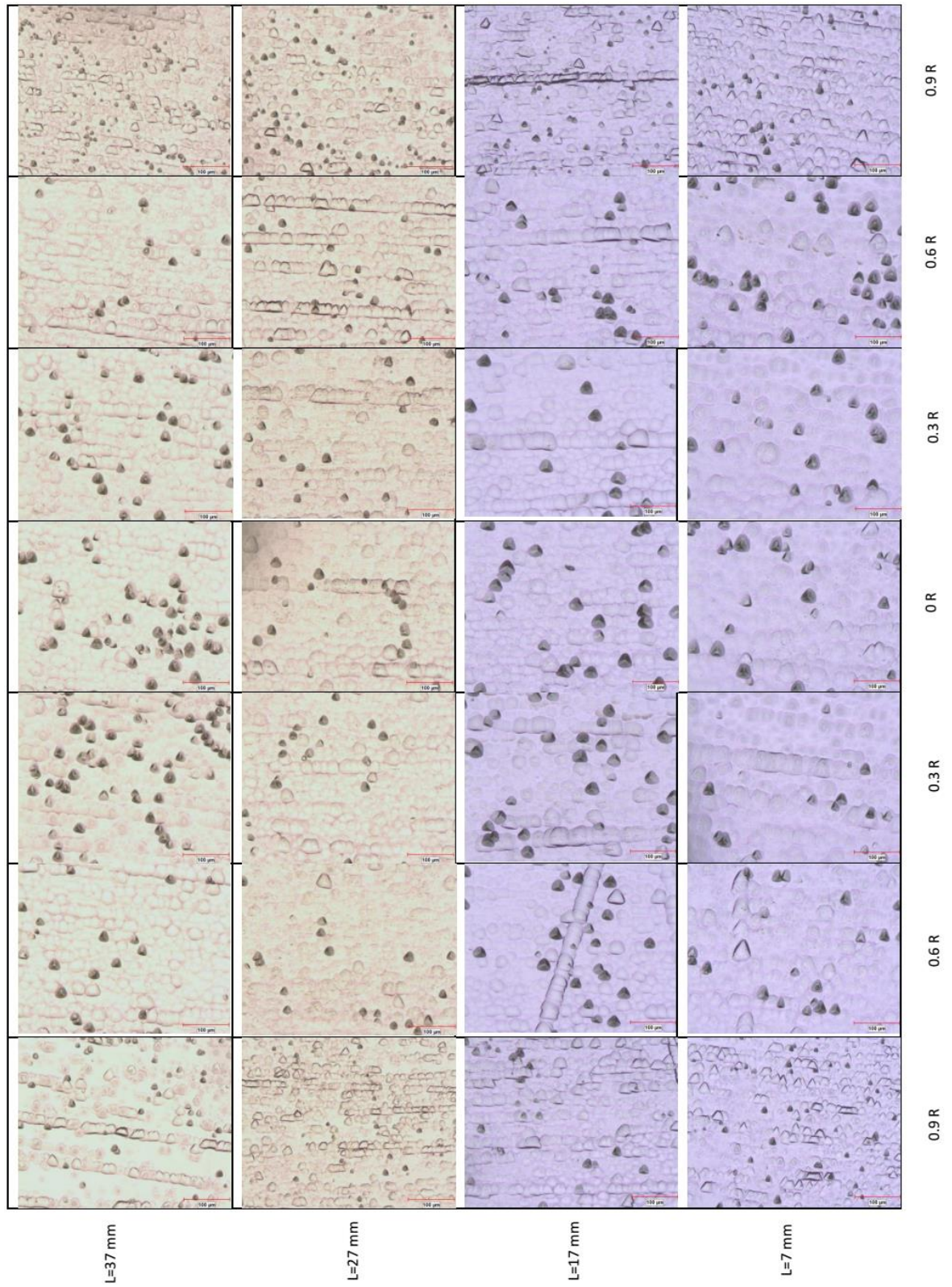


Figure B.3. Dislocations at different radial and axial positions in AHP20-5.



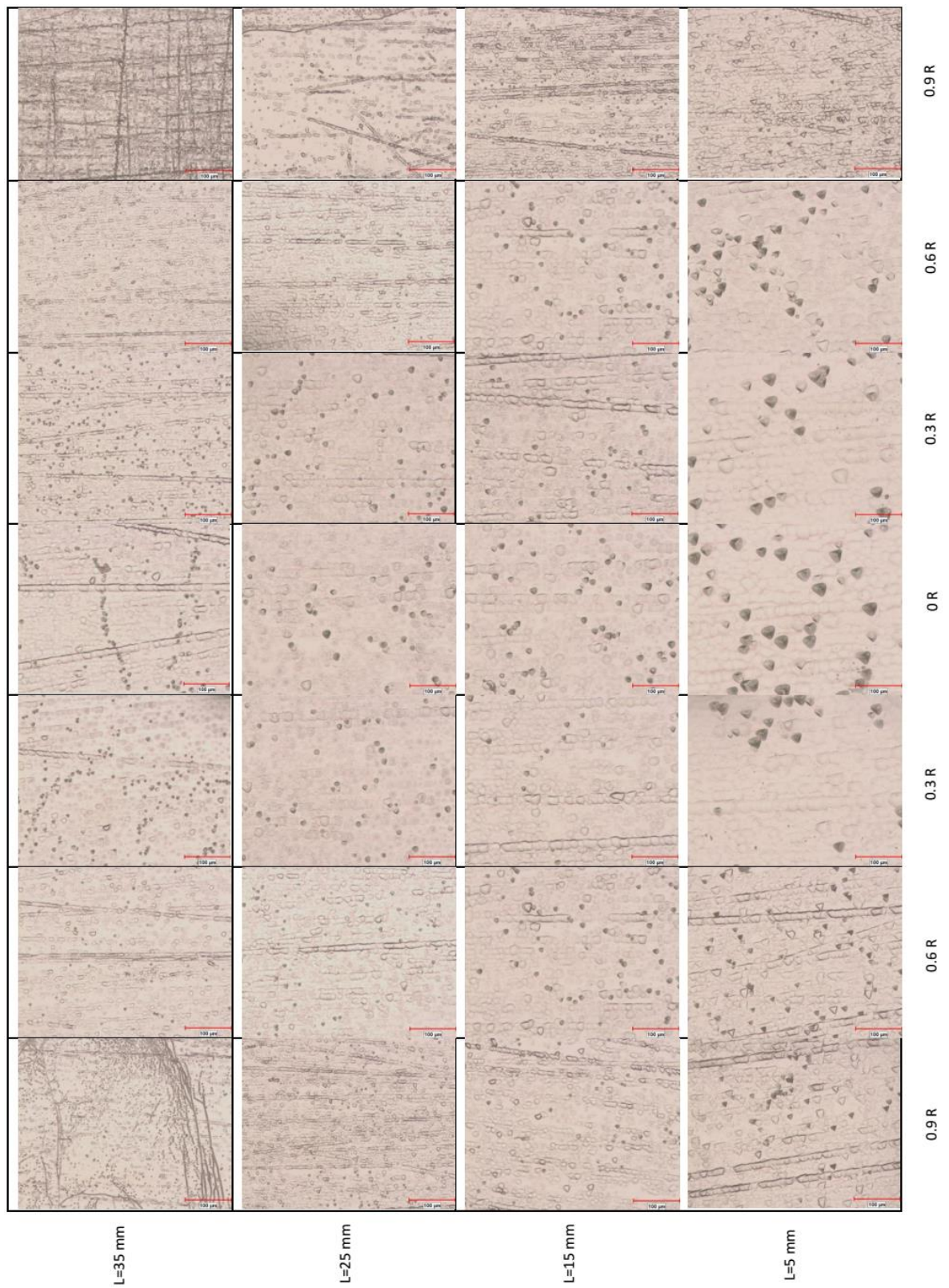


Figure B.4. Dislocations at different radial and axial positions in AHP20-14.

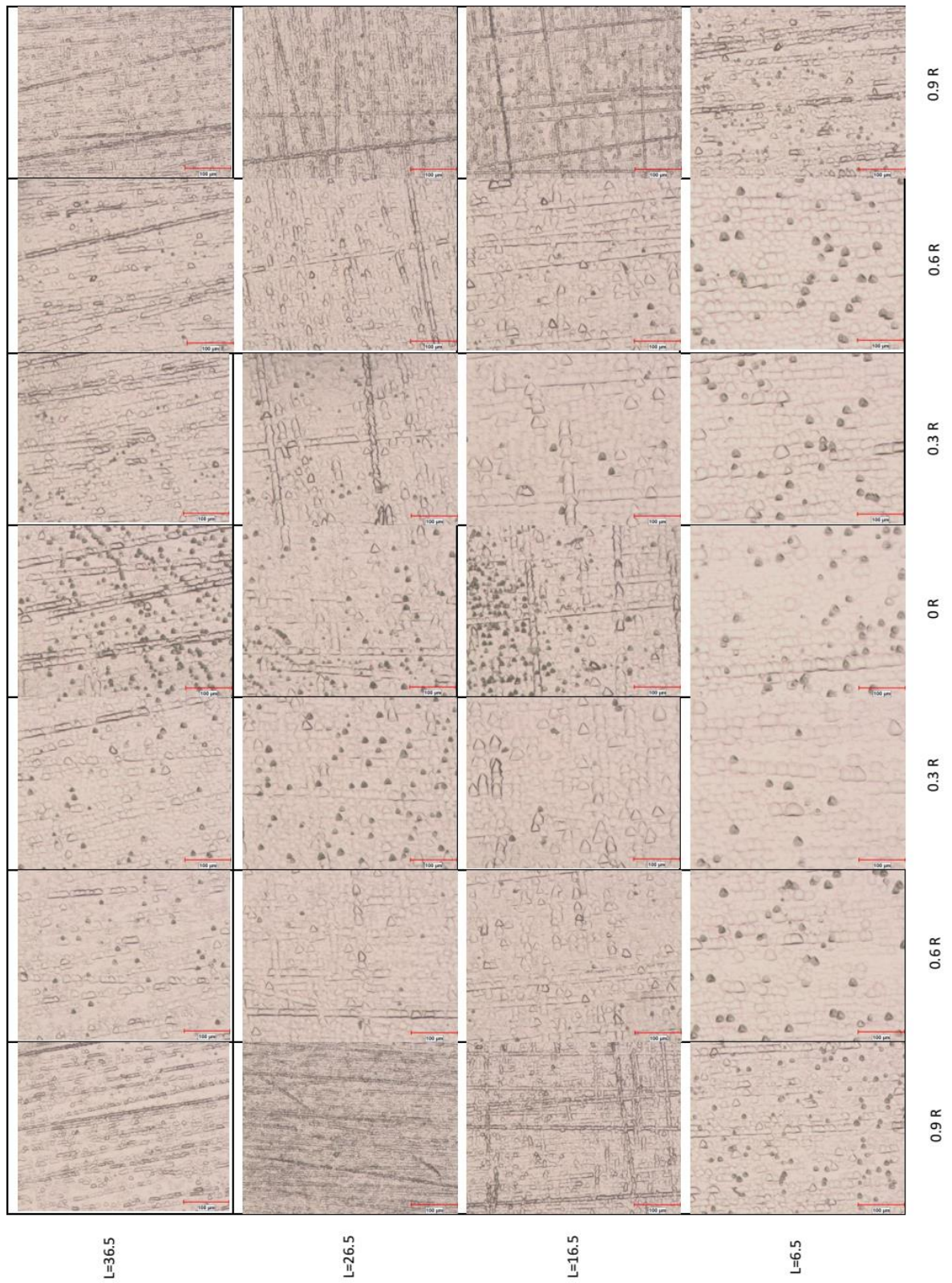


Figure B.5. Dislocations at different radial and axial positions in AVC20-10-2-0.25.



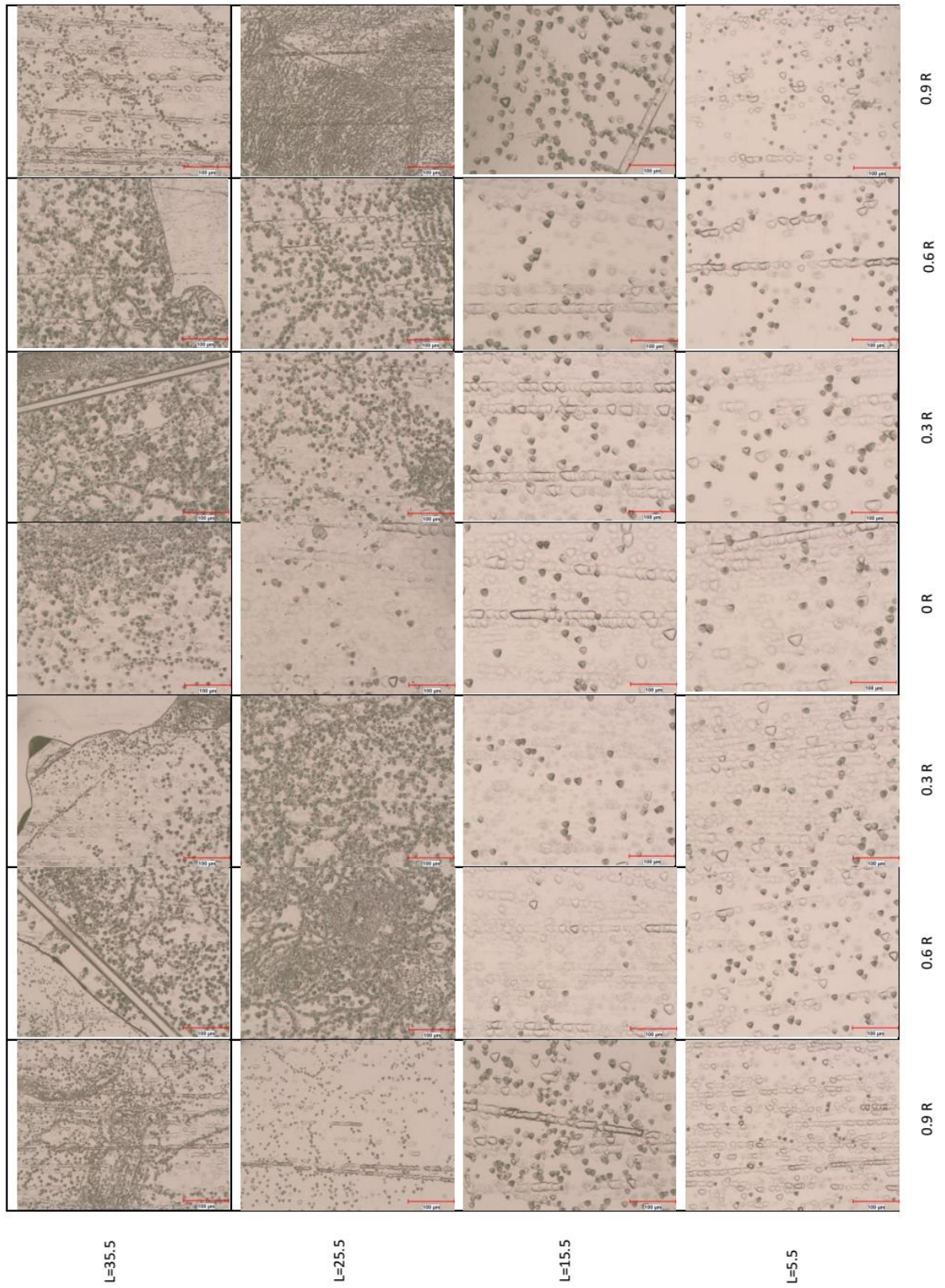


Figure B.6. Dislocations at different radial and axial positions in AVC20-15-0.25-25.